

## The tectonics of the Central Anatolian Crystalline Complex a structural, metamorphic and paleomagnetic study

Côme Lefebvre

**The tectonics of the Central Anatolian Crystalline Complex:  
a structural, metamorphic and paleomagnetic study**

*Côme Lefebvre*

UTRECHT STUDIES IN EARTH SCIENCES

No. 003

Members of the dissertation committee:

Dr. F.M. Brouwer  
Faculteit der Aard- en Levenswetenschappen, Vrije Universiteit  
Amsterdam, The Netherlands

Prof. dr. R. Oberhänsli  
Institut für Erd- und Umweltwissenschaften, Universität Potsdam  
Potsdam, Germany

Prof. dr. A.I. Okay  
Avrasya Yerbilimleri Enstitüsü, Istanbul Teknik Üniversitesi  
Istanbul, Turkey

Prof. dr. S.M. Schmid  
Institut für Geophysik, ETH Zürich  
Zürich, Switzerland

Prof. dr. M.J.R. Wortel  
Departement Aardwetenschappen, Universiteit Utrecht  
Utrecht, The Netherlands

The research of this thesis was carried out at:

Structural Geology and Tectonics group  
Department of Earth Sciences  
Faculty of Geosciences  
Utrecht University  
Budapestlaan 4  
3584 CD Utrecht  
The Netherlands

ISBN: 978-90-6266-283-8

Cover illustration:

*top*: Panorama view of the Ömerhacılı area (west of Kırşehir).

*bottom*: Micrograph of a calcite protomylonite from the Kaman area.

# **The tectonics of the Central Anatolian Crystalline Complex: a structural, metamorphic and paleomagnetic study**

Orta Anadolu Kristalen Kompleksinin tektoniği:  
yapısal, metamorfik ve paleomanyetik bir çalışma  
(Türkçe Öz ile birlikte)

La tectonique du Complexe Cristallin d'Anatolie Centrale:  
une étude structurale, métamorphique et paléomagnétique  
(avec un résumé en français)

De tektoniek van het Centraal Anatolische Kristallijne Complex:  
een structurele, metamorfe en paleomagnetische studie  
(met een samenvatting in het Nederlands)

Proefschrift

ter verkrijging van de graad van doctor aan de Universiteit Utrecht op gezag van de rector magnificus,  
prof.dr. G.J. van der Zwaan, ingevolge het besluit van het college voor promoties in het openbaar te  
verdedigen op vrijdag 11 november 2011 des ochtends te 10.30 uur

door

Côme Jean Charles Lefebvre

geboren op 23 november 1983  
te Lyon, Frankrijk

Promotor: Prof. dr. R.L.M. Vissers  
Co-promotoren: Dr. D.J.J. van Hinsbergen  
Dr. N. Kaymakci

This thesis was accomplished with financial support from the Netherlands Research Centre for Integrated Solid Earth Sciences (ISES), the Netherlands Organisation for Scientific Research (NWO) and the DARIUS Programme.

Copyright © 2011 Côme Lefebvre

Niets uit deze uitgave mag worden vermenigvuldigd en/of openbaar gemaakt door middel van druk, fotokopie of op welke andere wijze dan ook zonder voorafgaande schriftelijke toestemming van de uitgever.

All rights reserved. No part of this publication may be reproduced in any form, by print or photo print, microfilm or any other means, without written permission by the publishers.



## Table of contents

<b>Bibliography</b>	<b>9</b>
<b>Abstract</b>	<b>10</b>
<b>Öz</b>	<b>11</b>
<b>Résumé</b>	<b>12</b>
<b>Samenvatting</b>	<b>13</b>
<b>Introduction</b>	<b>15</b>
<b>Chapter 1</b>	
<b>Late Cretaceous extensional denudation along a marble detachment fault zone in the Kırşehir massif near Kaman, Central Turkey</b>	<b>19</b>
Abstract	
1.1 Introduction	20
1.2 Geological setting	21
1.3 Characteristics of the contact between the CAM and CAO in the vicinity of Kaman	24
1.4 The contact between the Kırşehir metamorphics and the Baranadağ quartz monzonite close to Ömerhacılı	31
1.5 Synthesis - Discussion	33
1.6 Conclusions	36
<b>Chapter 2</b>	
<b>P-T-t-d evolution and extensional exhumation history of a high-temperature complex (Hırkadağ Block, Central Anatolia)</b>	<b>39</b>
Abstract	
2.1 Introduction	40
2.2 Geological Setting	40
2.3 Metamorphism of the Hırkadağ Block	45
2.4 Structural analysis of the Hırkadağ Block	51
2.5 Geochronology	55
2.6 Discussion	56
2.7 Conclusions	58
<b>Chapter 3</b>	
<b>Reconstructing the geometry of central Anatolia during the late Cretaceous: Large-scale Cenozoic rotations and deformation between the Pontides and Taurides</b>	<b>61</b>
Abstract	
3.1 Introduction	62
3.2 Geology of the CACC	62
3.3 Paleomagnetic sampling, analysis and reliability check	65

---

3.4 Paleomagnetic results	69
3.5 Discussion	73
3.6 Conclusion	77
<b>Chapter 4</b>	
<b>Late Cretaceous exhumation and crustal flow in the CACC: a study on the structural and metamorphic evolution of the Kırşehir and Akdağ Massifs</b>	<b>85</b>
Abstract	
4.1 Introduction	86
4.2 Geological setting	86
4.3 Structure and metamorphism of the Akdağ Massif	91
4.4 Structure and Metamorphism of the Kırşehir Massif	95
4.5 $^{40}\text{Ar}/^{39}\text{Ar}$ geochronology	101
4.6 Discussion: development and evolution of the northern central Anatolian HT domes	104
4.7 Conclusion	107
<b>Chapter 5</b>	
<b>The CACC during the Late Cretaceous: tectonic evolution and geodynamic setting</b>	<b>111</b>
Abstract	
5.1 Introduction	112
5.2 Geology of the Central Anatolian Crystalline Complex	112
5.3 Restoration and internal architecture of the CACC in the late Cretaceous	114
5.4 Structural and magmatic evolution of the CACC	119
5.5 Plate tectonic setting and evolution of the CACC since the late Cretaceous	122
5.6 Implications at a plate tectonic scale	124
5.7 Conclusions	126
<b>Conclusion</b>	<b>129</b>
<b>References</b>	<b>131</b>



## Bibliography

### Published

**Lefebvre C.**, Barnhoorn A., van Hinsbergen D.J.J., Kaymakci N., Vissers R.L.M.,  
Extensional denudation along a marble detachment fault zone from the northern Central Anatolian massifs, Kaman, Central Turkey. *Journal of Structural Geology* 33, 1220-1236.

### Submitted

**Lefebvre C.**, Barnhoorn A., van Hinsbergen D.J.J., Kaymakci N., Vissers R.L.M.,  
Reply to Genç and Yürür's comments on: "Late Cretaceous extensional denudation along a marble detachment fault zone in the Kırşehir massif near Kaman, Central Turkey". *Journal of Structural Geology*

**Lefebvre C.**, Peters K.M., Wehrens P.C, Brouwer F.M., van Hinsbergen D.J.J., Kaymakci N., Vissers R.L.M., van Roermund H.L.M., Advokaat E.L., Hendriks B.W.H., Corfu F.,  
P-T-t-d evolution and extensional exhumation history of a high-temperature complex (Hırkadağ block, Central Anatolia). *Lithos*

Advokaat E.L., van Hinsbergen D.J.J., **Lefebvre C.**, Kaymakci N., Vissers R.L.M., Hendriks B.W.H.,  
Reconstruction of the post-middle Eocene Savçılı-Mucur fold-thrust zone near the Hırkadağ Block (central Turkey) reveals the relict upper Cretaceous-Paleogene Ayhan supradetachment basin. *Tectonics*

Gülyüz E., Kaymakci N., Meijers M.J.M, van Hinsbergen D.J.J., **Lefebvre C.**, Vissers R.L.M., Hendriks B.W.H., Peynirçoğlu A.A.,  
Late Eocene synsedimentary folding of the Çiçekdağı basin, Central Turkey, during the final stages of the Kırşehir block-Pontides collision. *Journal of the Geological Society*

### In Preparation...

**Lefebvre C.**, Meijers M.J.M, Kaymakci N., Peynirçoğlu A.A., Langereis C.G., van Hinsbergen D.J.J.,  
Reconstructing the geometry of central Anatolia during the late Cretaceous: Large-scale Cenozoic rotations and deformation between the Pontides and Taurides. *Earth and Planetary Science Letters*

**Lefebvre C.**, Chauvet A., Andréani M., Meresse F., Lagabrielle Y.,  
Serpentinites tectono-metamorphic evolution in oceanic detachment fault systems: Contribution from the study of the Inzecca ophiolite (Alpine Corsica). *Geochemistry, Geophysics, Geosystems*

# The tectonics of the Central Anatolian Crystalline Complex: a structural, metamorphic and paleomagnetic study

## Abstract

The Anatolian region is a segment of the Alpine-Himalayan orogen. The rocks presently exposed in Anatolia provide a geological record of the closure history of the Neotethyan Ocean(s) situated between the converging African and Eurasian continents during late Mesozoic – Cenozoic times. The location of the former northern Neo-Tethyan ocean is marked by the presence of an ophiolitic mélange forming the Izmir-Ankara-Erzincan Suture Zone (IAESZ). South of the IAESZ, the Central Anatolian Crystalline Complex (CACC) is the largest metamorphic domain exposed in Turkey, which mainly consists of metamorphic rocks, ophiolites and magmatic intrusions. This crystalline domain experienced a complex tectonic history involving late Cretaceous obduction of ophiolitic nappes onto Paleozoic-Mesozoic sedimentary units, development of a regional Barrovian metamorphism, and widespread magmatic intrusions. However, previous metamorphic, magmatic and structural studies in central Anatolia did not reach a consensus about a unique geodynamic scenario to explain in which setting the CACC evolved during the late Cretaceous.

This thesis provides a multi-scale and multi-disciplinary study of the tectono-metamorphic evolution of the CACC, and integrates the obtained results with data from the literature in order to propose a plausible tectonic model for the evolution of the CACC in the late Cretaceous. The tectono-metamorphic history of the central Anatolian metamorphic rocks has been investigated through detailed microstructural, metamorphic and geochronological analysis, together with local and regional mapping of ductile structures and metamorphic field gradients. An extended set of paleomagnetic data from the central Anatolian granitoids provides constraints for restoring the large-scale geometry of the CACC into its late Cretaceous configuration.

The main results of this thesis revealed that during the late Cretaceous the CACC consisted of a NNE-SSW elongated and narrow dome-shaped antiformal structure (~500x150km). In this configuration, regional Barrovian metamorphism was accompanied with a top-to-the-SSW ductile crustal flow in the deeper part of the antiform, while shallower levels were synchronously affected by a WNW-ESE directed exhumation. This exhumation was accommodated by two generations of detachments which operated at different stages of the evolution of the CACC. Post-tectonic magmatism affected the western side of the antiform in three successive magmatic events showing a chemical evolution from calc-alkaline in the west to alkaline in the east (i.e. from an external to a more internal position in the antiform). This magmatic trend together with published geochemical data from the central Anatolian plutonic rocks, has been recognized as a typical evolution of a magmatic arc in a supra-subduction environment. Therefore, the contemporaneous L/MP-HT metamorphic CACC and the subduction-related HP-LT Tavşanlı Zone most likely formed a paired metamorphic belt. Moreover, at the plate tectonic scale, the contemporaneous northward subduction below the Pontides along an EW-trending suture together with the newly established eastward subduction of a NNE-SSW trending subduction system below the CACC suggests the presence of a Trench-Trench-Trench (TTT) type triple junction at the intersection of these two subduction zones. Finally, during the Paleogene, the collision of the NNE-SSW-oriented antiformal structure with the central Pontides led to the break-up of the CACC into three distinctive domains as exposed today.

## Orta Anadolu Kristalen Kompleksinin tektoniği: yapısal, metamorfik ve paleomanyetik bir çalışma

### Öz

Anadolu bölgesi Alp-Himalaya Orojenik kuşağının bir parçası olup günümüzde bölgede yüzeyleyen kayaçlar Geç Mesozoyik-Senozoyik döneminde Afrika-Avrasya kıtalarının yaklaşması sonucu Neotetis okyanus(ları)nın kapanma tarihçesine ait jeolojik kayıtları içerir. İzmir-Ankara-Erzincan Kenet Kuşağı (İAEKK) boyunca yüzeyleyen ofiyolitli melanjin konumu eskiden Neotetisin kuzey kolunun bulunduğu yeri işaret eder. İAEKK'nın güneyinde bulunan ve metamorfik kayaçlar, ofiyolitler ile magmatik sokulumlardan oluşan Orta Anadolu Kristalen Kompleksi (OAKK) Türkiye'de yüzeyleyen en büyük metamorfik komplekstir. Bahsi geçen kristalen kompleks geç Kretasede Paleozoyik-Mesozoyik sedimanter birimler üzerine ofiyolitli napların yerleşmesi, buna bağlı olarak bölgesel Barrovian metamorfizması ve magmatik sokulum gibi karmaşık tektonik olaylara maruz kalmıştır. Buna rağmen, orta Anadolu bölgesinde daha önceden yapılmış olan metamorfik, magmatik ve yapısal çalışmalar bölgenin Kretasede evrilmiş olan OAKK'nin jeodinamik evrimi konusunda her hangi bir fikir birliğine varamamışlardır.

Çok ölçekli ve çok disiplinli çalışmaları içeren bu tez, OAKK'nin evrimine dair elde edilmiş yeni veriler yanında geç Kretasede evrilmiş olan OAKK'nin evrimi ile ilgili kabul edilebilir bir model ileri sürebilmek için literatür verilerini de entegre eder. Bu bağlamda, orta Anadolu metamorfitlerinin tektono-metamorfik tarihçesi, detaylı mikroyapısal, metamorfik ve jeokronolojik analizler yanında sünek yapıların ve metamorfik arazi gradiyeninin lokal ve bölgesel olarak haritalanması ile araştırılmıştır. Orta Anadolu granitoidlerinden geniş bir alandan toplanan paleomagnetik veri setleri ise geç Kretasede OAKK'nin büyük ölçekli geometrisinin yeniden kurulmasına izin veren sınır koşullarını sağlamıştır.

Özet olarak bu tezin ana sonuçları şunlardır OAKK'nin Geç Kretasede KKD-GGB uzanımlı dar ve dom (kubbe) yapısına sahip antiformal bir yapı olduğu ortaya konulmuştur (~500x150km). Bu konfigürasyonda, bölgesel Barrovian metamorfizmasına, antiformun derin kısımlarında meydana gelen ve üst kısmı GGB'ya akan sünek kıtasal akıntı ve bu akıntı ile eş zamanlı olarak antiformun sığ kısımlarında meydana gelen BKB-DGD yönlü yüzeylemeye eşlik etmiştir. Bu yüzeyleme işlemi OAKK'nin evriminin farklı aşamalarında meydana gelen iki fazlı sıyrılmaya bağlı olarak gelişmiştir. Antiformun batı kenarını etkilemiş olan post-tektonik magmatizma ardaşık üç farklı kimyasal evrim gösterir ve batıda kalk-alkali özellik gösterirken, doğuda alkaline dönüşür (yani antiformun iç kısımlarından dış kısımlarına doğru). Bu magmatik eğilim, Orta Anadolu plütonik kayaçlarından elde edilen ve daha önce yayımlanmış olan jeokimyasal veriler ile birlikte değerlendirildiğinde, magmatik yayın dalma-batma-üstü zonu ortam koşulları ile ilişkili tipik gelişimi olarak tanımlanmıştır. Dolayısıyla, eşyaşlı OAKK'ne ait Düşük/Orta Basınç-Yüksek Sıcaklık (D/OB-YS) yay metamorfizması ile dalma-batma ilişkili YB-DS Tavşanlı Zonu büyük bir ihtimalle eşlenik metamorfik kuşak oluştururlar. Bunun yanında, plaka tektoniği ölçeğinde ise D-B bir hat boyunca kuzeye, Pontidlerin altına olan dalma-batma sistemi ile bu çalışmada ortaya konulan ve KKD-GGB yönelimli olup doğuya OAKK'nin altına olan eşzamanlı dalma-batma zonu Hendek - Hendek - Hendek (HHH) tipi üçlü kesişim noktası oluştururlar. Son aşamada, KKD-GGB uzanımlı bu antiformal yapının Pontidlerle çarpışması, OAKK'nin parçalanarak üç ayrı bloğa bölünmesine ve Paleojen döneminde, bugünkü üçgen yapısına ulaşmasına neden olmuştur.

# La tectonique du Complexe Cristallin de l'Anatolie Centrale: une étude structurale, métamorphique et paléomagnétique

## Résumé

La région de l'Anatolie est traversée par une chaîne de montagnes qui relie les Alpes à l'Himalaya. Les roches qui affleurent actuellement en Anatolie nous renseignent sur l'histoire géologique de la région, impliquant la fermeture de l'océan Neotethys qui séparait les continents africain et eurasiatique à la fin de l'ère mésozoïque et pendant le Cénozoïque. L'existence de l'ancien océan Neotethys est aujourd'hui matérialisée par la présence d'un mélange de roches ophiolitiques, qui marque la zone de suture entre les deux continents. Au sud de cette suture, le Complexe Cristallin d'Anatolie Centrale (CCAC) est le plus grand domaine métamorphique de Turquie, qui se compose principalement de roches métamorphiques, ophiolitiques et magmatiques. Ce domaine cristallin a connu une histoire tectonique complexe impliquant l'obduction de nappes ophiolitiques crétacées sur des unités sédimentaires paléo-mésozoïques, le développement d'un métamorphisme régional de type barrovien, et une forte activité magmatique à la fin du Crétacé. Toutefois, les études précédentes menées en Anatolie centrale n'ont pas permis d'établir un consensus sur le scénario géodynamique dans lequel le CCAC a évolué au cours du Crétacé tardif.

Cette thèse propose une étude multi-échelle et pluri-disciplinaire de l'évolution tectono-métamorphique du CCAC, et intègre les résultats obtenus avec les données de la littérature afin de proposer un modèle unique et viable pour expliquer l'évolution du CCAC au Crétacé supérieur. L'histoire tectono-métamorphique des roches cristallines d'Anatolie centrale a été étudiée grâce à des analyses microstructurales, métamorphiques et géochronologiques, ainsi qu'à la cartographie locale et régionale de structures ductiles et de gradients métamorphiques. De plus, les données paléomagnétiques obtenues sur les granites d'Anatolie centrale ont permis de donner des contraintes sur la géométrie du CCAC au Crétacé tardif.

Les principaux résultats de cette thèse ont révélé que pendant le Crétacé supérieur, le CCAC formait un long dôme structural (~500x150km) orienté du NNE au SSO. Dans cette configuration et sous les conditions du métamorphisme barrovien, la partie profonde du dôme était affectée par un flux ductile crustal dirigé vers le NNE, tandis que les niveaux supérieurs enregistraient un mouvement ductile cisailant perpendiculaire à l'axe longitudinal du dôme. L'exhumation de ce dôme métamorphique a été accommodée par deux générations de détachements qui étaient actifs à différents stades de l'évolution du CCAC. Le magmatisme post-tectonique, concentré dans la partie ouest du dôme, présente trois événements successifs et montre une signature chimique évoluant de magmas calco-alcalins à alcalins, d'Ouest en Est. Cette évolution magmatique, en combinaison avec les données géochimiques de la littérature, a été interprétée comme typique d'un magmatisme d'arc. Par conséquent, les métamorphismes contemporains de basse/moyenne pression et haute température du CCAC et de haute pression et basse température de la zone de Tavşanlı à l'Ouest formaient probablement deux ceintures métamorphiques associées. Par ailleurs, les deux zones de subduction obliques et contemporaines, plongeant vers le nord sous les Pontides et vers l'est sous le CCAC, suggèrent la présence d'un point triple à l'intersection des deux fosses. Enfin, la collision du dôme métamorphique du CCAC avec les Pontides au Paléogène, serait responsable de la fragmentation du CCAC en trois domaines distincts, qui ont évolué séparément jusqu'à leur configuration actuelle.

# De tektoniek van het Centraal Anatolische Kristallijne Complex: een structurele, metamorfe en paleomagnetische studie

## Samenvatting

Het Anatolische gebied in centraal Turkije vormt een segment van de Alpen-Himalaya gebergtegordel. De gesteenten die nu in Anatolië aan de dag treden bevatten aanwijzingen over de sluitingsgeschiedenis van de vroegere Neotethys oceaan, die gedurende het late Mesozoïcum en Cenozoïcum gelegen was tussen de convergerende Afrikaanse en Euraziatische continenten. De locatie van deze vroegere Neotethys oceaan wordt gemarkeerd door een ofiolitische melange die de Izmir-Ankara Erzincan Sutura Zone (IAESZ) wordt genoemd. Het Centrale Anatolische Crystalline Complex (CACC) ten zuiden van de IAESZ is het grootste metamorfe domein in Turkije. Dit domein dat voornamelijk bestaat uit metamorfe gesteenten, ofiolieten en magmatische intrusies, heeft een complexe tektonische geschiedenis ondergaan waarin gedurende het late Krijt ofiolitische dekbladen op Paleozoïsche-Mesozoïsche sedimentaire eenheden werden gestapeld, de gesteenten op regionale schaal een Barrovian type metamorfose ondergingen, en geïntrudeerd werden door talrijke magmatische plutonen. Eerdere metamorfe, magmatische en structurele studies in centraal Anatolië hebben echter niet geleid tot een consensus over een geodynamisch scenario dat de ontwikkeling en geologische geschiedenis van het CACC gedurende het late Krijt verklaart.

Dit proefschrift geeft de resultaten van een multidisciplinaire studie op verschillende schalen van de tectono-metamorfe evolutie van het CACC, en integreert de verkregen resultaten met gegevens uit de literatuur, met het doel te komen tot een plausibel tectonisch model voor de evolutie van het CACC in het late Krijt. De tectono-metamorfe evolutie van de centraal Anatolische metamorfe gesteenten is onderzocht door gedetailleerde microstructurele, metamorfe en geochronologische analyse, in combinatie met locale en regionale kaartering van ductiele structuren en metamorfe veldgradiënten. Een uitgebreide set paleomagnetische gegevens uit de centraal Anatolische granitische gesteenten levert daarbij de randvoorwaarden voor een reconstructie van de grootschalige geometrie van het CACC gedurende het late Krijt.

De belangrijkste resultaten van dit proefschrift wijzen erop dat gedurende het late Krijt het CACC bestond uit een NNE-SSW verlopende, langgerekte en smalle (~500x 150 km) antifforme structuur. In deze configuratie ging de regionale Barrovian type metamorfose gepaard met een top-naar-het-SSW gerichte ductiele crustale vloeï in het diepere deel van de antifform, terwijl de ondiepere delen van de structuur gelijktijdig onderhevig waren aan WNW-ESE gerichte verschuiving en omhoogkomen van de gesteenten. Dit omhoogkomen werd geacomodeerd door twee generaties van rekstructuren die actief waren gedurende verschillende stadia van de evolutie van het CACC. Posttectonisch magmatisme beïnvloedde de westelijke zijde van de antifform, en bestond uit drie opeenvolgende magmatische stadia met een chemische evolutie van west naar oost, dat wil zeggen, van een meer externe naar een meer interne positie in de antifform, van kalk-alkalien naar alkaliën. Deze magmatische trend, in combinatie met gepubliceerde geochemische gegevens over de centraal Anatolische magmatische gesteenten, zijn kenmerkend voor de evolutie van een magmatische arc in een supra-subductie milieu. Dit leidt tot de conclusie dat het L/MP-HT metamorfe CACC en de subductie-gerelateerde HP-LT Tavşanlı Zone met eenzelfde ouderdom naar het westen naar alle waarschijnlijkheid een “paired metamorphic belt” vormden. Beschouwd op een plaattektonische schaal suggereert de noordwaartse subductie onder de Pontiden langs een EW verlopende sutuur, gelijktijdig met de hier voorgestelde oostwaartse subductie van een NNE-SSW verlopend subductiesysteem onder het CACC de aanwezigheid van een trench-trench-trench type (TTT) “triple junction” bij de intersectie van deze twee subductie zones. De collisie van de NNE-SSW georiënteerde antifforme structuur met de centrale Pontiden leidde tenslotte tot het opbreken, gedurende het Paleogeen, van het CACC in drie onderscheiden domeinen zoals die nu in centraal Anatolië bestaan.



# INTRODUCTION

The Alpine-Himalayan orogen essentially formed in response to the closure of the Neotethyan Ocean(s), associated with convergence and collision between the African and Eurasian continents during the Late Mesozoic - Cenozoic. This thesis focuses on the Anatolian segment of this belt. The segment of the orogen in Turkey comprises E-W trending, intensely deformed and partly metamorphosed nappes of both continental and oceanic affinity which include, from north to south, the Pontides, the Izmir-Ankara-Erzincan Suture Zone (IAESZ), the Anatolides and the Taurides (Figure 1.1) (Ketin 1966, Şengor and Yılmaz 1981, Okay and Tüysüz 1999). Within the Anatolides, two large-scale continental terrains (i.e. the Menderes Massif in western Turkey and the Central Anatolian Crystalline Complex (CACC) in central Turkey) consist of crystalline rocks showing evidence for regional Barrovian metamorphism and widespread magmatism. High-temperature metamorphism and subsequent exhumation of the CACC occurred in the late Cretaceous – Paleocene (e.g. Erkan 1976, Seymen 1981, Göncüoğlu 1986, Whitney et al. 2003, Boztuğ and Jonckheere 2007), while the Menderes Massif underwent a somewhat similar tectono-metamorphic evolution during Eocene – Miocene times (e.g. Şengor et al. 1984, Satir and Friedrichsen 1986, Hetzel et al. 1995, Bozkurt and Oberhänsli 2001, Ring et al. 2003, van Hinsbergen et al. 2010), thus approximately 40-50 Myr later than the CACC.

The CACC forms a 250 km scale triangular domain bounded by the Izmir-Ankara-Erzincan Suture Zone (IAESZ) to the north, the Central Anatolian Fault Zone to the southeast, and the Tuz Gölü Fault to the southwest (Figure 1.1). This wide domain exposes metamorphic and ophiolitic rocks together with igneous intrusions, covered mostly by Cenozoic deposits. It is generally accepted that during the late Cretaceous, Paleozoic-Mesozoic platform type sedimentary sequences were obducted by ophiolites with supra-subduction-zone geochemical signatures (e.g. Yaliniz and Göncüoğlu 1998). Following ophiolite emplacement, the underthrust sediments became metamorphosed under regional Barrovian conditions (Erkan 1976, Seymen 1981, Whitney and Dilek 2001). This was soon followed by widespread intrusion of plutons into the foliated metasediments and ophiolites (e.g.

Göncüoğlu et al. 1991, Akıman et al. 1993) (Figure 1.1). Exhumation of the CACC was followed by collision with the Pontides, starting in the latest Cretaceous - early Paleocene (Kaymakci et al, 2009, Meijers et al, 2010).

## Problem statement

During the late Cretaceous, the CACC experienced a complicated tectonic history, involving burial, metamorphism, magmatism and exhumation. Previous studies focused on several aspects of the evolution of the CACC via studies on metamorphic and magmatic petrology. Only a few studies concentrated on structural analysis of the crystalline rocks and the internal deformation of the CACC. Although several different tectonic scenarios related to the late Cretaceous evolution of the CACC have been proposed, no consensus has been reached to explain the origin of the abnormally high geothermal gradients associated with its metamorphism, nor with regard to the exhumation of these rocks and related geodynamic context.

## Approach

In order to unravel the late Mesozoic and Cenozoic geodynamic evolution of central Anatolia, it is crucial to document the regional evolution of metamorphism and internal deformation of the CACC. Therefore, this thesis concentrates mostly on the poorly explored northern central Anatolian Massifs comprising the Kırşehir Massif in the northwest and the Akdağ Massif in the northeast (Figure 1.1) and focuses on four different aspects:

### *Structural analysis*

Except for the southern Niğde Massif (Gautier et al. 2002, Whitney et al. 2003, Whitney et al. 2007, Gautier et al. 2008), the structural history of the CACC – especially that associated with its ductile deformation history – is hitherto virtually unstudied. Therefore, we conducted regional field mapping of both the ductile deformation associated with the regional Barrovian metamorphism and the brittle structures. In addition, we concentrated on the structural evolution of the contact between high-grade metamorphic rocks and the central Anatolian ophiolites, as this contact provides a

key to unravel the mechanisms accompanying the exhumation of the northern CACC. Finally, the regional pattern of deformation might be used to constrain the mechanisms responsible for the burial and exhumation of the CACC, and to restore its original geometry in the late Cretaceous.

### *Metamorphism*

The pressure (P) and temperature (T) evolution of the central Anatolian metamorphic rocks is investigated with two different approaches: (1) estimation of local and precise conditions of peak metamorphism in the context of exhumation of the central Anatolian crystalline rocks, and (2) the spatial distribution of regional metamorphic grade throughout the northern Anatolian Massifs, to constrain the extent and the geometry of the metamorphic domains.

### *Geochronology*

Coupled with the estimates of P-T conditions, radiometric dating techniques (i.e. U/Pb and  $^{40}\text{Ar}/^{39}\text{Ar}$  geochronology) are applied on metapelitic schists, granitoids and non-metamorphic volcanic rocks in order to arrive at an accurate timing of and the consecutive thermal states of the metamorphic rocks and their exhumation, and to obtain crystallisation ages of the igneous intrusions.

### *Paleomagnetism*

Following its exhumation in the Paleocene (Gautier et al. 2002, Boztuğ and Jonckheere 2007), the CACC collided with the central Pontides (Görür et al. 1984, Görür et al. 1998, Kaymakci et al. 2000, Kaymakci et al. 2003a, Kaymakci et al. 2003b, Kaymakci et al. 2009, Meijers et al. 2010), leading to collision-related compression in central Anatolia, evidenced by thrusting and folding of the Eocene and younger sediments overlying the CACC and the central Pontides (Şengör and Yılmaz 1981, Görür et al. 1984, Kaymakci et al. 2003b, Gülyüz et al. submitted). To restore the CACC in its pre-collisional configuration, a paleomagnetic study is conducted to estimate in how far the CACC was a coherent large-scale block during the early Tertiary, and whether or not its original geometry was similar to its modern configuration.

Using the above tools and data, this thesis aims to integrate and synthesize the published and newly collected data to propose a restoration of the CACC during late Cretaceous time. Based on this restoration, the thesis discusses the tectonic evolution, and proposes an alternative (plate) tectonic scenario pertinent to the genesis of the CACC.

## Outline of the thesis

This thesis is subdivided into 5 chapters:

- **Chapter 1** presents a multi-scale structural study from a tectonic contact between high-grade metamorphic rocks and non-metamorphic ophiolites in the northwestern Kırşehir massif. The Kaman area (NW of Kırşehir) is a strategic location where the three main central Anatolian crystalline rock-units (i.e. metamorphic, ophiolitic, and plutonic rocks) are juxtaposed. This chapter evaluates the relationship between the three crystalline units, their evolution and interaction, in the context of their exhumation, during the late Cretaceous in the Kaman region.

- Located in the center of CACC, just north of the Central Anatolian Volcanic Province (i.e. Cappadocia), the Hırkadağ Block is a small exhumed metamorphic and intrusive complex, adjacent to a well-preserved sedimentary basin that contains upper Cretaceous volcanics, volcanoclastics, and Tertiary sedimentary deposits (Köksal and Göncüoğlu 1997, Advokaat et al. submitted). **Chapter 2** presents a detailed P-T-t-d evolution for the crystalline rocks from the Hırkadağ block, constraining its metamorphic and tectonic history during exhumation. We present a detailed study integrating metamorphic petrography, thermobarometric calculations and thermodynamic modeling, together with U/Pb and  $^{40}\text{Ar}/^{39}\text{Ar}$  geochronology in order to unravel the P-T-t trajectories of the high-grade metamorphic rocks from the Hırkadağ Block. In addition, on the basis of new structural data the coeval deformation evolution of the Hırkadağ Block is presented, from earlier pervasive, syn-metamorphic ductile shearing, to brittle tectonics near the contact with the adjacent sedimentary basin.

- In **Chapter 3**, we address the original geometry of the CACC during the late Cretaceous and the issue of the Paleogene compressional evolution following the CACC-Pontide collision. With this aim, we use paleomagnetism as a tool to test whether or not the original geometry of the CACC was similar to its modern configuration or. For this purpose we focused on the upper Cretaceous plutons and sampled them to track if any vertical-axis rotations occurred since the late Cretaceous that may have changed the large-scale geometry of the area.

- The spatial distribution of metamorphism and contemporaneous ductile structures from the two large northern Akdağ and Kırşehir Massifs

are the main focus of the **Chapter 4**. Structural and metamorphic maps based on large-scale field mapping, together with  $^{40}\text{Ar}/^{39}\text{Ar}$  ages from metapelitic rocks, provide the structural, thermal and cooling characteristics associated with regional metamorphism and exhumation of the northern Anatolian massifs. Integrating the results of Chapter 3, a restoration is proposed of the northern CACC in its late Cretaceous configuration, and discussed in terms of its regional structural consistency.

- As a synthesis, **Chapter 5** provides a regional compilation of the structural and metamorphic evolution of the CACC, based on previously published work and the main findings of this thesis. A restored configuration of the entire CACC in the late Cretaceous is proposed. Based on this restoration, this chapter discusses the structural and magmatic evolution of the CACC, and highlights the implications at a regional plate tectonic scale.

# CHAPTER 1



# Late Cretaceous extensional denudation along a marble detachment fault zone in the Kırşehir massif near Kaman, Central Turkey

## Abstract

In the Central Anatolian Crystalline Complex (CACCC), 100 km scale metamorphic domains were exhumed in a context of north-south plate convergence during late Cretaceous to Cenozoic times. The timing, kinematics and mechanisms of exhumation have been the focus of previous studies in the southern Niğde Massif. In this study, we investigate the unexplored northern area regarding the tectonic features preserved on the edges of the Kırşehir Massif, based on detailed field-mapping in the Kaman area where high-grade metasediments, non-metamorphic ophiolites and monzonitic plutons are locally exposed together. Close to the contact with the ophiolites, west-dipping foliated marble-rich rocks display mylonites and discrete proto-mylonites with normal shear senses indicating a general top to the W-NW direction. Both of these structures have been brittlely overprinted into cataclastic corridors parallel to the main foliation. The mylonite series and superimposed brittle structures together define the Kaman fault zone. The study of the evolution of calcite deformation fabrics along an EW section supported by Electron Back Scattered Diffraction measurements (EBSD) on representative fabrics indicates that the Kaman fault zone represents an extensional detachment.

In Ömerhacı, in the vicinity of the Baranadağ quartz-monzonite, the metamorphic sequence shows static annealing of the calcite mylonitic fabrics. This evidence suggests that intrusion took place at shallow depth (~10km) into an already exhuming metamorphic sequence. As a consequence for the Kaman area, buried meta-sediments have been rapidly exhumed between 84 and 74Ma (~1km/Ma) where exhumation along a detachment zone, displaying a top to the W-NW shear motion, took place in the mid to upper crust prior to magmatic intrusion in the late Campanian. As the intrusion cut through the detachment fault, the main shearing deformation ceased. Brittle tectonics coupled with erosion likely took over during the final unroofing stages at a slower rate (<0.2km/Ma), until the pertinent rocks reached the Earth's surface in the late Paleocene.

Côme Lefebvre  
Auke Barnhoorn  
Douwe J.J. van Hinsbergen  
Nuretdin Kaymakci  
Reinoud L.M. Vissers

## 1.1 Introduction

Anatolia consists of a wide orogenic belt of Alpine age that exposes intensely deformed, metamorphosed and non-metamorphosed continental fragments, separated by oceanic sutures and/or high-pressure metamorphic belts (Şengör and Yılmaz 1981, Okay and Tüysüz 1999, Pourteau et al. 2010). In central Turkey, three continental domains have been recognized, i.e., (1) the Sakarya Block of the Pontides in the north that comprises a complex amalgamation of Paleozoic metamorphic terranes covered with unmetamorphosed Mesozoic succession, (2) the high-grade Kırşehir Crystallines (Bailey and McCallien 1950) or Central Anatolian Crystalline Complex (CACC) (Göncüoğlu et al. 1991) unconformably overlain by Tertiary clastics,

and (3) the non-metamorphosed Tauride thrust-belt (*sensu stricto*) in the south. The Pontides and CACC are separated by the Izmir-Ankara-Erzincan suture zone, characterized by Permo-Triassic to Cretaceous ophiolites. The CACC and the Taurides are separated by a zone of high-pressure metamorphic rocks of late Cretaceous-Paleocene age, and the Taurides are also tectonically overlain by ophiolites (Okay et al. 1998, Candan et al. 2005). Most authors therefore interpret a second suture zone, the Intra-Tauride suture, in between the CACC and the Taurides.

In contrast to the Pontides and Taurides, the CACC recorded mostly high-grade metamorphism, dominated by high-temperature, low-pressure metasediments (Erkan 1976, Göncüoğlu 1977, Whitney et al. 2001) intruded by widespread

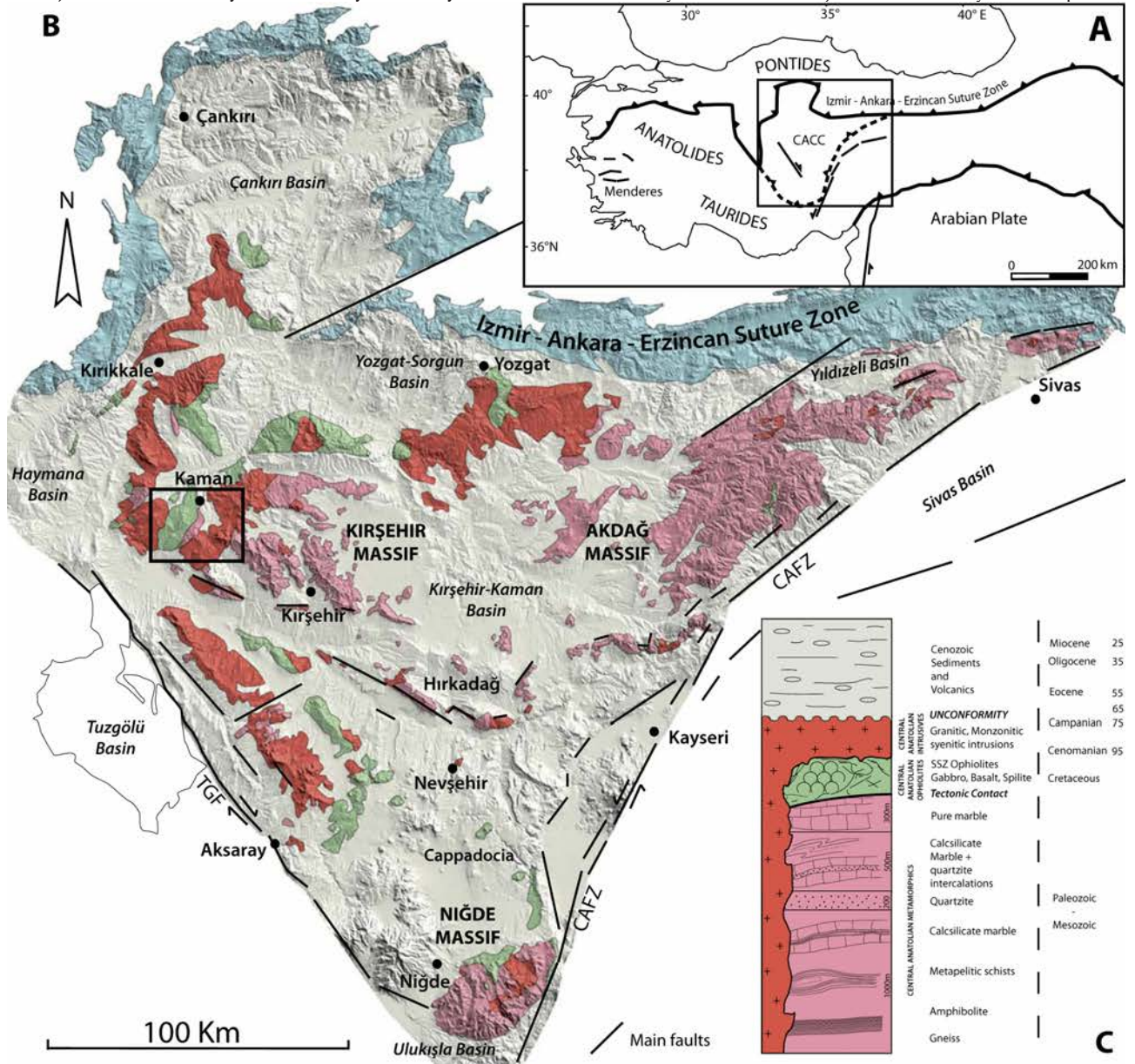


Figure 1.1 a) Location of the Menderes Massif and the Central Anatolian Crystalline Complex (CACC) in the Turkish orogenic system. b) Simplified geological map of the CACC projected on a Digital Elevation Model. The black rectangle indicates area of study presented in Figure 1. 5. c) Simplified tectono-stratigraphic column showing the relationships between the main units of the CACC (not to scale).

plutons (Figure 1.1). The age of metamorphism and magmatism is late Cretaceous (Figure 1.2) (Göncüoğlu 1986, Whitney et al. 2003, Whitney and Hamilton 2004, Boztuğ et al. 2009b). Given the regional occurrence of remnants of ophiolites overlying the CACC, metamorphism is generally ascribed to burial of the CACC below an ocean-derived sequence.

Although the age of exhumation of the CACC as a whole is relatively well constrained by  $^{40}\text{Ar}/^{39}\text{Ar}$  ages, apatite fission track data and unconformably overlying deposits, the mechanism of exhumation is poorly understood (Seymen 1981, Görür et al. 1998, Fayon et al. 2001, Gautier et al. 2002, Whitney et al. 2003, Boztuğ and Jonckheere 2007, Isik et al. 2008). Exhumation of high-grade metamorphic rocks is frequently associated with regional extension. For example, the Cycladic-Menderes province, of similar dimensions as the CACC, is one of the most famous extensional metamorphic provinces in the world, and exhumation from mid-crustal depths resulted from crustal extension in metamorphic core complexes (Lister 1984, Bozkurt and Oberhänsli 2001, Jolivet et al. 2010), after a phase of exhumation in an extrusion wedge or subduction channel (Jolivet et al. 2003, Ring et al. 2007, Ring et al. 2010). If regional extension played a role in the exhumation of the entire CACC, such extension has important geodynamical consequences that may even influence the interpretation of suture zone configurations prior to the late Cretaceous. So far, only in the southernmost part of the CACC – the Niğde massif – extensional exhumation has been established with a late Cretaceous to Paleocene age (Gautier et al. 2002, Whitney et al. 2003, Umhoefer et al. 2007). In contrast, exhumation of the northern massifs of the CACC was postulated to relate to erosion (Fayon et al. 2001). It has, however, also been proposed that extension in the northern CACC might have been much more important than thus far considered (Dirik et al. 1999, Okay and Tüysüz 1999, Gautier et al. 2008) and, recently, discrete extensional ductile shear zones in granitoids have been reported (Isik et al. 2008, Isik 2009).

In this chapter, we focus on the northwestern Kırşehir massif, and investigate whether tectonic extension has played a role in the exhumation of the Kırşehir metamorphics. Close to the city of Kaman, our study area provides good exposure of the contacts between the main lithological components: high-grade marbles overlain by an essentially non-metamorphic ophiolitic unit, and intruded by a monzonitic pluton (Figure 1.1). The two major contacts separating them have been investigated and include (1) a tectonic contact

close to Kaman separating the metamorphics from the ophiolites, and (2) the contact between the metamorphics and the monzonitic pluton in the vicinity of village of Ömerhacı. We present field as well as optical and electron microscopy-scale, geometrical and kinematic data from the calcareous metamorphic sequence of both areas, and discuss our observations in the context of the local and regional exhumation history of the CACC.

## 1.2 Geological setting

The Central Anatolian Crystalline Complex is bounded by major tectonic features: the İzmir–Ankara–Erzincan suture in the north, the dextral Tuz Gölü fault in the west and the sinistral Central Anatolian Fault Zone in the east (Figure 1.1). Inside the CACC, the main rock types encountered are: (1) Paleozoic metasediments tectonically overlain by (2) an ophiolitic sequence composed only of mafic bodies (and epi-ophiolitic cover) inferred to be of obducted origin, intruded by (3) felsic plutons and tectonically or unconformably covered by (4) non-metamorphosed volcanics and sediments of late Cretaceous to Quaternary age.

The oldest units consisting of metasediments are called Central Anatolian Metamorphics (CAM) (Göncüoğlu 1977, Göncüoğlu et al. 1991). Despite the many metamorphic formations described in the literature, the metamorphosed stratigraphy shows a strong similarity over much of the CACC: it consists of a coherent sequence (from bottom to top) of gneiss, micaschist, quartzite, amphibolite, calcsilicate and marble. In the lowermost gneissic sequence of the Seksenuşağı Formation from the Ortakoy region, *Heliolites packelmannophora* sp. and fragments of *Retiolites* sp. have been found pointing to a Silurian or early Devonian age (Kocak and Leake 1994). The correlation of the marble-rich upper unit with the carbonates from the Kütahya-Bolkardağ belt in the Taurides has been used to suggest a Triassic - early Cretaceous age (Göncüoğlu et al. 1992). It follows that a Paleozoic to Mesozoic age for the central Anatolian metasediments is reasonable. This sequence of rocks underwent multiple phases of folding and pervasive ductile shearing associated with regional metamorphism during Alpine burial, intrusion and exhumation-related processes (Göncüoğlu 1977, Seymen 1983, Tolluoğlu and Erkan 1989, Teklehaïmanot 1993).

The regional metamorphism ranges from greenschist to upper-amphibolite/granulite facies and is of high temperature - medium/low pressure Barrovian type (Erkan 1976, Seymen 1981). Temperature and pressure at metamorphic

peak conditions have been estimated at 700-800°C for 6-8 kbar overprinted by a local re-heating at lower pressure (2-4 kbar) (Kocak and Leake 1994, Whitney and Dilek 1998, Whitney et al. 2001). Using U-Pb SHRIMP analysis on monazite and zircon from high-grade metapelites (Whitney et al. 2003, Whitney and Hamilton 2004) (Figure 1.2), the age of the metamorphic peak in the Kırşehir and Niğde massifs has been constrained to around 91-84 Ma.

The transition to the structurally higher unit, the Central Anatolian Ophiolites (CAO) shows

evidence of fault-related features such as tectonic breccias interpreted to be the consequence of obduction-related emplacement (Seymen 1981, Yaliniz and Göncüoğlu 1998). The CAO is represented by fragments of a supra-subduction zone ophiolite (SSZ) of late Cretaceous age (90-85Ma) and partly by the upper Cretaceous accretionary complex of the “Ankara Mélange” comprising tectonized blocks of basalt, radiolarian chert, pelagic limestone and sandstone in a serpentinite matrix (Seymen 1981, Floyd et al. 2000, Yaliniz et al. 2000b).

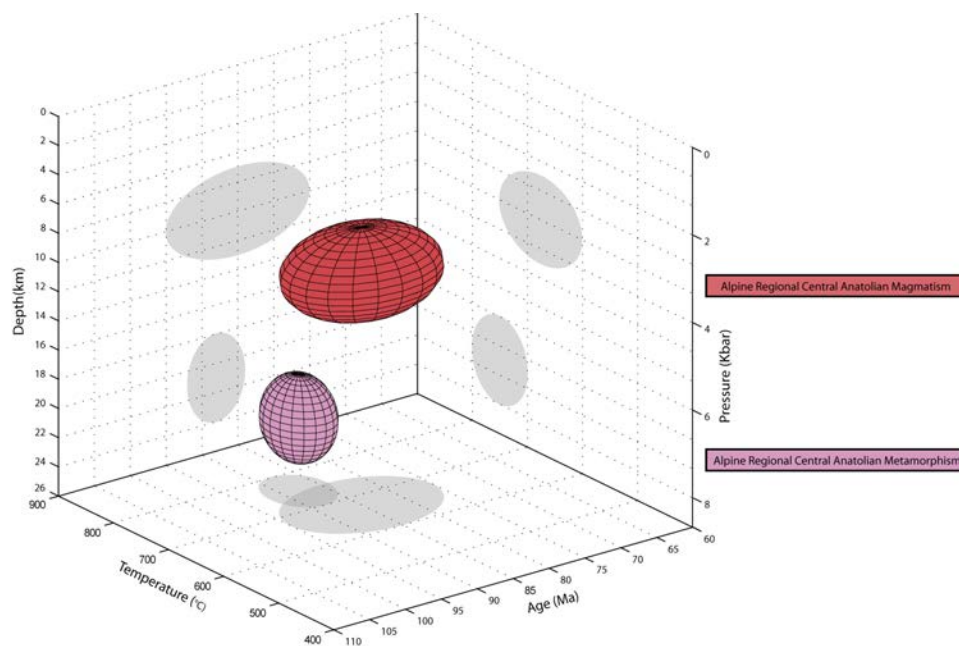


Figure 1.2 Pressure-Temperature-Time diagram representing constraints on Alpine regional metamorphic and magmatic events in Central Anatolia. For pertinent references see text.

Intruding both the CAM and CAO, the central Anatolian intrusives are widely exposed in the area (Erler and Göncüoğlu 1996). They are generally of granitic, granodioritic, monzonitic and syenitic composition, of calcalkaline to alkaline affinity, and display characteristics of I, S and A-type granites. Their trace element geochemistry plots in the island arc, within-plate, and syn- to post-collision granitoids fields of the discrimination diagrams (Akiman et al. 1993, Aydın et al. 1998, Ilbeyli et al. 2004). Intrusion timing is constrained by Rb/Sr whole rock, U/Pb on titanite and zircon and Pb/Pb evaporation on zircon methods, and ranges from 95 to 75 Ma (Göncüoğlu 1986, Whitney et al. 2003, Köksal et al. 2004, Boztuğ et al. 2007). Geothermobarometric calculations (Al and Ti on amphibole) indicate crystallization at ca. 600-750°C for a pressure of ca. 2.5-4.5 kbar (Ilbeyli 2005, Boztuğ et al. 2009a) (Figure 1.2).

An attempt has been made to classify the intrusives, distinguishing temporal and spatial magmatic supersuites in the area, into: (1) a Granite Supersuite associated with coeval gabbroic

plutons, (2) a Monzonite Supersuite and (3) a Syenite Supersuite (Kadioğlu et al. 2006) (Figure 1.3). Cogenetic extrusives represented by rhyolite, rhyodacite, dacite, andesite and latite are also exposed in the CACC, for example in the İdişdağ area close to the Hırkadağ area (Figure 1.1) (Köksal et al. 2001).

During and after exhumation of the crystalline rocks, Central Anatolian depressions were filled by volcanics and sediments. Peripheral basins floored by accretionary complexes record Late Maastrichtian to younger sedimentation (e.g. Çankırı, Haymana, Tuzgölü, Ulukışla basins) (Görür et al. 1984, Erdoğan et al. 1996, Görür et al. 1998, Çemen et al. 1999, Kaymakci et al. 2009). Intra-continental basins developed on top of the CACC since Paleocene-Eocene times (e.g. Yıldızeli, Yozgat-Sorgun, Kırşehir-Kaman basins) (Göncüoğlu 1992, Görür et al. 1998).

Three submassifs are commonly distinguished within the CACC: the Akdağmadeni or Akdağ Massif in the north-east (Vache 1963), the Niğde Massif in the south (Göncüoğlu 1977) and the

Kırşehir Massif in the north-west (Seymen 1981) (Figure 1.1).

The Kırşehir massif (Figure 1.3) is characterized by an overall dome-shaped structure delineated by shallowly dipping foliated metamorphic rocks. The metamorphic succession is estimated to be around 2000-2500 m thick, and is made up of four

units (Seymen 1981, Tolluoğlu and Erkan 1989) as follows. (1) The lowermost Kalkanlıdağ Formation is a thick unit (~1000 m) dominated by metapelitic to semi-pelitic calcareous compositions. It mainly consists of quartz-mica-schists interlayered with calcsilicate and gneissose calcschist. Few metabasites and quartzites also occur in the

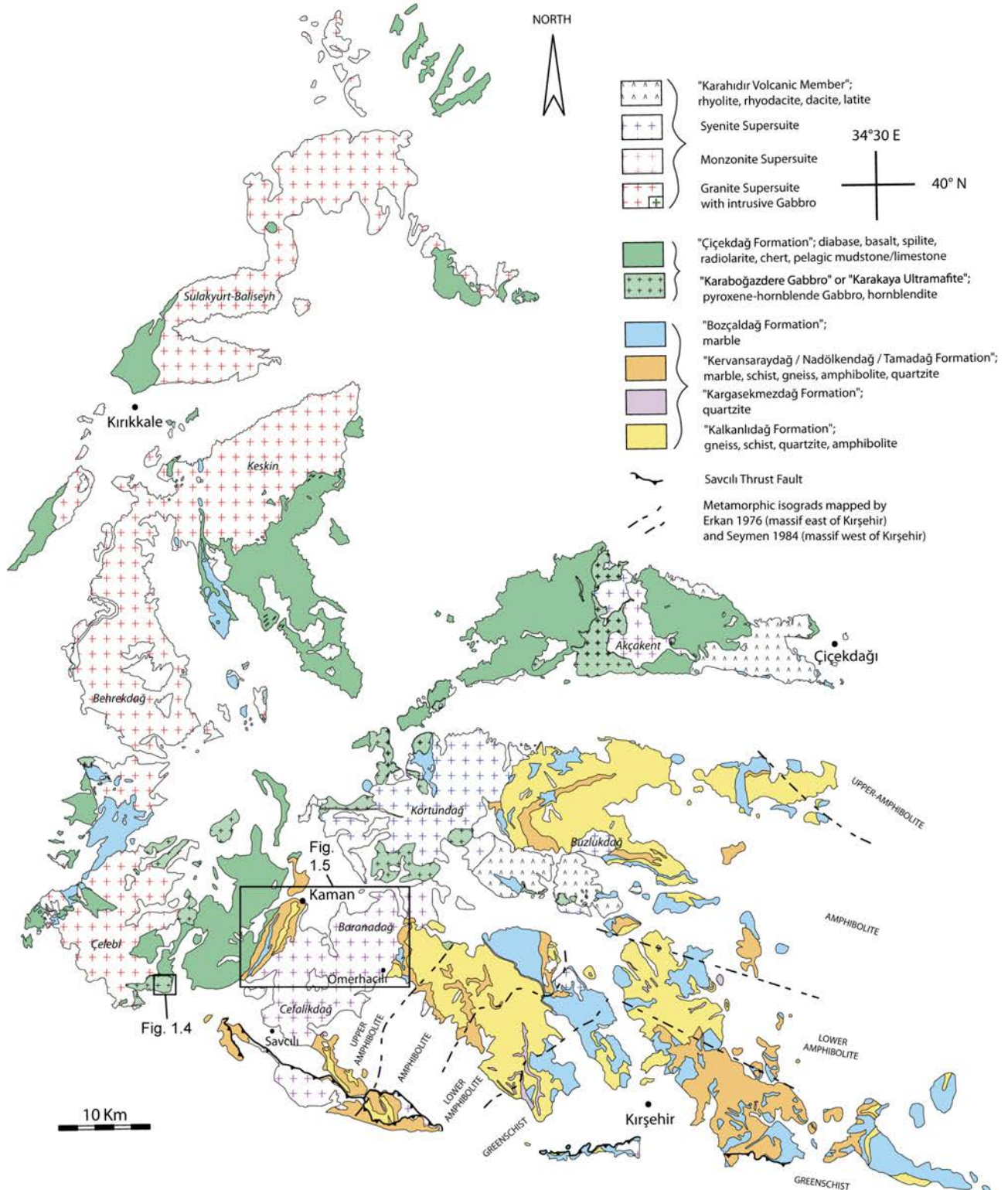


Figure 1.3 Geological map of the Kırşehir massif, modified from 1:1.000.000 geological maps (MTA sheets Kırşehir-G17, G18, G19, I30, I31, I32, J30). Names of the main plutons are indicated. Also shown are published metamorphic field boundaries (Erkan 1976 for the area east of Kırşehir city and Seymen 1984 for the western part of the massif). Black rectangles show the locations of Figures 1.4 and 1.5.

succession. (2) The Kargasekmezdağ Formation represents a homogenous quartzite layer of tens to hundreds of meters thick. (3) The Tamadağ or Nadölkendağ Formation (~500 m) shows the upward transition to dominantly calcareous rocks. The main lithologies are calcsilicate gneiss and impure marble, alternated with minor schist, amphibolite and quartzite bands. (4) The uppermost Bozçaldağ Formation consists of ~300 m of pure massive homogenous marble.

The spatial distribution of metamorphic grade throughout the Kırşehir massif has been examined using mineral isograd mapping. Three distinct metamorphic zones (corresponding to the greenschist facies and lower and upper amphibolite facies) point to an increase of the metamorphic peak temperature towards the north and north-east (Erkan 1976). The massif situated west of Kırşehir city has been revisited, and shows an increasing grade of metamorphism from east to west, up to granulite facies conditions in the westernmost part of the section (Seymen 1984) (Figure 1.3). In this area close to the city of Kaman, thermobarometric calculations on high-grade garnet-sillimanite schist yield metamorphic equilibration around 700-750 °C at 6-7 kbar, and give an age of  $84.1 \pm 0.8$  Ma constrained by U/Pb SHRIMP analyses on monazites (Whitney et al. 2001, Whitney and Hamilton 2004). Moreover, a migmatite-dome has been identified to the south, close to Savcılı village (Genç 2004). During metamorphism, the metasediments underwent polyphase deformation involving three stages of superimposed folding, followed by a fracturing episode (Seymen 1983, Tolluoğlu and Erkan 1989). Close to Kaman, a sharp tectonic contact separates the CAM from the CAO. The CAO is characterized by an ophiolitic sequence subdivided in the Karaboğazdere Gabbro or Karakaya Ultramafite consisting mainly of pyroxene-hornblende gabbro and hornblendite, and the Çiçekdağ Formation with diabase, basalt and spilite covered by epiophiolitic sediments such as radiolarite, chert and pelagic mudstone (Seymen 1981, 1982). The intrusives are organized in two linear NNE-SSW trending belts. Granites and intrusive gabbros are located to the west of Kaman, and include the Sulakyurt-Baliseyh, Keskin, Behrekdağ and Çelebi granitoids. To the east, monzonitic and syenitic intrusions are represented by the Kortundağ, Hamit, Çamsarı, Bayındır and Durmuşlu plutons (Akıman et al. 1993, Otlı and Boztuğ 1998) (Figure 1.3). The Baranadağ pluton which intrudes the Kaman metamorphic sequence is made up of the Baranadağ quartz-monzonite in the north-east and the Cefalikdağ quartz-monzonite in the south-west (Seymen 1982). The metaluminous

Baranadağ quartz-monzonite is characterized by K-feldspar megacrysts and mafic enclaves, geochemically classified as H-type (hybrid) calc-alkaline granitoids, but displaying a transition to alkaline chemistry, which would suggest a mature stage of post-collisional magmatism (Aydın and Önen 1999). Crystallization ages based on U/Pb on titanite and Pb-Pb evaporation on zircon are  $74.0 \pm 2.8$  Ma and  $74.3 \pm 4.5$  Ma, respectively (Köksal et al. 2004, Boztuğ et al. 2009a). The cooling history of the Baranadağ quartz-monzonite is constrained by Ar/Ar on amphibole data giving plateau ages of 69-72 Ma and apatite fission-track ages around 57-60 Ma (Boztuğ et al. 2009a).

The remainder of the massif consists of depressions preserving felsic volcanics and Eocene to younger deposits resting unconformably on top of the crystalline rocks (Figure 1.3). Later compression (thrusting and folding) is mostly localized in the basins situated along the edges of the massif (Tüysüz et al. 1995, Kaymakci et al. 2009). In the south, the 150 km long ESE-WNW trending Savcılı Thrust Zone is the major brittle movement zone crossing the CACC. This structure shows a NNE-vergent thrust motion between the late Eocene and late Pliocene (Figure 1.3) (Seymen 2000).

### 1.3 Characteristics of the contact between the CAM and CAO in the vicinity of Kaman

#### 1.3.1 Metamorphism

An important characteristic of the contact between the Kırşehir metamorphics and the overlying CAO is the marked difference in metamorphic grade across this contact. On the western side, intrusive and extrusive mafic components of oceanic crust are represented as gabbros and basaltic lavas. The very fine-grained igneous material has a greenish matrix and contains numerous spherules filled by amorphous quartz. The green color of this unit is likely due to the presence of prehnite and/or pumpellyite as a secondary mineral assemblage. In thin section, the coarser-grained material displays chlorite and actinolite replacing magmatic pyroxene and amphibole. Both of these secondary mineral assemblages are consistent with a low-greenschist facies overprint due to circulation of hot seawater in hydrothermal systems within the ocean floor. To the east, the metamorphic rocks exposed immediately below the contact are clearly high-grade micaschists, calcsilicates, marbles and amphibolites. Under the optical microscope, the typical mineral assemblages in metapelites are quartz + potassic feldspar + sillimanite + garnet + biotite  $\pm$  cordierite  $\pm$  spinel. Metamorphosed

marls contain calcite + quartz + clinopyroxene + plagioclase + garnet + sphene  $\pm$  wollastonite, and metabasites consist of hornblende + plagioclase  $\pm$  garnet  $\pm$  clinopyroxene  $\pm$  quartz. Each of the described compositions records mineral assemblages indicative of the upper amphibolites facies (confirming (Whitney et al. 2001), who estimated PT conditions around 750°C at 7kbar

using garnet-biotite geothermobarometry).

These markedly different conditions of metamorphism, preserved on either side of the contact near Kaman, indicate that the two units underwent separate metamorphic histories involving two clearly different pathways through the crust.

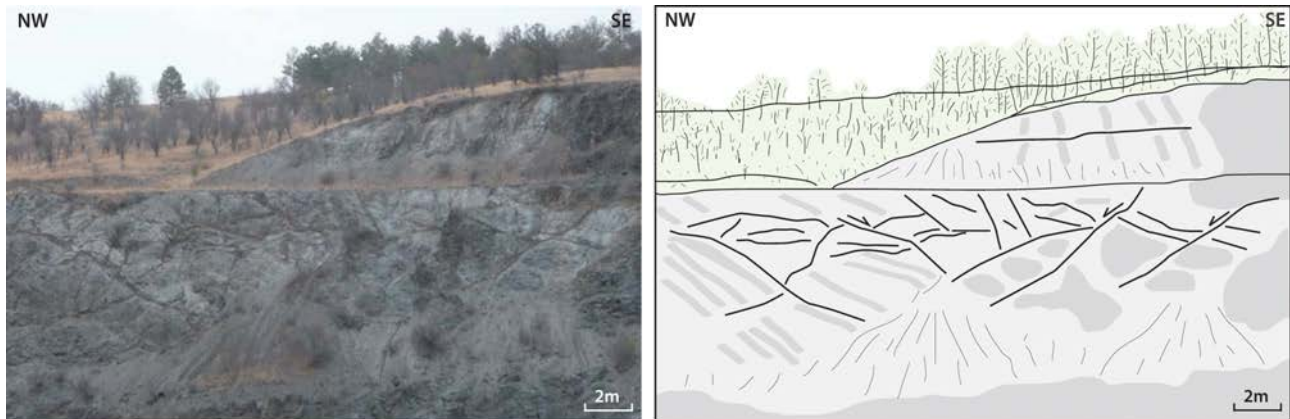


Figure 1.4 Field picture and interpreted sketch from an outcrop of sheared layered gabbro belonging to the ophiolitic sequence, close to the Hirfanlı dam. In the interpretation sketch, the gabbroic body is represented in grey. Dark grey patches and layers show either fresh and/or dark plagioclase-poor gabbro. Thick black lines show the distribution of discrete shear zones cutting through the gabbroic body.

### 1.3.2 Deformation

#### 1.3.2.1 Hangingwall: Ophiolitic sequence

To the west of Kaman, close to the Hirfanlı dam, a section through the SSZ-ophiolites exposes a layered gabbro in which clear deformational features can be observed even though the outcrop is highly altered and weathered (Figure 1.4). The layering of the gabbro is compositional: lighter gabbroic layers are mainly made of pyroxene, plagioclase and amphibole, which alternate with darker layers of essentially the same mineral composition but with a much lower volume percentage of plagioclase. This primary layering has been displaced at a later stage by ~5-20 cm wide shear zones, which appear darker in the field. The offsets observed on either side of these shear-zones indicate a normal shear motion. The shear planes are on average striking in a NE direction with a dip of ~40-50°. A set of two conjugate structures (one dipping towards the NW and one to the SE) can be distinguished (Figure 1.4). The age of this deformation can be constrained to the time interval between the formation of this piece of oceanic crust and the exhumation of the gabbro through the brittle field. There are, unfortunately, no exposures of the ophiolitic sequence closer to the contact with the Kırşehir metamorphics that would allow a further study of its deformation history.

#### 1.3.2.2 Footwall: High-grade carbonate-rich metasediments

##### - Overall structure -

In between the oceanic-derived rocks in the west and the monzonitic intrusives in the east, the Kaman metamorphics are exposed in a 2 km wide zone comprising foliated carbonate-rich metasediments. The geological map of the area (MTA sheet G17) and following publications (Seymen 1981), show the three main metamorphic units recognized in this zone (Figure 1.3). However, the presence of the Kalkanlıdağ Formation indicated to occur in the eastern part of the sequence has not been confirmed in the field. Instead, a major felsic dike (~250-350 m wide) is trending parallel to the main foliation. On the basis of our field observations we conclude that the Kaman metamorphics are mainly composed of pure and impure marbles intercalated with a few layers and lenses of calcsilicate, amphibolite and micaschist. The dominantly calcareous compositions indicate that the Kaman metamorphics represent the upper part of the metamorphosed lithological pile. Therefore, the detailed field map presented in Figure 1.5a-b only differentiates between massive marble and bands of calcsilicates, amphibolites and calcschists.

The overall structure is characterized by a well-developed pervasive foliation parallel to compositional layering of pure carbonate layers that alternate with layers of calcsilicate, schist and

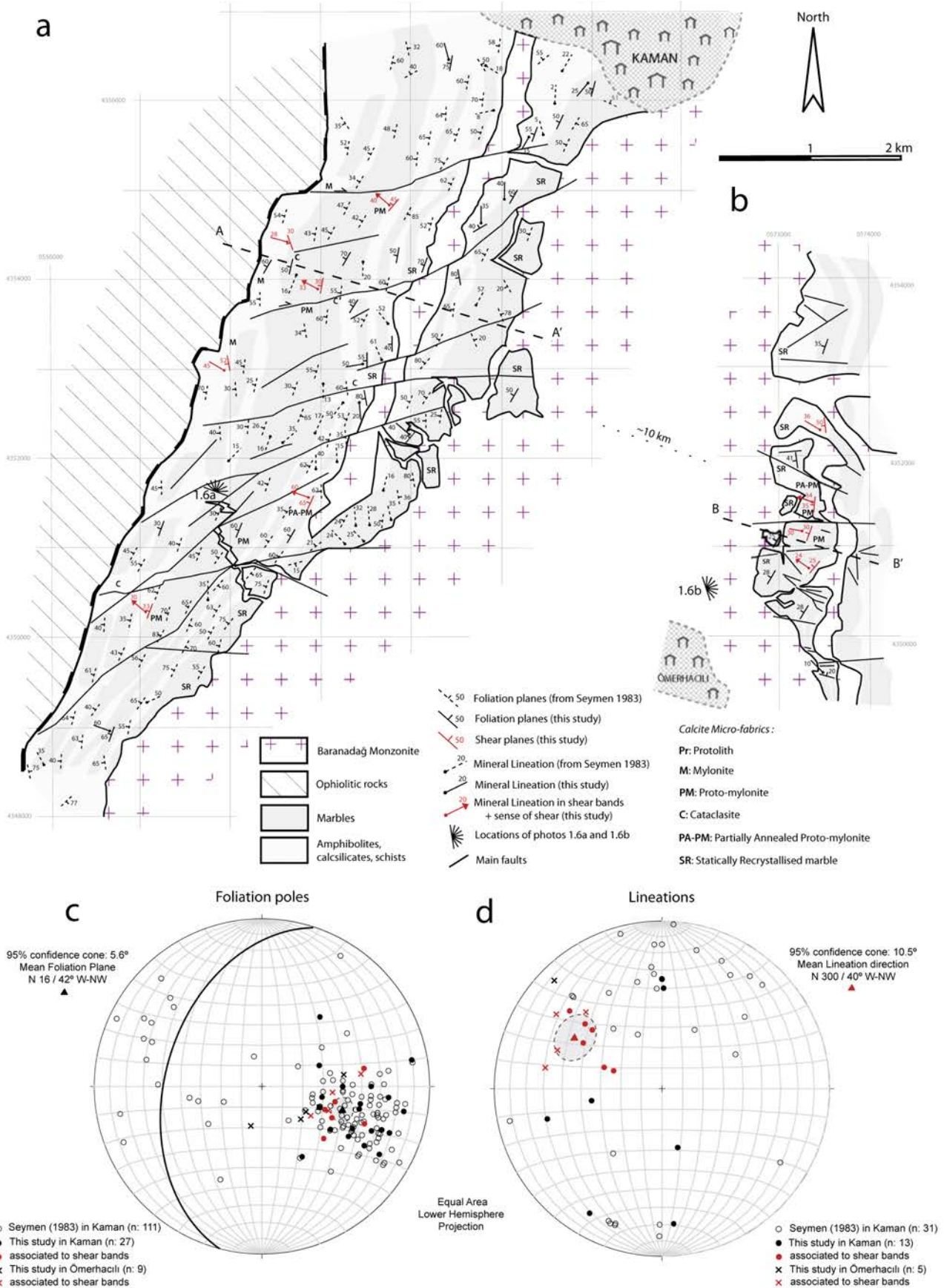


Figure 1.5 a-b) Geological and structural maps of the Kaman and Ömerhacılı areas, displaying the orientation of foliations and stretching lineations from Seymen 1983 and this study. Letter symbols indicate calcite fabrics observed in the field. Locations of panorama views and cross-sections of Figure 1.6 are shown. c) Equal area lower-hemisphere projections of foliation poles and mean foliation plane. d) Associated stretching lineations and mean lineation direction in cross-cutting shear bands.

amphibolite. Our measurements of the foliation planes and associated stretching lineations, compiled with previously published data (Seymen 1983), are shown in Figure 1.5a. The penetrative foliation is virtually parallel to the primary stratigraphic succession and delineates a consistent trend of about N015°E with dips commonly between 20° and 50° towards the W-NW (Figure 1.5c). Note that this trend corresponds to the strike of the contact with the ophiolite. Away from the contact the foliation tends to show progressively steeper dips. Local changes in orientation are the reflection of outcrop-scale folding of the foliated banding. Optical microscopy analyses in pure and impure marbles do not show any distinct grain shape preferred orientation (GSPO), and do not preserve any stretching direction. However, foliation planes in schist and amphibolite layers, preserved stretching lineations defined by elongated mica flakes and amphiboles. In those lithologies, the measured lineations are relatively scattered, but tend to NNE-SSW-trending shallow plunges (Figure 1.5d). No convincing shear sense criteria have been observed in the field, due to the dominance of calcareous compositions and lack

of relief exposing fresh vertical sections.

#### - Calcite fabrics -

Towards the contact, the lithology is mainly composed of pure calcite marble. In order to study the kinematics and the deformation history related to the tectonic contact, we focused on the evolution of calcite fabrics along an east-west traverse through the carbonate-rich sequence (Figure 1.6). Within the section, five marble types have been identified presumably recording different states of strain and temperature conditions during recrystallisation. On the basis of the proportion of dynamically recrystallized grains of calcite observed under optical microscope, we identified: protolith (<10%), protomylonite (10-50%), and mylonite (50-90%) types. Brecciated marbles have been defined as cataclasite, and statically recrystallized marble occurs in the vicinity of the intrusive bodies (Figures 1.7, 1.8). The different marble fabrics defined above show a specific spatial distribution over the area as they occur only in particular parts of the studied section as illustrated in the cross section of Figure 1.6. Samples from each marble-type have been studied in optical microscopy using

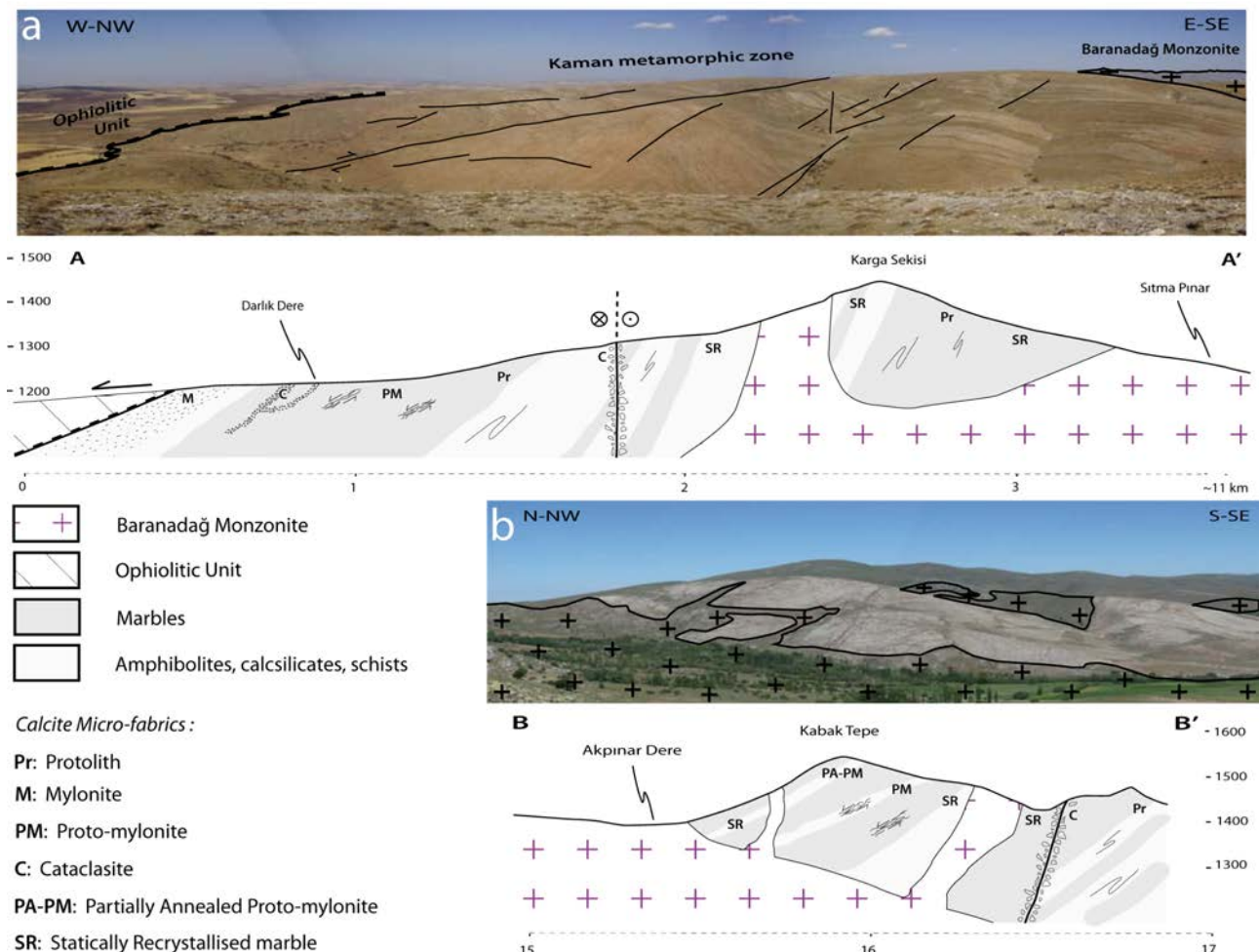


Figure 1.6 Panorama views and cross-sections through Kaman (a) and Ömerhacılı (b) areas (see Figure 1.5 for location). Bold letter symbols indicate the distribution of the main calcite fabrics within the calcareous metamorphic sequence.

ultra-thin sections ( $\sim 10\text{-}15\mu\text{m}$  thick), and crucial fabrics have been investigated using the Electron Back-Scattered Diffraction (EBSD) technique in the scanning electron microscope. Samples for EBSD analysis were polished with colloidal silica (particle size 40 nm) for approximately one hour and subsequently coated with a thin carbon layer. The SEM working conditions are an acceleration voltage of 25 kV, a working distance of 20 mm and a sample tilt of  $70^\circ$ . High-resolution EBSD maps combining both beam and stage mapping modes were performed with step sizes of 3 and 4

$\mu\text{m}$  over large areas across the sample (up to  $6\times 1$  mm in size). Representative smaller areas were chosen from the large EBSD maps to illustrate the relationships between the different fabrics within the calcite protomylonites (Figure 1.9).

#### Protolith (Pr)

The so-called protolith consists of a coarse-grained marble ( $\sim 0.5\text{-}3$  mm grain size in average) mostly developed in the central part of the studied section. It represents the dominant fabric of the area and is associated with decimeter to meter wide, grey/

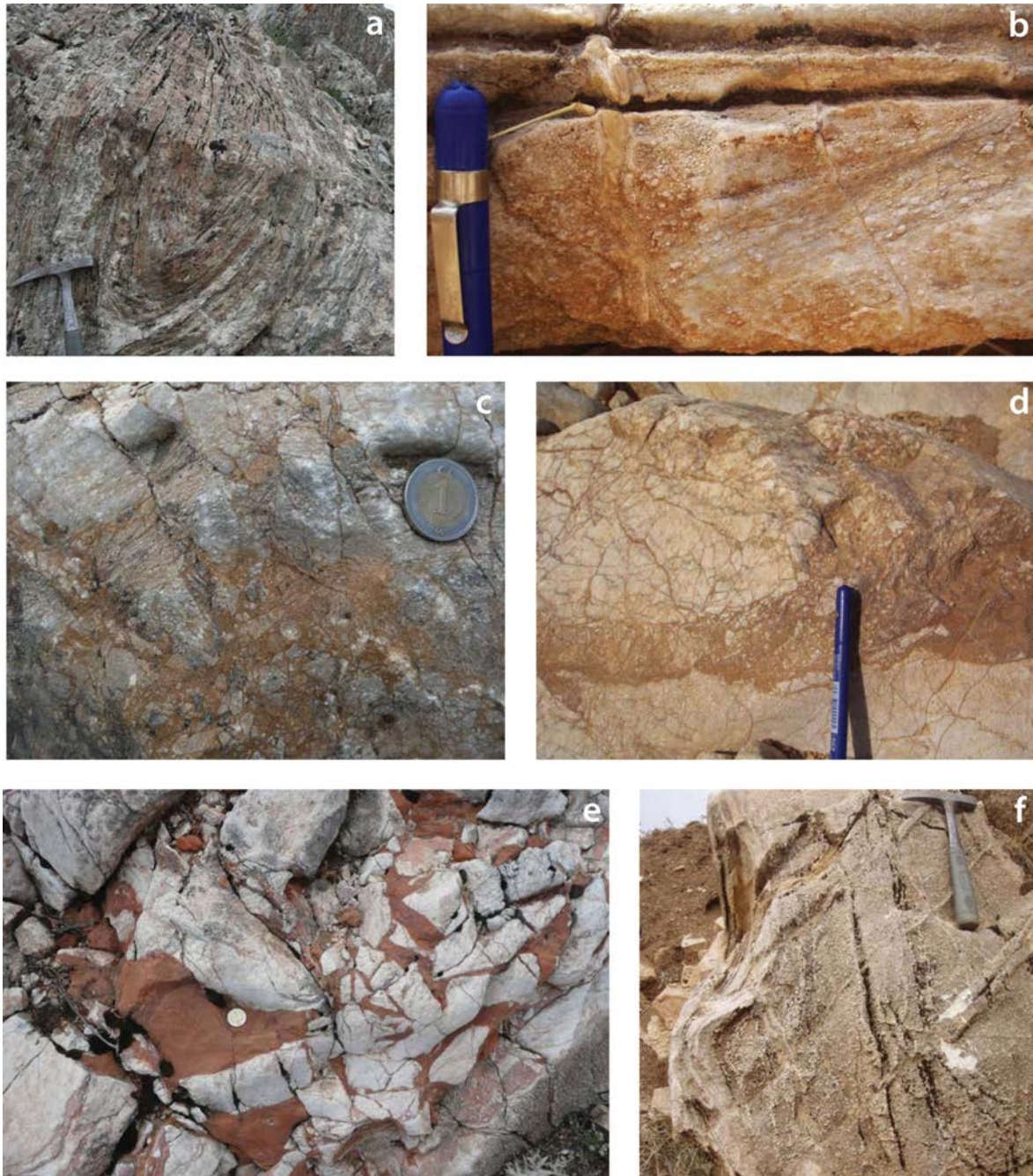


*Figure 1.7* Field pictures of typical marble types in Kaman area (all pictures have been taken in a north-easterly direction). a) Isoclinally folded calcisilicates. b) Crosscutting relationship between the main foliation plane and the protomylonitic shear bands. c) Protomylonitic and mylonitic marble types involved in a brecciated zone. d) Cataclastic corridors affecting protolith type marble. e) Tectonic breccias in the vicinity of a major strike-slip fault crossing the section. f) Vertically oriented and folded very coarse grained marble cut by oblique veins in the vicinity of Baranadağ pluton.

blue and white colored banding accentuating the main foliation plane. In thin section, the grains are equigranular, euhedral to subhedral in shape, and do not show any undulose extinction. They are characterized by a high density of twin lamellae, which exhibit one to three set of twins with a vague preferred orientation. The twins are relatively thick ( $>1\mu\text{m}$ ) and straight, which corresponds to type II twins following the classification of (Burkhard 1993).

#### Proto-mylonite (PM)

Protomylonitic fabrics are characterized by a drastic grain size reduction as compared with the protolith-type described above. In the field, protomylonites occur as localized bands (0.1-10 cm wide) crosscutting the main foliation planes (Figure 1.7b), mostly within the first kilometer away from the ophiolite. The protomylonite bands are oriented parallel to the strike of the main foliation but with slightly steeper dips (Figures 1.5a-c, 1.6a). They entirely consist of calcite grains distributed in large and elongated porphyroclasts surrounded by small equant recrystallized grains. The smaller grains are organized in bands crossing through and replacing pre-existing larger crystals, indicating that the change in grain size is accompanied by deformation. The bands where the deformation is concentrated are interpreted as shear bands. These bands are anastomosed around the porphyroclasts, and form conjugate zones parallel and oblique to the main shear plane (Figure 1.8a). On the shear plane, the long axes of elongate porphyroclasts provide a clear marker of the stretching direction associated with the shearing. The lineations associated with those shear bands recognized over the area document a mean trend to N300°, at plunges of about 40° (Figure 1.4d). In the field, the geometry of asymmetric  $\sigma$ -clasts has been used as a shear sense indicator consistently pointing to a top-to-WNW motion (Figure 1.8a).

For microscopic observation, protomylonitic samples have been prepared perpendicular to the shear bands and parallel to the mineral lineation. The shear zone boundary is used as a reference plane and shown horizontal. Numerous large calcite crystals contain a regular and dominant set of twins that are faintly bent and thus present a slightly sigmoidal shape, steeper in the centers of the grains and curving into the shear bands (Figure 1.8c). Using the terminology of Burkhard (1993) these twins belong to type III indicating deformation temperatures above 200 °C. The orientation of the dominant set of twins shows a regular and systematic 30° clockwise relationship with the bands of reduced grain size. In addition to the asymmetry of the large grains, the persistent

obliquity of these twins may be used to determine the shear sense (Bestmann et al. 2000), indicating a sinistral displacement with respect to the reference frame as shown in Figure 1.8c. Placed back in its field context, the shearing motion indicates a normal sense where the top block is moving towards the W/NW (as also inferred in the field). The pronounced undulose extinction of many of the porphyroclasts stresses the importance of internal deformation processes such as intracrystalline slip (dislocation glide) associated with twinning.

In the shear bands, the fine-grained fabric has been characterized using electron backscatter diffraction (EBSD) measurements (Figures 1.9a, 1.9b). Within those bands, we distinguished two domains with different grain size of  $\sim 17\mu\text{m}$  and  $45\mu\text{m}$  in average (corresponding histograms in Figure 1.9c).

The smaller grain domain is only composed of very fine-grained calcite grains, which are separated from each other by high angle orientation boundaries ( $>20^\circ$ ). They contain no internal structures, no twinning and show sharp extinction, as expected from subgrain rotation during dynamic recrystallization. They present an elongated shape and inclination of 10-20° clockwise to the reference plane. Pole figures of the recrystallized fine grains show typical calcite recrystallisation textures with the c-axes more or less perpendicular to the shear plane and the a-axes lying within the shear plane (c-slip on a plane) (Figure 1.9d). The strong CPO patterns also point to dislocation creep activity during the formation of the protomylonites.

The larger grain domain shows a similar oblique elongation pattern as the smaller grains. The larger grains show strong undulose extinction patterns, the formation of subgrains close to the grain boundaries and significant progressive rotation of the crystal lattices within the grains (misorientations of  $\sim 20^\circ$  for within the 200-250 $\mu\text{m}$  grains and  $\sim 10^\circ$  within the 100 $\mu\text{m}$  grains). CPO of the coarse grains show oblique c-axes at 45° to the shear plane which reflect the incomplete recrystallisation of the host grain within the larger grain domains that is in good agreement with microstructural observation. The presence of two domains with different grain sizes may result from the progressive localization of the deformation during exhumation.

#### Mylonite (M)

As strain intensity increases, the marble fabrics evolve into very fine-grained ribbon mylonites as illustrated in the hand specimen shown in Figure 1.8a. This microstructure is mainly present at the immediate vicinity of the contact (Figure 1.6a).

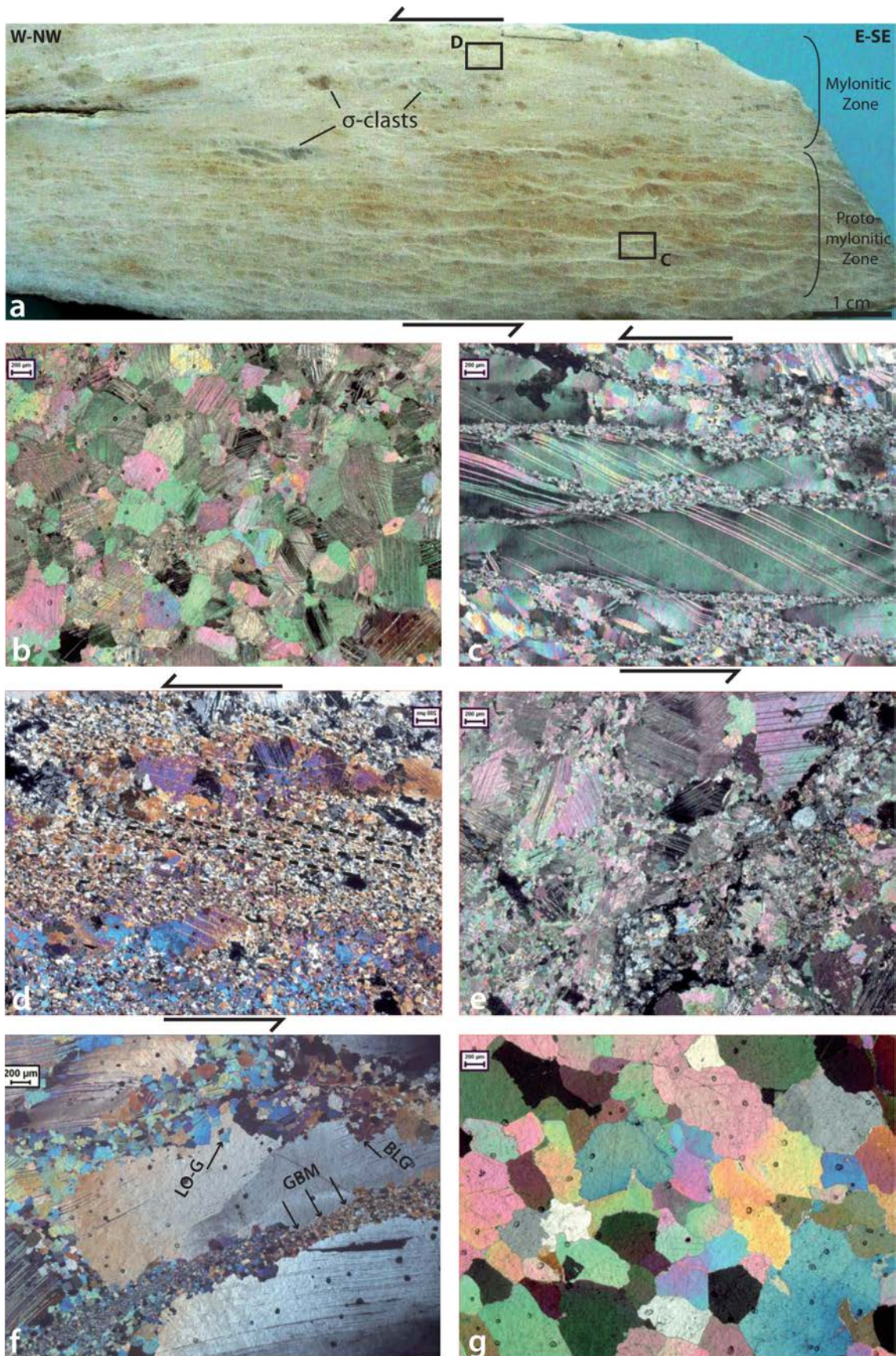


*Figure 1.8* a) Hand specimen of protomylonite and mylonite marble types with calcite  $\sigma$ -clast shear sense indicator. All calcite microstructures from (b) to (g) are shown at same magnification (scale bar = 200  $\mu\text{m}$ ) and oriented NW-SE (looking NE) as in Figure 1.7; b) Protolith type fabric, c) Protomylonite type fabric, d) Mylonite type fabric, dashed lines accentuate the grain shape preferred orientation of the dynamically recrystallized grains, e) Cataclasite type fabric, f) Partially Annealed Protomylonite type fabric, LO-G: Leftover grain, GBM: Grain boundary migration, BLG: Bulging, g) Statically recrystallised marble type fabric.

The mylonite type fabric consists of large clasts, which have been almost entirely dynamically recrystallized into small grains with an average grain size of 13  $\mu\text{m}$ . Porphyroclast remnants are elongated parallel to the shear bands while dynamically recrystallized grains present an oblique shape preferred orientation (Figure 1.8d). Small grains are relatively equigranular with no internal deformation structures. We also noted the presence of secondary phases likely due to enhanced fluid infiltration at the contact with the ophiolites.

#### Cataclasites (C)

Cataclastic marble has been subdivided in 2 types:

(1) Corridors of breccia which are concentrated in a zone between 100 and 400 m away from the contact with the ophiolite, have preferentially developed parallel to the main foliation and dip at moderate angles towards the west north-west. Decimeter to meter thick ultracataclastic joints and microbreccias occur locally and are organized in connected branches. The brecciated zones cut across, hence mechanically rework the protolith, protomylonite and mylonite marble types (Figure 1.7c). The host rock surrounding the brecciated zones experienced an intense in-situ brittle fracturing mainly characterized by millimetre scale cracks and joints (Figure 1.7d). Within the brecciated corridors, we observed a gradual fragment size reduction from the fault-wall toward the central part of the deformed zones, often accompanied with a marked change in matrix color from brown to yellow. The matrix contains a high percentage of secondary phases such as quartz and dolomite (Figure 1.8e). All of these features from the faulted rocks are consistent with fluid-assisted brittle mechanisms of grain size reduction.

(2) Massive tectonic breccias which are associated with steep strike-slip faults crossing the entire Kaman zone and the intrusives with a  $\sim\text{N}070^\circ\text{E}$  trend. These major dextral strike-slip faults are consistently plunging at high angles towards the south and carry a small normal component (low angle oblique slickenlines on fault planes). Megabreccias that developed only a few meters away from the fault zone contains decimeter to meter scale broken fragments, separated from each other by a fine-grained red matrix. The red color of the matrix is likely due to ferric oxi-hydroxide mineralizations by enriched fluids circulating into open faults. The presence of graded and crosscutting lamination of the fine-grained matrix in between clasts present in the fault zone suggests the activity of fluids, transport and deposition of material within fault related voids (Figure 1.7e).

#### Statically recrystallized marble (SR)

Further east, the marble grain size increases up to centimeter-sized crystals at the vicinity of the western border of the Baranadağ intrusive and associated major dikes (up to  $\sim 300$  m-wide) (Figure 1.6a). Within this zone, the main foliation becomes steeper until nearly vertical. Marbles that are situated in direct contact with the intrusives are crosscut by oblique crosscutting veins (Figure 1.7f). The very coarse grains of calcite are equigranular and characterized by an euhedral and polygonal shape, no undulose extinction, rare twins, and no features pointing to internal deformation. All of these microstructural properties are consistent with static recrystallisation of the marble at high temperature (Figure 1.8g).

#### 1.4 The contact between the Kırşehir metamorphics and the Baranadağ quartz monzonite close to Ömerhacılı

From Kaman, the Baranadağ quartz-monzonitic pluton extends over twelve kilometers toward the east. The eastern border of the magmatic body near the village of Ömerhacılı is characterized by an irregular contact with the metamorphic rocks. Close to Ömerhacılı, the metamorphics locally display exposures of pure marble where we carried out a detailed structural analysis (Figure 1.5b). The surrounding metamorphic rocks of the area show a gradual transition to more pelitic compositions, suggesting that these rocks represent a somewhat lower part of the lithological succession. The irregular pattern of the contact between igneous and metamorphic rocks is enhanced by the presence of numerous one to ten metre scale dikes cutting at a high angle across the shallow-dipping foliated host rock. In a few cases, marble blocks have been isolated as roof pendants on top of the pluton. The monzonitic intrusion contains very coarse euhedral phenocrysts of potassic feldspar accompanied by smaller minerals of plagioclase, hornblende and quartz. These minerals do not show any trace of ductile deformation and the entire magmatic body is generally considered as undeformed.

The carbonate-rich rocks preserve a main foliation pattern, which is very similar to the one described from Kaman (average trend is  $\text{N}015^\circ\text{E}$ , dipping  $33^\circ$  toward the W-NW) (Figure 1.5c). Close to the dykes, we observed mega crystals of calcite with grain sizes typically in the range of centimeters. This macro-fabric is preserved in the marbles at distances of up to hundreds of meters away from the dykes and the main pluton. At about 200-400 meters away from the main intrusive contact, a progressive transition occurs

from complete static recrystallisation to protolithic ribboned marble. In the transition zone, discrete crosscutting protomylonitic bands have been found with peculiar coarse-grained porphyroclasts. We termed this special fabric Partially Annealed Protomylonite (PA-PM) as we can recognize an intermediate stage between protomylonitic and statically recrystallized marble (Figure 1.8f).

Protomylonitic features are represented by the presence of large twinned clasts with serrated grain boundaries, surrounded by interconnected bulged grains, and parallel to oblique bands of dynamically recrystallized smaller grains. The twins of the large grains are straight, slightly bend and discontinuous which make them belonging to type IV twins indicating temperatures above

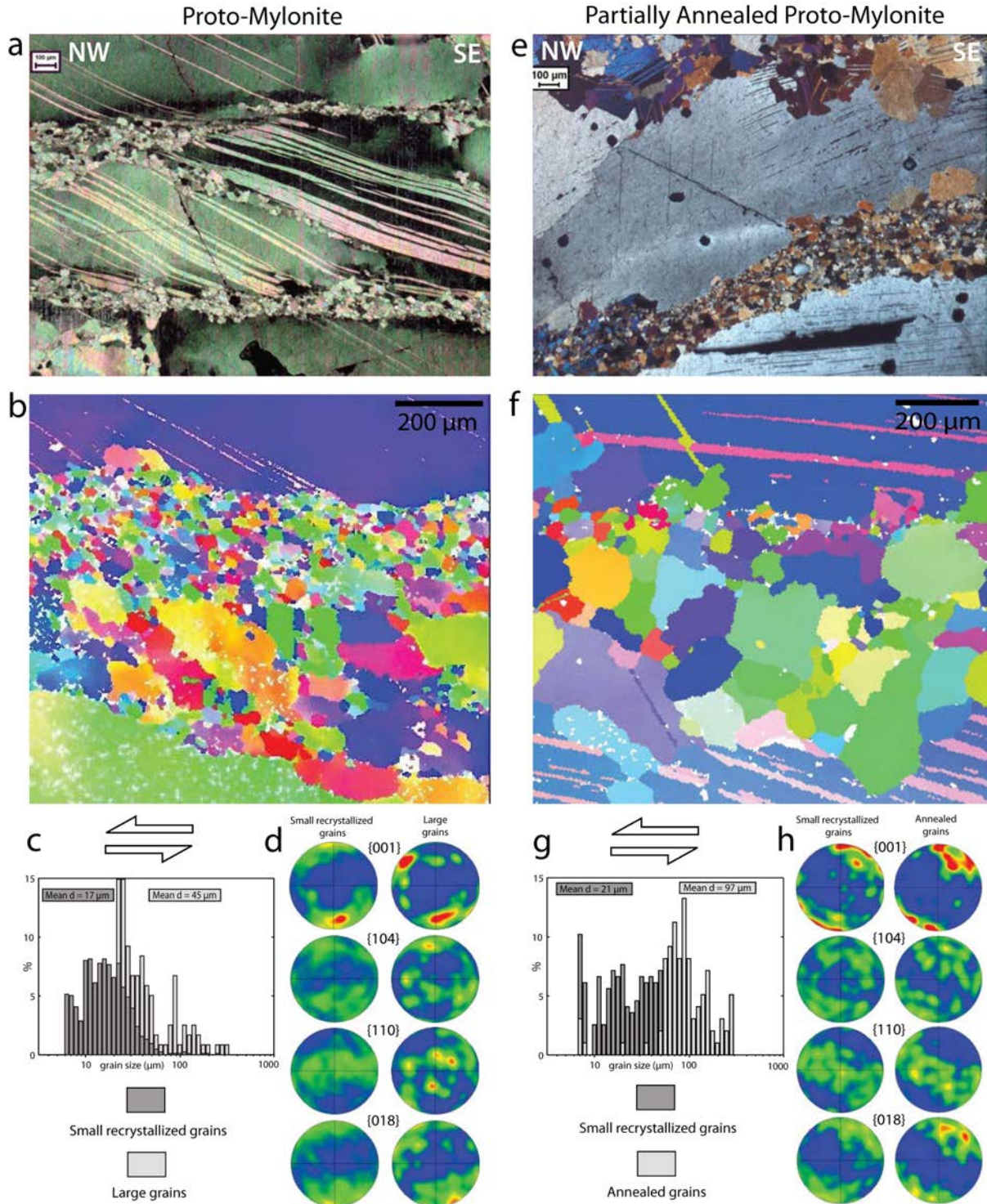


Figure 1.9 a,e) Micrographs of the protomylonite and partially annealed protomylonite type fabrics at higher magnification, b,f) Orientation maps measured by EBSD, focused on the fine grained shear bands (measurements are contrast-coded by orientation), c,g) Grain size histograms from recrystallised grains in the shear bands Grain boundaries have been defined by lattice misorientations larger than  $10^\circ$ . d,h) Contoured c-, r-, a- and e-axes pole figures based on EBSD measurements for the small and large grains within (c) and (d).

250 °C (Burkhard 1993). The static growth of these grains is identifiable from the presence of leftover small grains consumed by the larger ones, grain boundary migration over the shear bands, highly lobate grain boundaries and bulging of twin boundaries (Figure 1.8f). Those features are characteristic of processes involving annealing of the protomylonite bands during high-temperature static recrystallisation.

We investigated the fine-grained fabrics within the shear bands using EBSD techniques. The shear band analyzed contains two types of recrystallized grains: 1) small equant grains with an average size of 21  $\mu\text{m}$ . Those small grains have the same size and shape as the dynamically recrystallized grains from the Kaman protomylonites and we infer that they were formed during dynamic recrystallization and progressive localization of deformation; 2) larger grains (average grain size 97  $\mu\text{m}$ ) with very irregular lobate grain boundaries. Those grains contain very little or no internal deformation and show growth of certain grains at the expense of other grains (Figures 1.9e-f). We interpret these larger grains as the result of static annealing at higher temperatures due to the intrusion of the pluton after protomylonitic deformation.

Pole figures show that the small dynamically recrystallized grains have a similar CPO as the larger annealed recrystallized grains. The typical CPO formed in the grains from the shear band is apparently retained in the newly grown annealed grains. It follows that annealing did not obliterate the previously formed deformation-related CPO, which is in good agreement with similar results from experimental annealing studies (Barnhoorn et al. 2005) (Figure 1.9h).

The orientations of shear zones, mineral lineations and associated senses of shear for the Ömerhacı area are summarized in Figure 1.5. The inferred shearing orientation and kinematics on shear bands show a pattern, which is nearly identical to that in Kaman, with a consistent top-to-WNW shear motion.

## 1.5 Synthesis - Discussion

### 1.5.1 *The first extensional detachment described from the northern CACC*

The carbonate-rich metasediments exposed around Kaman belong to the upper part of the metamorphosed lithology. The nature of the deformation of these metamorphic rocks in the vicinity of the ophiolite-derived materials places constraints on the nature of the contact. The mineral assemblages from the essentially unmetamorphosed ophiolitic hanging wall and the

high-grade marble-rich footwall indicate a major metamorphic gap across the contact. In terms of deformation, the hanging wall is affected by conjugate semi-brittle normal faults.

In the footwall, five distinctive marble type fabrics have been identified. The coarse-grained protolith type associated with the main metamorphic foliation is crosscut by discrete protomylonitic and mylonitic shear bands. Shear sense indicators such as asymmetric calcite  $\sigma$ -clasts, consistent sets of oblique twins in calcite porphyroclasts and dynamically recrystallized grain shape preferred orientations all indicate top-to-WNW normal shearing. Towards the contact, the ductile structures have been overprinted by brittle structures and reworked into localized cataclastic breccia zones developed in the same low angle orientation below the ophiolite. Therefore, the structural evolution recorded in the marbles and presented in the cross section of Figure 1.5 suggests a continuous deformation history from ductile to brittle conditions during cooling and exhumation and is clearly consistent with the typical evolution described from extensional detachment zones (Lister and Davis 1989).

In addition, the spatial distribution and evolution of the calcite fabrics in the Kaman area is very similar to that described from the shear zone complex on Thassos Island in Greece, associated with a major crustal-scale extensional detachment, and also developed in a marble-dominated lithology (Bestmann et al. 2000).

We note that the term Kırşehir Metamorphic Core Complex (KMCC) has already been proposed in the literature (Genç 2004), but referring to an inferred post Middle-Eocene detachment fault in the vicinity of Savcılı village. However, the nature of this structure is currently debated, as other authors argue for a thrust contact (Seymen 2000, Isik et al. 2010).

### 1.5.2 *Stages of deformation, and the rate and timing of exhumation in Kaman*

Our structural analysis on marble fabrics provides important constraints on the successive events that affected the Kaman-Ömerhacı area. We supplement these results with published geochronological data to construct Pressure-time and Temperature-time trajectories for the Kırşehir metamorphics from their regional metamorphism to their final unroofing. In order to summarize this information in a simple way, we propose a conceptual geotectonic model in four stages illustrating the main evolution of the metamorphic rocks and their exhumation (Figures 1.10a-b).

### Stage 1: Alpine regional metamorphism

From the Kaman zone, constraints on peak metamorphic conditions are pressure-temperature estimates on high-grade garnet-sillimanite metapelites giving  $\sim 700\text{-}750$  °C for 6-7 kbar, and a growth age of monazite of  $84.1 \pm 0.8$  Ma (U/Pb SHRIMP analysis) (Whitney et al. 2001, Whitney and Hamilton 2004). Therefore, during Santonian times the Kaman zone was buried at  $\sim 20$  km depth and underwent clearly high temperature metamorphic conditions. During this regional high temperature event, deformation led to the development of the main syn-metamorphic foliation, and associated isoclinal folds. We ascribe the protolith-type marble and its highly twinned, coarse equigranular calcite microstructure to this regional high temperature stage.

### Stage 2: Fast exhumation accompanied with ductile shearing

Following peak metamorphism, the metamorphic sequence rose up through the crust to relatively shallow levels where it became intruded by large plutons. Titanite and zircon crystallization ages on the neighboring quartz-monzonites are  $\sim 74$  Ma, and intrusion occurred at relatively shallow crustal levels (10-12 km depth) (Köksal et al. 2004, Boztuğ et al. 2009a). Age and depth of both metamorphism and magmatism indicate that the Kaman zone travelled some 10 km vertically through the crust in a time span of 10 Ma, which corresponds to a fast rate of exhumation during the early Campanian ( $\sim 1$  km/Ma). In the case of the Kaman area, we suggest that this stage of fast exhumation was accommodated, in the upper crust, by ductile shear zones cutting through the metamorphic foliation. These shear bands indicate ongoing localization of the deformation, leading to a microstructure of internally deformed coarse-grained clasts and very fine dynamically recrystallized grains. The absence of dolomite in the protomylonite-type marble has unfortunately precluded in-situ thermometry (Mg equilibrium between calcite and dolomite) to estimate the ambient temperature range during the formation of the protomylonitic fabric. However, by comparison with very similar microstructures from the Thassos Island shear zone (Bestmann et al. 2000, Bestmann and Prior 2003), and combined with the published recrystallized grain size/temperature dependence trend in naturally deformed calcite rocks (de Bresser et al. 2002), it seems reasonable to estimate the metamorphic temperature during the development of the protomylonitic shear bands (with an average size of dynamically recrystallized grains of  $\sim 20\mu\text{m}$ ) in Kaman around 300-400°C.

### Stage 3: Magmatic intrusion at shallow crustal levels

In addition to the clearly crosscutting relationships between the metamorphic rocks and the magmatic plutons and dikes in the field, microstructural evidence strongly suggests static overgrowth (annealing) of the protomylonitic microstructure in the Ömerhacılı area. The only appreciable explanation for this post-deformational annealing is local heating in the vicinity of the intruding pluton. Al/Ti thermometers on amphiboles indicate a temperature of crystallization of the monzonite at 600-750°C (İlbeyli 2005, Boztuğ et al. 2009a). This demonstrates that the intrusion reheated a relatively cooled metamorphic sequence during late Campanian times. Consistent with this idea, (Genç 2004) has noted that the hosted migmatite dome close to Savcılı displays discordant, sub-vertical and east-west trending gold-bearing quartz veins formed during magmatism and suggesting release of metamorphic fluids from depth while the metamorphic rocks already arrived at shallow crustal levels. Intrusion of the Baranadağ quartz monzonite postdated ductile deformation, as it displays intrusive rather than tectonic contacts with the metamorphic host rocks, and shows no evidence for ductile fabrics itself. On both sides of the magmatic body, there is no significant change in main direction of foliation planes and associated cross-cutting sets of shear zones. Therefore, we interpret that the original geometry of the pre-intrusion deformation zone remained unchanged during the magmatic event.

At the scale of the CACC, it is generally accepted that the CAM and the ophiolites (CAO) were both intruded by mostly undeformed intrusives (Erlor and Göncüoğlu 1996). Therefore, and in view of the crosscutting and static heating relationships between the metamorphic and magmatic rocks; we suggest that the accommodation of the ductile deformation via detachment faults located at the boundary between the metamorphics and the ophiolites such as described in Kaman, ceased at this time. A similar scenario has already been proposed for the Mojave Desert (California), where the cessation of active extensional detachment zone has been ascribed to intrusion of a high-level pluton across it (Davis et al. 1993). Any ongoing extensional denudation must have occurred by brittle faulting.

### Stage 4: Final exhumation at slower rate

After intrusion, the metamorphic/igneous complex behaved as one single crustal unit.  $^{40}\text{Ar}/^{39}\text{Ar}$  dating of amphiboles from the Baranadağ quartz-monzonite yielded cooling ages of 69-72 Ma (cooling below  $\sim 500$  °C) and apatite fission-track

*Figure 1.10* a) Pressure/time and Temperature/time trajectories for the Kaman metamorphics based on present microstructural evidence and geochronological data from the literature. b) Conceptual tectonic model in 4 stages illustrating the tectono-metamorphic evolution of the Kaman-Ömerhacılı rocks during their exhumation. For each stage, typical calcite microstructures as observed in the field are linked to the model.

analysis gave ages around 57-60 Ma (Boztuğ and Jonckheere 2007, Boztuğ et al. 2009a). Based on the apatite fission-track data, a rapid exhumation rate ( $>1$  km/Ma) has been estimated for all of the Camsarı, Hamit, Durmuşlu and Baranadağ plutons (Boztuğ et al. 2009a). However, the apatite fission-track age versus elevation plot from the Baranadağ quartz-monzonite itself, rather suggests a slower exhumation rate below 0.2 km/Ma (Figure 10a).

The intrusive body is not ductily deformed, but was affected by brittle deformation after its emplacement, as faults displace the boundaries of the pluton. This brittle phase led to a well-developed network of N70°E trending steep dextral strike slip faults with a small normal component, cutting across both the metamorphic rocks and the monzonites. We tend to conclude that the later stages of exhumation in the Kaman and Ömerhacılı areas proceeded at a slower rate than previously considered, and that this part of the exhumation history was accommodated by brittle tectonics coupled with erosion until reaching the surface in Late Paleocene (Kaymakci et al. 2009).

### *1.5.3 Role of tectonics during exhumation at the scale of the CACC*

The presence of an extensional detachment below the ophiolitic unit in the Kaman region is a newly recognized feature and supports the role of tectonics during the exhumation of the Kırşehir massif. However, the presence of domains of massive marbles intruded by the Çelebi granitoids west of Kaman indicates that the inferred structure might not be the original place where the detachment rooted in the middle or lower crust. We may consider that the main extensional zone is located in the west (30-40 km away) and that the Kaman zone represents the prolongation of a large-scale flat-lying detachment zone. However, our structural data in Kaman do not provide any evidence for the activity of the fault zone under amphibolite conditions, as the inferred marble ductile shear bands indicate deformation at upper crustal levels. A possible alternative interpretation would be that the contact close to Kaman is a secondary or coeval imbricated inner detachment within a larger extensional setting, such as described from the Menderes massif (Bozkurt and Oberhänsli 2001, Ring et al. 2003, van Hinsbergen 2010).

At the scale of the Kırşehir massif, large exposures of volcanic rocks represent the cogenetic extrusives related to the central Anatolian intrusives. These volcanic rocks rest directly on top of the metamorphics with a faulted contact (for example close to Sorgun, Figure 3),

which indicates that tectonics must be responsible for a significant part of the final exhumation of the Kırşehir metamorphic rocks to the surface.

At the scale of the CACC, other extensional features have already been previously described. In the Niğde massif, rocks from the lower metamorphic unit record top-to-the-NE/ENE shearing along the contact with ophiolitic gabbros (Gautier et al. 2002), and discrete ductile extensional shear zones cutting through the Yozgat and Ağaören batholiths respectively record top-to-NW and top-to-SW motions, dated around 72 Ma (Isik et al. 2008, Isik 2009).

Our results support Gautier's (2002) suggestion that a synchronous high-magnitude extension may have occurred at the scale of the CACC during the late Cretaceous. However, the regional east-west direction of extension during exhumation (Gautier et al. 2008) is difficult to explain in its present configuration, as shearing motions show no clear consistency at the larger scale.

In order to completely evaluate the kinematics of exhumation-related shearing in the CACC, future work would be necessary on tectonic structures potentially present at the edges of the Akdağ massif.

Finally, structural and metamorphic studies carried out in the southern Niğde massif have documented that the lower unit of metasediments is associated with the highest grade of metamorphism while the upper unit mostly recorded lower grade conditions (Whitney and Dilek 1998). In contrast, the upper unit of the metasedimentary pile near Kaman also shows the highest grade of metamorphism. It seems, therefore at the scale of the CACC, that there is no systematic relationship between the position in the metamorphic unit and the metamorphic grade.

## **1.6 Conclusions**

In the area around Kaman and Ömerhacılı, high-grade metamorphic rocks of the Kırşehir massif are exposed underneath virtually non-metamorphic ophiolites, close to the Baranadağ pluton. Field- and microscale structures from the marble-rich footwall sequence indicates that the contact with the overlying ophiolites represents an extensional detachment zone. Kinematic indicators from protomylonitic shear bands point to a top-to-the-W-NW motion.

The tectonometamorphic evolution of the area, from regional Alpine peak metamorphism to final unroofing at the Earth's surface, involved two different stages of exhumation.

(1) The metamorphic rocks underwent localized ductile shearing between 20 and 10 km

depth involving an upper-crustal extensional detachment zone, leading to fast exhumation at a rate of  $\sim 1\text{km/Ma}$ . This occurred between peak metamorphism ( $\sim 84\text{ Ma}$ ) and shallow crustal intrusion of the Baranadağ pluton ( $\sim 74\text{Ma}$ ). Prior to intrusion, the metamorphic sequence cooled down to  $300\text{-}400^\circ\text{C}$  in Late Campanian times.

(2) The second and final phase of exhumation, bringing the metamorphic/igneous complex to the surface during the Paleocene, occurred at a much slower rate, and was accommodated by brittle upper crustal tectonics coupled with erosion processes.

In combination with the existing data, the Kaman structures demonstrate that tectonics did play an important role in the regional-scale exhumation of metamorphic rocks in the CACC. The newly recognized extensional detachment in the northern Kırşehir massif may be part of a larger scale system, which may have rooted further west.

## Acknowledgements

We thank Steve Smith and Uwe Ring for critical reviews on the published version of this chapter. This study was financially supported by the Netherlands Research Centre for Integrated Solid Earth Sciences (ISES), the Netherlands Organisation for Scientific Research (NWO) and the DARIUS Programme.

# CHAPTER 2



# P-T-t-d evolution and extensional exhumation history of a high-temperature complex (Hırkadağ Block, Central Anatolia)

## Abstract

The Central Anatolian Crystalline Complex (CACC) is a large continental domain exposed in central Turkey. This domain was affected during the Late Cretaceous by high temperature metamorphism. As a result of this event, Paleozoic sediments became metamorphosed, initially under Barrovian conditions, then overprinted by high temperature – low pressure metamorphism, and intruded by widespread batholiths. The Gülşehir area in the central part of the CACC is a unique place where the coeval evolution of a crustal high temperature complex (metamorphic and intrusive rocks) and its overlying basin may be investigated. In this study we focus on the crystalline Hırkadağ Block, where we applied an integrated approach involving metamorphic, structural and geochronological analysis in order to elucidate its tectonic history through its crustal journey toward the Earth surface. Our metamorphic study reveals that high temperature metamorphic conditions reached  $\sim 7\text{-}8$  kbar/ $700^\circ\text{C}$  and were relatively homogenous at the scale of the Hırkadağ Block. Coeval with the regional metamorphism, the rocks were intensely deformed involving isoclinal folding, the development of a pervasive foliation and top-to-the-SE shearing. This was followed by decompression to pressures of  $\sim 3\text{-}4$  kbar at  $800^\circ\text{C}$ , which may be linked with local granodioritic intrusions taking place at  $\sim 77$  Ma. The Hırkadağ high-grade metamorphic and intrusive rocks then started to cool down during the latest Cretaceous, as indicated by  $68.8 \pm 0.9$  Ma (biotite) and  $67.0 \pm 1.2$  Ma (potassium feldspar)  $^{40}\text{Ar}/^{39}\text{Ar}$  cooling ages. Evidence for tectonic exhumation has been identified within the marbles at the NE margin of the Hırkadağ Block, in the form of discrete protomylonitic and mylonitic shear bands showing a consistent N40-60 top-to-NE sense of shear. Further east, the contact between brecciated mylonitic marbles and non-metamorphic conglomerates preserves the typical structural features of an upper-crustal detachment, similar in many respects to the one recently described further to the NW, near Kaman. Viewed at the scale of the CACC, the metamorphic and structural characteristics of the Hırkadağ Block seem to justify correlation of the Gülşehir area with those of the Ağaçören intrusives and Niğde Massif, rather than with the Kırşehir Massif as commonly proposed in the past.

Côme Lefebvre  
Kalijn M. Peters  
Philip C. Wehrens  
Fraukje M. Brouwer  
Douwe J.J. van Hinsbergen  
Nuretdin Kaymakci  
Reinoud L.M. Vissers  
Herman L.M. van Roermund  
Eldert L. Advokaat  
Bart W.H. Hendriks  
Fernando Corfu

## 2.1 Introduction

Low pressure-high temperature (LP-HT) metamorphic rocks exposed in orogenic belts offer a good opportunity to investigate crustal processes associated with regional convergence. Such domains of LP-HT metamorphism, commonly characterized by the occurrence of high-grade metamorphic rocks associated with magmatic intrusions, evolve in tectonic settings involving an anomalously high geothermal gradient. In order to identify possible processes explaining the resulting high temperatures at shallow-crustal levels and subsequent exhumation of these rocks, integrated studies on natural examples that preserved such elevated thermal conditions are required. The Central Anatolian Crystalline Complex (CACC), located within the Turkish segment of the Alpine orogenic belt, provides a natural laboratory where a wide crystalline domain was affected by short-lived regional high temperature metamorphism during the Late Cretaceous (Figure 2.1a) (Ketin 1966, Göncüoğlu 1977). This HT event, which lasted for ~20 Ma (from ~95 to 75 Ma) caused upper amphibolite/granulite to greenschist facies regional metamorphism of a sequence of Paleozoic-Mesozoic platform sediments (Erkan 1976, Seymen 1981). Following peak metamorphism, ubiquitous granitic, monzonitic and syenitic plutons intruded at upper crustal levels (Akiman et al. 1993), whilst remains of coeval sub-aerial volcanism are locally preserved. The Gülşehir area (Figure 2.2) exposes two exhumed metamorphic/intrusive blocks, separated by a well-preserved sedimentary basin that contains upper Cretaceous volcanics (Köksal and Göncüoğlu 1997). The region thus presents an excellent opportunity to investigate the evolution of an exhuming crustal HT complex at depth, and its relationship with the coeval sub-aerial processes occurring at and near the Earth's surface.

We present a detailed geological study of the HT Hırkadağ Block, located in the centre of CACC. We integrate petrographical data from its high grade metasediments with whole-rock and mineral chemical analyses, mineral equilibria calculations and thermodynamic modeling, in order to estimate their P-T conditions and trajectories. In addition, we present a detailed structural map of the entire Hırkadağ Block, focusing on the tectonic evolution from pervasive ductile shearing at peak metamorphic conditions to localized brittle tectonics near the contact with the adjacent sedimentary basin.

New titanite U/Pb geochronology on a granodioritic intrusion in the Hırkadağ Block and biotite and K-feldspar  $^{40}\text{Ar}/^{39}\text{Ar}$  thermochronology on the metapelitic rocks provide time-constraints

on the cooling history of the Hırkadağ HT complex through its crustal journey toward the Earth surface. Finally, the central location of the Gülşehir area at equal distances from the three major Central Anatolian metamorphic massifs calls for discussion of the structural coherency of the Central Anatolian Crystalline Complex as a whole.

## 2.2 Geological Setting

Turkey consists of a segment of the EW trending Alpine-Himalayan orogenic belt (Figure 2.1) and is composed of a complex amalgamation of continental and oceanic fragments (Şengör and Yılmaz 1981). In the north, Paleozoic metamorphic rocks covered by Mesozoic sequences form the Pontides of Eurasian affinity. The Pontides are bounded in the south by the Izmir-Ankara-Erzincan suture zone (IAESZ), demarcating the position of the northern branch of the Neotethys (Okay and Tüysüz 1999). South of the suture, the Anatolide and Tauride belts of Gondwana affinity represent south-derived micro-continental fragments that collided with Eurasia in late Cretaceous to Eocene times (Görür et al. 1984, Kaymakci et al. 2009, Meijers et al. 2010). The two largest metamorphic massifs of the Anatolides comprise the Menderes Massif in the west and the Central Anatolian Crystalline Complex (CACC) in the central part of Turkey (Figure 2.1).

### 2.2.1 Central Anatolian Crystalline Complex (CACC)

Immediately south of the central segment of the Izmir-Ankara-Erzincan suture zone, the CACC (Göncüoğlu et al. 1991) which is also known as Kırşehir Block (Görür et al. 1984) is located and it is defined as a large continental domain dominated by crystalline rocks, including metasediments (central Anatolian Metamorphics, CAM), ophiolitic remnants (central Anatolian Ophiolites, CAO) and magmatic intrusions. In the west and the east, it is separated from the Anatolide and Tauride belts by two major intra-continental transcurrent faults: the Tuzgölü Fault and the Central Anatolian Fault Zone, respectively. The CAM are the oldest rocks in the region, consisting of metamorphosed Paleozoic-Mesozoic sequences comprising clastic rocks and platform carbonates (Göncüoğlu 1977, Göncüoğlu et al. 1991). The CAM are geographically distributed over three sub-massifs: 1) the Akdağ Massif in the north-east (Vache 1963), 2) the Niğde Massif in the south (Göncüoğlu 1977) and the 3) Kırşehir Massif in the north-west (Seymen 1981) (Figure 2.1b). In the Kırşehir Massif, a regional metamorphic field

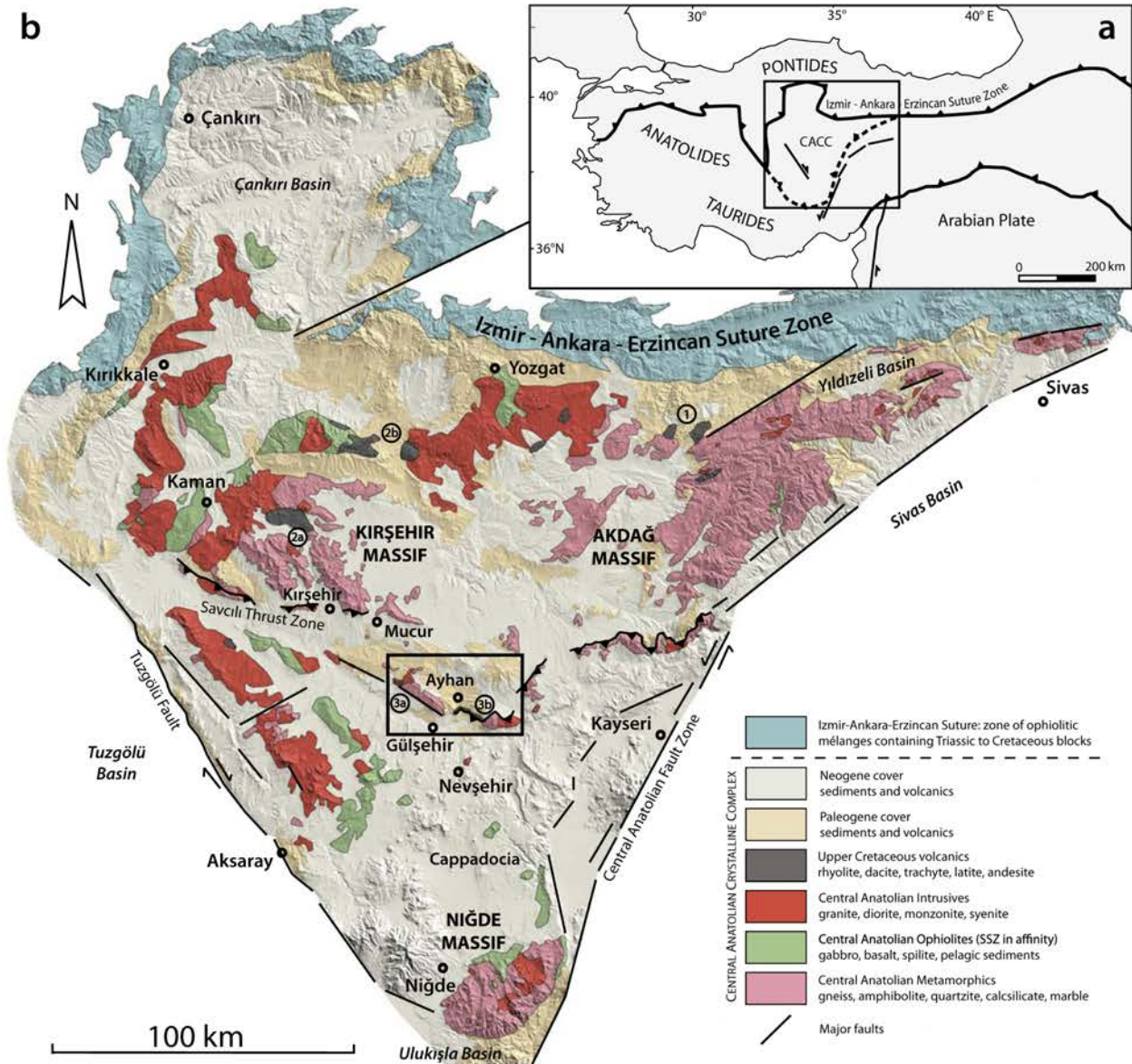


Figure 2.1 a) Simplified tectonic outline of Turkey, b) Simplified geological map of the Central Anatolian Crystalline Complex (CACC) draped onto a shaded relief image prepared from digital elevation model. Numbers show the locations of previously described exposures of upper Cretaceous volcanics (see text for corresponding references). Rectangle indicates the Gülşehir area presented in Figure 2.2.

gradient has been identified ranging from upper amphibolite/granulite facies to greenschist facies over a horizontal distance of ~50 km (Erkan 1976, Seymen 1981). Thermobarometric estimates of peak metamorphic conditions of high-grade schists range from 700 to 800°C at 6-8 kbar, with locally a re-heating overprint at lower pressures (2-4 kbar) (Kocak and Leake 1994, Whitney and Dilek 1998, Whitney et al. 2001). The timing of regional metamorphism is constrained by ~91-84 Ma U/Pb ages of monazite and zircon (Whitney et al. 2003, Whitney and Hamilton 2004). Few remnants of oceanic crust, tectonically emplaced on top of the CAM, witness late Cretaceous obduction. These klippen of oceanic material, defined as the Central Anatolian Ophiolites (CAO), show the typical geochemical features of Supra-Subduction-

Zone Ophiolites (SSZO) (Göncüoğlu and Türel 1993, Yaliniz and Göncüoğlu 1998, Yaliniz 2008). Soon after obduction widespread magmatism, mostly seen in the western part of the CACC, formed elongated felsic, mafic and intermediate plutons intruding through both the CAM and CAO (Figure 2.1b) (Erler and Göncüoğlu 1996). This magmatic event, which lasted for ~20 Ma (from ~95 until 75 Ma), comprises a large range of compositions varying from granitic, granodioritic, gabbroic, monzonitic to syenitic, with calcalkaline to alkaline affinity (Akıman et al. 1993, Boztuğ et al. 2007). There is no consensus about the tectonic setting in which the Central Anatolian magmatism evolved, as geochemical discrimination diagrams suggest volcanic arc, within-plate, and syn- to post-collisional origins for the formation of the

granitoids (Göncüoğlu and Türeli 1994, Kadioğlu et al. 2003, Ilbeyli et al. 2004).

In two localities evidence has been provided that exhumation of the HT rocks was associated with extensional detachments between a high-grade metasedimentary footwall and a non-metamorphic ophiolite hanging wall, i.e., in the Niğde Massif (Gautier et al. 2002) and near Kaman in the Kırşehir Massif (Lefebvre et al. 2011). In addition, discrete ductile shear zones affecting granitoids near Yozgat and Ağaören indicate that at least some of the intrusives have been syntectonically emplaced during an extension phase (Isik et al. 2008, Isik 2009). The timing of unroofing of the high grade metamorphic and intrusive rocks is constrained by apatite fission track ages from the intrusive suites indicating an early to middle Paleocene (57–62 Ma) cooling to temperatures below  $\sim 100^{\circ}\text{C}$  (Boztuğ and Jonckheere 2007).

The sub-aerial counterpart of the late Cretaceous intrusions is represented by few remnants of Upper Cretaceous felsic to intermediate volcanics, which have been preserved in three main areas: (1) The Saraykent volcanics are calc-alkaline andesites to rhyolitic flows, followed by subalkaline rhyolitic ignimbrites and tuffs located at the western margin of the Akdağ Massif (labeled as 1 in Figure 2.1b) (Kuşcu and Floyd 1995, Gençalioğlu-Kuşcu and Floyd 2002). These volcanics and neighboring granitoids are considered as cogenetic (Dökmeçi

1980). (2) The Karahıdır and Kötüdağ volcanics crop out in the center and north of the Kırşehir Massif, respectively (labeled as 2a and 2b in Figure 2.1b), and comprise rhyolites, rhyodacites, dacites and some latites (Seymen 1982). According to Tolluoğlu (1993), the Buzlukdağ Syenitoid and adjacent Karahıdır volcanics formed from different magmatic sources. (3) In the Gülşehir area near Gümüşkent, the Kızıltepe volcanics (labeled as 3a in Figure 2.1b) consist of rhyolites, trachytes, trachy-andesites, andesites and latites, which are interpreted as cogenetic with surrounding plutons (Aydın 1985). To the east, the “Karahıdır” volcanics, named after similar types of volcanics exposed in the center of Kırşehir Massif, are mainly trachyte, andesite and latite, and show geochemical similarities with the Işı Dağı Syenitoid (labeled 3b in Figure 2.1b) (Köksal and Göncüoğlu 1997, Köksal et al. 2001). Late Cretaceous to early Tertiary volcanics have also been documented in the sedimentary records from the basins surrounding the CACC such as the andesite-dominated suite of calc-alkali lavas from the Şarkışla area of the Sivas basin (Gökten and Floyd 1987), and basaltic to andesitic submarine pillow lavas, lava flows and volcanoclastic rocks from the southern Ulukışla Basin (Clark and Robertson 2002). Following magmatic lava extrusion, the major basins of Central Anatolia evolved during the Cenozoic, accumulating several

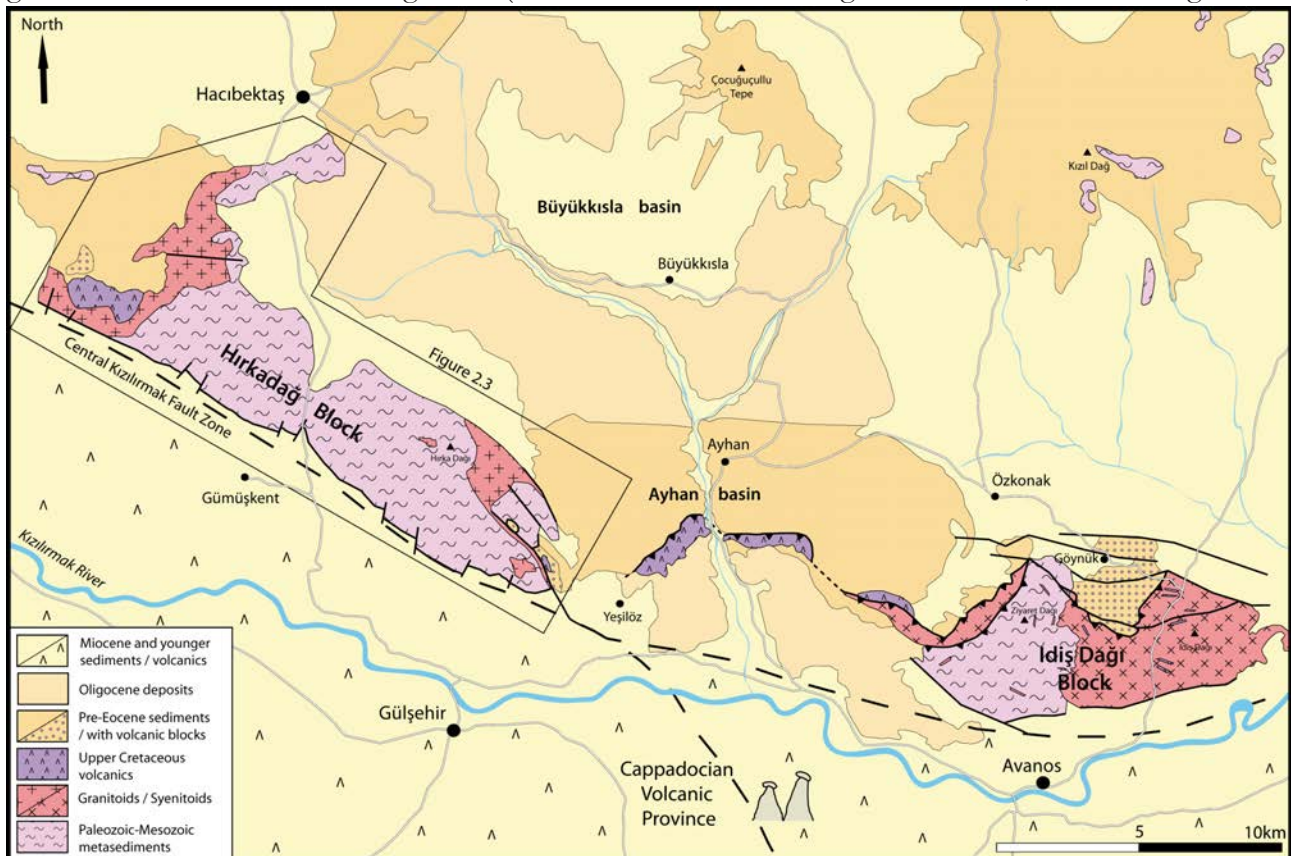


Figure 2.2 Simplified geological and tectonic map of the Gülşehir area.

kilometers of clastic material in the Tuzgölü and Sivas basins (Çemen et al. 1999, Dirik et al. 1999).

### 2.2.2 *The Gülşehir area*

The Gülşehir area (Figure 2.2) is located in the center of the CACC, at the northern boundary of the Central Anatolian Volcanic Province of Cappadocia. It contains two crystalline blocks, the Hırkadağ Block in the west and İdiş Dağı Block in the east, separated by the Ayhan basin.

The two crystalline blocks are isolated from the major central Anatolian metamorphic massifs by Palaeocene to Oligocene basins and some important faults (Figure 2.2). The metamorphic rocks of the Hırkadağ Block comprise similar lithologies to those described from the north-westerly Kırşehir and southerly Niğde massifs (Seymen 1981, Aydın 1985, Atabay et al. 1987, Lulu 1993). In the east, the İdiş Dağı metamorphic rocks are intruded by alkali-feldspar and quartz-syenites, which were geochemically classified as post-collisional A-type igneous rocks and are believed to have intruded later than the granitoids (Figure 2.2) (Göncüoğlu et al. 1993, Köksal and Göncüoğlu 1997). The Ayhan basin has a ~5 km thick stratigraphy of mainly continental clastics. Its basal unit contains conglomerate with intercalated andesitic volcanics of  $72.1 \pm 1.7$  Ma, overlain by Eocene (Lutetian) limestones and lacustrine marls and turbidites (Figure 2.2) (Advokaat et al. submitted). Syn-sedimentary normal faults and tapering features against a large basin bounding normal fault in the south suggest that it was an extensional basin from the onset of sedimentation. The Ayhan basin is currently separated from the Hırkadağ Block by recently active high-angle normal faults, but synsedimentary deformation and intra-basinal unconformities, as well as the absence of any metamorphic or granitic debris in the lower part of the stratigraphy indicate that these faults were mainly active during infilling of the Ayhan basin. Both the western part of the Ayhan basin and the northeast margin of the Hırkadağ Block are unconformably covered by post-Lutetian red beds of the Büyüksıla basin (Advokaat et al. submitted), whereas the northern border of the İdiş Dağı Block is thrust over the Ayhan basin fill (Köksal and Göncüoğlu 1997). Regionally, the Ayhan basin was most probably involved in part of the Savcılı thrust zone, which runs approximately E-W along the southern margin of the Kırşehir massif (Seymen 2000).

### 2.2.3 *The Hırkadağ Block*

The Hırkadağ Block is a NW-SE trending, 4 km

wide belt, which is topographically higher than the surrounding areas (Figure 2.3). Historically, the Hırkadağ Block has been separately studied in domains exposed west and east of the Kırşehir-Nevşehir road (Aydın 1985, Lulu 1993). In this study, we compiled and investigated both the western and eastern parts of the Hırkadağ Block, and traced the boundaries of the metamorphic units initially recognized in the east (Lulu 1993) towards the west (Figure 2.3). Three lithological units were identified in the metamorphic rocks of the Hırkadağ Block. From bottom to top and from south to north, they include (1) a lower unit characterized by the presence of quartzites and pelitic garnet-sillimanite schists, (2) an intermediate unit dominated by calc silicate rocks, and (3) an upper unit of mainly massive marbles. The lower unit (equivalent to the Gümüşler Formation (Lulu 1993)) consists of alternating locally muscovite-bearing quartzite beds and garnet/sillimanite-bearing schists, as well as calc-silicates and banded marbles. Individual quartzite beds may form up to ten meter-thick layers, and the quartzite-schist sequence is up to several hundreds of meters thick. The intermediate unit in the central part of the Hırkadağ Block, equivalent to the Kaleboynu Formation (Lulu 1993) is mostly composed of calc-silicate rocks with variable silicium and calcium content, interbedded with meter-scale marble and quartzite layers. Where quartzites are present, these are associated with metapelitic schists. Minor occurrences of granitic and pegmatitic dikes with cm-scale feldspar crystals are present. The upper unit, equivalent to the Aşığıdiği Formation of Lulu (1993), is characterized by massive marbles and minor calc-silicate rocks. The marbles are coarse- to fine-grained, and do not present any compositional banding, in contrast to those found in the lowermost unit.

The westernmost and easternmost parts of the Hırkadağ Block are intruded by a network of felsic dykes and veins, which are likely connected to larger granodioritic bodies. The Akçataş Granitoids intrude in the western part of the Hırkadağ Block, and are mainly composed of granite, granodiorite, quartz diorite, monzonite and syenite, which crystallized at shallow depth (Aydın 1985). In the east, the granodiorites have been referred to as the “Uçkapılı Granodiorite” to emphasize similarities with plutonic rocks exposed at Uçkapılı village in the Niğde region (Lulu 1993). The Hırkadağ intrusives are mainly composed of coarse K-feldspar, plagioclase and quartz, do not contain any trace of ductile fabrics and show clear cross-cutting relationships with the foliated country-rocks.

Previous estimates of peak metamorphic



its SW margin. The occurrence of horizontally overlying Quaternary travertine along this fault zone and connected fault branches suggests recent tectonic activity (Toprak 1994). Along the NE margin, the Büyükkışla Formation, composed of red conglomerates, reworked Eocene limestones and clasts derived from older rocks in the region, unconformably overlies the Hırkadağ Block (Advokaat et al. submitted). A normal fault contact relationship is reported in the south (Lulu 1993). Due to poor exposure of the westernmost granitoids of the Hırkadağ Block, the nature of the contact with pre-Eocene volcanics and conglomerates still remains unknown.

The eastern part of the Hırkadağ Block is separated from the Göynük/Elmadere Formation and the Saytepe Formation by a tectonic contact.

This contact, exposed in the Gürleğen valley, has previously been considered as a flat-lying thrust bringing the crystalline rocks eastward on top of the Göynük/Elmadere Formation (Lulu 1993). Although the nature of the contact is difficult to determine (Whitney and Dilek 2001), the presence of crystalline rocks in a lower structural position with respect to the Göynük/Elmadere Formation and the occurrence of flat-lying travertine deposits along the valley are in good agreement with a geometry of a high-angle normal fault (Figure 2.4). This contact may have shared activity with branches of the Kızılırmak Fault to the SE, but structural and stratigraphic analysis of the Ayhan basin has shown that most of the displacement along this fault took place prior to the Lutetian (Middle Eocene) (Advokaat et al. submitted).

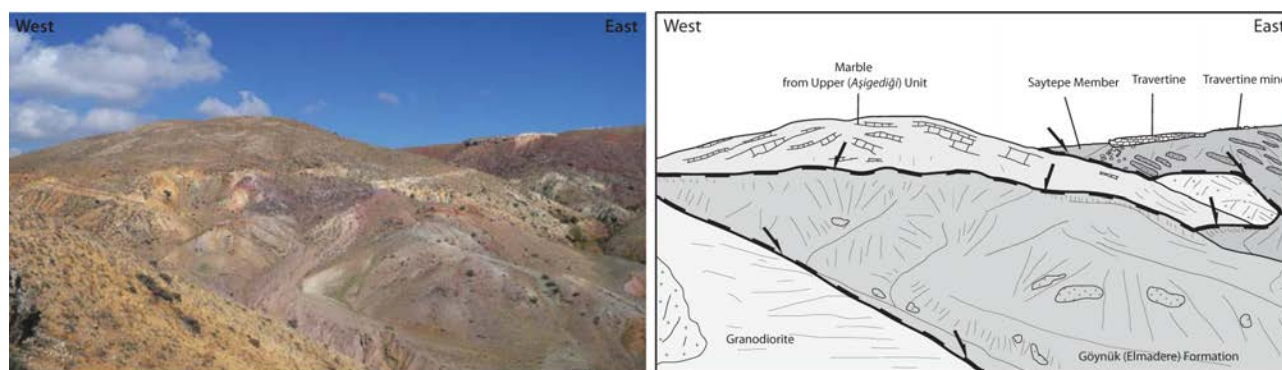


Figure 2.4 Field aspect and interpretation of the tectonic contact, in the Gürleğen valley, between the Hırkadağ Block with the Ayhan basin. Black arrows denote the trace and direction of motion of the fault.

### 2.3 Metamorphism of the Hırkadağ Block

We sampled metapelitic, quartzitic and calcsilicate rocks equally distributed across the Hırkadağ Block to obtain insight in the metamorphic gradient across the area, mainly along SW-NE transects. We focused on rocks with pelitic compositions and applied bulk-rock and mineral chemistry analysis as well as conventional thermobarometry and thermodynamic modeling of phase assemblages, to obtain quantitative estimates of the pressure and temperature conditions during HT metamorphism. The mineral abbreviations used below follow the updated nomenclature proposed by Whitney and Evans (2010).

#### 2.3.1 Petrology and mineral assemblages

Thin sections of metamorphic rock samples were studied under the optical microscope to assess stable mineral assemblages and metamorphic grade. We selected ten fresh specimens for bulk rock and mineral chemistry analyses. These comprise five metapelites, one quartzite and four metacarbonates, widely distributed throughout

the study area (Figure 2.3). An overview of the mineral assemblages in the selected samples is given in Table 2.1.

##### 2.3.1.1 Metapelite samples

Three of the studied metapelitic samples (H12G, H20C and H2058C) belong to the lower unit, and two come from the intermediate unit (H19H and H2158B; Figure 2.3).

Sample H12G contains a clear foliation defined by biotite-rich bands including spinel and in smaller amounts of fibrolite, that separate light colored zones with coarse-grained quartz and feldspar. The dark biotite-rich layers bend around large anhedral pinkish garnet porphyroblasts. Two generations of garnet have been recognized in thin section: an older, smaller (up to 8 mm) idioblastic garnet and a younger generation of larger xenoblastic garnet crystals. The younger garnet seems to replace biotite and contains inclusions of sillimanite. Spinel replaces sillimanite needles, and also seems to overgrow some biotite flakes with a preferred shape orientation. The sample shows a main mineral assemblage of Sil + Bt + Grt1 + Pl ± Kfs

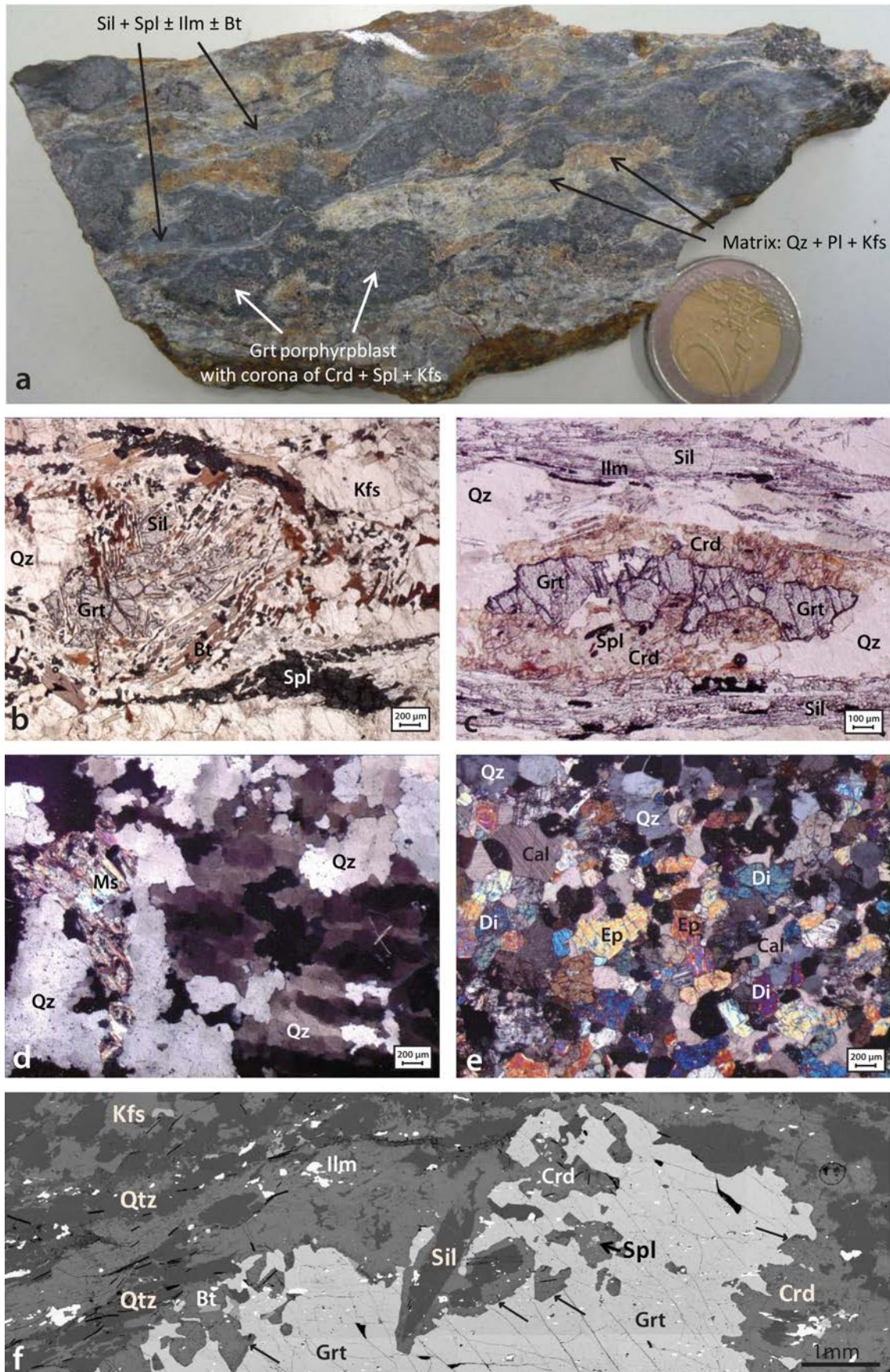


Figure 2.5 a) Photograph of foliated sillimanite-bearing schist with large garnet porphyroblasts, sample H20C, (b) micrograph showing typical mineral assemblage from metapelite sample H19H, (c) micrograph of typical mineral assemblage in metapelite sample H2158B, (d) micrograph showing “checkerboard texture” in quartzitic sample H20B, (e) micrograph showing mineral assemblage in metacalcareous sample H11B, (f) Back-Scattered Electron image of part of a cm-scale garnet in sample H20-C, showing reaction rim of cordierite surrounding the garnet with well developed crystal faces (indicated with arrows).

± Qz, replaced by a later assemblage containing Grt2 + Spl as reaction products of sillimanite.

Sample H19H shows a similar microstructure as H12G, but the dark-colored layers defining the foliation are dominated by spinel and sillimanite, with spinel overgrowing both sillimanite and biotite. This sample contains an early mineral assemblage of Sil + Bt + Grt + Kfs ± Ms ± Qz ± Ilm, and a younger mineral assemblage of Sil + Bt + Pl + Spl, developing at the expense of garnet porphyroblasts (Figure 2.5b).

Sample H20C has a foliation mainly defined by aggregates of fibrous sillimanite and ilmenite. The matrix is dominated by quartz, with undulose extinction, and cordierite with relatively large poikiloblastic garnet crystals (up to 1 cm). Garnet is surrounded by cordierite that shows symplectitic intergrowth with quartz at the contact with the garnet rim (Figure 2.5f). The presence of cordierite near garnet is often associated with well-developed crystal faces of the garnet. Sillimanite shows two preferred orientations, which may be inherited from an earlier crenulation cleavage. Sample H20C presents a mineral assemblage of Sil + Grt + Qz ± Pl ± Bt ± Ilm, partially replaced by a secondary assemblage of Crd + Spl + Kfs + Qz.

Sample H2058C is very similar to H20C in mineral composition. The foliation is defined by bands of fibrolite, and cordierite is present especially around garnet porphyroblasts where highly resorbed garnet rims result from the replacement by cordierite and minor spinel. The stable mineral assemblage identified comprises Sil + Grt + Qz ± Bt ± Ilm, partially overprinted by Crd + Spl + Kfs + Qz.

Sample H2158B was collected along the NE margin of the Hırkadağ Block. The microstructure of the rock is dominated by large poikiloblastic garnet surrounded by aligned fibrolite and a matrix of quartz and potassic feldspar. Initial garnet and sillimanite are partially replaced by cordierite and spinel, respectively (Figure 2.5c). The corresponding mineral assemblages are: Sil +

Grt + Qz ± Kfs ± Bt ± Ilm, followed by Crd + Spl + Qz.

### 2.3.1.2. Quartzite

Optical analysis of a sample (H20B) collected from a meter scale quartzitic band from the lower unit reveals a content of ~90-95% of quartz coexisting with minor interstitial phyllosilicates, such as muscovite and chlorite. The large quartz grains are strongly affected by the pervasive development of “checkerboard type” subgrains (Figure 2.5d).

### 2.3.1.3 Metacarbonate

Four calcisilicate rocks were selected for detailed analysis, one from the lower unit (H20D), two from the intermediate unit (H17E and H20E) and one from the upper unit (H11B) (Figure 2.3).

Samples H11B and H17E from the NE margin of the Hırkadağ Block show similar mineral assemblages. They are mainly composed of equigranular calcite, diopside and plagioclase. Both epidote and chlorite occur as local minor overgrowths on clinopyroxene (Figure 2.5e). The following mineral assemblage has been identified: Cal + Di + Pl + Qz + Ttn + Rt ± Scp ± Ep ± Chl.

Sample H20D derives from the SW margin of the Hırkadağ Block. The rock forming minerals comprise plagioclase and potassic feldspar. Based on their microstructure and contact relationships, two generations of plagioclase were recognized. A first-generation plagioclase occurs as inclusions in a second plagioclase. In the matrix, the second type of plagioclase seems in equilibrium with wollastonite and diopside. The mineral assemblage is Pl + Kfs + Di + Wo + Cal + Ttn ± Qz.

Sample H20E contains a clear compositional banding of layers containing quartz, biotite, plagioclase and potassic feldspar alternating with layers of calcite, diopside, plagioclase, epidote and titanite. The mineral assemblages in the two types of layers are Bt + Pl + Kfs + Qz and Cal + Di + Pl + Ep + Ttn, respectively.

	Sample	Main minerals										Accessory phases									
		Grt	Spl	Bt	Sil	Pl	Kfs	Qz	Crd	Cal	Di	Chl	Ms	Scp	Ilm	Wo	Zrn	Ep	Crn	Rt	Ttn
MP	H12-G	x	x	x	m	x	x	x							x		x				
	H19-H	x	x	x	x	x	x	x						m			x			x	
	H20-C	x	m	m	x	x	x	x	x					m			x				
	K2058C	x	m	m	x		x	x	x								x				
	K2158B	x	x	x	x		x	x	x								x			x	
Q	H20B							x						x	x						x
MC	H11B					x		x		x	x	m		m				m			x
	H17E					x		x		x	x	m		m				m			x
	H20D					x	x	m		x	x					x					x
	H20E			x		x	x	x		x	x							x			x

Table 2.1 Mineral compositions of samples analysed in this study. Crosses denote the presence of a given mineral in the sample. Minor (accessory) phases are indicated with ‘m’.

### 2.3.2 Textures and mineral chemistry of metapelites

One metapelitic schist (sample H20C, Figure 2.5a) was selected for detailed chemical analysis, as it preserves mineral assemblages representative of the peak metamorphic conditions in the Hirkadağ Block. The mineral assemblage generally observed in the pelitic schists of the study area is: (1) Sil + Grt + Qz ± Pl ± Bt ± Ilm, overprinted by (2) Crd + Spl + Kfs + Qz.

Garnet, spinel, sillimanite, biotite, feldspar and cordierite were used for thermobarometric calculations described in paragraph 3.3. The chemical analyses were carried out using the JEOL JXA-8600 Superprobe at the Faculty of Geosciences at the University of Utrecht. The acceleration voltage during the analyses was 15 kV, at a beam current of 20 nA with a spot size of ~1-3 μm.

Garnet – Garnet in the metapelitic rocks from the Hirkadağ massif is mostly mm-scale but up to 1 cm large idioblastic to xenoblastic grains occur that show a poikiloblastic to skeletal structure. Smaller garnet contains less inclusions and is often fractured. Most garnet crystals are surrounded by a reaction rim of cordierite and quartz, in which the grain boundary between garnet and cordierite is a perfect garnet crystal face (Figure 2.5f). The larger garnet grains are fragmented with a skeletal structure and a reaction rim consisting of biotite, plagioclase, spinel and small amounts of sillimanite. Garnet compositions are fairly similar for all analyzed grains and range within Alm75-84Grs3-9Pyr11-14Spess1-2 (Table 2.2).

The large garnet grains are zoned with an Fe/(Fe+Mg) ratio increasing towards the garnet rim, which implies decreasing temperature during garnet growth. The presence of cordierite and the newly grown crystal faces at the contact between cordierite and garnet suggest that the core composition of this garnet reflects near-peak temperatures and the rim reflects retrograde conditions.

Spinel – Spinel from the Hirkadağ massif is dark green in color. In sample H20C, spinel only occurs as a minor phase as inclusions within garnet. In this case, the spinel is surrounded by cordierite, and is not in direct contact with garnet. The foliation in this sample is mainly defined by aggregates of fibrous sillimanite and ilmenite, whilst biotite is only found in the surroundings of garnet. Spinel is rich in iron and has a composition close to the hercynite endmember (FeAl<sub>2</sub>O<sub>4</sub>), with small amounts of Mg (2.4 wt% MgO) and Zn (3.4 wt% ZnO; Table 2.2).

Sillimanite – All of the metapelites studied contain abundant fibrous sillimanite (fibrolite;

Figure 2.5), with minor amounts of prismatic sillimanite. The foliation is mainly defined by aggregates of fibrolite and ilmenite, with minor biotite and spinel replacing sillimanite needles.

Biotite – Flakes of biotite occur mainly in bands defining a foliation of the metapelitic rocks reminiscent of a gneissic banding. Biotite also occurs as inclusions in garnet porphyroblasts. Biotite is pleochroic and has a brown color, which is often darker in the center of the grains. Biotite is one of the minerals replacing garnet. The Fe and Mg content of biotite in the Hirkadağ samples varies from 0.49 < Fe/(Fe+Mg) < 0.62.

Feldspar – In the metapelite samples, feldspar is most abundant in the light-colored bands, and often coexists with quartz. Potassium-feldspar is only present in small amounts in bands that consist of cordierite with minor quartz and plagioclase. At reaction rims around garnets, as well as in garnet pseudomorphs, plagioclase is found as a reaction product together with spinel, quartz, biotite and lesser amounts of K-feldspar and sillimanite. Both plagioclase and K-feldspar occur as inclusions in garnet, in some cases surrounding other inclusions like sillimanite and spinel. Some highly altered grains show relics of cross-hatched twinning, indicating the existence of a former microcline that has been altered to a micropertthite. Feldspar compositions are Ab56An43Or1 for plagioclase and Ab16An1Or83 for K-feldspar (Table 2.2).

Cordierite – A relatively large part of the metapelite matrix is made up by cordierite. Cordierite also occurs as a reaction product surrounding garnet, showing well developed crystal faces at the boundary with garnet (Figure 2.5f) as outlined above. Representative compositions of cordierite in the matrix and inclusions in garnet are given in Table 2.2. The XMg (Mg/(Mg+Fe<sup>2+</sup>)) ratio in cordierite ranges from 0.44 to 0.53.

### 2.3.3 Pressure-Temperature conditions

Based on mineral chemistry data from pairs of minerals, equilibrium temperature estimates were calculated using the garnet-biotite (GB) exchange thermometer (Bhattacharya et al. 1992) and the thermometer based on Ti saturation in biotite (Henry et al. 2005). Pressure is calculated with the garnet-aluminosilicate-silica-plagioclase (GASP) and the garnet-plagioclase-muscovite-biotite (GPMB-Fe and GPMB-Mg) net transfer barometers (Ghent and Stout 1981, Mckenna and Hodges 1988). The estimated values for temperature and pressure conditions of equilibration are given in Table 2.2 and marked with black dots in the PT diagram (Figure 2.6).

For the previously described H20C metapelitic

Sample Mineral	H20C Grt core	H20C Grt rim	H20C Bt matrix	H20C Bt matrix	H20C Pl matrix	H20C Kfs matrix	H20C Spl matrix	H20C Sil average	H20C Ms matrix	H20C Crd inclusions	H20C Crd matrix
SiO <sub>2</sub>	37.83	37.26	34.32	35.37	56.59	63.22	0.01	36.33	45.07	47.55	46.91
Al <sub>2</sub> O <sub>3</sub>	20.92	20.80	17.89	17.20	26.97	18.73	57.21	62.69	34.74	32.54	32.10
FeO	34.21	38.02	22.24	18.07	0.15	0.00	36.61	0.32	1.44	10.82	12.60
MnO	0.65	0.75	0.02	0.03	0.01	0.00	0.01	0.00	0.00	0.08	0.09
MgO	3.76	2.89	7.57	10.70	0.01	0.00	2.42	0.01	0.64	6.92	5.58
CaO	3.12	1.06	0.00	0.00	8.85	0.12	n.a.	0.00	0.02	0.00	0.02
K <sub>2</sub> O	n.a.	n.a.	9.20	9.54	0.08	14.03	n.a.	0.01	9.90	0.00	0.13
Na <sub>2</sub> O	0.01	0.02	0.15	0.16	6.38	1.84	n.a.	0.00	0.66	0.07	0.10
TiO <sub>2</sub>	0.25	0.09	3.36	3.31	0.00	0.02	0.04	0.01	0.09	0.00	0.00
Cr <sub>2</sub> O <sub>3</sub>	0.01	0.01	0.06	0.05	0.01	0.00	0.17	0.04	0.00	0.00	0.01
V <sub>2</sub> O <sub>3</sub>	n.a.	n.a.	n.a.	n.a.	n.a.	n.a.	0.37	n.a.	n.a.	n.a.	n.a.
NiO	n.a.	n.a.	n.a.	n.a.	n.a.	n.a.	0.10	n.a.	n.a.	n.a.	n.a.
ZnO	n.a.	n.a.	n.a.	n.a.	n.a.	n.a.	3.37	n.a.	n.a.	n.a.	n.a.
Total	100.77	100.89	94.81	94.44	99.05	97.97	100.32	99.42	92.56	97.99	97.56
Si	3.00	2.99	2.67	2.71	2.56	2.96	0.00	0.99	3.08	4.97	4.97
Al	1.96	1.97	1.64	1.55	1.44	1.03	1.93	2.01	2.80	4.01	4.01
Fe-tot	2.27	2.56	1.45	1.16	0.01	0.00	0.88	0.01	0.08	0.95	1.12
Mn	0.04	0.05	0.00	0.00	0.00	0.00	0.00	0.00	0.00	0.01	0.01
Mg	0.45	0.35	0.88	1.22	0.00	0.00	0.10	0.00	0.06	1.08	0.88
Ca	0.27	0.09	0.00	0.00	0.43	0.01		0.00	0.00	0.00	0.00
K			0.91	0.93	0.00	0.84		0.00	0.86	0.00	0.02
Na	0.00	0.00	0.02	0.02	0.56	0.17		0.00	0.09	0.01	0.02
Ti	0.01	0.01	0.20	0.19	0.00	0.00	0.00	0.00	0.00	0.00	0.00
Cr	0.00	0.00	0.00	0.00	0.00	0.00	0.00	0.00	0.00	0.00	0.00
Zn							0.07				
Cations	8.00	8.02	7.78	7.80	5.00	5.00	3.00	3.01	6.99	11.03	11.04
X(Mg)	0.14	0.11	0.38	0.51			0.11			0.53	0.44
X(Fe)	0.75	0.84					0.89			0.47	0.56
X(Ca)	0.09	0.03			XAn: 0.43	XAn: 0.01					
X(Mn)	0.01	0.02			XOr: 0.01	XOr: 0.83					
Fe/(Fe+Mg)	0.84	0.88			XAb: 0.56	XAb: 0.16					
Thermo/Baro	Assemblage	GB (°C)	GASP (kbar)	GPMB-Fe (kbar)	GPMB-Mg (kbar)	Average P (kbar)					
H20C	1	742	7.99	9.45	6.91	9.12					
H20C	2	520				ca. 3-4					

Table 2.2 Representative mineral compositions from sample H20-C (oxides in wt%). The bottom part of the table displays the calculated PT conditions via thermobarometry, for two depicted stable mineral assemblages.

sample, calculated equilibrium conditions for the early mineral assemblage, including data from garnet cores, are 742°C (GB thermometer) and 8.1 kbar in (average pressure of GASP, GPMB-Fe and GPMB-Mg barometers; Table 2.2). Calculations with garnet rim compositions and associated biotite give an equilibrium temperature of 520°C (GB thermometer), while the pressure is estimated around 3-4 kbar based on the occurrence of cordierite as replacement of garnet (Spear and Cheney 1989) (Table 2.2).

### 2.3.4 Bulk rock composition and thermodynamic modeling

The bulk rock composition of the sample H20C has been determined by X-ray fluorescence (Thermo ARL 9400 XRF) on fused glass beads and pressed powder pellets at Utrecht University. The resulting major element composition is used to calculate the stability fields of mineral assemblages in a specified PT space, via the construction of PT-fixed-composition phase diagram sections (or pseudosections) using the Theriak/Domino software package (de Capitani 1994, de Capitani and Petrakakis 2010). We chose to run the

calculations for the CNKFMASH system as we are looking at a rock sample of metapelitic affinity and used a thermodynamic database based on Holland and Powell (1998). For the calculations, a surplus amount of water is added, to permit the occurrence of hydrous minerals like micas and cordierite.

Figure 2.6 presents the modeled Domino pseudosection with the stability fields of all stable mineral assemblages for a PT-space ranging from 500-850°C and 1-11 kbar. On the PT pseudosection, areas representing assemblage stability fields are labeled with their stable assemblages. The location in PT-space of the first assemblage is determined using isopleths of pyrope in garnet, and albite in plagioclase, together with the absence of kyanite, suggesting PT conditions at about 7.5 kbar and 690°C. Microstructural relationships show that the first assemblage is partly replaced by the second assemblage (Grt → Crd + Qz and Sil → Spl) and hence the two assemblages can be linked following a decompressional path at increasing temperature conditions. The replacement of garnet by cordierite occurs at a pressure of about 4 kbar. The growth of spinel (hercynite) indicates heating to at least 800°C. The inferred PT path is shown in Figure

2.6 and compared with the PT-estimates obtained by thermobarometry. The thermobarometric PT-estimate for the first mineral assemblage plots near the PT path inferred from Domino calculations. However, for the second mineral assemblage, the peak temperature of  $>800^{\circ}\text{C}$  based on the occurrence of spinel and cordierite inferred from the Domino pseudosection is not reflected by the geothermobarometric estimates, which are probably affected by post-peak re-equilibration of the Grt-Bt rim pairs. We therefore do not use the low temperature estimate in our further considerations. The high temperature conditions inferred from the output of thermodynamic calculations and thermobarometry suggest that the rock likely underwent some degree of

partial melting. However, direct evidence for the presence of a melt within the high grade metapelites is difficult to assess. As reported in the literature, some quartzofeldspathic layers may represent anatectic leucosomes from migmatitic segregations but later deformation makes their structural interpretation debatable (Whitney and Dilek 2001). On the other hand, the presence of a melt may be evidenced by the K-feldspar + quartz ( $\pm$  plagioclase)-rich zones separated from zones rich in aluminosilicate minerals, and by the well developed crystal faces at the boundary between primary garnet and secondary cordierite which suggests an environment with an interstitial liquid phase (MacKenzie and Adams 2003).

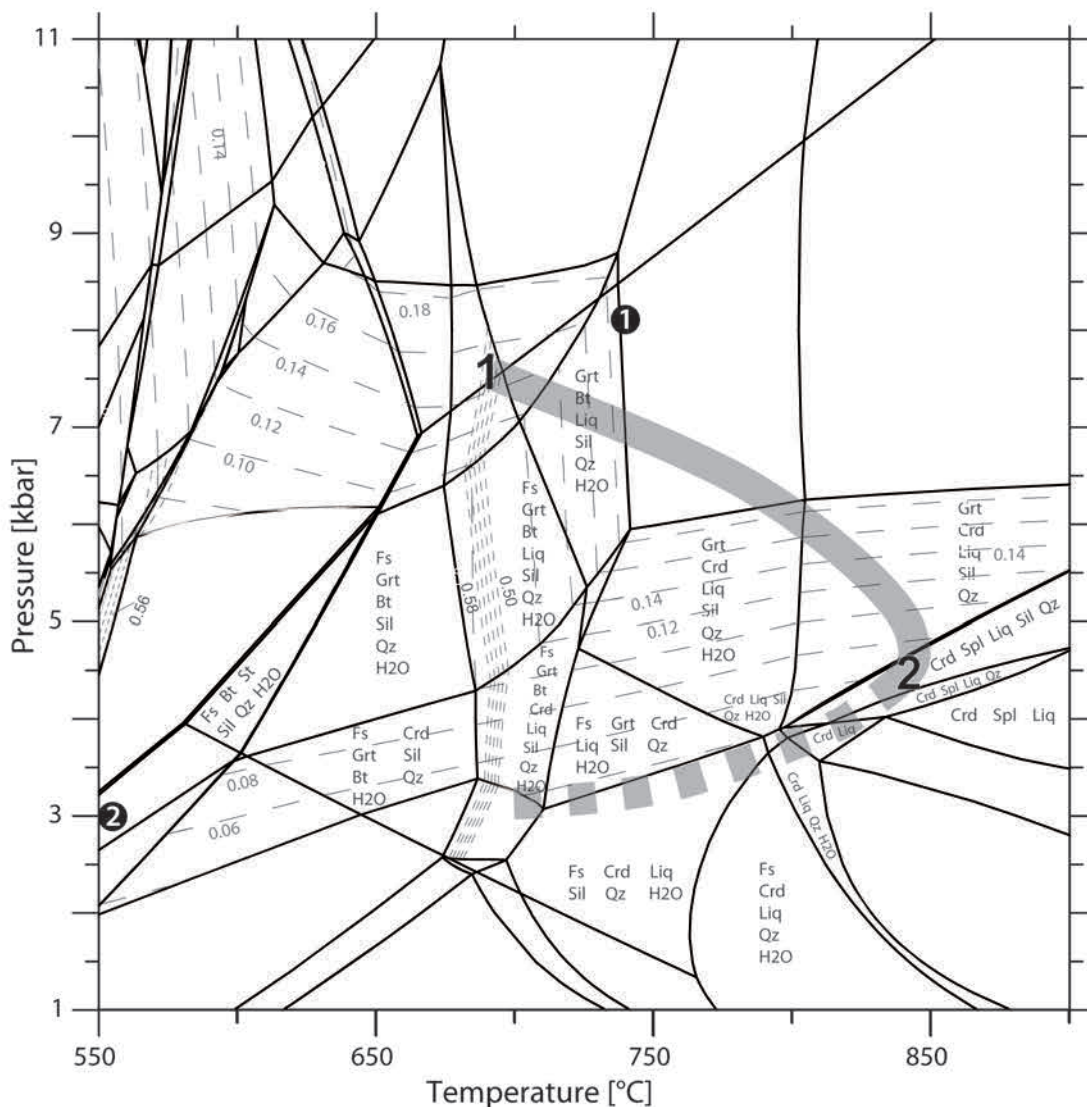


Figure 2.6 CNKFMASH pseudosection calculated with Domino for the bulk rock composition of sample H20C, with water added. The relative proportion of the elements used as input for Domino calculations is: Si(1047)Al(431)Fe(128)Mg(32)Ca(10)K(41)Na(17)H(500)O(?). The main mineral assemblages are listed in the diagram. The PT fields where the described assemblages are assumed to be stable are numbered 1 and 2, referring respectively to the early and late mineral assemblages. Isopleths of pyrope ( $X_{\text{Mg}}=0.15$ ) and albite ( $X_{\text{Ab}}=0.56$ ) are represented with coarse and fine dotted lines, respectively. The thick grey line indicates the inferred PT path connecting the two stable assemblages; its potential continuation after field 2 is indicated as a dashed line. Estimates calculated using conventional thermobarometry are plotted as black circles.

## 2.4 Structural analysis of the Hırkadağ Block

### 2.4.1 Overall structure

The structure of the Hırkadağ Block is illustrated in Figure 2.7 showing a compilation of data collected by Aydın (1985) in the area west of the Kırşehir-Nevşehir road, and Lulu (1993) for the eastern part, complemented with our own measurements across the Hırkadağ Block. The rocks have a pervasive metamorphic foliation (Sm), which is

almost always transposed parallel to the original sedimentary bedding (S0). Pelitic rocks from the lower unit exposed along the SW margin preserve well-developed, intense ductile deformation features. These quartz-rich sillimanite- and garnet-bearing schists have a strongly developed cleavage, which is sometimes truncated by large garnet porphyblasts. Pure quartzite occurs as massive meter-scale bands, which do not present a clear foliation. In contrast, toward the NE and upward in the succession, the more calcareous lithologies do

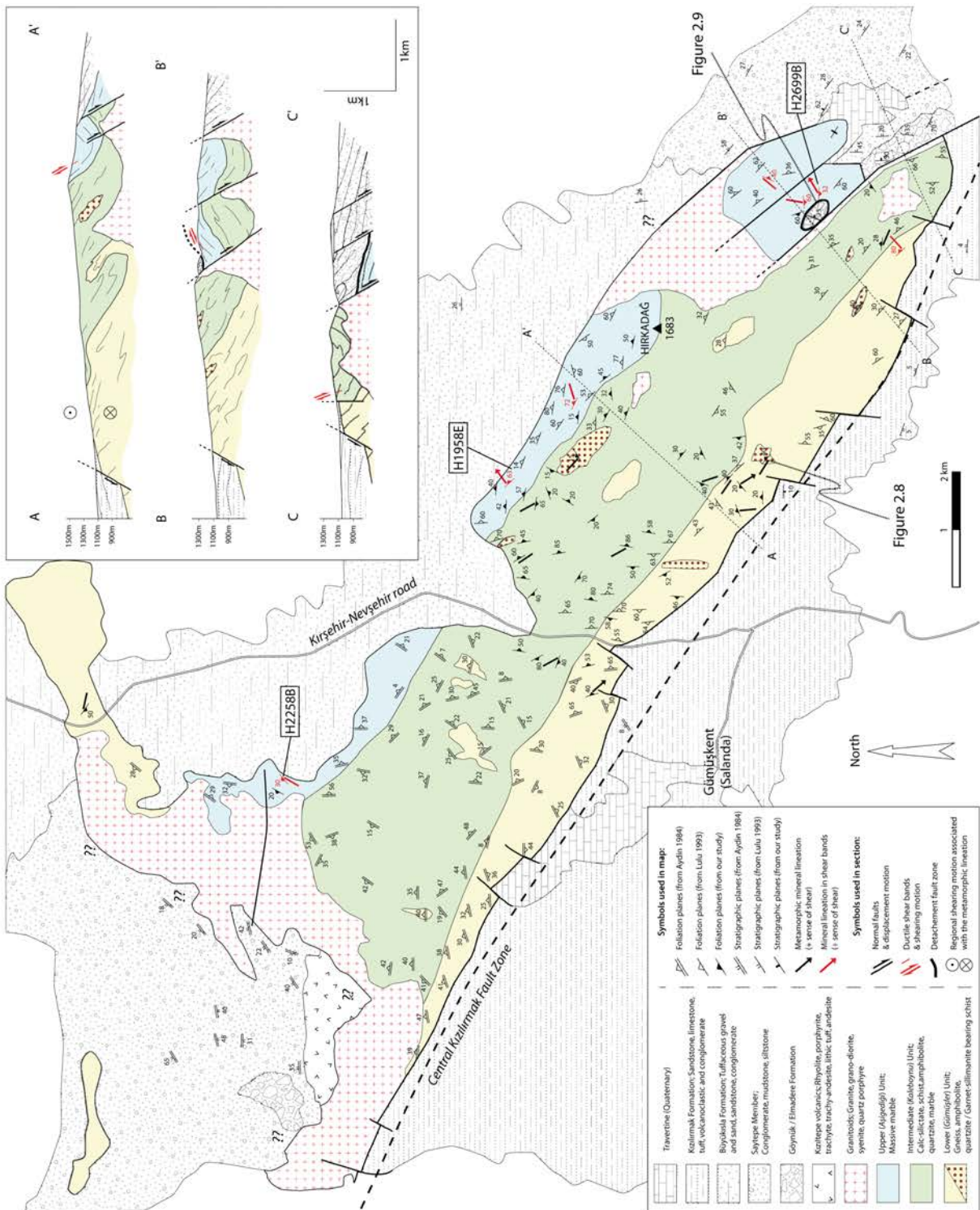


Figure 2.7 Detailed structural map of the Hırkadağ Block showing bedding, foliation planes and mineral lineations in both HT and mylonitic rocks from this study, supplemented with literature data. Three SW-NE cross-sections through the Hırkadağ Block are presented. Locations of marble samples with mylonitic shear bands are shown.

not preserve evidence for this ductile deformation, presumably because pervasive recrystallization affected these calcite-rich compositions. Calc-silicates and banded impure marbles often appear as competent layers from a few to hundreds of meters thick. Massive marbles alternating with meter-scale calc-silicate bands from the upper unit in the northeast show a consistent orientation of dipping layers, striking parallel to the contact with the Büyükkışla basin. The main trend of the pervasive  $S_m$  foliation is oriented NW-SE, with approximately NE-directed dips. In metapelitic compositions, stretched sillimanite and biotite form lineations on the foliation planes, while in the metacarbonates elongated amphibole and some pyroxene define a stretching lineation. The main trend of these lineations is around N120-150, and few identifiable kinematic indicators show a top-to-the-SE sense of shear (black lines in Figure 2.7). Apparently competent calc-silicate beds are

boudinaged, and foliation boudinage may occur at the necks of the boudins (Figure 2.8a). In the SW, foliated calc-silicates deformed into various types of folds, ranging from tight to isoclinal symmetric and asymmetric folds. The general strike of axial planes of the isoclinal folds and the boudinage neck-lines coincides with the orientation of the regional foliation ( $S_m$ ) and suggest that these folds and boudinage result from the same deformation phase (Fm).

In some localities,  $S_m$  and associated Fm are refolded into meter-scale tight folds (Figures 2.8b, 2.8d). This refolding phase has led to the formation of a new axial planar foliation (referred as  $S_{m+1}$ ). This secondary structure is characterized by the presence of relatively open folds, has shallower dips than  $S_m$ , and presents a general WNW-ESE strike alternatively dipping toward the ENE and WSW. The scale of these younger folds varies from cm to hundreds of meters in wavelength.

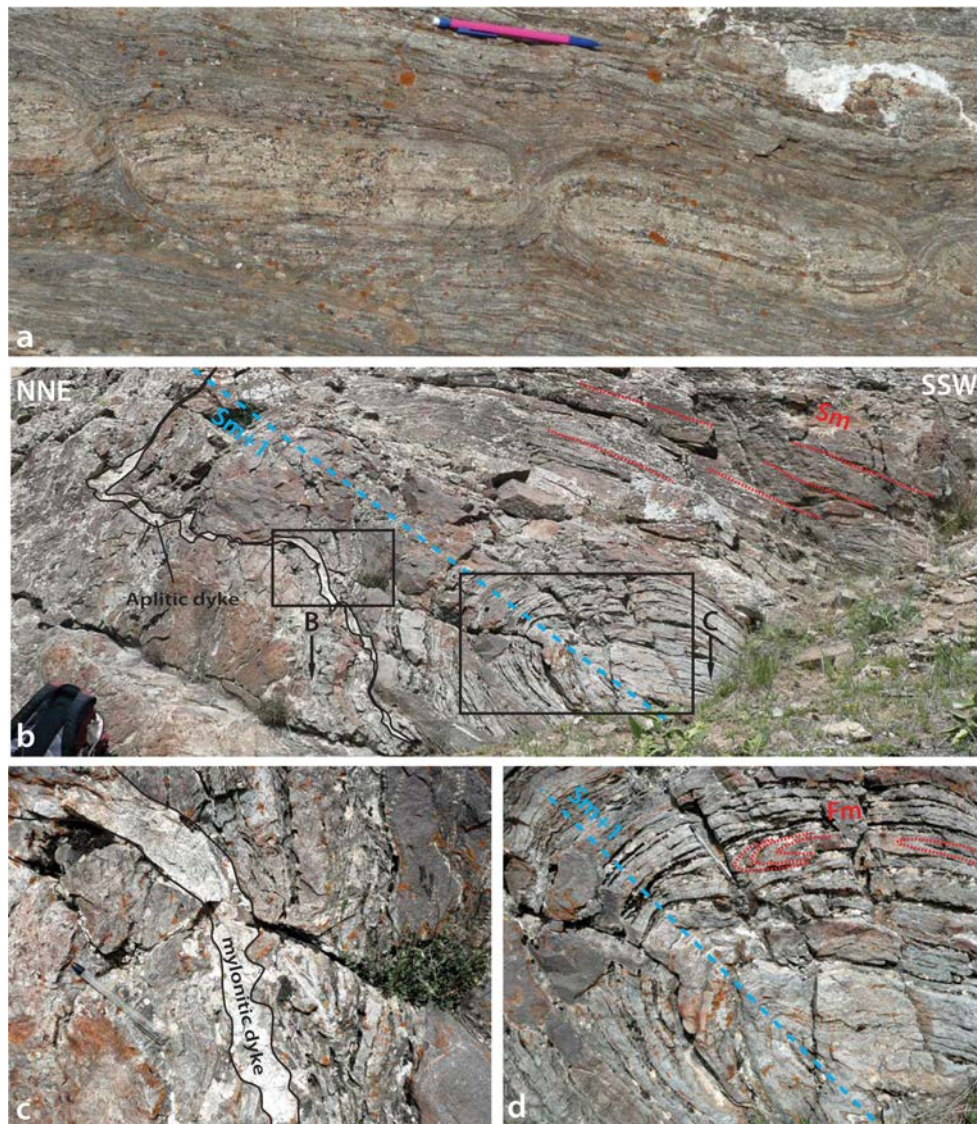


Figure 2.8 a) Boudinage in layered calc-silicates of the Hırkadağ Block. b-c-d) Field aspects of structures depicting the relationships between folds of different generations and cross-cutting aplitic dykes from the SW margin of the Hırkadağ Block. See text for further explanation.

Within the northern area, massive marbles of the upper unit display another type of deformation. The large meter-scale beds made up of coarse-grained calcite are locally cross-cut by protomylonitic to mylonitic shear bands ranging from 1 to 10 cm wide (Figure 2.7). The mylonitic shear bands strike mostly parallel to the main foliation but the dips are steeper and range around  $60^\circ$  NE, such that they cut the main foliation. Few mylonitic lineations indicate  $\sim N40^\circ-60^\circ$ . The microstructure and fabric of three selected calcite shear bands in samples H2258B, H1958E, and H2699B have been studied by optical microscopy (Figure 2.9).

The shear bands are developed in nearly pure carbonates, with few grains of quartz, muscovite and chlorite. Microstructurally they are characterized by large  $\sigma$ -type, or even fish-type calcite porphyroclasts surrounded by very small calcite grains, organized in fine bands between the porphyroclasts. The fine-grained bands define the main shear plane (Figure 2.9). Within the elongated large calcite porphyroclasts, we observe a clear network of two sets of bended and curved twins, of which one set is better developed. The consistent obliquity of the twins with respect to the planes of grain size reduction may be used as an indicator to determine the shear sense (Bestmann et al. 2000). Both calcite twin obliquity and  $\sigma$ -type porphyroclasts point to a normal top-to-NE ( $\sim N40^\circ-60^\circ$ ) shear motion. Although the three selected samples show different degrees of dynamic recrystallization, the sense of shear in the three samples consistently indicates a top-to-the-NE motion along the NE marble-rich margin of the Hirkadağ Block (Figure 2.9).

#### 2.4.2 Relationships between deformation and metamorphism

Field and thin-section observations demonstrate that the main foliation  $S_m$  is associated with the peak metamorphic mineral assemblage. For metapelitic compositions, the mineral assemblage that marks this foliation is  $Sil + Grt + Qz \pm Kfs \pm Bt \pm Ilm$  (Figures 2.5a and 2.5c). In the SW of the study area, the main foliation  $S_m$  dips toward the NE and a large fold of the  $S_m+1$  phase refolds isoclinal  $F_m$  folds. A 5-10 cm wide aplitic dyke cuts the  $S_m$  foliation, but becomes progressively mylonitized at the hinge of the  $S_m+1$  folds (Figure 2.8c). This relationship suggests that intrusion of the aplitic dyke and the  $S_m+1$  deformational phase may have been coeval. Note, however, that this observation was made at only one specific locality, and it remains unclear whether such a relationship between aplite injection and deformation holds

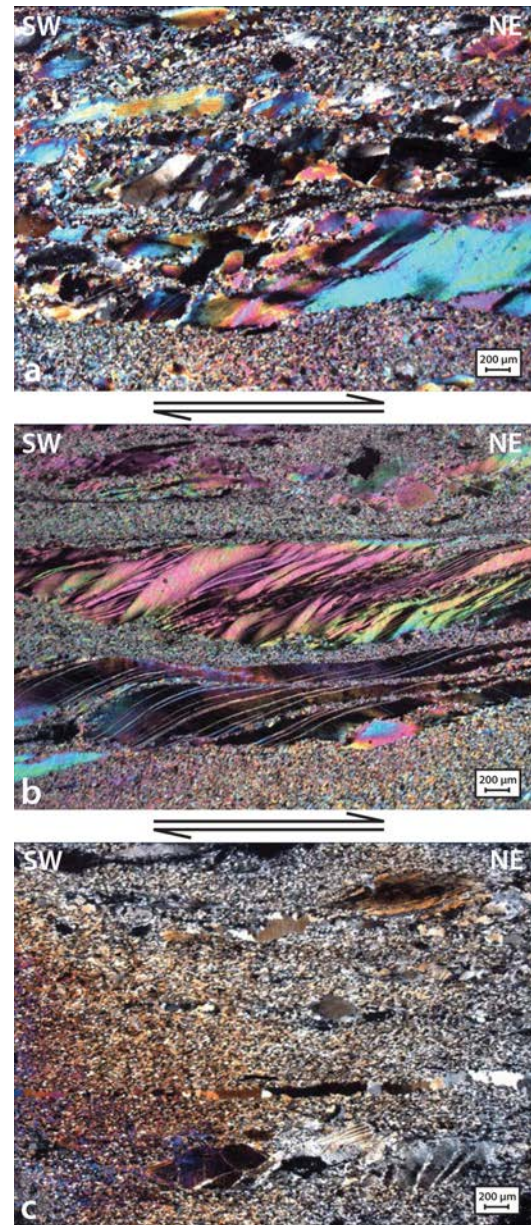


Figure 2.9 Micrographs showing mylonitic shear bands from the marble-rich northern border of the Hirkadağ Block. Locations of the samples are shown in Figure 2.7. a) sample H2258B, b) sample H1958E, and c) sample H2699B. Arrows denote inferred shear senses.

for the entire Hirkadağ Block.

Along the northern contact, mylonitic shear bands developed in the marbles contain muscovite and chlorite as minor phases suggesting greenschist facies retrograde conditions. Moreover, the development of mylonites in calcite-rich rocks is characteristic of relatively low temperature conditions (de Bresser et al. 2002). Both of these observations therefore suggest that the pervasive shearing of the upper carbonate formation occurred during exhumation. Mylonites in these upper carbonates are associated with cataclasites in a locality in the east of the Hirkadağ Block, in the Sığırkalan area, which we studied in detail as described below.

### 2.4.3 The Sığırkalmı area

The eastern contact of the Hırkadağ Block with the Ayhan basin is defined by NW-SE striking high-angle normal faults. The Sığırkalmı area (Figure 2.10a) is located in the footwall of the basin-bounding fault, and represents a back-tilted fault block. In the NE, massive marbles of the upper metamorphic unit form a large antiform that plunges toward the SW below a klippe of non-metamorphosed sedimentary rocks. At the contact, marbles are intensively mylonitized and overprinted by several meters of cataclasites and breccias, associated with a brown to yellow-colored matrix with secondary mineral phases such as quartz and dolomite (Figure 2.10b). Fragments in the breccia include the marble-rich protolith with mylonitic and protomylonitic bands (Figure 2.10d). Above the cataclastic marbles,

purple conglomerates are found that contain pebbles exclusively consisting of dark-colored volcanic rocks (Figure 2.10c). There is no trace of pebbles derived from metamorphic source rocks. The pebbles in the purple conglomerates closely resemble the stratigraphically lowest unit of the Ayhan Basin, which contains synsedimentary intercalated ~72 Ma old andesitic lavas (Advokaat et al. submitted). Those conglomerates preserve bedding planes which are shallowly dipping toward the SW and occasionally displaced by faults (Figure 2.10b). Taken together, this contact which is obviously tectonic, involves a ductile-to-brittle shear-zone in the footwall marbles, and a non-metamorphosed conglomerate containing volcanic pebbles of most likely late Cretaceous age (~72 Ma) and lacking any metamorphic debris forming the hanging wall.

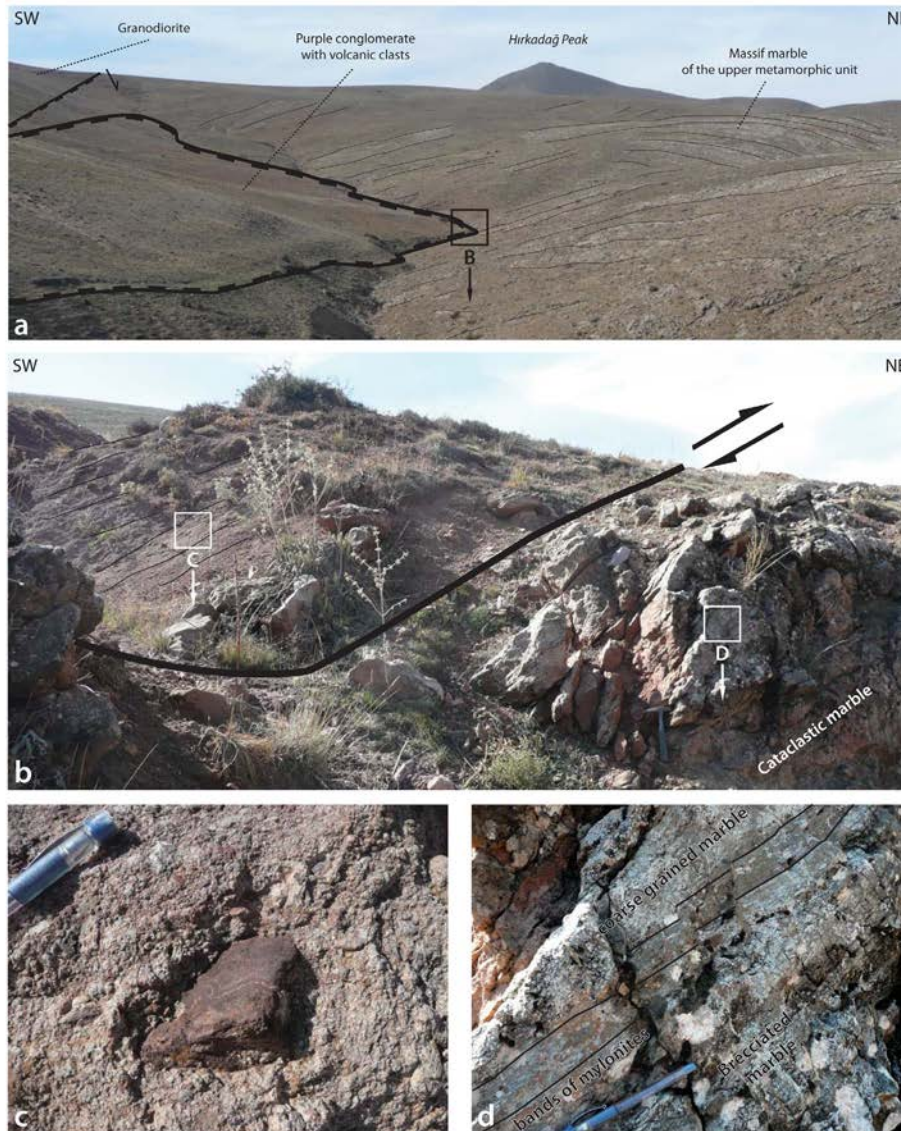


Figure 2.10 Field structures in the Sığırkalmı area: a) Panoramic view of Sığırkalmı area and structural relationship between massive marble of the upper unit and the overriding purple conglomerate, b) Detail of the contact between the marbles and the conglomerates, c) Volcanic pebbles in the purple conglomerates, d) Brecciated mylonitic bands from the marble directly below the contact.

## 2.5 Geochronology

To obtain chronological control on the cooling of the high-grade metamorphic and intrusive rocks, we dated (1) the granodioritic pluton that intruded in the NE of the Hirkadağ Block (Figure 2.3) by titanite U/Pb dating and (2) the garnet-sillimanite schists of the lowermost formation, using K-feldspar and biotite  $^{40}\text{Ar}/^{39}\text{Ar}$  analysis.

### 2.5.1 Timing of magmatism: titanite U/Pb geochronology

The H26099C sample was prepared by crushing in a jaw crusher, pulverizing in a blade mill, preliminary enrichment of the heavy minerals on a Wilfley table, and final separation in heavy liquid and a Frantz magnetic separator. The analyzed titanite was abraded (Krogh 1982) and dissolved with HF in Savillex vials on a hot plate, after adding a mixed  $^{205}\text{Pb}$ - $^{202}\text{Pb}$ - $^{235}\text{U}$  spike. Chemical separation was done either with a single stage HBr-HCl procedure or with a two stage HBr-HCl-HNO<sub>3</sub> procedure (Corfu 2004). The latter was also used for the separation of Pb and U from hornblende that was analyzed for the purpose of common Pb correction for titanite. Other details of the analytical procedure are given in Corfu

(2004). The data were calculated using the decay constants of Jaffrey et al. (1971). Regression and plotting was done using IsoPlot of Ludwig (2003). The initial Pb obtained from the hornblende was used to correct the relatively high initial common Pb concentration (8-11 ppm) of titanite, which yields a U-Pb concordia age of  $77.2 \pm 0.4$  Ma, for an assumed blocking temperature of  $\sim 625^\circ\text{C}$ ; (Titton and Grunefelder 1968; Figure 2.11b).

### 2.5.2 $^{40}\text{Ar}/^{39}\text{Ar}$ thermochronology

Sample H19107H (Figure 2.5b) was crushed, sieved and washed in acetone and distilled water. Biotite and K-feldspar crystals were separated in heavy liquid and a Frantz magnetic separator and fresh inclusion-free grains were handpicked under the binocular microscope.

The transformation of  $^{39}\text{K}(n, p)$  to  $^{39}\text{Ar}$  was performed during irradiation at the IFE Kjeller reactor in Norway, using the Taylor Creek Rhyolite as flux monitor ( $28.619 \pm 0.034$  Ma; Renne et al. 2010). Samples were step-heated in the  $^{40}\text{Ar}/^{39}\text{Ar}$  lab at the Geological Survey of Norway using a Merchantek MIR-10 CO<sub>2</sub> laser. The extracted gases were swiped over getters (SAES AP-10) for 2 minutes, and then for 9 minutes in a separate part of the extraction line. The peaks were determined

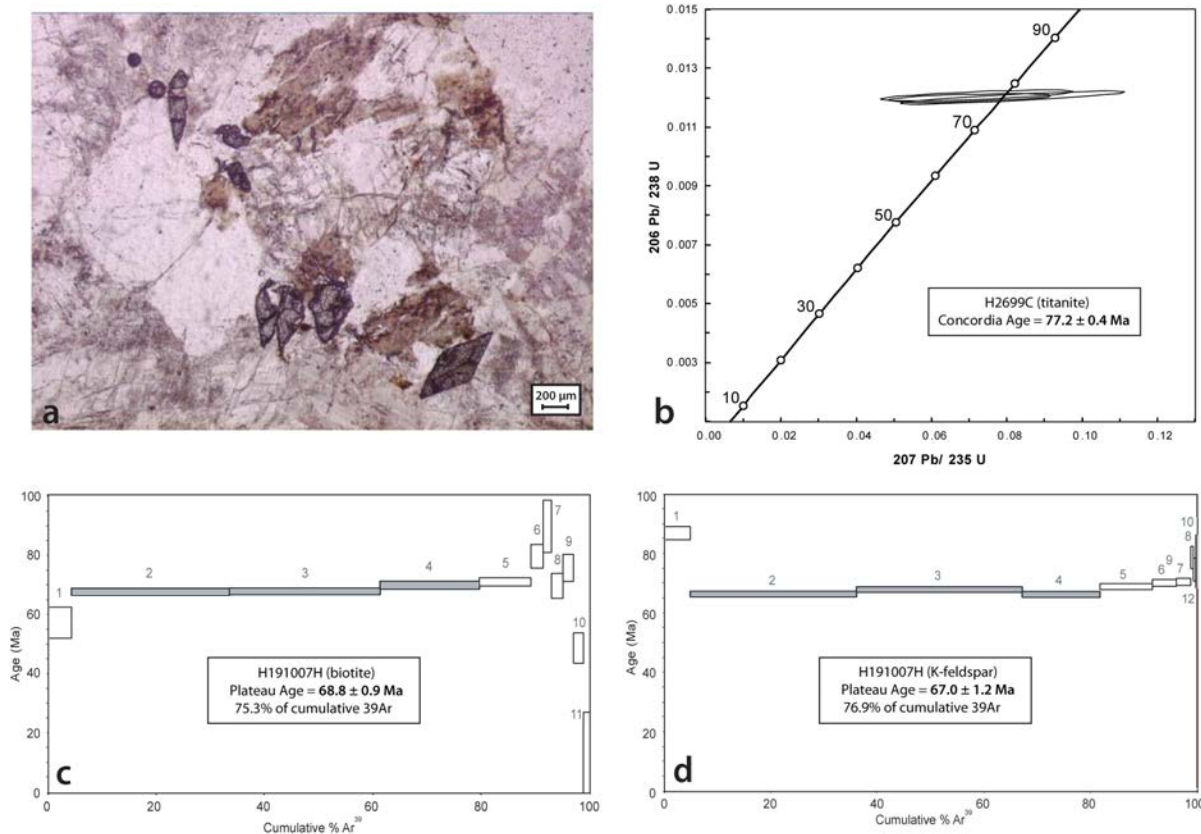


Figure 2.11 a) Micrograph showing idiomorphic titanite crystals in granodiorite sample H2699C, b)  $^{206}\text{Pb}/^{238}\text{U}$  versus  $^{207}\text{Pb}/^{235}\text{U}$  plot and concordia age from three titanite fractions of sample H2699C, c) Age versus cumulative Ar (%) diagram resulting from step heating of a biotite separate from sample H191007H, and d) Age versus cumulative Ar (%) diagram resulting from step heating of a K-feldspar separate from sample H191007H.

by peak hopping (at least 8 cycles) on masses  $^{41}\text{Ar}$  to  $^{35}\text{Ar}$  using a Balzers electron multiplier mounted on a MAP 215-50 mass spectrometer. Every 4th analysis was a blank. Data from unknowns were corrected for blanks prior to being reduced with the IAAA software package (Interactive Ar-Ar Analysis, written by M. Ganerød, NGU Trondheim, Norway) that implements the equations in McDougall and Harrison (1999) using the decay constants of Renne et al. (2010) and the trapped ratio of  $298.56 \pm 0.31$  of Lee et al. (2006). Data reduction in IAAA incorporates corrections for interfering isotopes (based on  $\text{K}_2\text{SO}_4$  and  $\text{CaF}_2$  salts included in the irradiation package), mass discrimination, error in blanks and decay of  $^{37}\text{Ar}$  and  $^{39}\text{Ar}$ . We define a plateau according to the following requirements: at least three consecutive steps overlapping at the 95% confidence level, which together represent at least 50% of total released  $^{39}\text{Ar}$  and mean square of weighted deviates (MSWD) less than the two tailed student T critical value (Spiegel 1991) (Figures 2.11c and 2.11d). We use the weighted York-2 method to calculate the inverse isochron results, with statistically valid isochrons having a MSWD value less than the two-tailed F-test critical value. Biotite produced a plateau age of  $68.8 \pm 0.9$  Ma for an assumed blocking temperature of  $\sim 300\text{-}350^\circ\text{C}$  (Grove and Harrison 1996), while K-feldspar yielded a plateau age of  $67.0 \pm 1.2$  Ma for an assumed blocking temperature of  $\sim 200\text{-}250^\circ\text{C}$  (Harrison and McDougall 1982, McDougall and Harrison 1999) (Figures 2.11c-d).

## 2.6 Discussion

Below we integrate the results from our metamorphic, structural and geochronological study of the Hırkadağ Block to infer its tectono-metamorphic evolution and its position within the regional evolution of the CACC.

### 2.6.1 The tectonic history of the Hırkadağ Block

The structural, metamorphic and geochronological data presented above can be summarized in a P-T-t-d evolution of the Hırkadağ metamorphic rocks. The initial HT metamorphic conditions reached  $\sim 7\text{-}8$  kbar/ $700^\circ\text{C}$  and were associated with isoclinal folding, the formation of the main pervasive foliation, and top-to-the-SE HT shearing. These inferred regional metamorphic conditions correspond to the upper amphibolite facies. In contradiction with previous studies, no major differences in metamorphic grade have been identified in this study between the samples collected throughout the Hırkadağ

Block. The reaction rims forming around garnet porphyroblasts are interpreted to reflect decompression, similar to the case of the metapelitic rocks of the Musgrave Complex, central Australia (Clarke and Powell 1991). During decompression to pressures around  $\sim 3\text{-}4$  kbar, metamorphic temperatures rose to  $800^\circ\text{C}$  (Figure 2.6). Note that these petrological results are in good agreement with already published data from similar rocks of the Hırkadağ Block (Whitney and Dilek 2001). The HT-LP stage may coincide with local granodioritic intrusions taking place at  $\sim 77$  Ma, and deformation was restricted to large-scale open folding, without pervasive deformation on the microscale. Note, however, that in the Hırkadağ Block, there are no additional constraints on the process that transported the metamorphic rocks from lower-middle toward upper-crustal depths, reflected by decompression from  $\sim 7\text{-}8$  kbar to  $\sim 3\text{-}4$  kbar.

Along the NE margin of the Hırkadağ Block, the structurally high massive marbles are cross-cut by (proto-)mylonitic shear bands containing minor muscovite and chlorite, suggesting shearing at low temperature, greenschist facies conditions, consistent with temperature estimates for the activation of shear localization in pure calcite material (de Bresser et al. 2002). At the scale of the massif, the mylonitic shear bands are consistently associated with a normal top-to-the-NE sense of shear.  $^{40}\text{Ar}/^{39}\text{Ar}$  ages of  $68.8 \pm 0.9$  Ma for biotite and  $67.0 \pm 1.2$  Ma for K-feldspar from southern metapelites date the cooling of the Hırkadağ Block below  $\sim 350^\circ\text{C}$  and  $\sim 250^\circ\text{C}$ , respectively, and this cooling may therefore coincide with deformation along the greenschist facies top-to-the-northeast mylonites. In the Sığırkalın area, discrete calcite mylonites are overprinted by cataclastic brittle deformation along the same foliation plane, juxtaposing non-metamorphic conglomerates on top of the Hırkadağ high-grade metamorphic and igneous rocks. Within the adjacent Ayhan Basin, similar conglomerates are intercalated with  $\sim 72$  Ma old volcanics (Advokaat et al. submitted). This implies that the sediments in the hanging wall of the fault were deposited at the surface while the high grade footwall was still at depth corresponding to an ambient temperature of  $\sim 400^\circ\text{C}$  (Figure 2.12a). Correction for a post-Lutetian  $\sim 30^\circ$  northward tilt of the redbeds that unconformably cover the Hırkadağ Block (Advokaat et al. submitted) restores the mylonites to a low-angle northeastward orientation and direction of transport. We infer that the Sığırkalın structure represents a top-to-the-NE extensional detachment, along which the Hırkadağ basement was exhumed from depths of greenschist facies

conditions to the surface. The detachment fault is cross-cut at high-angles by NW-SE trending brittle normal faults that were active during the deposition of the middle part of the Ayhan basin, sometime before the Lutetian (49–41 Ma; Figure 2.12a). The Ayhan basin provides evidence for syn-sedimentary normal faulting from the onset of sedimentation  $\sim 72$  Ma ago, which occurred in a NE-SW extension direction after correction for post-Lutetian compression (Advokaat et al. submitted).

The cooling trajectory of the Hırkadağ Block (Figure 2.12a) reveals rapid cooling from  $\sim 650$  to  $\sim 250^\circ\text{C}$  between  $\sim 77$  and 67 Ma, i.e. a cooling rate of  $\sim 40^\circ\text{C}/\text{Ma}$ .

### 2.6.2 Implications for exhumation mechanisms within the CACC

A contact very similar to the Sığırkılın structure was found in the Kırşehir massif near Kaman, where an upper crustal extensional detachment was identified (Lefebvre et al. 2011, Chapter 1). The main difference is that the hanging wall of the newly recognized Hırkadağ detachment consists of supradetachment basin sediments, whereas the hanging wall of the Kaman detachment is made up of ophiolitic material. At the scale

of the CACC, both the Kaman detachment in the NW of the Kırşehir Massif (Lefebvre et al. 2011), and extensional detachments in the southern Niğde Massif (Gautier et al. 2002) separate high-grade metasediments from the essentially non-metamorphosed Central Anatolian Ophiolites, while the Hırkadağ detachment has supradetachment basin sediments in the hanging wall that were deposited onto an unexposed pre-Late Cretaceous basement.

It is also interesting to note that the mineral lineations associated with the regional HT-MP metamorphism are oblique to the stretching lineations from the cross-cutting localized calcite shear-bands related to the Hırkadağ detachment. From this, we infer that the extensional detachment was not active during HT metamorphism, and probably did not penetrate into the lower-middle crust. This situation is very similar to the one described near Kaman (Lefebvre et al. 2011), where the detachments appear to be responsible for the later stages of exhumation to the surface, after a first phase of exhumation from HT-MP to HT-LP conditions (Figure 2.6). However, the above characteristics differ from the described detachment in the southern Niğde Massif (Gautier et al. 2002, Gautier et al. 2008), where HT metamorphic deformation during HT

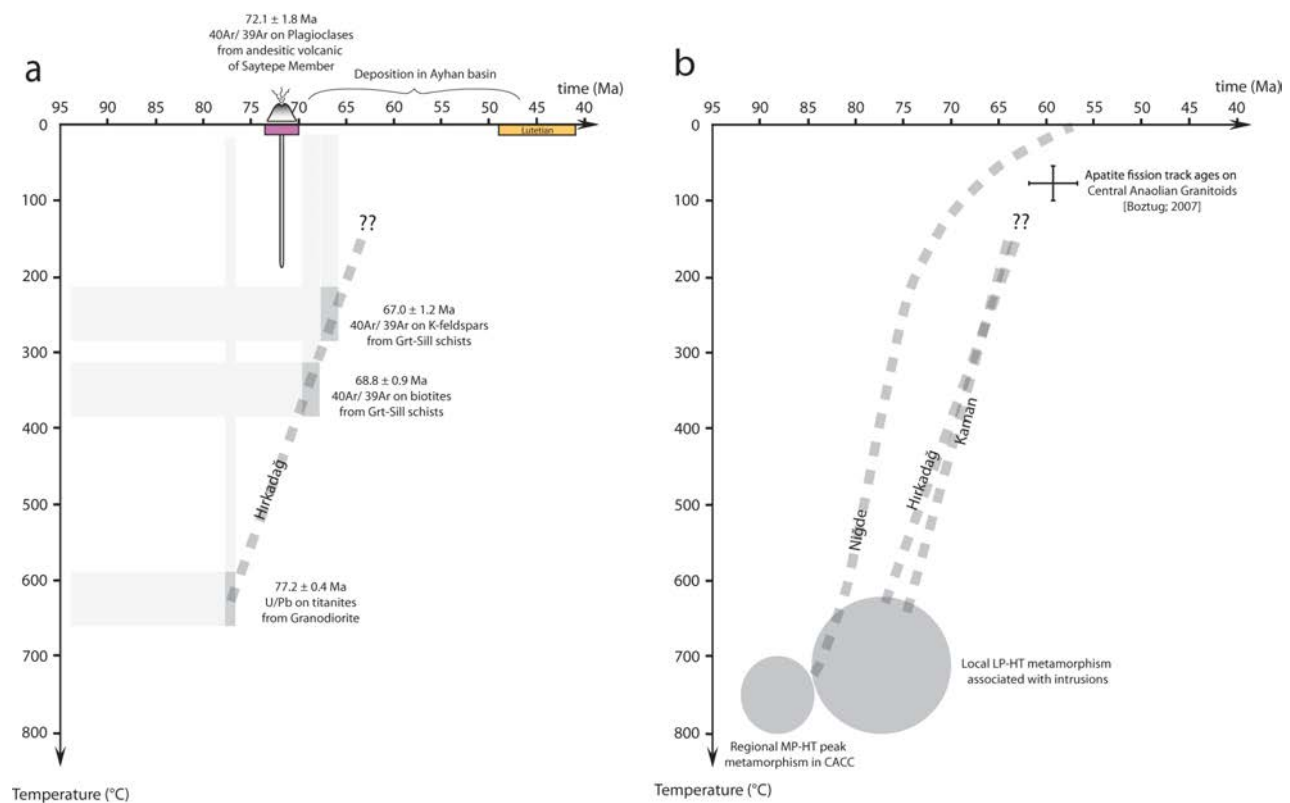


Figure 2.12 a) Temperature versus Age diagram illustrating the cooling trajectory of the Hırkadağ Block from our geochronological data.  $40\text{Ar}/^{39}\text{Ar}$  age of plagioclase from an andesite of the Saytepe Member of the Ayhan basin after Advokaat et al. (submitted), b) Same diagram as in (a), supplemented with previously published cooling trajectories from other localities in the CACC, i.e., the Niğde Massif (Gautier et al., 2008) and the Kaman area (Lefebvre et al. 2011). Apatite fission track ages from the central Anatolian Intrusives (Boztug and Jonckheere 2007) are also reported.

metamorphism occurred along parallel foliations and in the same directions as the younger semi-brittle deformation along the detachment below the gabbros of the CAO. Therefore, it seems that 2 types of detachment coexist in the CACC: (1) the Niğde detachment that penetrates into the lower crust, whereas (2) the Kaman and Hırkadağ detachments seem to only exhume rocks from upper crustal levels (depths of greenschist-facies conditions). A difference between these detachment systems is also apparent from their associated cooling histories (Figure 2.12b). The general cooling rate and age of the Hırkadağ Block is very similar to the one reconstructed from the Kaman area (Köksal et al. 2004, Boztuğ et al. 2009a, Lefebvre et al. 2011). On the other hand, the cooling history from the southern Niğde massif shows a higher cooling rate of  $\sim 60^\circ\text{C}/\text{km}$  and occurred  $\sim 5\text{-}10$  Ma earlier than in Kaman and Hırkadağ (Figure 2.12b) (Gautier et al. 2008).

### 2.6.3 Correlation of the Hırkadağ Block to the Kırşehir or Niğde massifs?

Located approximately midway between the larger crystalline massifs of Kırşehir and Niğde, and based on a similar metamorphic lithostratigraphy, geographic vicinity and similarity of high-grade metamorphic conditions, the Hırkadağ and IdişDağı Blocks are commonly correlated with the Kırşehir Massif (Atabey et al. 1987, Whitney and Dilek 2001). However, this correlation poses a few problems: First, the regional upper amphibolite / granulite facies metamorphism reported from the Hırkadağ Block is not consistent with the general metamorphic pattern and field gradient in the Kırşehir Massif indicating a regional decrease of metamorphic conditions from NW toward SE (Seymen 1981). The metasediments from the Kırşehir Massif exposed near Mucur (Figure 2.1) only underwent greenschist peak metamorphic conditions, which is thus in marked contrast with the consistently high-grade metamorphic Hırkadağ Block. Secondly, the northern marble detachment and associated mylonites from the Hırkadağ Block have N40-60 stretching lineation directions with a consistent top-to-NE sense of shear, i.e., at high angles to the N300 oriented top-to-WNW shearing reported from the Kaman detachment (Lefebvre et al. 2011). In contrast, the stretching lineation directions of the Hırkadağ detachment are more similar to those in the Niğde Massif where the extensional detachment-related stretching lineations trend around N60, with associated top-to-NE shearing (Gautier et al. 2008). NE-SW trending stretching lineations were also reported from shear zones in the Ağaören

granitoids to the west of Gülşehir area (Isik 2009). We therefore propose that the Niğde, Ağaören and Hırkadağ crystalline complexes represent a single coherent deep-crustal domain.

## 2.7 Conclusions

In order to elucidate the processes associated with the late Cretaceous HT event, the tectonic history of the Hırkadağ Block has been addressed through an integrated approach involving metamorphic, structural and geochronological analysis. The tectonic history of the Hırkadağ Block includes a regional HT-MP metamorphic event associated with pervasive top-to-the-SW ductile deformation. The replacement of garnet and sillimanite by cordierite and spinel in metapelitic rocks indicates a HT-LP overprint following an isothermal decompression which brought the metasedimentary pile at upper crustal levels. Geochronology of the intrusive granodiorite bodies likely responsible for the localized granulite facies overprint yields titanite U/Pb ages of  $77.2 \pm 0.4$  Ma. Following the magmatism, the Hırkadağ HT complex cooled down rapidly, reaching  $\sim 350^\circ\text{C}$  by  $68.8 \pm 0.9$  Ma and  $\sim 250^\circ\text{C}$  by  $67.0 \pm 1.2$  Ma, indicated by  $^{40}\text{Ar}/^{39}\text{Ar}$  cooling ages from biotite and K-feldspar, respectively.

Exhumation of the crystalline rocks is documented within the northern marbles by the presence of discrete protomylonitic and mylonitic shear bands having N40-60 stretching lineation directions with a consistent normal top-to-NE sense of shear. The Sığırkalan area exposes the contact associated with this shearing event between high-grade deformed marbles (with ductile mylonitic shear bands overprinted by cataclasites) and late Cretaceous, non-metamorphosed conglomerates containing volcanic pebbles. This structure has been interpreted as an upper crustal detachment fault, similar to what has been reported in the NW Kaman area.

## Acknowledgements

This work was financially supported by the Netherlands Research Center for Integrated Solid Earth Sciences (ISES), the Netherlands Organization for Scientific Research (NWO) and the DARIUS Programme. Kalijn M. Peters, Philip C. Wehrens and Eldert L. Advokaat acknowledge financial support from the Molengraaff foundation. DJJvH acknowledges financial support from Statoil (SPlates model project). Osman and Yasin (from Kirkit Pension in Avanos) are kindly thanked for their logistical support around the study area.



---

# CHAPTER 3



# Reconstructing the geometry of central Anatolia during the late Cretaceous: Large-scale Cenozoic rotations and deformation between the Pontides and Taurides

## Abstract

The Central Anatolian Crystalline Complex (CACC) is considered as a continental fragment which evolved within the Africa-Eurasia convergence zone during the period of closure of the Neotethyan realm. Today, the CACC is located in the central part of Turkey, between the Pontides in the north and the Tauride Block in the south. Its modern triangular geometry (~250x250x250 km) is bounded by major tectonic structures separating it from the surrounding metamorphic massifs. The massifs mainly consist of metamorphic, ophiolitic and intrusive igneous rocks that are covered by Cenozoic deposits. This crystalline domain experienced a complicated tectonic history involving late Cretaceous obduction of ophiolitic nappes onto Paleozoic-Mesozoic sedimentary units, followed by widespread magmatic intrusion and unroofing in Paleogene times. The intrusives, mainly of granitic, granodioritic, monzonitic and syenitic composition were emplaced between 95 and 75 Ma. Granites and some mafic intrusive bodies are distributed along the outer margin of the massif while the monzonites and syenites occupy a more internal position. Those plutons are organized in linear magmatic belts which form a curved NW-ward convex trend along the western and northern margins of the CACC. In this study we applied paleomagnetic techniques on non-deformed upper Cretaceous granitoids to test whether the present-day geometry of the complex is different from its initial geometry. We focused on the outer granitoids and associated mafic enclaves where we sampled fifteen localities each consisting of 5-8 sites (783 cores) distributed over the entire CACC.

Our results distinguish three domains with significantly different vertical-axis rotations: (1) in the north-east, the Yerköy-Yozgat block (YYB) records ~30° clockwise rotation, (2) in the north-west, the Kırıkkale-Kaman block (KKB) shows no significant rotation and (3) in the south-west, the Ağaören-Aksaray block (AAB) shows ~35° counter-clockwise rotation. This proves that the original geometry of the CACC in the late Cretaceous was significantly different and suggests that it has been affected by major internal deformation since then. We explain the accommodation of part of this deformation by the presence of two transpressional fault zones: the sinistral Hirfanlar-Hacibektaş Fault Zone (HHFZ) and the dextral Delice-Kozaklı Fault Zone (DKFZ). Comparison with existing paleomagnetic data suggests that the rotations likely occurred prior to the Eocene. We propose that this major deformation phase associated with the rotations are best explained as a result of collision of the CACC with the Pontides, following the recently established latest Cretaceous to earliest Paleocene oroclinal bending scenario of the central Pontides.

Côme Lefebvre  
Maud J.M. Meijers  
Nuretdin Kaymakci  
Ahmet A. Peynircioğlu  
Cor G. Langereis  
Douwe J.J. van Hinsbergen

### 3.1 Introduction

The Central Anatolian Crystalline Complex (CACC) and the Menderes Massif (in western Anatolia) are the largest metamorphic domains cropping out in Turkey. Both massifs cover areas of tens of thousands of square kilometers and share similar tectonic histories involving regional Barrovian metamorphism and subsequent exhumation of high-grade metamorphic rocks at the Earth's surface (e.g. Erkan 1976, Göncüoğlu 1977, Akkök 1983) (Figure 3.1a). However, the two massifs strongly differ in age, as the high-temperature metamorphism and exhumation of the CACC occurred in the late Cretaceous – Paleocene (e.g. Whitney et al. 2003, Boztuğ and Jonckheere 2007), while the Menderes Massif mainly underwent a similar tectono-metamorphic evolution during Eocene – Miocene times (e.g. Şengör et al. 1984, Satir and Friedrichsen 1986, Hetzel et al. 1995), thus approximately 50 Myr later than the CACC. The geodynamic evolution of the Menderes massif is explained by collision-related metamorphism, followed by exhumation in the extensional Aegean-west Anatolian back-arc (Ring et al. 2003, van Hinsbergen et al. 2010). The geodynamic context of the latest Cretaceous to Paleocene exhumation and extension history of the CACC, however, remains poorly understood. The main reason is that following exhumation and extension in the late Cretaceous, the CACC collided with the central Pontides (Görür et al. 1984, Görür et al. 1998, Kaymakci et al. 2000, Kaymakci et al. 2003a, Kaymakci et al. 2003b, Kaymakci et al. 2009, Meijers et al. 2010), leading to collision-related compression in central Anatolia throughout the Eocene (Şengör and Yılmaz 1981, Görür et al. 1984, Kaymakci et al. 2003b, Gülyüz et al. submitted). The expression of this collisional period is mainly identified within the large peripheral basins (e.g. Çankırı, Tuzgölü, Sivas basins) and narrow intra-CACC basins (e.g. Kırıkkale, Çiçekdağ and Ayhan basins) where fold and thrust belts developed (e.g. Görür et al. 1984, Poisson and Guezou 1996, Köksal and Göncüoğlu 1997, Görür et al. 1998, Dirik et al. 1999, Kaymakci et al. 2009, Advokaat et al. submitted, Gülyüz et al. submitted) (Figure 3.1b). Among the best-described compressional features in central Anatolia is the ~150 km long EW-trending Savcılı thrust zone, which separates southern massifs (Niğde Massif, Hırkadağ/IdişDağı Blocks and Ağaçoören Intrusive Suite) from the northern massifs (Kırşehir and Akdağ Massifs) (Oktay 1982, Seymen 2000, Advokaat et al. submitted) (Figure 3.1b). At present, the CACC forms a 250x250x250 km triangular domain, where linear magmatic belts of upper Cretaceous age are

exposed along the southwestern, northwestern and northern margins of the massifs defining a roughly NW-ward convex trend. Based on the study of the tectonic evolution of the central Anatolian basins and scarce paleomagnetic data (e.g. Sanver and Ponar 1981), Görür et al. (1984, 1998) proposed several possible paleotectonic reconstructions, and speculated that the modern configuration resulted from severe internal deformation and large-scale block rotations that transformed an originally elongated block into the present triangular configuration as a result of its collision with the Pontides.

In this study, we use paleomagnetism as a tool to test whether the original geometry of the CACC during the late Cretaceous was similar or not to its modern configuration. We concentrate on the upper Cretaceous granitoids containing mafic enclaves, which form elongated composite plutons of ~30x100km (Figure 3.1). We sampled 783 cores from fifteen localities that were evenly distributed over the CACC, in order to track if any vertical-axis rotations occurred since the late Cretaceous and potentially changed the geometry of the area. We also compare our results with previous paleomagnetic studies carried out on upper Cretaceous – Miocene rocks within the CACC.

### 3.2 Geology of the CACC

As a segment of the Alpine-Himalayan orogenic belt, Turkey comprises a complex assemblage of continental and oceanic fragments, which witness the ongoing tectonic activity that occurred in the region (e.g. Ketin 1966, Şengör and Yılmaz 1981, Moix et al. 2008). In the north, the EW-trending Pontides contain Paleozoic metamorphic rocks overlain by a non-metamorphic Mesozoic cover (Şengör and Yılmaz 1981). The Pontides are bounded by the Black Sea in the north and the Izmir-Ankara-Erzincan suture zone (IAESZ) in the south (Figure 3.1a). The IAESZ marks the location of the former northern branch of the Neo-Tethyan Ocean, and comprises Triassic to Cretaceous oceanic remnants (radiolarites, carbonates, MORB-type basalts) and foreland basin clastics, deformed into a mélange (Brinkmann 1972, Şengör and Yılmaz 1981). To the south of the suture are metamorphic rocks of the 'Anatolides', including the CACC, and non-metamorphic rocks of the 'Taurides', both overlain by late Cretaceous ophiolites. Pan-African metamorphic basement and Paleozoic fauna demonstrate that the Anatolide-Tauride block(s) were derived from Gondwana (e.g. Okay 1989, Kröner and Şengör 1990). In central Turkey, the boundaries of the

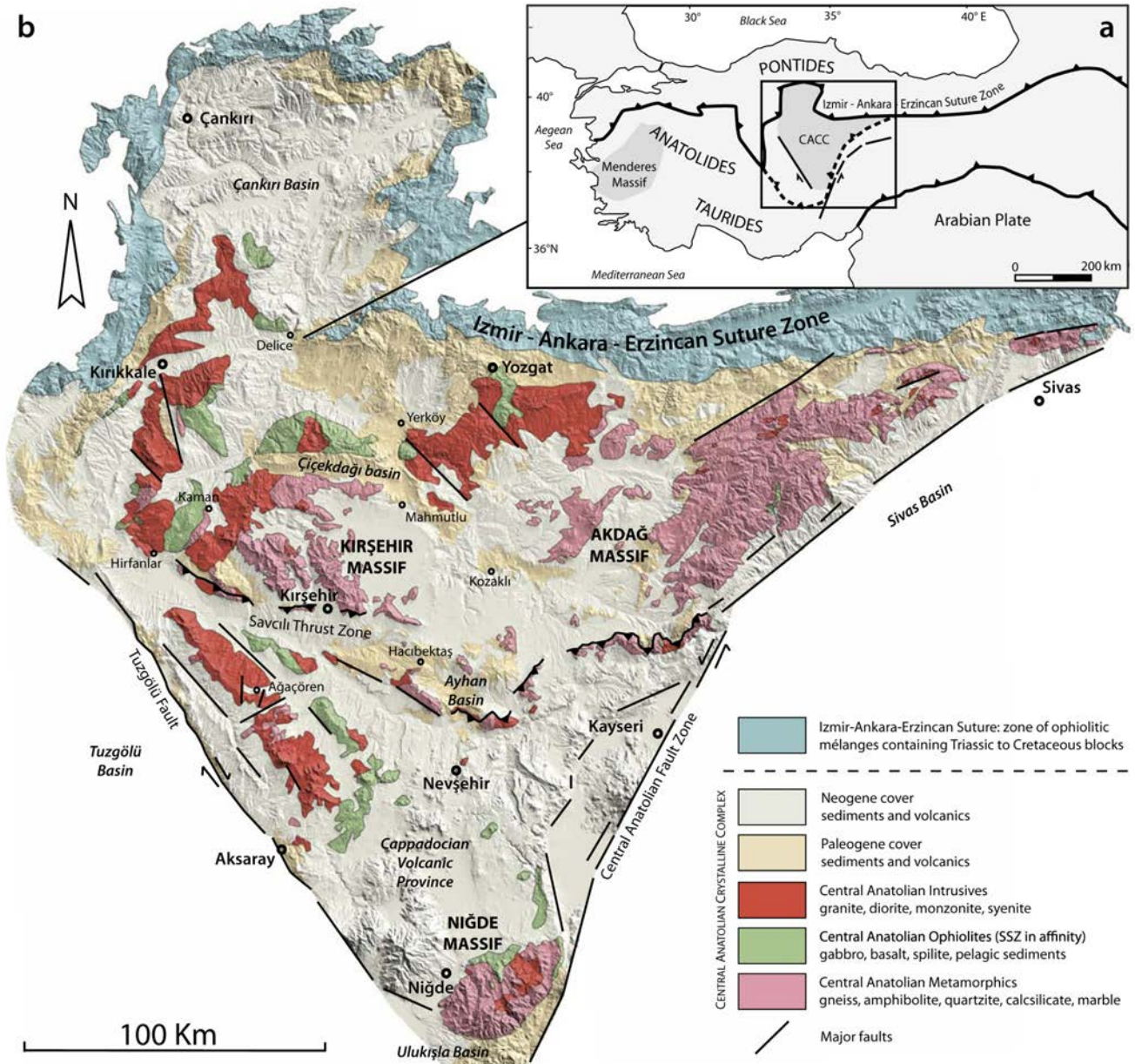


Figure 3.1 a) Simplified tectonic map of the Turkish orogenic system. The two grey areas indicate the location of the two largest metamorphic massifs in Turkey: the Menderes Massif and Central Anatolian Crystalline Complex (CACC); b) Simplified geological map of the CACC draped onto a Digital Elevation Model.

CACC are defined by intra-continental fault zones such as the main thrust of the IAESZ in the north, the dextral Tuz Gölü fault in the west and the sinistral Central Anatolian Fault Zone in the east, giving the CACC its triangular appearance (Figure 3.1b). The oldest rock units cropping out within the area consists of a metamorphosed Paleozoic to Mesozoic succession of clastic deposits and platform carbonates (Göncüoğlu et al. 1992, Kocak and Leake 1994). During the Turonian – Santonian, these platform sediments underthrust below a supra-subduction type oceanic crust (referred as Central Anatolian Ophiolites (CAO)) (Yaliniz and Göncüoğlu 1998, Yaliniz et al. 2000b), underwent regional Barrovian metamorphism ranging from upper-amphibolite to greenschist facies, and therefore became the

Central Anatolian Metamorphics (CAM) (Erkan 1976, Seymen 1981, Göncüoğlu et al. 1991) (Figure 3.1). Metamorphism at peak conditions is estimated around 700-800°C for 6-8 kbar with local re-heating at 2-4 kbar (Kocak and Leake 1994, Whitney et al. 2001; Chapter 2), and is associated with pervasive ductile deformation that developed penetrative foliation, isoclinal folds and shearing (Seymen 1983, Tolluoğlu and Erkan 1989, Chapter 2). Following peak metamorphism, widespread plutons intruded into both the CAM and CAO (Erdoğan et al. 1996, Erler and Göncüoğlu 1996). This magmatic event formed large, elongated plutons (~100km long) that are preferably localized at, and follow the trend of the western and northern boundaries of the CACC (Akiman et al. 1993) (Figure 3.1b). The composition of

these intrusives covers a wide range, comprising both mafic and felsic intrusives, including gabbros, and granites, monzonites and syenites, respectively (Figure 3.2).

Various classification types have been used and discussed in the literature in order to characterize the central Anatolian composite magmatics: (1) the alumina saturation index varying from peraluminous, metaluminous to peralkaline (e.g. Erler and Göncüoğlu 1996, Aydın et al. 1998, Düzgören-Aydın et al. 2001), (2) the coexistence of S- (or C-), I- (or H-), and A-type granitoids illustrating the multiple magmatic sources (e.g. Aydın et al. 1998, Boztuğ 2000, Düzgören-Aydın et al. 2001), (3) the presence of calc-alkaline, sub-alkaline and alkaline rock units (e.g. Ilbeyli et al. 2004, Ilbeyli 2005, Kadioğlu et al. 2006), (4) discrimination diagrams based on trace-elements indicating volcanic arc granite (VAG), syncollisional granite (Syn-COLG), and within-

plate granite (WPG) fields for the granitoids, and mainly WPG field for the syenitoids (e.g. Akiman et al. 1993, Boztuğ 2000, Ilbeyli 2005, Kadioğlu et al. 2006).

Constraints on the age of emplacement of the plutons provided in the literature indicate that the magmatic pulse lasted from ~95 to 75 Ma (based on Rb/Sr whole rock, U/Pb on titanite and zircon and Pb/Pb evaporation on zircon methods) (Göncüoğlu 1986, Whitney et al. 2003, Köksal et al. 2004, Boztuğ et al. 2007). However, the oldest crystallization ages are problematic, as they are in contradiction with field structural relations indicating that the central Anatolian magmatism postdates peak metamorphism in the CAM (estimated at 91-84Ma (Whitney et al. 2003, Whitney and Hamilton 2004)). The diverse and complex magmatic series exposed in central Anatolia also show indications for their spatial and temporal evolution: (1) the oldest granite

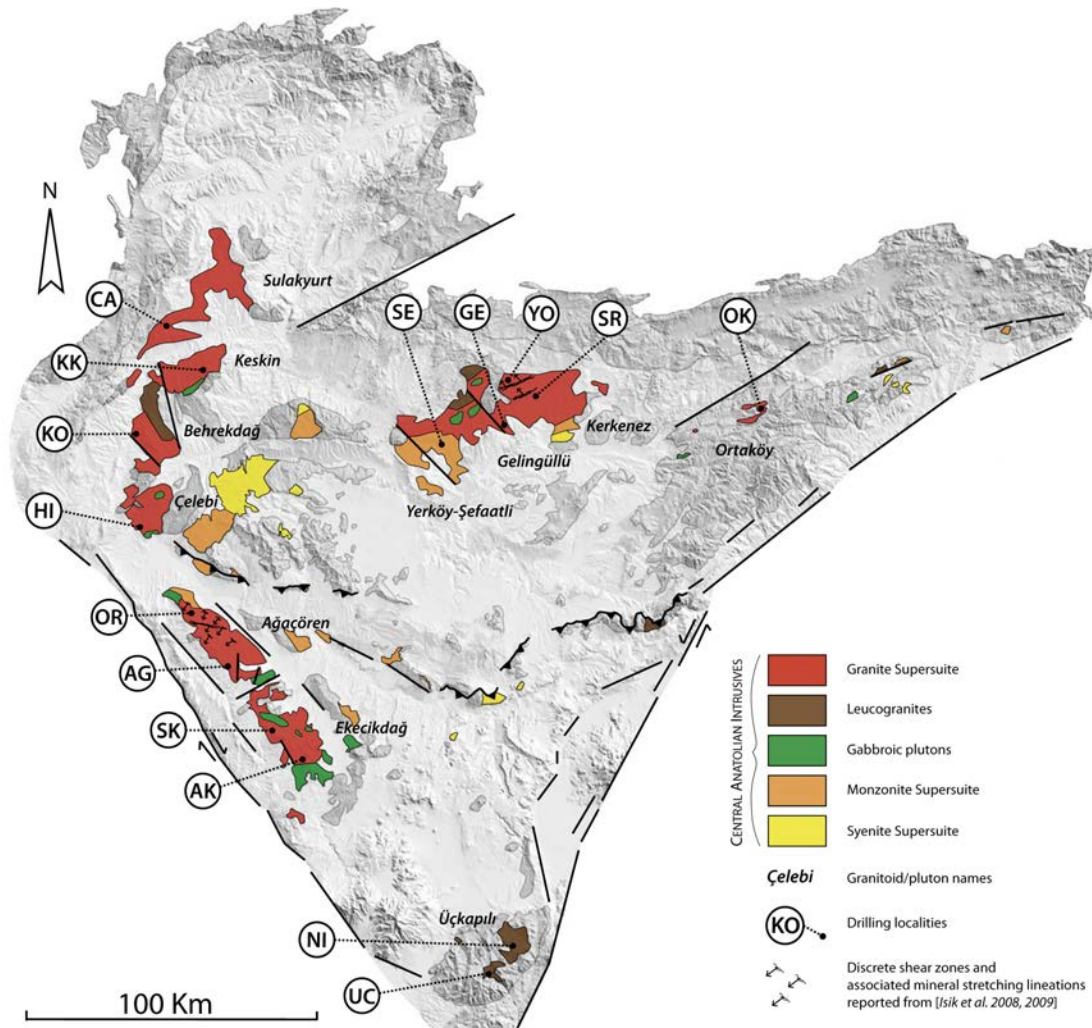


Figure 3.2 Composite map of the CACC showing: (1) the distribution of the main central Anatolian magmatic supersuites (modified after (Kadioğlu et al. 2006)) and leucogranites (modified after (Tatar et al. 1996)); (2) the pattern of brittle faults affecting the plutons (after (Erler & Göncüoğlu 1996)) and the discrete shear zones cutting across the Ağaçören and Kerkenez granitoids (after (Isik et al. 2008, Isik 2009)); and (3) the locations and sampling codes of the fifteen paleomagnetic sampling localities, with the names of associated granitoids (after (Akiman et al. 1993) for the western granitoids and after (Erler & Göncüoğlu 1996) for the Yozgat Batholith).

supersuite occurs directly along the western and northern edges of the CACC forming the outer magmatic belt, (2) toward the center of CACC, the monzonite supersuite is intruding into the granites, (3) and the youngest syenite supersuite occurs as small plutonic bodies and is generally exposed in the inner part of the complex (Kadioğlu et al. 2006) (Figure 3.2).

Except for foliated syn-collisional leucogranites and some of the outer granitoids affected by discrete extensional ductile shear zones, the central Anatolian intrusives are generally considered as ductily undeformed (Akiman et al. 1993, Boztuğ 1998, Düzgören-Aydın et al. 2001) (Figure 3.2). Exhumation of the metamorphic/magmatic complex was associated with extension, as evidenced by extensional detachment structures at the interface between the high-grade metamorphic rocks and essentially non metamorphic remnants of ocean-derived crust, identified in the Niğde massif (Gautier et al. 2002), in the Kırşehir Massif near Kaman (Lefebvre et al. 2011), and in the Hırkadağ Block in the center of the CACC (Chapter 2). In addition, a few discrete late Cretaceous ductile shear zones were recognized within the Yozgat and Ağaören granitoids (Isik et al. 2008, Isik 2009) (Figure 3.2). The final unroofing stage of the central Anatolian crystalline rocks is constrained by apatite fission track data on

granitoids, which indicate a Paleocene age (~57-62 Ma) (Boztuğ and Jonckheere 2007). Synchronously with this exhumation, basins of central Anatolia were actively filled by volcanic and sedimentary deposits (e.g. Görür et al. 1998, Dirik et al. 1999, Kaymakci et al. 2009, Advokaat et al. submitted).

### 3.3 Paleomagnetic sampling, analysis and reliability check

#### 3.3.1 Paleomagnetic sampling

In total, 783 cores were sampled at 15 localities (of 5-8 sites each) distributed within the upper Cretaceous magmatic bodies. The drilling localities are concentrated within the outer magmatic belt, in order to compare intrusive rocks from the same magmatic period and with relatively similar composition (Figure 3.2). Despite the lack of exposure in some magmatic massifs and the presence of a network of brittle faults and several discrete shear zones (Figure 3.2), we aimed at sampling unfoliated, brittlely undeformed and fresh outcrops of igneous rock.

All fifteen sampling localities are individual plutons that are geographically distributed within four main composite batholiths or magmatic suites (see Figure 3.2 and Table 3.1), with mineral compositions that range from monzogranite to

Localities	Batholith/magmatic suite	Granitoid	Granite-type	Dating Method	Age (Ma)	Samples ; Reference
AG	Ağaören Intrusive Suite	Ağaören SE	HBG	Rb/Sr (whole-rock)	110 ± 14	Güleç 1994
AK	Ağaören Intrusive Suite	Ekecikdağ SE	HBG		no data	
CA	NW intrusive belt	Sulakyurt	HKG		no data	
GE	Yozgat Batholith	Gelingüllü	BG		no data	
HI	NW intrusive belt	Çelebi	HKG		no data	
KK	NW intrusive belt	Keskin	HKG	Pb-Pb (zircon)	77.0 ± 7.8	Hasandede ; Boztuğ et al. 2007
				K-Ar (hbl)	65-80*	
				K-Ar (hbl)	79.5 ± 1.7	İlbeyli et al. 2004
				Pb-Pb (zircon)	92.4 ± 5.6	
K-Ar (hbl + biot)	80-75*	Konur ; Boztuğ et al. 2008				
NI	Niğde Massif	Üçkapılı NE	BMG		no data	
OK	Akdağmadeni Suite	Ortaköy	HBG		no data	
OR	Ağaören Intrusive Suite	Ağaören NW	HKG		no data	
SE	Yozgat Batholith	Yerköy-Şefaati	HBG	K-Ar (hbl + biot)	80-68*	"ST" ; Boztuğ et al. 2008
SK	Ağaören Intrusive Suite	Ekecikdağ NW	BG	<sup>40</sup> Ar/ <sup>39</sup> Ar (biot)	77.6 ± 0.3*	5 ; Kadioğlu et al. 2003
SR	Yozgat Batholith	Kerkenez NW	HKG	<sup>40</sup> Ar/ <sup>39</sup> Ar (hbl)	81.2 ± 0.5*	03V-56 ; Isik et al. 2008
				<sup>40</sup> Ar/ <sup>39</sup> Ar (Ksp)	82.4 ± 0.3	03V-56 ; Isik et al. 2008
UC	Niğde Massif	Üçkapılı SW	BMG	Rb/Sr (whole-rock)	95 ± 11	Göncüoğlu, 1986
				Rb/Sr (biot)	77.8 ± 1.2	Göncüoğlu, 1986
				K-Ar (biot)	78-75	Göncüoğlu, 1986
				U-Pb SHRIMP (zircon)	92-85	98-16 ; Whitney et al. 2003
				<sup>40</sup> Ar/ <sup>39</sup> Ar (biot)	76.2 ± 0.2	95-59 ; Whitney et al. 2003
				<sup>40</sup> Ar/ <sup>39</sup> Ar (biot)	79.5 ± 1.2	98-17 ; Whitney et al. 2003
				<sup>40</sup> Ar/ <sup>39</sup> Ar (Ksp)	70.3 ± 0.2	98-17 ; Whitney et al. 2007
				<sup>40</sup> Ar/ <sup>39</sup> Ar (biot)	75.1 ± 1.0	N49 ; Gautier et al. 2008
				<sup>40</sup> Ar/ <sup>39</sup> Ar (musc)	76.0 ± 0.8	N67 ; Gautier et al. 2008
				<sup>40</sup> Ar/ <sup>39</sup> Ar (biot)	80 ± 0.2	Sarıhanlı ; Boztuğ et al. 2009
YO	Yozgat Batholith	Kerkenez centre	HKG	<sup>40</sup> Ar/ <sup>39</sup> Ar (biot)	80 ± 0.2	Sarıhanlı ; Boztuğ et al. 2009

Table 3.1 Table displaying the main features of each of the sampling localities: their batholiths/magmatic suite and individual granitoids to which they belong to, the granite-type: BG = biotite granite, BMG = biotite-muscovite granite, HBG = hornblende-biotite granite, HKG = hornblende-potassic feldspar granite, and the existing radiometric data with associated references and used dating methods. The ages marked by an asterisk are the ages used in Figure 3.7.

quartz monzonite (e.g. (Akıman et al. 1993)). The fifteen sampling localities are distributed as follows: (1) In the north-west of the CACC, a ~100km long N-NNE trending magmatic belt (referred as “NW intrusive belt” in Table 3.1) consists mainly of medium to coarse grained quartz monzonites and granites containing mafic enclaves (İlbeyli et al. 2004). Four sampling localities have been distributed in individual granitoids from north to south: the CA locality from the Sulakyurt granitoid, KK from the Keskin granitoid, KO from the Behrekdağ granitoid, and HI from the Çelebi granitoid. Our samples consist mainly of hornblende – potassic feldspar granites (an enlarged macroscopic scan of representative sample HI2.3 is presented in Figure 3.3a). (2) In the west, a ~100km long magmatic belt situated along the NW-SE trending Tuzgölü fault is called the Ağaçören Intrusive Suite (AIS) (Kadıoğlu and Güleç 1996). The AIS is subdivided in the Ağaçören granitoid (Kadıoğlu and Güleç 1996) in the north and the Ekecikdağ granitoid in the south (Türelı 1991). The granitoids mainly consist of coarse to porphyritic monzogranites, containing mafic enclaves. Four localities have been sampled from north to south: OR and AG from the Ağaçören granitoid and SK and AK from the Ekecikdağ granitoid. Our samples consist of hornblende-biotite, biotite and hornblende – potassic feldspar granites (an enlarged macroscopic scan of representative sample AK6.3 is presented in Figure 3.3b). (3) In the north, the large Yozgat Batholith mainly consists of monzogranite and quartz monzonite, and includes eight granitoid subdivisions (Erler and Göncüoğlu 1996). In our study, we sampled the western Yerköy-Şefaati granitoid (SE locality), the central Gelingüllü granitoid (GE locality) and the north-eastern Kerkenez granitoid (YO and SR localities, in the north and center of the pluton respectively). We completed the sampling with a locality further east of the Yozgat Batholith in the Ortaköy granitoid

(OK locality) near the city of Akdağmadeni. Our samples consist of hornblende-biotite, hornblende – potassic feldspar and biotite granites (an enlarged macroscopic scan of representative sample SE4.7 is presented in Figure 3.3c). (4) Isolated in the southern Niğde Massif, the Üçkapılı granodiorite represents the southernmost pluton of the CACC. It consists of a two-mica monzogranite with a weakly developed ductile fabric (Göncüoğlu 1986). The two sampling localities are NI and UC, and were collected from the central and north-eastern part of the granitoid, respectively. Our samples mainly consist of biotite-muscovite granites (see Figure 3.3d for an enlarged macroscopic scan of representative sample NI2.3).

Age estimates of the sampled granitoids are based on existing radiometric data belonging to the same magmatic pluton. Available ages, dating methods and associated references are reported in Table 3.1. Each locality was sampled within a single granite body and comprises five to eight sites that contain approximately seven to eight samples each. Note that the age of the magnetization is a cooling age, and therefore is younger than the crystallization age of the granitoids. Ideally, sites within a locality were spaced ~50-100 m, over which cooling may be sufficiently diachronous to average paleosecular variation. Per site the samples were drilled within several meters using a gasoline powered motor drill; details are presented in the Supplementary Table. Sample orientations were measured with a magnetic compass and corrected for present-day declination (~4.8°E). Because we sampled plutonic bodies, we have no control on the paleohorizontal at the time of acquisition of the magnetization and therefore we are not able to apply a possible tilt correction. To check the validity of our data sets, we compared the paleolatitudes calculated from the data of our localities to those calculated from the apparent polar wander (APW) path (Torsvik et al. 2008).

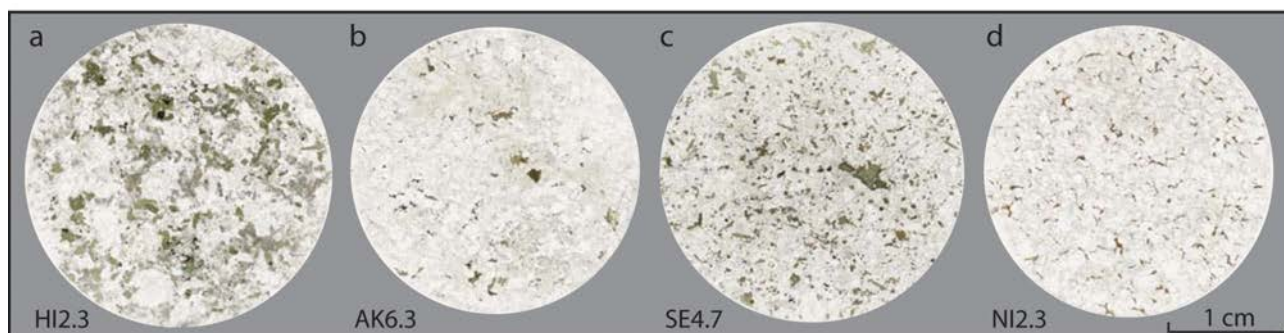


Figure 3.3 Enlarged macroscopic scans of representative sampled cores from: a) HI2.3, a hornblende – potassic feldspar granite (HKG), b) AK6.3, a hornblende-biotite granite (HBG), c) SE 4.7, a hornblende-biotite granite (HBG), and d) NI2.3, a biotite-muscovite granite (BMG).

### 3.3.2 Paleomagnetic analysis

The 783 samples were cut into standard specimens, providing in most cases 2 or more specimens per core (referred as A and B specimens). A total of 1022 specimens were demagnetized. Thermal (TH) demagnetization (80 specimens) was carried out to check the validity of alternating field (AF) demagnetization (942 specimens). AF demagnetization was carried out on the in-house developed robotized 2GDCSQUID magnetometer (noise level 10-12 Am<sup>2</sup>). The 10 specimens of OR01-OR10 (as a part of locality OK) were added to this study. The demagnetization of the NRM is displayed in orthogonal vector diagrams (Figure 3.4) (Zijderveld 1967). Characteristic remanent magnetization (ChRM) directions were determined using principle component analysis (Kirschvink 1980) on approximately 5-7 successive temperature or AF steps in the majority of the specimens. Samples that yielded NRM components that were intermediate between two overlapping temperature or coercivity ranges, were analyzed using the great-circle approach of McFadden and McElhinny (1988). This method determines the direction on the great circle that lies closest to the average direction of well-determined NRM directions. The great-circle approach was only used in a very limited number of cases: in total on four specimens from sites KK5, SK4 and SK6 (see Supplementary data).

The magnetic carrier of the ChRM in the samples is magnetite, evidenced by maximum unblocking temperatures and fields around 580°C and ~40-90mT (see Figure 3.4). Near-identical results for thermal and AF demagnetization on specimens from the same sample were found (Figure 3.4). The ChRM in several sites is removed in a high coercivity range (~25-90 mT), which generally agrees with higher unblocking temperatures (~480°-580°C) in the specimens taken from the same samples (e.g. Figures 3.4 o-p, aa-ab, ad-ae). Demagnetization of the ChRM at low AF steps (~5-55mT) generally coincides with lower unblocking temperatures (e.g. Figures 3.4l-m, af-ag and am-an).

Within a locality, and even within a site, specimens may carry both normal and reversed polarities. In most cases however, polarities were the same within one site. In several sites, samples were heavily affected by lightning (e.g. Figures 3.4u and al), evidenced by their high intensities and single-component demagnetization diagrams. Most samples are affected by an overprint, which is likely a present-day field overprint (e.g. Figures 3.4a, n, y, z). Samples taken close to samples that were reset by a lightning strike often show a related

overprint.

We calculated site means from the ChRM directions and virtual geomagnetic pole (VGP) means using Fisher statistics (Fisher 1953). Specimens affected by lightning as well as specimens with odd directions (e.g. N/up) were omitted from further analysis. Additionally, a fixed 45° cut-off was applied on each site to remove outliers. Per locality, the means of the individual sites were plotted and a 45° cut-off was applied to remove divergent sites. The errors in declination ( $\Delta D_x$ ) and inclination ( $\Delta I_x$ ) were calculated separately, following Butler (1992) from the A95 (the 95% cone of confidence of the VGPs). This approach is favored because it describes the directional distributions more realistically: they become increasingly ellipsoidal (elongated) with lower latitudes (Creer et al. 1959, Tauxe and Kent 2004, Deenen et al. 2011).

On most sites, we carried out measurements to determine the anisotropy of magnetic susceptibility (AMS) to assess the presence of a tectonic fabric, and whether formation of a fabric may have influenced the paleomagnetic direction. Even without tectonic deformation, most granites have a magmatic mineral fabric that results from alignment of phenocrysts during intrusion (magmatic foliation), which may be traced through AMS analysis (Denèle et al. 2011). For every locality, we used Jelinek statistics (Jelinek 1981, 1984) for the calculation of the three tensor mean axes.

### 3.3.3 Reliability and statistical treatment

In this study, we solely present data from granite bodies. Because directions obtained from individual sites may have cooled rapidly, they may under-represent paleosecular variation (PSV). For the sampled granite bodies, we do not have information on cooling rates but we may safely assume that on the scale of a locality they are much longer (tens to hundreds of thousands of years) than typical time scales over which paleosecular variation is averaged (thousands of years). We followed the N-dependent reliability criteria for paleomagnetic data of Deenen et al. (2011) which assess whether the statistical values of paleomagnetic data populations can be explained by paleosecular variation alone. These criteria are expressed as a confidence envelope between maximum and minimum values for A95 (A95max and A95min), which are dependent on the number of samples (N). In contrast to the often used criteria of Van der Voo (1990), the criteria provided by Deenen et al. (2011) are therefore specifically determined for each data set.

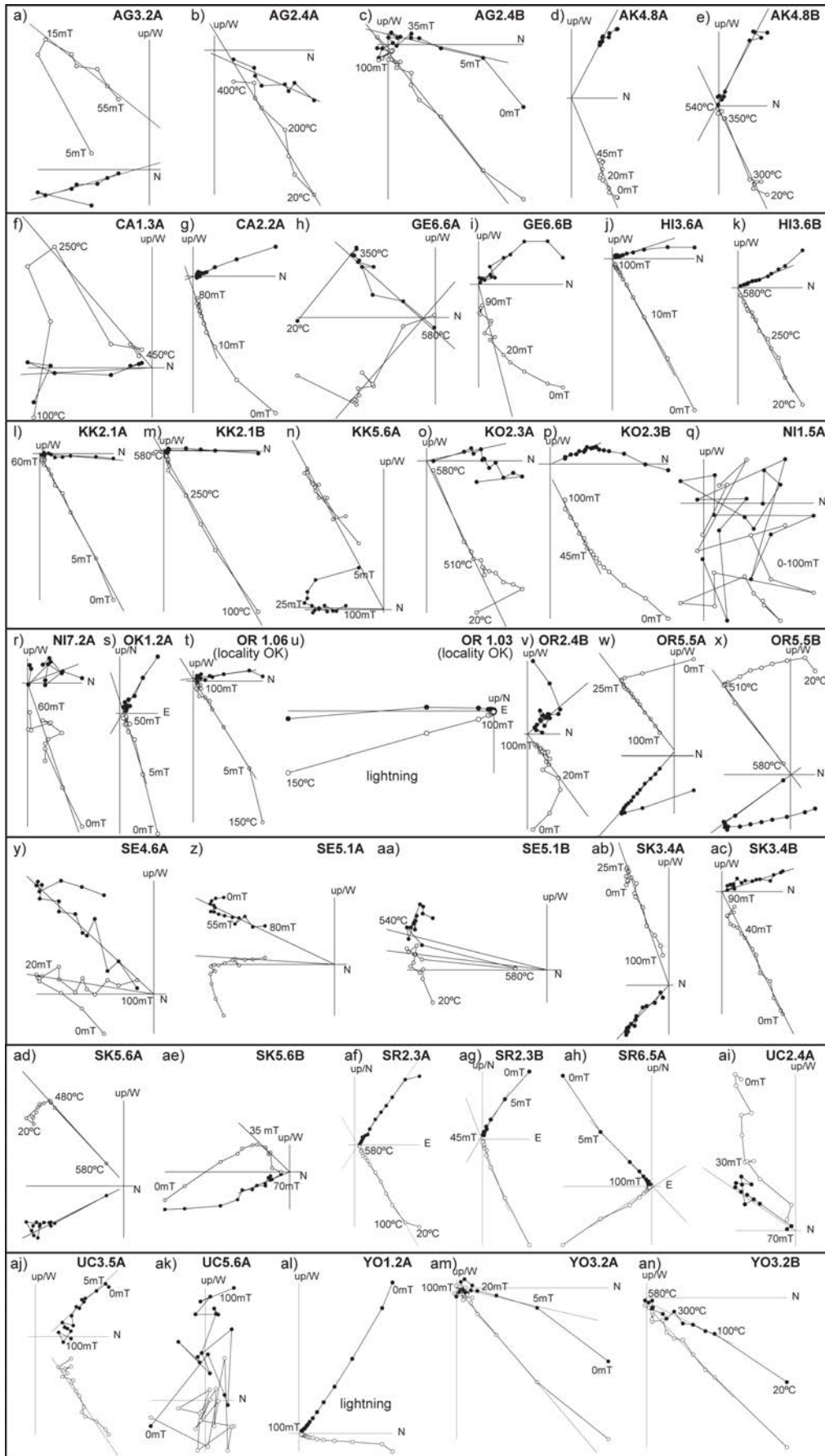


Figure 3.4 Orthogonal vector diagrams (Zijderveld 1967) showing representative demagnetization diagrams for all localities. Closed (open) circles indicate projection on the horizontal (vertical) plane. All diagrams are in a tilt corrected reference frame. Often, both alternating field (steps in milliTesla, mT) and thermal (steps in °C) demagnetization diagrams are shown for two specimens from the same sample to show their similarity.

Therefore, we checked for A95max and A95min values on the locality level (Table 3.2) as a measure of data quality. All our data pass the check, except for KK and KO which have A95 values slightly lower than A95min, and high precision parameters (k values well above 100), indicative of a spot reading of the field.

However, the high quality of the data sets both in terms of demagnetization behavior and the fact that at the site level A95 and k values suggest having recorded PSV, warrant to include these localities into our rotation analysis for the CACC.

### 3.4 Paleomagnetic results

#### 3.4.1 Paleomagnetic rotations

Examples of orthogonal vector diagrams (Zijderveld, 1967) and equal area projections of the ChRM of all localities and sites are displayed Figures 3.4 and 3.5. Details per locality and per site can be found in the Supplementary data and the Supplementary Table. Table 3.2 displays a synthesis of all calculated means and statistics for each locality.

According to the criteria above, 11 localities were accepted for further analysis. The 4 rejected

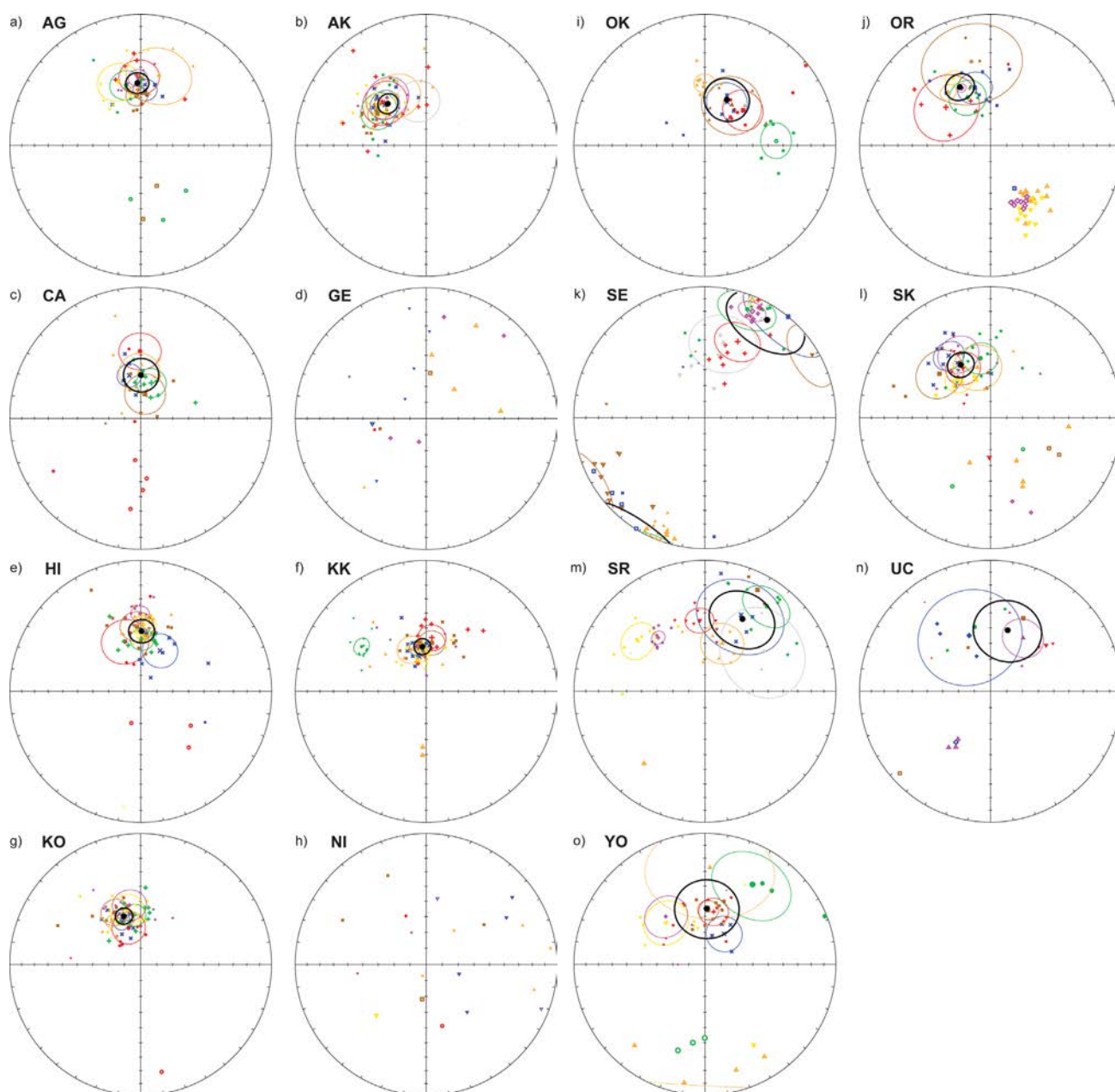


Figure 3.5 Equal area projections of the ChRM directions for all localities and sites (Table 3.2, Supplementary Table). Open (closed) symbols denote projection on upper (lower) hemisphere. Large symbols and circles in corresponding colors represent respectively the mean directions per site and their cone of confidence ( $\alpha_{95}$ ). Black symbols and circles represent respectively the mean direction per locality and their cone of confidence ( $\alpha_{95}$ ). Per site, rejected data points (after application of the fixed  $45^\circ$  cut-off) are displayed with small symbols.

site	N <sub>cores</sub>	N <sub>demag</sub>	N <sub>a</sub>	N <sub>45</sub>	N <sub>t</sub>	N <sub>s</sub>	dec	inc	k	$\sigma_{95}$	K	A95	A95 <sub>min</sub>	A95 <sub>max</sub>	$\lambda$	$\Delta D_x$	$\Delta I_x$	
AG	55	75	55	55	7	7	356.8	50.5	79.2	6.8	54.8	8.2	7.8	24.1	31.2	9.6	9.1	
AK	60	84	76	76	8	8	317.4	54.3	80.1	6.2	41.9	8.7	7.4	22.1	34.8	10.6	8.8	
CA	41	43	40	37	5	5	0.4	62.9	52.1	10.7	31.5	13.8	8.9	29.7	44.3	19.5	11.	2
GE	51	53			7		no averages calculated											
HI	54	79	77	76	7	7	0.8	52.0	62.2	7.7	43.7	9.2	7.8	24.1	32.6	10.9	9.8	
KK	50	93	89	89	7	6	355.0	61.9	172.4	5.1	84.9	7.3	8.3	26.5	43.1	10.0	6.	1
KO	57	81	74	72	7	7	340.8	57.9	135.2	5.2	79.8	6.8	7.8	24.1	38.6	8.7	6.3	
NI	46	46			7		no averages calculated											
OK	41	41	36	33	5	4	25.8	58.1	45.6	13.7	23.8	19.2	9.8	34.2	38.8	25.0	17.	.6
OR	51	75	59	58	7	7	332.2	48.2	50.3	8.6	40.8	9.6	7.8	24.1	29.2	11.0	11.	2
SE	49	71	71	68	7	7	32.5	12.4	9.2	21	14.2	16.6	7.8	24.1	6.3	16.7	32.1	
SK	55	79	66	64	7	7	330.5	51.7	58.5	8	39.5	9.7	7.8	24.1	32.3	11.5	10.4	
SR	64	69	54	53	8	6	27.5	37.7	13.4	19.0	14.5	18.2	8.3	26.5	21.1	19.6	26.	.2
UC	57	57	17	15	7	5	15.7	50.0	15.3	20.2	9.3	26.5	8.9	29.7	30.8	31.3	29.7	
YO	52	76	49	46	7	7	1.9	54.9	10.8	19.2	7.6	23.4	7.8	24.1	35.4	29.2	23.3	
AAB						29	334.0	52.1	37.5	4.4	23.3	5.7	4.4	9.8	32.7	6.7	6.0	
AAB - without AG						22	326.6	51.7	54.4	4.2	36.3	5.2	4.9	11.7	32.3	6.2	5.6	
KKB						25	353.8	58.5	61.5	3.7	37.4	4.8	4.7	10.8	39.2	6.2	4.4	
KKB - without KO						18	358.9	58.4	61.4	4.4	40.7	5.5	5.3	13.3	39.0	7.1	5.0	
YYB						17	29.7	32.6	8.4	13.1	12.4	10.6	5.5	13.8	17.8	11.1	16.5	

Table 3.2 Table displaying all calculated means per locality and their statistical parameters. Ncores= number of sampled cores, Ndemag= number of demagnetized specimens, Na= number of interpreted specimens, N45= number of specimens included in the calculation for the mean ChRM direction after applying the 45° fixed cut-off, Nt= total number of sampled sites at the given locality, Ns= number of sites within a locality on which the statistics are based (see Supplementary data for details), dec= declination, inc= inclination, k= estimate of the precision parameter determined from the ChRM directions, A95= cone of confidence determined from the ChRM directions, K= precision parameter determined from the mean virtual geomagnetic pole directions (VGPs), A95= cone of confidence determined from the mean VGP direction, A95min (A95max)= minimum (maximum) value of the A95 for the given dataset based on (Deenen et al. 2011),  $\lambda$ = paleolatitude,  $\Delta D_x$  ( $\Delta I_x$ )= declination (inclination) error calculated from the A95.

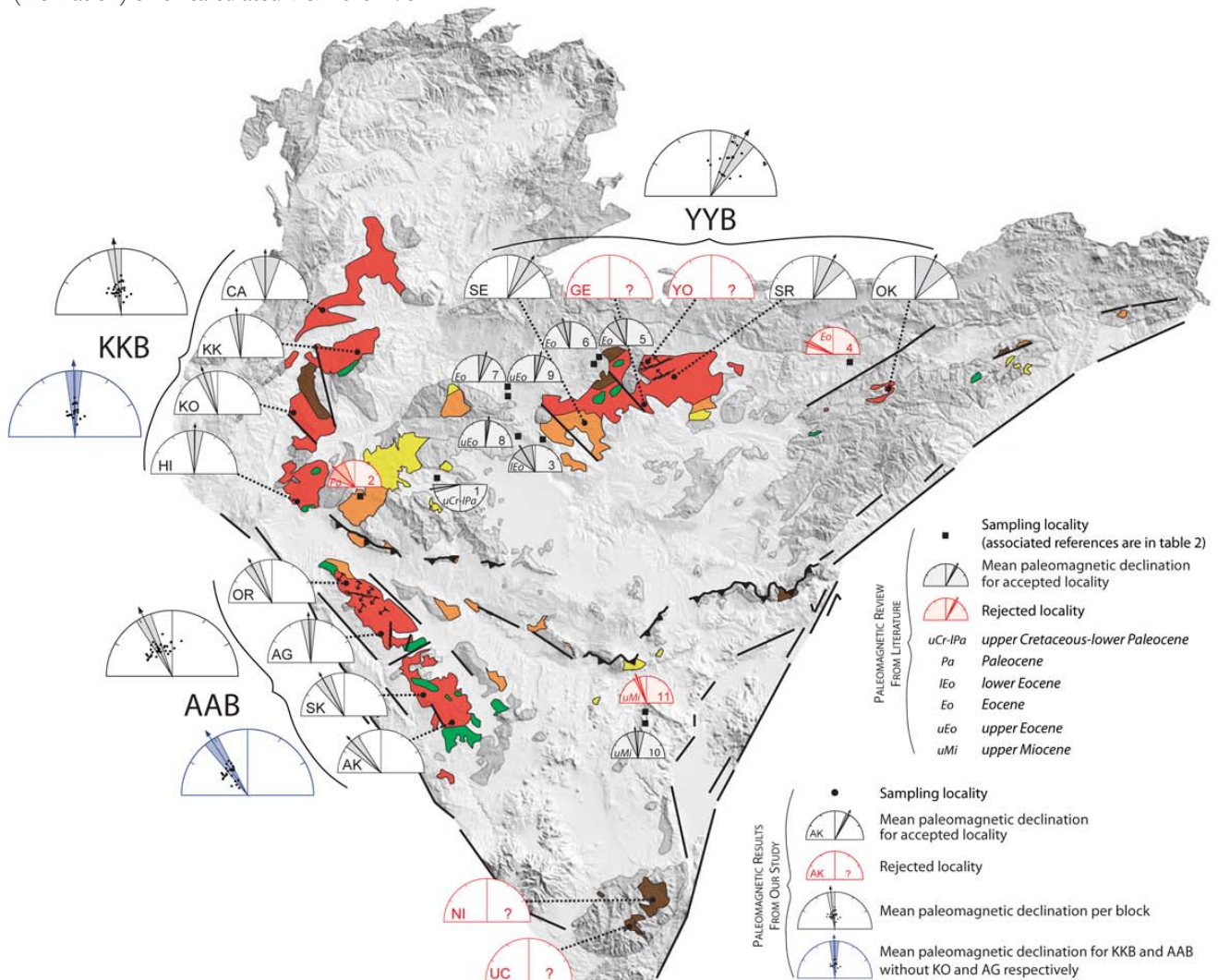


Figure 3.6 Overview of all declinations and their errors ( $\Delta D_x$ ) per locality plotted on the regional geological map. Rejected localities in red. The locality means per block (AAB, KKB and YYB) are indicated, as well as the locality means for KKB and AAB without KO and AG, respectively (in blue). Smaller declination plots represent the reviewed data from literature (Table 3.3).

localities (GE and YO from the Yozgat Batholith, and NI and UC from the Niğde Massif) generally display poor demagnetization diagrams and very scattered ChRM directions per site and per locality (see Supplementary Data). The accepted localities display a distinct pattern of rotation at the scale of the CACC (Figure 3.6). On the basis of this pattern, we distinguished three domains with consistent and similar rotations, that we defined as ‘blocks’ for which we calculated mean rotations by averaging all site means per block (Figure 3.6, Table 3.2):

(1) in the north-east, the three localities (SE, SR and OK) of the Yerköy-Yozgat block (YYB) (i.e. the Yozgat Batholith) show substantial  $29.7^{\circ} \pm 11.1^{\circ}$  clockwise (CW) rotation.

(2) in the north-west, the Kırıkkale-Kaman block (KKB) (i.e. the “NW intrusive belt”) the mean of localities CA, KK, KO and HI does not show a significant rotation:  $6.2^{\circ} \pm 6.2^{\circ}$  counterclockwise (CCW). Locality KO differs from the main tendency of the KKB presenting a significant CCW rotation; the mean rotation of the KKB block without locality KO would be  $1.1^{\circ} \pm 7.1^{\circ}$  CCW.

(3) in the south-west, the Ağaçören-Aksaray block (AAB) (i.e. the AIS) displays a significant counterclockwise (CCW) rotation. The mean rotation of localities OR, AG, SK and AK is  $26.0^{\circ} \pm 6.7^{\circ}$  CCW. Here, the AG locality deviates from the main CCW tendency within the AAB; the mean rotation of the AAB block without locality AG would result in a larger CCW rotation of  $33.4^{\circ} \pm 6.2^{\circ}$ .

### 3.4.2 Comparison to the Apparent Polar Wander (APW) path

Since we sampled plutonic rocks, we have no firm control on the paleohorizontal of the granitoids, and therefore, a possible tilt correction cannot be applied. To check if the calculated inclinations are within a ‘reasonable’ range, we translate the measured inclinations to paleolatitudes, and compare these with paleolatitudes of Eurasia in an age versus latitude plot (Figure 3.7). We calculated the expected paleolatitudes of the Eurasian and African margins at the position of the city of Kırşehir (Figure 3.1) with their error envelopes derived from the A95 values of the Eurasian and

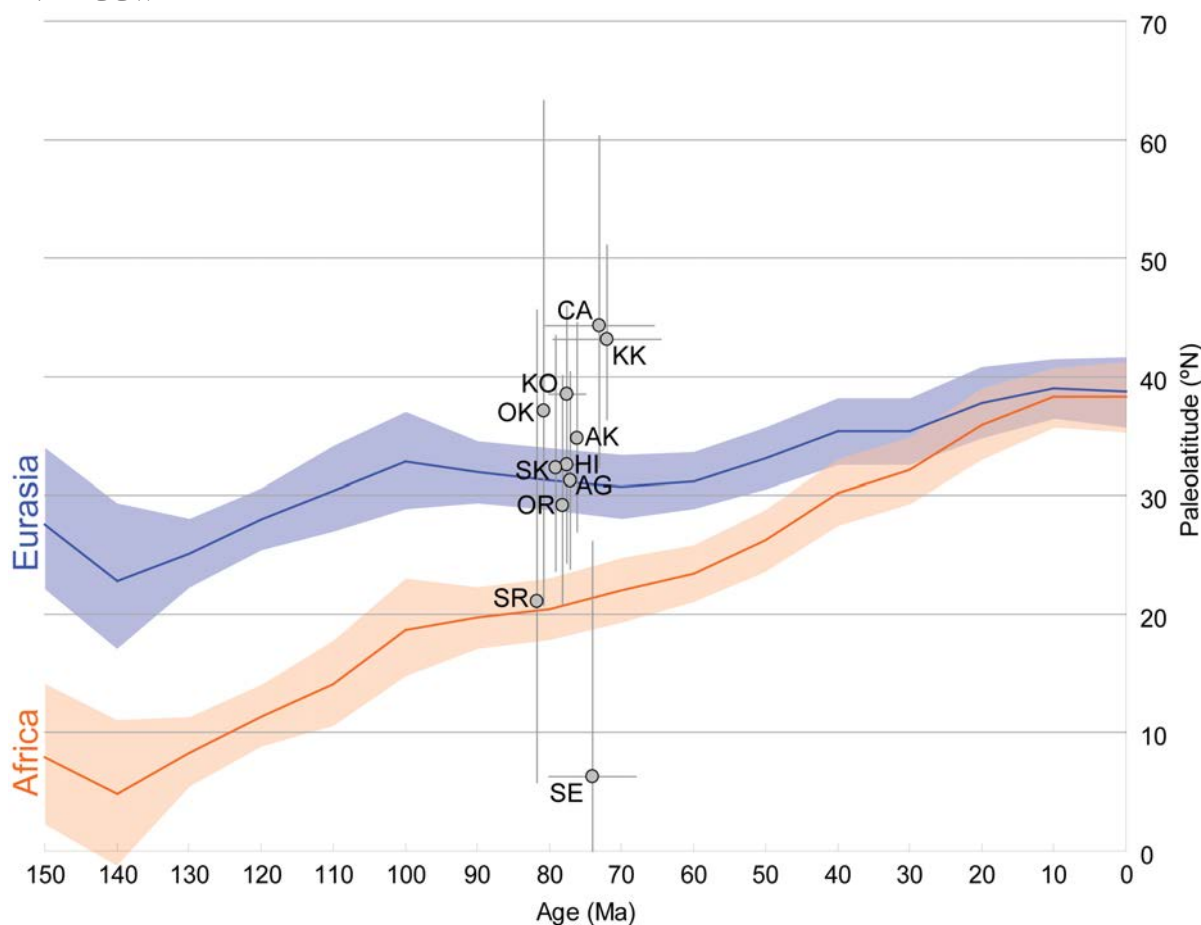


Figure 3.7 Age versus latitude plot showing the curves for Africa and Eurasia calculated from the APW paths (Torsvik et al. 2008) with their  $\Delta\lambda$  error (using the  $\Delta I_x$  calculated from A95, shaded area). Calculated paleolatitudes from the accepted localities, are plotted with their  $\Delta\lambda$  error (calculated from the  $\Delta I_x$ ). The available radioisotopic ages used in the plot are the ones marked with an asterisk in Table 3.1; the choice of the age for the undated granitoids is explained in the paleomagnetic results section. Some ages were slightly shifted for the purpose of better display.

African APW paths (Torsvik et al. 2008). We used the existing cooling ages as presented in Table 3.1 ( $^{40}\text{Ar}/^{39}\text{Ar}$  and K-Ar ages marked by an asterisk). For the localities of which no radiometric ages are available, we used the age from the immediate neighboring plutons (AK $\approx$ AG $\approx$ OR $\approx$ SK, CA $\approx$ KK, HI $\approx$ KO and OK $\approx$ SR). The paleolatitudes presented in Figure 3.7 plot within error on the Eurasian APW path, except for sites KK (too high paleolatitude) and SE (too low). Obviously, the CACC had a Cretaceous position between Eurasia and Africa, and all inclinations should plot somewhere between these APWP's. In addition, given probable late Cretaceous-Paleocene initial collision of the CACC with the Pontides (Kaymakci et al. 2003a, Meijers et al. 2010), the paleolatitude of the CACC was probably closer to Eurasia than to Africa. The inclinations that we obtain are within  $10^\circ$  of the expected inclination, and tilting may be the cause of this slight offset. However, tilts on the order of  $\sim 10^\circ$  at mid-latitude may change the declinations by a few degrees, but are unlikely to cause the pattern we observe.

### 3.4.3 Anisotropy of Magnetic Susceptibility (AMS)

In Figure 3.8, we present the results of AMS measurements for nine of the sampled localities. The AMS tensor shows oblate (HI, KK, OR, SE, SK) and prolate shapes (AG, AK, KO and SR). The orientation of the AMS tensor shows no correlation with the mean ChRM direction (blue stars in Figure 3.8) at a locality, but shows significant variations within each of the three defined blocks (KKB, AAB and YYB) (Figure 3.6). It is interesting to note that the long axis orientations of the prolate ellipsoids of AG and AK (for AAB) and SR (for YYB) seem to correspond approximately with the strike of the mineral stretching lineations reported from discrete ductile shear zones within Ağaçören and Yozgat Batholith (Isik et al. 2008, Isik 2009) (Figure 3.6). In general, however, there is no consistent or clear correspondence between AMS results, rotations and main tectonic directions, which would suggest that the magnetic fabric most likely represents magmatic foliations at the scale of individual plutons.

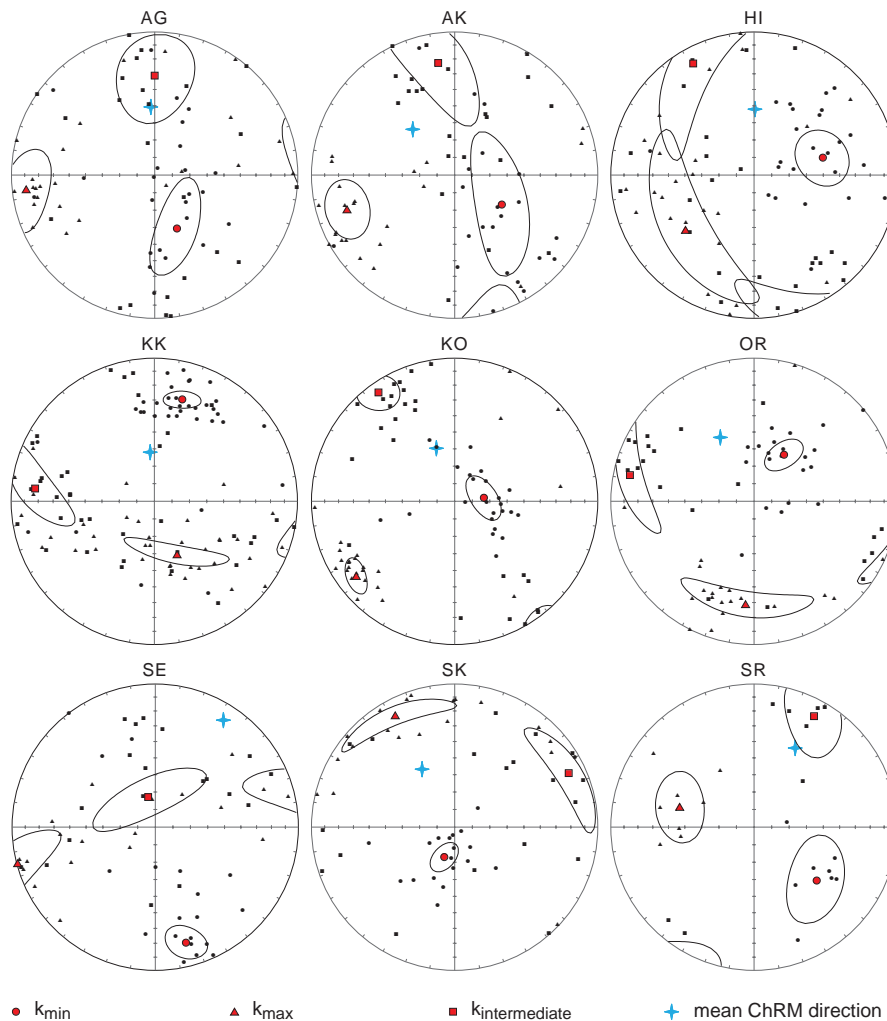


Figure 3.8 Equal area projections of the anisotropy of magnetic susceptibility (AMS) of ten localities. Circle, square and triangle symbols indicate the mean of the tensor mean axes ( $k_{\min}$ = circles,  $k_{\text{int}}$ = squares,  $k_{\max}$ = triangles) and their 95% error ellipses (Jelinek 1981). Stars indicate the ChRM direction of the locality mean.

### 3.4.4 Previous paleomagnetic studies within the CACC: a short review

We aim to reconstruct the original configuration of the CACC and hence we only considered data from the CACC sensu stricto. Data from basins straddling the CACC were not taken into account, because these basins are likely affected by the major faults that define the boundaries of the CACC (e.g. the NAFZ and the Tuz Gölü fault). For the purpose of this study, we reviewed available data from upper Cretaceous to Miocene rocks that postdate the sampled granitoids (Table 3.3). We calculated statistics on virtual geomagnetic poles (VGP's) (K, A95) by averaging all site means to locality means as described in the Paleomagnetic analysis section after applying a 45° cut-off on the sites. From the data collected by Piper et al. (2002) from the Miocene to Pleistocene volcanic fields of Cappadocia (Figure 3.1), we calculated an average for Miocene lavas. For Platzman et al. (1998) we obtained the A95 (and thus ΔDx and ΔIx) by using the Creer transformation (Creer 1962) on the A95. Data sets from magmatic rocks with less than four sites per locality were excluded from further analysis, because paleosecular variation was likely not averaged. This led to exclusion of the Paleocene data from Kissel et al. (2003), the Eocene data from Akdağmadeni from Tatar et al. (1996) and the Miocene data from Platzman et al. (1998). In Figure 3.6, all reviewed data are presented together with the new obtained results from our study. The previous paleomagnetic studies are mainly concentrated in the northern and central part of the CACC. Those studies were performed on material that was deposited/emplaced on top of the outer granitoids of the KKB and YYB. Except for the study on the upper

Cretaceous - Paleocene rocks from Sanver and Ponat [1980] (study 1 in Table 3.3), the existing data suggest no consistent vertical axis rotation pattern in the northern part of the CACC near Yozgat, with both mild westerly and easterly post-Eocene deviations of the declination. The volcanic fields of Cappadocia experienced no significant post-Miocene vertical axis rotation.

### 3.5 Discussion

Paleomagnetic results from fifteen sampled localities belonging to the upper Cretaceous outer granitoids of the CACC show generally good results. Of the fifteen sampled localities, four localities have been rejected for further analysis because of inconsistent demagnetization behaviour, resulting in very scattered ChRM directions per site and per locality. Those four localities belong to the Niğde Massif (NI and UC) and the Yozgat Batholith (GE and YO).

It has been reported that some part of the Uçkapılı two-mica granite of the Niğde massif is considered as a late-kinematic intrusion as it locally presents a clear ductile fabric (Gautier et al. 2002). We also observed this feature in the field, and even though we aimed at sampling the most preserved bodies, it seems that the ductile fabric affected the entire granitoid and therefore deteriorated the paleomagnetic signal. As a consequence, we do not have any rotational constraints from the southernmost batholith of the CACC.

In the Yozgat Batholith (localities GE and YO), a dense network of deformation has affected the magmatic rocks (Erlor and Göncüoğlu 1996, Isik et al. 2008). The presence of major brittle faults, like the NW-SE trending faults in the vicinity of the GE locality (see Figure 3.2) likely disrupted

Description	lat	lon	Age	Dec	Inc	λ	N	N <sub>45</sub>	k	α <sub>95</sub>	K	A95	ΔDx	ΔIx	Reference
1 Volcanics, Kaman	39.2	33.9	upper Cret.-Pal. <sup>1</sup>	261.5	28.5	15.2	16	12	24.0	9.0	27.8	8.4	8.7	13.9	Sanver and Ponat (1980)
2 Volcanics and intrusives, Kaman	39.2	33.9	Paleocene	312.9	48.8	29.4	3	3	60.4	16.0	36.4	20.7	24.0	24.1	Kissel et al. (2003)
3 Volcanics, Kirsehir	39.5	34.5	lower Eocene <sup>1</sup>	148.7	-54.6	35.2	10	8	11.3	17.2	8.6	20.1	24.8	20.1	Sanver and Ponat (1980)
4 Volcanics, Akdagmadeni	39.7	35.8	Eocene	293.9	43.5	25.4	3	3	573.0	5.2	429.4	6.0	6.6	7.7	Tatar et al. (1996)
5 Volcanics, Yozgat	39.8	34.7	Eocene	158.4	-46.5	27.8	5	5	17.9	18.6	14.6	20.7	23.6	25.1	Tatar et al. (1996)
6 Volcanics and sediments, Yozgat	39.8	34.4	Eocene	166.9	-12.5	6.3	7	7	8.0	22.8	15.5	15.8	15.9	30.6	Kissel et al. (2003)
7 Volcanics, Cicekdagi	39.6	34.4	Eocene	194.3	-61.0	42.0	6	6	77.7	7.6	37.7	11.1	15.0	9.4	Gülyüz et al. (submitted)
8 Sediments, Cicekdagi	39.5	34.5	upper Eocene	6.7	38.1	21.4	88	77	17.3	4.0	16.3	4.1	4.4	5.9	Gülyüz et al. (submitted)
9 Sediments, Cicekdagi	39.7	34.4	upper Eocene	13.0	19.3	9.9	17	15	13.7	10.7	14.6	10.4	10.6	19.1	Gülyüz et al. (submitted)
10 Ignimbrites, Cappadocia	38.6	34.8	upper Miocene <sup>2</sup>	353.7	52.0	32.6	5	5	39.0	12.4	23.0	16.3	19.5	17.4	Piper et al. (2002)
11 Volcanics, Nevsehir	38.7	34.8	upper Miocene <sup>3</sup>	159.0	-40.0	22.8	1	1	176.0	5.8	178.3	5.7	6.2	7.9	Platzman et al. (1998)

For data sets 8 and 9 the number of specimens are indicated. For all other data sets N and N<sub>45</sub> refer to the number of sites within a locality.

Studies that were accepted for further analysis are indicated in **bold**.

<sup>1</sup>ages poorly determined, <sup>2</sup>mean was determined from Miocene data, <sup>3</sup>site N6, consists of only one flow.

Table 3.3 Table showing all reviewed paleomagnetic data from previous studies. Description= rock type plus the study location, plus the number we assigned to the study, lat (lon)= latitude (longitude) of the study location, Age= age of the sampled rocks, Dec (Inc)= declination (inclination) of the paleomagnetic results, λ= corresponding paleolatitude, N= number of specimens, N<sub>45</sub>= number of specimens after applying the 45° fixed cut-off, k= estimate of the precision parameter determined from the ChRM directions, α<sub>95</sub>= cone of confidence determined from the ChRM directions, K= precision parameter determined from the mean virtual geomagnetic pole directions (VGPs), A95= cone of confidence determined from the mean VGP direction, ΔDx (ΔIx)= declination (inclination) error calculated from the A95.

the structural coherence of the rock-unit and caused alteration and weathering that affected the magnetic signal. Since brittle faults are also present close to the sampling localities KO and AG (Figure 3.2), the same arguments may apply to explain why the results of these localities (slightly) differ from the main tendency of the KKB and the AAB.

### 3.5.1 Structures accommodating differential block rotations within the CACC.

Based on the rotation pattern of the eleven accepted localities, we subdivide the CACC into three distinctive blocks with consistent declinations. Note that these blocks also coincide with the magmatic suites. (1) the Yerköy-Yozgat block (YYB) in the northeast, that records  $\sim 30^\circ$  CW rotation, (2) the Kırıkkale-Kaman block (KKB) in the northwest, that shows no significant rotation and (3) the Ağaçören-Aksaray block (AAB) in the southwest, that shows  $\sim 35^\circ$  CCW rotation. These blocks coincide with the Yozgat Batholith, the “NW intrusive belt” and the Ağaçören Intrusive Suite, respectively. As each of those  $\sim 100$  km long batholiths records independent rotations, they can be described as paleomagnetically rigid structural entities during their post-emplacement tectonic evolution. In other words, they may be dissected by faults, but they are coherent in terms of vertical axis rotations. The boundaries of each of the blocks or batholiths appear to be “truncated” (see Figure 3.9a) and separated by narrow Eocene basins as the Çiçekdağı and Büyükkısla basins (Figure 3.1). Within those basins, intense compressional deformation and significant horizontal shortening have been recently reported (Advokaat et al. submitted, Gülyüz et al. submitted). Considering the rotational pattern of the three blocks and the geology of the CACC, we propose the existence of two major transpressional strike-slip fault zones that have played a role in accommodating the vertical axis rotations and associated displacements from a stage where all the granitoids were linked and aligned (Figure 3.9). Those proposed fault zones can also be recognized in the topography, as they form narrow depressions with an average topographic drop of a few hundreds of meters below the average plateau elevation (Figure 3.1). We define the two strike-slip fault zones as following:

(1) We postulate that the WNW-ESE trending Hirfanlar-Hacibektaş lineament (Figure 3.9) represents the left-lateral transpressional Hirfanlar-Hacibektaş Fault Zone (HHFZ), which accommodated  $\sim 35^\circ$  of counterclockwise rotation between the KKB and AAB (Figures 3.1 and 3.9a). The lateral sinistral displacement estimated by the

offset of the outer magmatic belt is approximately 15 km (see schematic restorations in Figures 3.9d-e). However, a relative rotation of  $35^\circ$  between KKB and AAB would also lead to a  $\sim$ N-S shortening component. This is consistent with the presence of the previously defined NNE-vergent Savcılı thrust zone which may have accommodated some of the convergence between KKB and AAB. In addition, the fold-and-thrust belt that accommodated the  $\sim 20$ - $30$  km of shortening calculated for the Ayhan basin witnesses the intense compressional regime which dominated the region (Advokaat et al. submitted).

(2) We postulate that the NW-SE trending Delice-Kozaklı lineament (Figure 3.9) represents the right-lateral transpressional Delice-Kozaklı Fault Zone (DKFZ), which accommodated  $\sim 30^\circ$  of clockwise rotation between the KKB and YYB. Along the DKFZ, the lateral dextral displacement estimated by the offset of the outer magmatic belt is as much as  $\sim 90$  km. Supporting the presence of the DKFZ, a fold and thrust belt where Eocene limestones and younger detrital rocks are tilted in vertical positions, has recently been identified between Mahmutlu and Yerköy (Figure 3.1) (Genç and Yürür 2010). In addition, a network of NW-SE trending brittle faults has been reported in the western part of the Yozgat Batholith (Erler and Göncüoğlu 1996). Their orientations seem to coincide with the proposed strike of the DKFZ. Indirectly, the relatively high and low inclinations (with respect to the age versus latitude curve of Eurasia in Figure 3.7) of the localities CA and KK (northern tip of the KKB) and SE (western border of the YYB) may be linked to the deformation associated with the nearby right lateral DKFZ.

In Figure 3.9, we illustrate various possible restorations for the central Anatolian granitoids and magmatic supersuites, based on the observed rotation patterns. We outlined the outer granitoids from the AAB, KKB and YYB and estimated the orientation of the long axis from the batholiths (Figure 3.9a). We note that the orientations of their long axis coincide with the orientations of alignment of the highest peaks from the batholiths. The center of each block has been chosen as the rotation point for the restorations (Figure 3.9). Four possible original configurations of the CACC are presented: reconstructions including and excluding the deviating AG and KO localities (for AAB and KKB, respectively) and reconstructions including and excluding movement along the DKFZ and HHFZ (Figure 3.9). In their restored configurations, the three elongated magmatic belts appear in a similar, N to NNE orientation and become approximately aligned into a single entity by motion along the DKFZ and HHFZ as

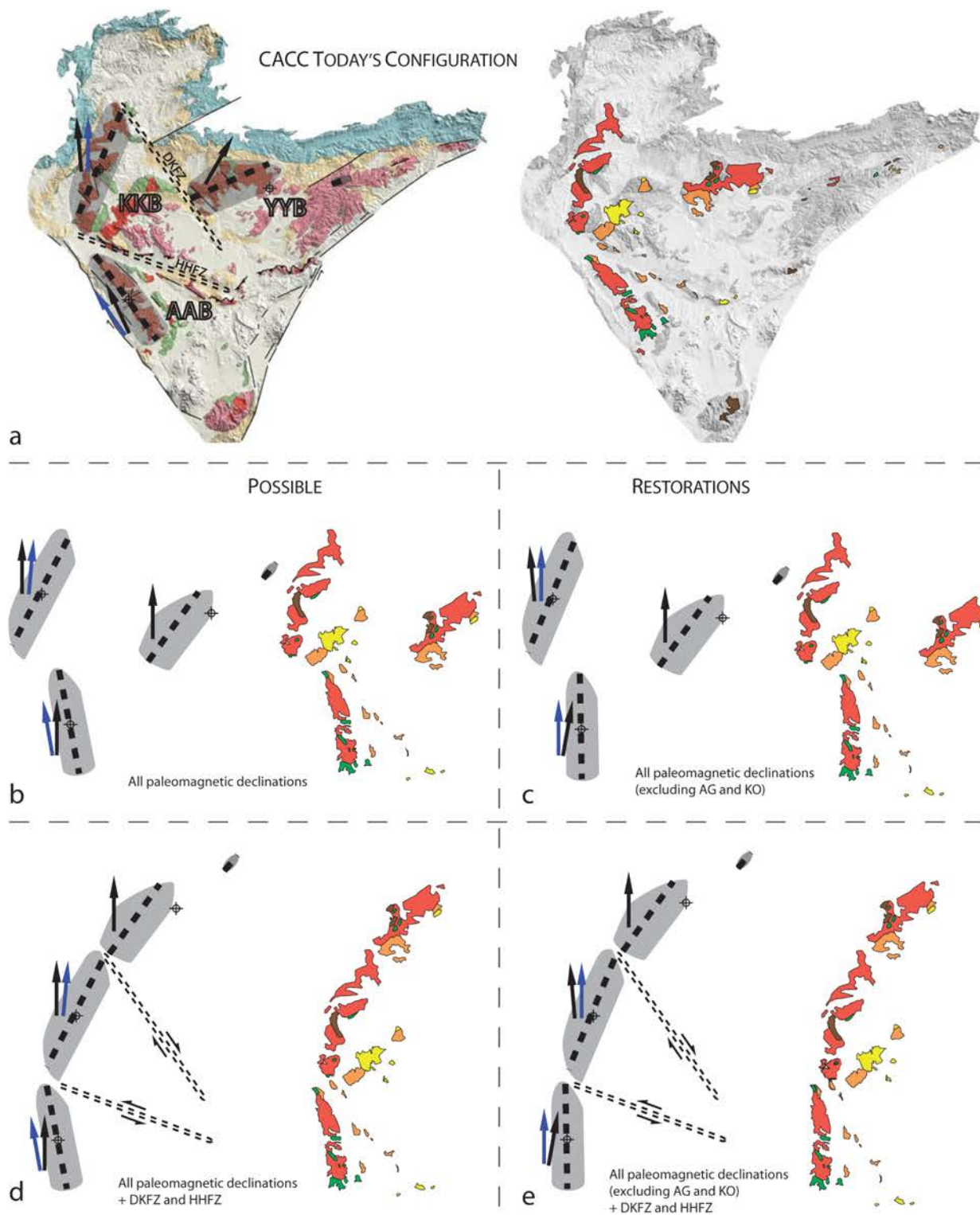


*Figure 3.9* Various possible restoration scenarios of the late Cretaceous central Anatolian granitoids and magmatic Supersuites based on their rotations: a) present-day configuration of the CACC. To the left, simplified geological map of the CACC, similar to what is presented in Figure 3.1. The grey domains represent the areas covered by the outer granitoids from the AAB, KKB and YYB; the dark dashed lines indicate the orientation of the long axis of the ellipsoid-like shaped batholiths. The black arrows indicate the mean declination per block. The blue arrows indicate the mean declination per block without taking AG and KO into account. In each block, the cross marks its center and the rotation pole we use for the restorations. The two elongated dashed zones mark the possible trace of the dextral Kozaklı-Delice Fault Zone (DKFZ) and the sinistral Hırfanlar-Hacıbektas Fault Zone (HHFZ). In the right, a background map of the CACC with the distribution of the main central Anatolian magmatic supersuites, similar to what is presented in Figure 3.2. (b,c,d and e) Different possible restorations of the block rotations illustrated for the elongate-shaped granitoids (to the left), and for the whole magmatic supersuites (to the right): b) for all mean declinations per block, with the absence of major strike-slip fault zones, c) idem excluding AG and KO, d) for all mean declinations per block, with the presence and motion along the two major strike-slip fault zones, and e) idem excluding AG and KO.

described above. We infer that this configuration is probably the pre-rotational one, because the magmatic belts of granite, monzonite and syenite each align together. In the restored configuration, the granites are all concentrated on the western side of the NNE-SSW elongated structure, while monzonites and syenites occur consistently on the eastern side (Figure 3.10a).

The other important implication of a NNE-SSW-oriented linear geometry of the CACC is that the progressive northward collision of the CACC with the central Pontides resulted into the break-up of the elongated structure into three distinctive domains. In the restored configuration, the YYB represents the northernmost part of the CACC and therefore would be the first to collide with the accretionary prism of the IAESZ (Figure 3.10b).

In the speculative scenario presented in Figure 3.10, we propose that, following frontal collision, the YYB underthrusts below the IAESZ, and resisted to the ongoing convergence. As a consequence, the YYB likely rotated counterclockwise, while the KKB extrudes toward the north-west, “pushing

away” the IAESZ and creating the Omega shape of the Çankırı basin (Figures 3.10c-d). Together with the relative motion between the KKB and AAB, those deformations would imply a total of 25% N-S shortening of the CACC (Figure 3.10d).

### 3.5.2 Timing of rotations

The rotations must postdate granitoid intrusion, and cooling to below the curie temperature of magnetite, the main dominant carrier of the magnetization.

Most localities recorded both normal and reverse paleomagnetic field directions (see Figure 3.5). Most sites have a single polarity, but we also frequently observed normal and reversed polarities within a single site. At locality SK, we report the unique record of a change from reversed to normal polarity within the same core: the deeper part of the core (A) recorded a reversed polarity, whereas the shallow part (B) recorded a normal polarity (SK3.4A and B in Figures 3.4ab-ac) (Figure 3.11). This indicates that the Earth’s magnetic field

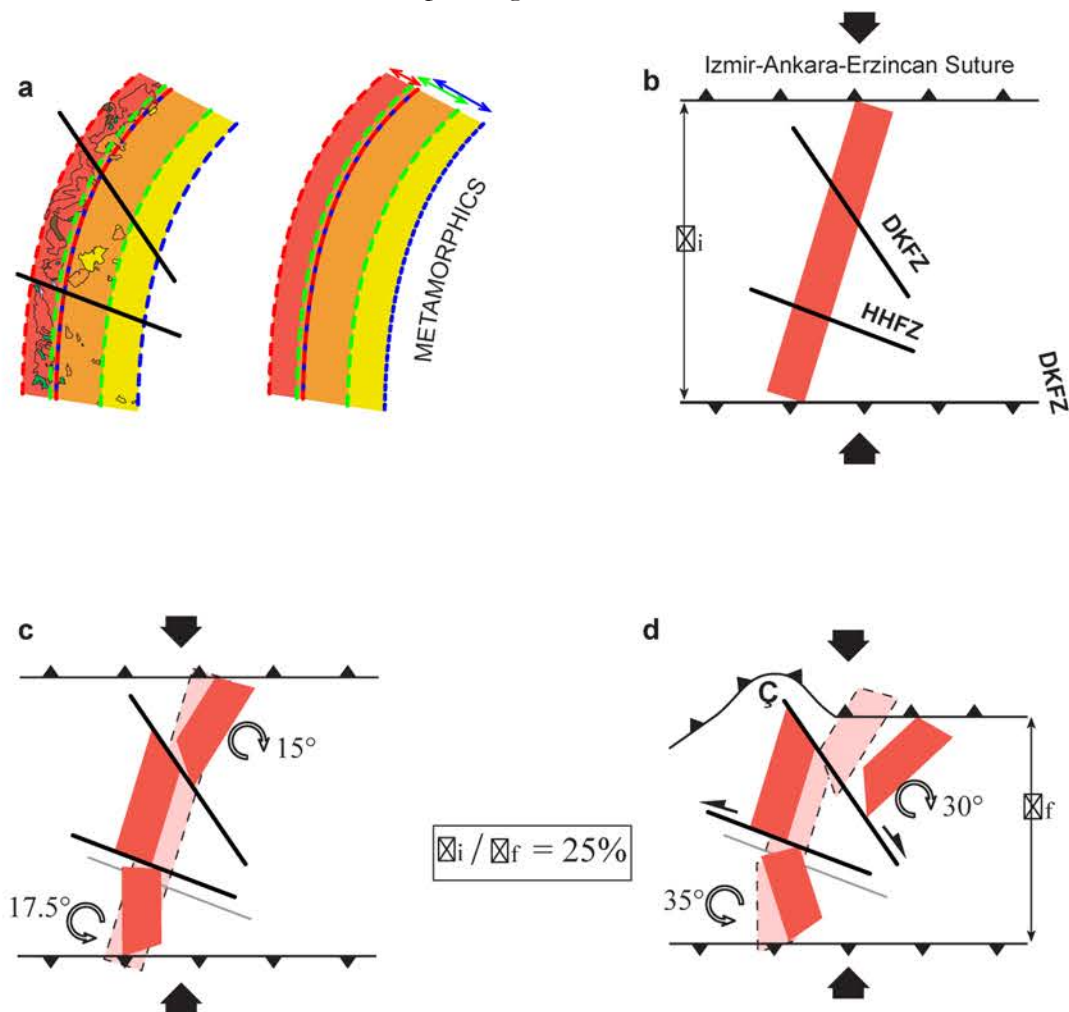


Figure 3.10 Cartoons illustrating simplified scenario for the rotational evolution of the CACC. a) arrangement of supersuites of CACC after back rotation and translation along the DKFZ (90 km) and HHFZ (15 km), b) initial configuration of CACC, c) configuration at half-way rotation; Note that the rotation of YYB and AAB are not necessarily contemporaneous, d) Present configuration. Ç: Çankırı Basin.

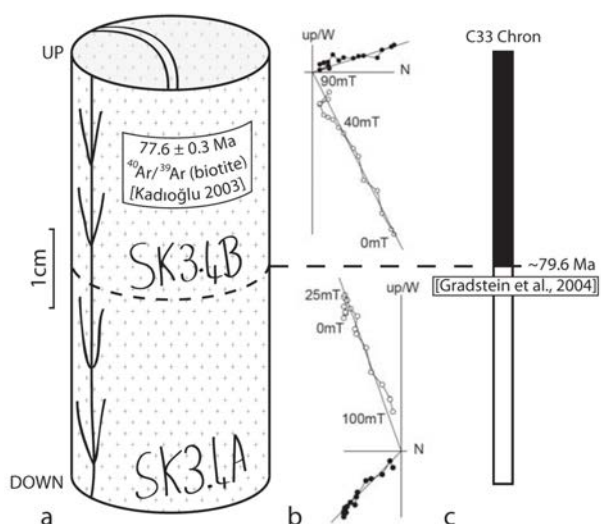


Figure 3.11 Paleomagnetic characteristics of the SK3.4 sample: a) schematic representation of the SK3.4 core with A and B specimens. The  $^{40}\text{Ar}/^{39}\text{Ar}$  age on biotites from the same granitoid is also reported (Kadioğlu et al. 2003); b) Orthogonal vector diagrams of demagnetization for both SK3.4A and SK3.4B specimens; c) Representation of the Campanian C33 Chron with its switch from reversed to normal polarity at  $\sim 79.6$  Ma (Gradstein et al. 2004).

switched from reversed to normal polarity during cooling of the granite. At the exact location of locality SK, Kadioğlu et al. (2003) performed  $^{40}\text{Ar}/^{39}\text{Ar}$  dating on biotites from the granitoid and found a cooling age (below  $\sim 350^\circ\text{C}$ ) of  $77.6 \pm 0.3$  Ma (Table 3.1). The recorded reversal may correspond to the reversed to normal polarity change at Chron C33 (Campanian) at  $\sim 79.6$  Ma (Gradstein et al. 2004) (Figure 3.11), which would imply that the magnetization was acquired earlier at a higher temperature, e.g. close to the Curie temperature of magnetite ( $\sim 580^\circ\text{C}$ ).

The sparse existing paleomagnetic data from the Eocene and Miocene volcanic and sedimentary cover rocks of the southern and northern CACC do not seem to present any significant and regionally consistent rotation (Figure 3.6). This may imply that the relative KKB/YYB rotation predates the deposition of the Eocene and younger cover rocks, but to confirm and refine the timing of block rotations in central Anatolia, an extended sampling of Eocene and younger rock units is needed and will be part of future work. However, we are unable to accurately constrain the timing of relative rotation between the KKB and AAB because there are no available paleomagnetic data from a Paleogene age. Recently, the compressional deformation described in the Büyükkısla basin revealed a post-Lutetian shortening, which may have accommodated a considerable part of the KKB/AAB rotation.

At a larger scale, we concur with Görür et al. 1984, that the internal deformation and vertical

axis rotations within the CACC most likely relate to the collisional processes between the CACC and the Pontides. This scenario is also in good agreement with the recently established latest Cretaceous to earliest Paleocene inception of oroclinal bending of the central Pontides, as the CACC is located exactly south of the apex of the orocline (Kaymakci et al. 2003a, Meijers et al. 2010). It seems therefore likely that the rotations and compression of central Anatolia occurred throughout the Paleocene and Eocene.

Apart from timing and mechanism of block rotations, the restored configuration in which the late Cretaceous geometry of the CACC aligns the various magmatic supersuites (Figures 3.9 and 3.10), suggests that the tectonic setting responsible for the central Anatolian magmatism created a NNE-SSW oriented, linear plutonic belt of  $\sim 300 \times 50\text{km}$  producing magmas for a period of  $\sim 20$  Myr, and which spatially and compositionally evolved through time (from calc-alkaline silica-rich magmas in the west to alkaline silica-poor magmas in the east). Taking also the geochemistry into consideration, which revealed that the granite and monzonite magmas derived from a modified and metasomatized mantle source (İlbeyli 2005, Kadioğlu et al. 2006), it seems likely that the central Anatolian magmatism occurred above an active subduction zone.

The paleomagnetic data presented in this chapter have important implications for the evolution of the region, especially concerning the geodynamic and tectonic evolution of central Turkey within a major convergent setting, as the present geometry of the CACC does not seem to be representative of its Cretaceous configuration.

### 3.6 Conclusion

Our new paleomagnetic results from upper Cretaceous granitoids of central Anatolia show evidence for significant post-emplacment rotations. Three domains each presenting a consistent rotational pattern have been distinguished:

- (1) the Yerköy-Yozgat block (YYB) in the north-east recording  $\sim 30^\circ$  CW rotation,
  - (2) the Kırıkkale-Kaman block (KKB) in the north-west showing no significant rotation and
  - (3) the Ağaören-Aksaray block (AAB) in the south-west recording  $\sim 35^\circ$  CCW rotation.
- We propose that these blocks were separated from each other by two transpressional strike-slip fault zones: the sinistral Hirfanlar-Hacibektaş Fault Zone (HHFZ), and the dextral Delice-Kozaklı Fault Zone (DKFZ), which accommodated both rotations and translations of the blocks. Based on previous paleomagnetic

data and the recently established latest Cretaceous to earliest Paleocene oroclinal bending scenario of the central Pontides, it seems likely that the rotation and internal deformation in the CACC occurred throughout most of the Paleocene-Eocene. The most important outcome of this study is the restored original configuration of the CACC, showing that the three blocks were largely aligned in a N-NNE orientation at an early stage of their history. This bears important implications on tectonic reconstructions and evolutionary models of central Turkey because most of the actual models consider the present geometry of the CACC as original.

### Acknowledgements

The authors would like to thank Pınar Ertepinar and Murat Özkaptan for their help during the sampling in the field. Merijn de Block, Annique van der Boon, Lydian Boschman, Jort Koopmans, Matthijs Kroon, Roeland Nieboer, Katrien van Oversteeg, Joost Roholl and Anna van Yperen, Msc students from Utrecht University, are also thanked for their help for additional demagnetization and AMS measurements they performed during the 2011 Paleomagnetism course at Fort Hoofddijk. The help and technical support of Mark Dekkers and Tom Mullender is highly appreciated.

This work was financially supported by the Netherlands Research Centre for Integrated Solid Earth Sciences (ISES), the Netherlands Organisation for Scientific Research (NWO) and the DARIUS Programme.

### -- Supplementary data

Initial intensities of samples affected by lightning were not included in the description of the localities. An overview of all locality statistics can be found in Table 3.2. An overview of all site statistics is given in the Supplementary Table.

#### AG

At locality AG, 55 cores were sampled over seven sites. Initial intensities of site AG typically range 3.5-80 mA/m. In total, 65 specimens were demagnetized, out of which seven specimens thermally. AF and TH demagnetization show similar results (Figures 3.4a and 3.4c). Nine samples show reversed polarities (twelve specimens). In most specimens, a gyroremanent magnetization

(GRM) develops after  $\sim 45$  mT during AF demagnetization. The mean ChRM direction ( $N_s=7$ ) is:  $D=356.8^\circ$ ,  $I=50.5^\circ$  (Table 3.2, Figure 3.5a).

#### AK

We sampled 60 cores over seven sites at locality AK. Initial intensities range typically 0.1-4.5 mA/m. From the 84 demagnetized specimens, seven specimens were demagnetized thermally. AF and TH demagnetization show similar results (Figures 3.4d-e). In the majority of the specimens, a GRM starts to develop from  $\sim 30$ -40 mT during AF demagnetization. The mean ChRM direction ( $N_s=8$ ) is:  $D=317.4^\circ$ ,  $I=54.3^\circ$  (Table 3.2, Figure 3.5b).

#### CA

At locality CA, 41 samples were collected from five sites. Initial intensities range 10-800 mA/m. From the 43 demagnetized specimens, five specimens were TH demagnetized. ChRM directions of AF and TH demagnetization resemble. Six samples have a reversed polarity. In most AF demagnetized specimens, a GRM forms from  $\sim 50$  mT onward. The mean ChRM direction of locality CA ( $N_s=5$ ) is:  $D=0.4^\circ$ ,  $I=62.9^\circ$  (Table 3.2, Figure 3.5c).

#### GE

At locality GE, we collected 51 cores from seven sites. Initial intensities range 0.3-250 mA/m. From the 53 demagnetized specimens, seven specimens were demagnetized thermally. Nearly all specimens show very erratic behavior (as for e.g. NI1.5A, see Figure 3.4q), and TH and AF demagnetization on the same sample gave often very different results (e.g. Figure 3.4h-i). Mean ChRM directions per site are very scattered (see Supplementary Table and Figure 3.5d) and often showed impossible directions (e.g. N/up). No mean ChRM direction could be calculated.

#### HI

Locality HI comprises seven sites and 54 cores. Initial intensities range 0.1-1 A/m. Seven specimens were demagnetized thermally on a total of 80 demagnetized specimens. AF and TH demagnetization give similar results (Figure 3.4j-k). Four samples have reversed polarities. In many samples, a GRM starts to develop from  $\sim 40$  mT onward during AF demagnetization. The mean ChRM at locality HI ( $N_s=7$ ) is:  $D=0.8^\circ$ ,  $I=52.0^\circ$  (Table 3.2, Figure 3.5e).

#### KK

Locality KK comprises 7 sites with a total of 50 cores. Initial intensities range 1-150 mA/m. Seven

specimens were demagnetized thermally on a total of 93 demagnetized specimens. TH and AF demagnetization show similar results (Figures 3.4l-m). One sample (two specimens) shows a reversed polarity (Figure 3.4n). For one sample (two specimens) we used the great-circle approach to determine the directions. In many samples, a GRM starts to develop from ~40 mT onward during AF demagnetization. For the two specimens from sample KK5.5 we used the great-circle approach. One site (KK3) has a very different ChRM direction than the other six sites (Figure 3.5f), therefore we decided to reject for calculation of the mean ChRM direction. The mean ChRM at locality KK (Ns= 6) is:  $D= 355.0^\circ$ ,  $I= 61.9^\circ$ . The low A95 value ( $7.3^\circ$ ), which is lower than the A95min ( $8.3^\circ$ ) possibly implies that we did not entirely average out secular variation. The calculated paleolatitude is very similar to the present-day geocentric axial dipole field at the locality ( $59.0^\circ$ ), which might suggest a remagnetization of the rocks. However, we cannot correct for tilt of the granites (possibly resulting in too steep inclinations) and the rotation of locality KK is very similar to localities in this part of CACC. Furthermore, the A95 is only slightly lower than the A95min, and therefore we argue that the ChRM directions of site KK are of primary origin.

#### KO

Locality KO comprises seven sites and 57 samples. Seven specimens were demagnetized thermally, 74 using AF demagnetization. TH and AF demagnetization show similar results (Figures 3.4o-p). Initial intensities range 50-600 mA/m. One sample shows a reversed polarity. A GRM starts to develop from ~50 mT onward in many samples during AF demagnetization. The mean ChRM of locality KO (Ns= 7) is:  $D= 340.8^\circ$ ,  $I= 57.9^\circ$ . The A95 value ( $6.8^\circ$ ) of the locality is lower than the A95min ( $7.8^\circ$ ). This could possibly indicate that we did not fully cover secular variation. Its calculated paleolatitude is within error in agreement with the Eurasian age versus latitude curve that was derived from the APW path [Torsvik et al. 2008]. Because the A95 is only slightly lower than the A95min, we consider the ChRM directions of primary origin.

#### NI

At locality NI, we sampled seven sites with a total of 51 samples. All 46 specimens were AF demagnetized (Figures 3.4q-r). Initial intensities range ~50-6000  $\mu$ A/m. Most specimens give very erratic results upon demagnetization. Results per site are very scattered and very different in between sites (Figure 3.5h). Because of the poor quality of the demagnetization diagrams, the little

coherence within and between the sites and the low number of interpreted ChRM directions (see Supplementary Table and Figure 3.5h), we did not calculate a mean ChRM direction.

#### OK

At locality OK, four sites were drilled and those were combined with site OM1. In total the site consists of 41 samples. Initial intensities range ~80-400 mA/m. All 41 specimens were AF demagnetized (Figure 3.4s-u). A GRM starts to develop upon AF demagnetization from 20-30 mT. Four of the five sites show similar ChRM's and by applying the  $45^\circ$  cut-off, one site (OK3) is being removed for the calculation of the mean ChRM. Site OK3 displays directions that are probably resulting from reversed directions that were later overprinted. Unfortunately, we could not apply a great-circle approach due to the absence of setpoints. The mean ChRM direction of locality OK (Ns= 4) is:  $D= 25.8^\circ$ ,  $I= 58.1^\circ$  (Table 3.2, Figure 3.5i).

#### OR

Locality OR comprises seven sites, with a number of 75 samples. Six specimens were demagnetized thermally and the remaining 69 specimens using AF demagnetization (Figures 3.4v-x). AF and TH demagnetization show similar results (Figures 3.4w-x). Initial intensities range 0.7-2000 mA/m. Sites OR5, OR6 and OR7 and one sample (one specimen) from site OR2 yields a reversed magnetic polarity (Figures 3.5j). In specimens from sites OR1-4 a GRM starts to develop from ~40 mT upon AF demagnetization (Figure 3.5j). A GRM is only present in exceptional cases in OR5, OR6 and OR7. Most samples from site OR4 are affected by lightning. The mean ChRM direction calculated (Ns= 7) is:  $D= 332.2^\circ$ ,  $I= 48.2^\circ$  (Table 3.2, Figure 3.5j).

#### SE

Seven sites with a total of 49 cores were drilled at locality SE. Six specimens were demagnetized thermally and 65 specimens using AF demagnetization (Figures 3.4y-aa). AF and TH demagnetization give similar results (Figures 3.4z-aa). Initial intensities range ~1-60 mA/m. Many demagnetization diagrams are affected by a GRM upon AF demagnetization from ~30-40 mT. The inclination in most specimens of all seven sites is very shallow, and therefore N/up as well as S/down directions often occur. All sites however, are internally consistent and consistent within the locality. The mean ChRM direction calculated from site SE (Ns= 7) is:  $D= 32.5^\circ$ ,  $I= 12.4^\circ$  (Table 3.2, Figure 3.5k).

### SK

Seven sites with a total number of 55 cores were drilled at locality SK. Seven specimens were TH demagnetized and the remaining 72 specimens were AF demagnetized (Figures 3.4ab-ae). AF and TH demagnetization do not always give the same results. Initial intensities range ~50-1500  $\mu\text{A}/\text{m}$ . In sites SK4 and SK6 the ChRM direction of one specimen was determined using the great-circle approach. In five of the seven sites (SK1 and SK4-7) reversed polarities were recorded (12 specimens from 10 cores). In a single sample (SK3.4), the A and B specimen yielded different polarities: the A sample a reversed and the B sample a normal polarity (Figures 3.4ab-ac). In many specimens a GRM developed at alternating fields higher than ~35 mT. The mean ChRM calculated for site SK ( $N_s=7$ ) is:  $D=330.5^\circ$ ,  $I=51.7^\circ$ .

### SR

A total number of 64 cores were sampled divided over 8 sites at locality SR. Eight specimens were TH demagnetized and 61 specimens using AF demagnetization (Figures 3.4af-ah). TH and AF demagnetization yield similar results (Figures 3.4af-ah). Initial intensities range 40-1000 mA/m. One specimen yields a reversed polarity. In most specimens a GRM developed upon AF demagnetization at fields higher than ~35mT. Data from site SR2 contain only two directions that make sense for a northern hemisphere setting, and therefore statistics over these data could not be calculated. After applying a  $45^\circ$  cut-off on the eight site averages, site SR6 and SR7 were rejected. Those are the only sites with clear counterclockwise rotations, the remainder of the datasets suggests clockwise rotations at the locality. We should remark here that sites SR6 and SR7 were taken in close proximity of each other and further away from sites SR1-SR5. SR6 and SR7 were also sampled closer to the edge of the granite body, as well as SR8. The mean ChRM direction at site SR ( $N_s=6$ ) is:  $D=27.5^\circ$ ,  $I=37.7^\circ$  (Table 3.2, Figure 3.5m).

### UC

At site UC we collected 56 samples over seven sites. All 57 specimens were AF demagnetized (Figures 3.4ai-ak). Initial intensities range ~50-600  $\mu\text{A}/\text{m}$ . Five samples yielded reversed polarities. We interpreted only 17 directions that we used to calculate site averages, as most diagrams displayed erratic behavior (e.g. Figure 3.4ak) or did not make sense for granites that were emplaced in the N-hemisphere. From sites UC5 and UC7 we could not determine any direction. Sites UC1, UC3 and UC4 consist of only two directions after application

of a  $45^\circ$  cut-off and therefore no statistics could be calculated from these two sites individually. The mean ChRM direction for locality UC ( $N_s=5$ ) is:  $D=15.7^\circ$ ,  $I=50.0^\circ$  (Table 3.2, Figure 3.5n). The K-value is very low, however, and considering the quality of the dataset, we will not take these data into account for our study.

### YO

At locality YO we sampled seven sites with a total number of 52 samples. Six specimens were TH demagnetized, the remaining 70 specimens using AF demagnetization (Figures 3.5am-an). AF and TH demagnetization do not always resemble. Initial intensities range ~15-800 mA/m. Many specimens are affected by lightning in sites YO1 and YO2 (Figure 3.4al). Directions within most sites and between sites are very scattered and often did not make any sense for granites emplaced in the N-hemisphere. However, there are several reversed polarities recorded within sites YO1, YO5 and YO6. The mean ChRM direction for locality YO ( $N_s=7$ ) is:  $D=1.9^\circ$ ,  $I=54.9^\circ$  (Table 3.2, Figure 3.5o). The K-value of the locality is very low ( $K=7.6$ ), and the  $A_{95}$  of  $23.4^\circ$  nearly exceeds the  $A_{95\text{max}}$  ( $24.1^\circ$ ). Considering this and the low coherence and quality of the data sets, we will not take this locality into account for our study.

Site	UTM zone	Location	N <sub>cores</sub>	N <sub>demag</sub>	N <sub>a</sub>	N <sub>45</sub>	N <sub>t</sub>	dec	inc	k	̸ <sub>95</sub>	K	A95	A95 <sub>min</sub>	A95 <sub>max</sub>	λ	̸ <sub>D<sub>x</sub></sub>	̸ <sub>I<sub>x</sub></sub>	
AG			55	75	55	55	7	356.8	50.5	79.2	6.8	54.8	8.2	3.4	6.6	31.2	9.6	9.1	
AG1	36S	0570135 4307216	8	14	8	8		358.6	46.6	23.4	11.7	18.4	13.	3	7.4	22.1	27.9	15.1	16.1
AG2	36S	0570134 4307231	6	8	8	8		4.4	54.9	61.2	7.1	32.0	9.9	7.4	2	2.1	35.4	12.2	9.9
AG3	36S	0570101 4307185	9	10	10	10		346.1	50.8	26.9	9.5	20.9	10	.8	6.8	19.2	31.5	12.7	11.9
AG4	36S	0569630 4306797	8	9	8	8		355.1	58.8	74.3	6.5	51.8	7.8	7.	4	22.1	39.5	10.1	7.0
AG5	36S	0570538 4307124	8	10	5	5		14.7	44.0	17.2	19.0	20.0	17.5		8.9	29.7	25.8	19.5	22.3
AG6	36S	0570912 4307837	8	12	8	8		340.3	47.4	20.8	12.4	19.6	12.	8	7.4	22.1	28.5	14.6	15.2
AG7	36S	~50 m E of AG6	8	12	8	8		357.6	47.2	97.4	5.6	79.5	6.3	7.4		22.1	28.4	7.2	7.5
AK			60	84	76	76	8	317.4	54.3	80.1	6.2	41.9	8.7	3.0	5.4	34.8	10.6	8.8	
AK1	36S	0599199 4271638	9	12	12	12		315.5	52.5	10.9	13.7	8.6	15	.7	6.3	17.1	33.1	18.8	16.6
AK2	36S	0599199 4271638	7	9	9	9		314.2	53.5	33.3	9.1	19.8	11.9	7	.1	20.5	34.0	14.4	12.3
AK3	36S	0599086 4271914	7	9	9	9		305.7	52.9	21.6	11.3	13.4	14.6		7.1	20.5	33.5	17.6	15.3
AK4	36S	0599113 4271982	9	12	12	12		303.1	53.2	52.1	6.1	34.1	7.	5	6.3	17.1	33.8	9.0	7.8
AK5	36S	0598946 4272376	7	9	9	9		329.5	53.7	14.5	14.0	9.6	17.5	7	.1	20.5	34.2	21.3	18.0
AK6	36S	0599350 4271542	7	13	13	13		309.8	49.7	35.0	7.1	30.6	7.	6	6.1	16.3	30.5	8.8	8.6
AK7	36S	0599528 4271512	7	9	5	5		320.6	51.0	35.3	13.1	25.5	15.4		8.9	29.7	31.7	18.2	16.8
AK8	36S	0599576 4272074	7	11	7	7		349.6	61.8	22.0	13.2	10.8	19.	3	7.8	24.1	43.0	26.9	16.1
CA			41	43	40	37	5	0.4	62.9	52.1	10.7	31.5	13.8	4.0	8.4	44.3	19.5	11.2	
CA1	36S	0548897 4424432	8	8	7	5		359.3	47.4	39.5	12.3	43.4	11.7		8.9	29.7	28.5	13.3	13.9
CA2	36S	0548892 4424498	7	7	7	7		344.9	62.2	67.2	7.4	40.6	9.6	7.	8	24.1	43.5	13.3	7.9
CA3	36S	0549210 4424349	10	11	9	9		16.7	66.9	33.1	9.1	15.5	13.5		7.1	20.5	49.5	21.1	9.9
CA4	36S	0549231 4424433	6	7	7	6		9.8	74.6	29.1	12.6	10.8	21.3	8.	3	26.5	61.1	48.8	12.9
CA5	36S	0549245 4424459	10	10	10	10		358.3	61.3	16.1	12.4	11.3		15.0	6.8	19.2	42.4	20.5	12.7
GE		no averages calculated	51	53															
GE1	36S	0673571 4386500	9	10															
GE2	36S	0673558 4386494	7	8															
GE3	36S	0673518 4386483	7	7															
GE4	36S	0673499 4386488	7	7															
GE5	36S	0665518 4388856	7	6															
GE6	36S	0665622 4388925	7	8															
GE7	36S	0665637 4388906	7	7															
HI			54	79	77	76	7	0.8	52.0	62.2	7.7	43.7	9.2	3.0	5.4	32.6	10.9	9.8	
HI1	36S	0540132 4349168	7	10	8	8		342.4	57.2	16.0	14.3	11.6	17.	0	7.4	22.1	37.8	21.7	16.0
HI2	36S	0540327 4349251	7	10	10	9		25.4	61.8	23.8	10.8	13.4	14.	6	7.1	20.5	43.0	20.2	12.2
HI3	36S	0540345 4349118	7	11	11	11		1.2	57.3	42.6	7.1	25.4	9.2	6	.5	18.1	37.9	11.7	8.6
HI4	36S	0540284 4349077	8	12	12	12		356.6	48.8	20.1	9.9	18.5	10	.4	6.3	17.1	29.7	12.0	12.0
HI5	36S	0537791 4349715	9	13	13	13		1.9	47.2	59.8	4.4	49.3	6.0	6	.1	16.3	28.4	6.8	7.2
HI6	36S	0537898 4349684	8	12	12	12		2.8	47.9	38.0	7.1	59.9	5.7	6	.3	17.1	29.0	6.5	6.7
HI7	36S	0538114 4349649	8	11	11	11		359.4	40.3	75.6	5.3	80.4	5.	1	6.5	18.1	23.0	5.5	7.0
KK			50	93	89	89	6	355.0	61.9	172.4	5.1	84.9	7.3	2.8	4.8	43.1	10.0	6.1	
KK1	36S	0566110 4406075	7	14	12	12		6.1	56.1	27.4	8.4	19.0	10.2		6.3	17.1	36.7	12.8	9.9
KK2	36S	0566183 4406137	7	13	13	13		347.7	62.3	82.0	4.6	55.6	5.	6	6.1	16.3	43.6	7.7	4.6
KK3	36S	0566306 4406163	7	12	12	12		304.7	39.6	77.0	5.0	85.7	4.7	6.3	17.1	22.5	5.1	6.5	
KK4	36S	0566404 4406255	7	13	13	13		6.8	59.4	29.3	7.8	14.8	11.2		6.1	16.3	40.2	14.7	10.0
KK5	36S	0566451 4406292	7	13	13	13		340.1	62.3	24.2	8.6	14.1	11	.4	6.1	16.3	43.6	15.8	9.4
KK6	36S	0566534 4406372	8	15	15	15		354.1	66.5	62.7	4.9	27.5	7.	4	5.8	14.9	49.0	11.3	5.5
KK7	36S	0566109 4406055	7	13	11	11		351.4	62.7	26.7	9.0	15.8	11	.9	6.5	18.1	44.1	16.7	9.7
KO			57	81	74	72	7	340.8	57.9	135.2	5.2	79.8	6.8	3.1	5.5	38.6	8.7	6.3	
KO1	36S	0537187 4382808	8	12	12	11		341.8	65.9	21.0	10.2	17.2	1	1.3	6.5	18.1	48.2	17.1	8.5
KO2	36S	0537245 4382739	9	12	10	10		336.3	60.9	86.9	5.2	52.5	6.	7	6.8	19.2	41.9	9.0	5.7
KO3	36S	0537170 4382656	8	12	11	11		352.2	58.8	42.7	7.1	23.9	9.	5	6.5	18.1	39.5	12.4	8.6
KO4	36S	0536997 4382717	8	11	11	11		333.7	53.4	29.6	8.5	21.2	10	.1	6.5	18.1	34.0	12.2	10.4
KO5	36S	0536930 4382667	8	12	10	10		326.0	57.6	158.5	3.8	95.0	5	.0	6.8	19.2	38.2	6.4	4.7
KO6	36S	0536758 4382551	8	11	9	9		345.8	54.5	26.8	10.1	19.5	12.	0	7.1	20.5	35.0	14.7	12.1
KO7	36S	0536748 4382453	8	11	11	10		349.2	51.9	23.7	10.1	15.0	1	2.9	6.8	19.2	32.5	15.4	13.8
NI		no averages calculated	46	46															
NI1	36S	0673368 4206820	7	7															
NI2	36S	0673299 4207310	7	7															
NI3	36S	0673376 4207520	8	8															
NI4	36S	0673432 4207845	8	8															
NI5	36S	0673501 4207881	7	7															
NI6	36S	0673574 4208004	7	7															
NI7	36S	0675334 4208271	2	2															
OK			41	41	36	33	4	25.8	58.1	45.6	13.7	23.8	19.2	4.2	9.1	38.8	25.0	17.6	
OK1	36S	0244572 4395755	8	8	7	7		47.4	57.4	24.3	12.5	27.4	11.7	7	.8	24.1	38.0	14.9	10.9
OK2	36S	0244767 4396334	8	8	7	5		27.1	59.5	38.9	12.4	29.8	14.2	8	.9	29.7	40.3	18.8	12.6
OK3	37S	0750999 4397858	7	7	7	7		86.3	-44.5	35.4	10.3	27.0	11.8	7.8	24.1	-26.2	13.2	14.9	
OK4	37S	0751419 4396777	8	8	6	5		33.7	59.6	18.3	18.4	10.6	24.7	8	.9	29.7	40.4	33.3	21.8
OR1	37S	0244764 4396135	10	10	9	9</													

SE		49	71	71	68	7	32.5	12.4	9.2	21	14.2	16.6	3.1	5.7	6.3	16.7	32.1		
SE1	36S	0646043	4384264	7	11	11	11	23.4	36.8	13.1	13.1	22.5	9.	8	6.5	18.1	20.5	10.5	14.3
SE2	36S	0646057	4384307	7	8	8	6	219.5	0	10.1	22.1	11.5	20.6	8.3		26.5	0.0	20.6	41.2
SE3	36S	0646052	4384372	7	12	12	12	21.4	12.1	9.6	14.7	13.9	12	6	.3	17.1	6.1	12.1	23.2
SE4	36S	0646071	4384416	7	11	11	10	239.6	-5.5	10.3	15.8	15.9	1	2.5	6.8	19.2	-2.8	12.5	24.8
SE5	36S	0646040	4384589	7	14	14	14	201.9	3.7	68.4	4.8	176.9	3	5	.9	15.6	1.9	3.0	6.0
SE6	36S	0646045	4384182	7	8	8	8	14	40.9	9	19.6	10	18.5	7.4	22.1	2	3.4	20.2	25.1
SE7	36S	0646009	4384126	7	7	7	7	24	-11.9	75.3	7	161.8	4.8	7.8	24	.1	-6.0	4.8	9.3
SK				55	79	66	64	7	330.5	51.7	58.5	8	39.5	9.7	3.2	6.0	32.3	11.5	10.4
SK1	36S	0587796	4282026	8	10	9	9	330.7	54.4	25	10.5	18.2	12.4	7	.1	20.5	34.9	15.2	12.5
SK2	36S	0587733	4281961	8	10	10	10	325.9	42.3	28.6	9.2	24.2	10		6.8	19.2	24.5	11.0	13.2
SK3	36S	0587873	4281900	8	15	13	13	350.3	52	17.2	10.3	11.1	13	6	.1	16.3	32.6	15.5	13.9
SK4	36S	0587588	4282112	8	13	10	10	310.5	47.3	11.4	14.9	9.9	16	.2	6.8	19.2	28.5	18.5	19.3
SK5	36S	0587949	4281957	8	12	8	7	345.3	57.3	18.1	14.6	10.6	19.	4	7.8	24.1	37.9	24.9	18.2
SK6	36S	0587810	4281789	7	9	7	7	320.7	58.7	50.2	8.6	29	11.4	7.8		24.1	39.4	14.8	10.3
SK7	36S	0587828	4281748	8	10	9	8	332.8	44.8	21.8	12.1	18.1	13.	4	7.4	22.1	26.4	15.0	16.8
SR				64	69	54	53	6	27.5	37.7	13.4	19.0	14.5	18.2	3.5	6.7	21.1	19.6	26.2
SR1	36S	0677743	4402361	8	8	8	8	355.6	44.9	45.9	8.3	37.4	9.2	7.	4	22.1	26.5	10.3	11.5
SR2	36S	0677888	4402274	8	9	4	4	25.4	35.8	14.3	25.2	22.2	19.9	9	.8	34.2	19.8	21.2	29.6
SR3	36S	0678071	4402290	8	9	9	9	36.0	20.7	15.8	13.4	17.1	12.8	7	.1	20.5	10.7	13.0	23.2
SR4	36S	0678311	4402378	8	9	2	2	27.4	13.9										
SR5	36S	0678348	4402362	8	8	8	8	19.9	58.1	19.0	13.1	13.5	15.6	7	.4	22.1	38.8	20.2	14.3
SR6	36S	0678994	4402557	8	9	9	9	306.9	36.1	22.8	11.0	18.8	12.2	7.1		20.5	20.0	13.0	18.0
SR7	36S	0679000	4402413	8	9	9	9	318.8	44.8	158.9	4.1	139.2	4.4	7.1		20.5	26.4	4.9	5.5
SR8	36S	0679084	4401771	8	8	5	4	56.1	44.9	12.2	27.4	10.6	29.6	9	.8	34.2	26.5	33.5	37.1
UC				57	57	17	15	5	15.7	50.0	15.3	20.2	9.3	26.5	5.8	14.9	30.8	31.3	29.7
UC1	36S	0666068	4198154	8	8	3	2	50.3	44.2										
UC2	36S	0666108	4198147	8	8	4	4	339.0	52.4	9.6	31.3	6.4	39.5	9.	8	34.2	33.0	49.3	41.8
UC3	36S	0666108	4198180	8	8	2	2	346.0	48.0										
UC4	36S	0666140	4198138	8	8	2	2	24.1	38.8										
UC5	36S	0666208	4198144	9	9														
UC6	36S	0666256	4198138	8	8	6	5	31.5	50.6	39.2	12.4	30.6	14.1	8	.9	29.7	31.3	16.6	15.6
UC7	36S	0666173	4198137	8	8														
YO				52	76	49	46	7	1.9	54.9	10.8	19.2	7.6	23.4	3.7	7.3	35.4	29.2	23.3
YO1	36S	0667721	4406410	7	11	6	6	30.8	29.7	9.7	22.7	10.4	21.8	8	.3	26.5	15.9	22.7	35.6
YO2	36S	0667954	4406560	7	11	4	4	32.3	67.6	70.1	11.1	28.1	17.6		9.8	34.2	50.5	28.4	12.6
YO3	36S	0667924	4406810	7	11	11	10	9.4	56.5	30.6	8.9	16.6	12.2		6.8	19.2	37.1	15.4	11.7
YO4	36S	0667498	4406463	8	12	10	10	3.3	55.9	60.3	6.3	36.6	8.1	6	.8	19.2	36.4	10.1	7.9
YO5	36S	0668920	4405834	8	12	5	5	183	-26.9	5.8	34.8	6.2	33.3	8.	9	29.7	-14.2	34.5	56.4
YO6	36S	100 m N of YO7		8	10	9	8	316.7	54.1	17.1	13.8	12.2	16.5	7	.4	22.1	34.6	20.2	16.8
YO7	36S	0669046	4405699	7	9	4	3	305.5	68.8	29.5	23.1	11.3	38.5		11.0	41.0	52.2		26.8

Total number of samples/specimens: 783 1022 763 742

*Supplementary Table* Location of the sites in UTM coordinates with the corresponding UTM zones. . Ncores= number of sampled cores, Ndemag= number of demagnetized specimens, Na= number of interpreted specimens, N45= number of specimens included in the calculated for the mean ChRM direction after applying the 45° fixed cut-off, Nt= total number of sampled sites at the given locality, dec= declination, inc= inclination, k= estimate of the precision parameter determined from the ChRM directions,  $\alpha_{95}$ = cone of confidence determined from the ChRM directions, K= precision parameter determined from the mean virtual geomagnetic pole directions (VGPs),  $A_{95}$ = cone of confidence determined from the mean VGP direction,  $A_{95min}$  ( $A_{95max}$ )= minimum (maximum) value of the  $A_{95}$  for the given dataset based on (Deenen et al. 2011),  $\lambda$ = paleolatitude,  $\Delta D_x$  ( $\Delta I_x$ )= declination (inclination) error calculated from the  $A_{95}$ .



# CHAPTER 4



# Late Cretaceous exhumation and crustal flow in the CACC: a study on the structural and metamorphic evolution of the Kırşehir and Akdağ Massifs

## Abstract

The Central Anatolian Crystalline Complex (CACC) is a large domain in central Turkey, where a widespread high temperature event occurred during the late Cretaceous. This domain displays three different sub-massifs (i.e. the Akdağ and Kırşehir Massifs in the north, and the Niğde Massif in the south) mainly composed of metamorphic, ophiolitic and intrusive rocks. The structural, metamorphic and tectonic history of the two northern massifs of the CACC is poorly constrained. In this study, we provide detailed and widespread structural data on the ductile deformation history (foliations and stretching lineations) as well as index metamorphic minerals and mineral assemblages constraining the spatial distribution of regional metamorphism, based on regional field mapping in the Akdağ and Kırşehir Massifs. Both massifs represent >100km wide gently dipping dome-shaped antiforms. In each dome, two distinctive coeval syn-metamorphic shearing directions exist, and they are revealed by the regional pattern of stretched metamorphic minerals. These two shearing are contemporaneous but took place at a high angle to each other, one representative for the core, and one for the margins of the antiform. We propose that shearing directions represent the motion of ductile materials from within the cores of the antiforms, whereas the margins record deformation associated with exhumation along extensional detachment systems. The trace of the sillimanite-in isograd throughout the area separates high-grade from medium/low-grade metamorphic zones. After correcting the two large antiforms for paleomagnetically assessed post-exhumational vertical axis rotations and large-scale strike-slip faulting, the structure and metamorphic zonation of the Akdağ and Kırşehir Massifs form a coherent pattern. In the restored configuration, the shearing in the core of the antiforms displays consistent top-to-the-SSW sense of shear, and the margins show top-to-the WNW shear sense in the NW and top-to-the-ESE shear sense in the SE. In places, extensional detachments can be identified with similar shear criteria, showing regional WNW-ESE extension.  $^{40}\text{Ar}/^{39}\text{Ar}$  cooling ages of both massifs cluster between 75 and 70 Ma. We conclude that the northern metamorphic massifs probably formed (part of) a single NNE-SSW trending dome-shaped antiform that formed during late Cretaceous high-temperature metamorphism and exhumation of the crystalline complex.

## 4.1 Introduction

The Central Anatolian Crystalline Complex (CACC) is the largest metamorphic domain in Turkey. It comprises a wide continental domain with high-grade metamorphic rocks (central Anatolian metamorphics, CAM), that formed following late Cretaceous ophiolite obduction (central Anatolian ophiolites, CAO). After its exhumation, the CACC collided with the Pontides (Eurasia) in the early Cenozoic. The CACC comprises three sub-massifs, of which the southern Niğde crystalline dome is as yet the most intensively studied. Petrological and geochronological data have revealed the presence of regional Barrovian metamorphism, which took place between 91 and 84 Ma (Whitney and Dilek 1998, Whitney et al. 2003). Following high temperature - moderate pressure metamorphism (HT-MP), the Niğde crystalline dome started to exhume and cool in the late Cretaceous (88-74Ma, based on various  $^{40}\text{Ar}/^{39}\text{Ar}$  ages on metamorphics) (Whitney et al. 2003, Whitney et al. 2007, Gautier et al. 2008). The tectonic character of this exhumation phase was evidenced in the field by the presence of a ductile-to-brittle extensional detachment, separating footwall metamorphics from hangingwall ophiolite-related gabbros (Gautier et al. 2002). Two distinctive but contemporaneous ductile shearing deformations were reported at the scale of the dome (Gautier et al. 2008): a top-to-NE/ENE shearing related to the displacement along the detachment, and a top-to-SSW shearing at deeper structural levels. Gautier et al. (2008) proposed that this coeval deformation may reflect lower crustal flow taking place in the core of the dome, and speculated that this might reflect a regional channel flow at the scale of the CACC.

The two northern massifs of the CACC (i.e. Kırşehir and Akdağ Massifs) cover a large area, representing ~80% of the total surface exposure of metamorphic rocks in central Anatolia (Figure 4.1). Recently, in the western part of the Kırşehir Massif, near Kaman, two sets of lineations have also been identified in high grade metacalcareous rocks (Lefebvre et al. 2011). However, unlike in the Niğde Massif, these did not form simultaneously. Near Kaman, the dominant metamorphic foliation carries NNW-SSE-trending HT mineral lineations. Close to the contact with the ophiolites, mylonitic marble bands associated with a top to the W-NW normal shear sense cut across the regionally dominant foliation (Lefebvre et al. 2011). The remainder of the Kırşehir Massif and the entire Akdağ Massif are still unexplored in term of structural data constraining regional shear patterns and exhumation histories. Moreover, the spatial

distribution of regional metamorphic grade recorded within the (CAM) is still debated for the Kırşehir Massif, and is essentially unknown in the Akdağ Massif (Erkan 1976, Seymen 1981, Şahin and Erkan 1999, Whitney et al. 2001). In this chapter, we present an extensive data set compiled into structural and metamorphic maps of the Akdağ and Kırşehir Massifs, to constrain the crustal scale processes which accompanied the exhumation of the CAM during the late Cretaceous.

Based on large scale field mapping of the metamorphic rocks from the northern massifs, our study provides a detailed and widespread dataset of foliation planes, allowing the construction of cross-sections, assessment of direction and sense of shear determination from stretched metamorphic minerals, and distribution of index minerals from metapelites, at the scale of the entire Akdağ and Kırşehir Massifs. In addition, to assess the cooling history of the metamorphics during their exhumation, we performed  $^{40}\text{Ar}/^{39}\text{Ar}$  age dating on metapelitic schists from both massifs. We will discuss the structural and thermal characteristics of exhumed HT domes at the scale of each massifs and of the entire CACC.

## 4.2 Geological setting

### 4.2.1 The Central Anatolian Crystalline Complex

The present-day geological outline of Turkey has been shaped by a complicated and long-standing tectonic history of convergence between the African and Eurasian plates (Şengör and Yılmaz 1981). This convergence has built a complex amalgamation of continental and oceanic fragments that are derived from an equally complex paleogeography in the Neo-Tethyan domain between Africa and Eurasia. This resulted in presently more or less east-west oriented orogenic belts. These include the Pontides in the north, the metamorphic Anatolides in central Turkey, and the Taurides to the south (Ketin 1966). The Pontides and the Anatolides/Taurides are separated by the Izmir-Ankara-Erzincan Suture Zone (IAESZ) which comprises an ophiolitic mélange of remnants of Neo-Tethyan oceanic crust (Brinkmann 1972, Şengör and Yılmaz 1981). South of the IAESZ, the Anatolide belt is characterized by several metamorphic continental domains of Pan-African affinity (Okay and Tüysüz 1999). The largest one is the Central Anatolian Crystalline Complex (CACC) located in central Turkey and consists mainly of metamorphic, ophiolitic and igneous rocks covered by Cenozoic deposits. This crystalline domain experienced a complicated tectonic history involving late Cretaceous burial and

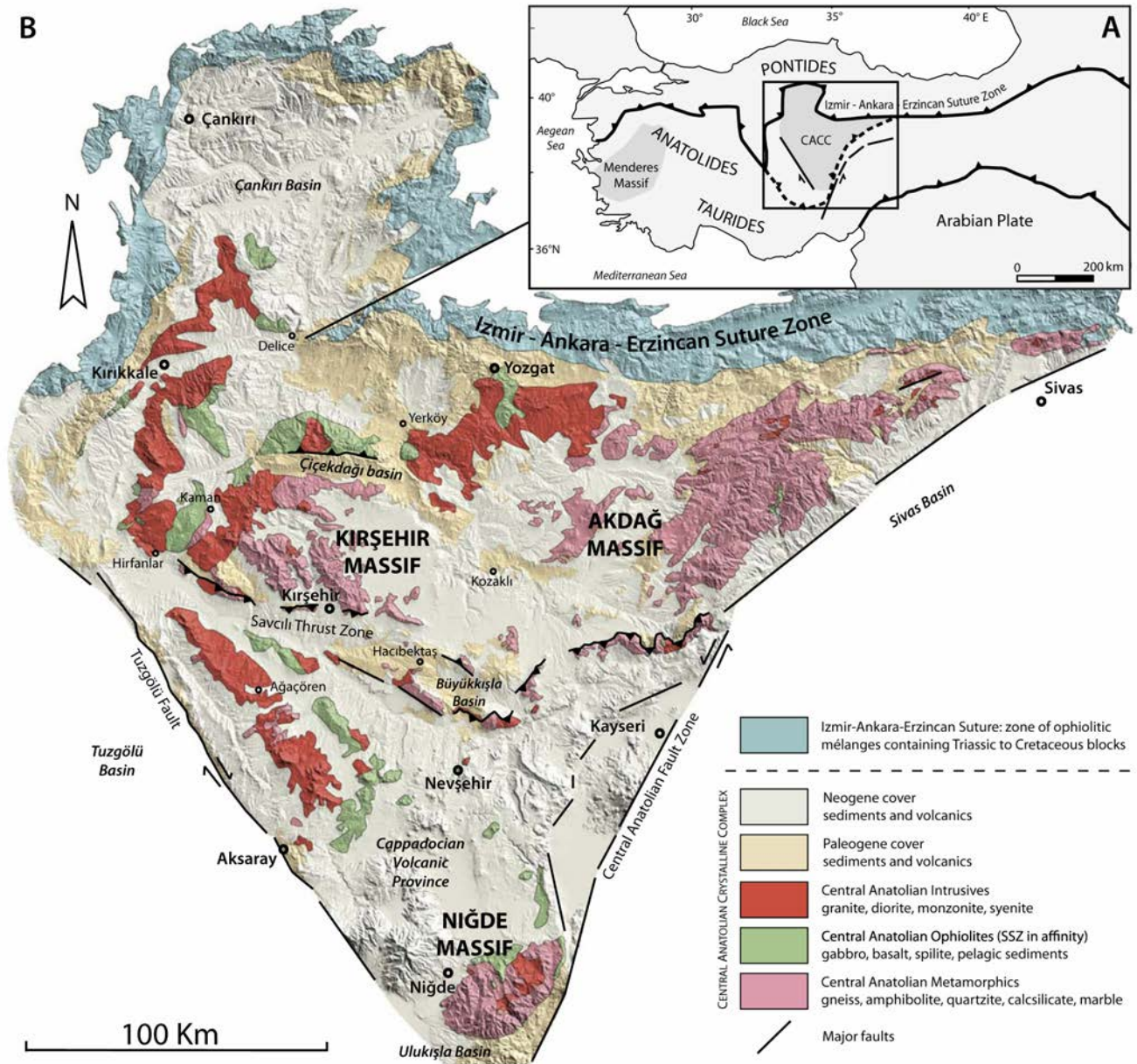


Figure 4.1 a) Simplified tectonic map of the Turkish orogenic system. The two grey areas indicate the locations of the two main metamorphic massifs in Turkey: the Menderes Massif and Central Anatolian Crystalline Complex (CACC), b) Simplified geological map of the CACC draped onto a Digital Elevation Model.

metamorphism of Paleozoic-Mesozoic sediments (the CAM) below ophiolites (the CAO), followed by widespread magmatic intrusions (magmatic supersuites of Central Anatolian intrusives) and subsequent exhumation in Paleocene times (Figure 4.1) (Göncüoğlu et al. 1991c, Kadioğlu et al. 2006). Exhumation was followed by collision of the CACC with the Pontides at the end of Cretaceous to Paleocene (Kaymakci et al. 2009, Meijers et al. 2010).

Three metamorphic massifs are geographically distinguished in the CACC: the Akdağmadeni or Akdağ Massif in the north-east (Vache 1963), the Niğde Massif in the south (Göncüoğlu 1977) and the Kırşehir Massif in the north-west (Seymen 1981) (Figure 4.1).

#### 4.2.2 The Akdağ Massif

The Akdağ Massif is the largest metamorphic massif of central Anatolia (~150x50km), whereas it is the least studied one. In the north, it is overlain by the ophiolitic mélangé of the Izmir-Ankara-Erzincan Suture Zone (IAESZ) (Figures 4.1 and 4.2). This contact represents different phases of south-vergent thrusting which are likely related to the late Cretaceous - Paleogene Pontides-CACC collision and to the late Cenozoic Arabia-Eurasia collision during which some of the earlier structures were reactivated (Poisson and Guezou 1996, Kaymakci et al. 2010). In the south, the Akdağ Massif is separated from the Sivas basin by the sinistral strike-slip Central Anatolian Fault Zone

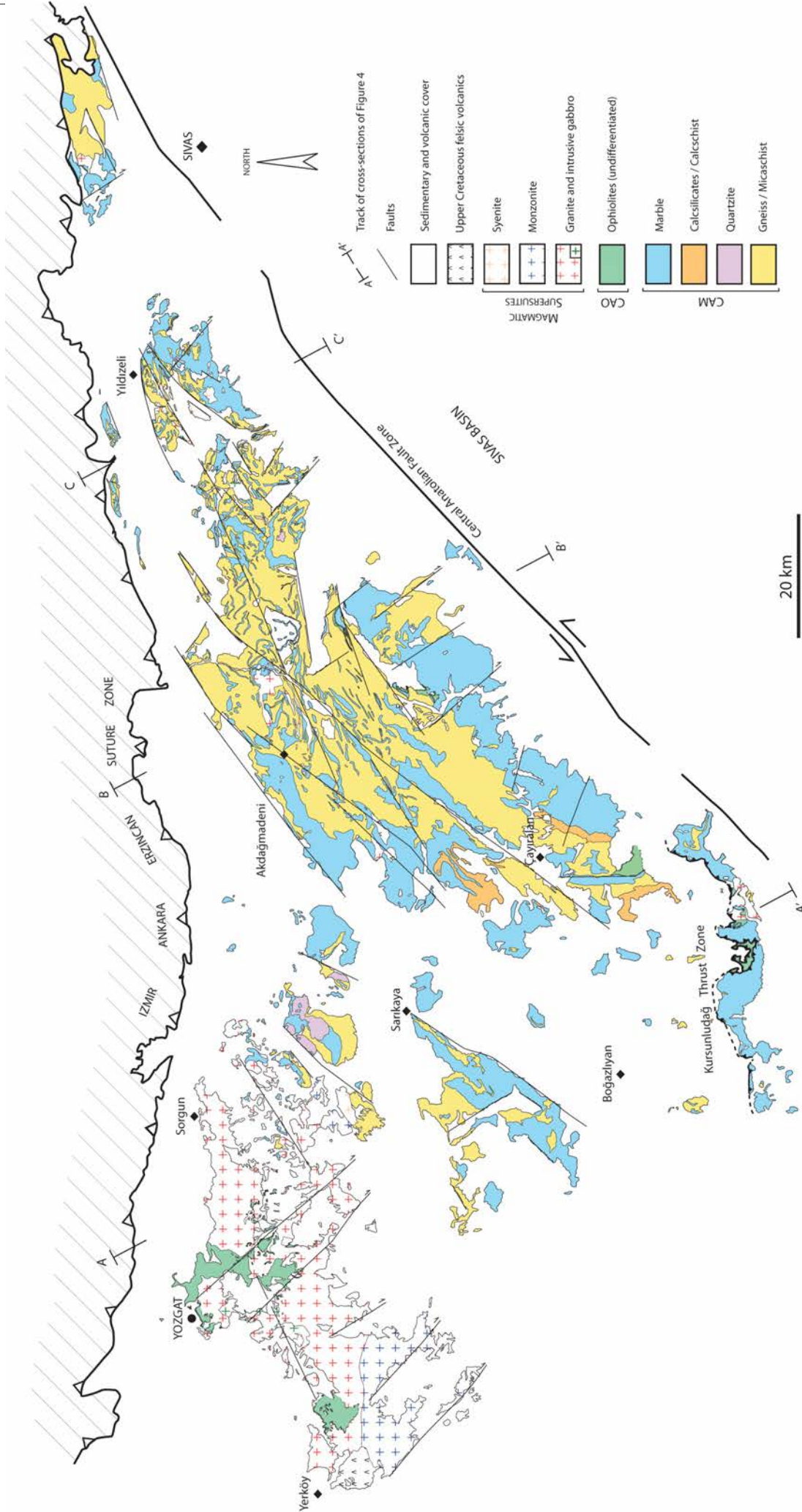


Figure 4.2 Geological map of the Akdağ Massif.

(CAFZ) (Koçyiğit and Beyhan 1998). The Akdağ Massif itself has a clear NE-SW main trend and consists almost entirely of metamorphic rocks. The metamorphic rocks are tectonostratigraphically a few kilometers thick and comprise from bottom to top the following main rock types: metapelites, semi-metapelites, metacarbonates and metabasites (as lenses and intercalations in all metamorphic units) (Vache 1963, Dökmeci 1980). Erkan (1980) reported that the characteristic metamorphic paragenesis in metapelites south of Akdağmadeni contains kyanite + staurolite and sillimanite + potassic feldspar. On the basis of staurolite + kyanite + garnet and staurolite + sillimanite parageneses, a high temperature medium pressure regional metamorphism was proposed by Özcan (1980). Two metamorphic zones were depicted from the Yukarıçulhalı-Başçatak area (see Figure 4.2) where sillimanite + kyanite paragenesis in the west indicate high-grade metamorphic conditions, while in the east biotite + garnet point to medium-grade conditions (Şahin and Erkan 1994). Based on index mineral and mineral assemblages from the metapelites, the regional metamorphism was estimated to have occurred at 400-700°C and 3.6-6.5 kbar (Şahin and Erkan 1999). Thermobarometric calculations on sillimanite, kyanite and staurolite-bearing schists from the high grade NE-SW oriented central belt suggest pressures of 5-8 kbar and temperatures of 550-675°C (Whitney et al. 2001).

The intrusive rocks located west of the Akdağ Massif are part of the Yozgat Batholith that mainly consists of monzogranite and quartz monzonite, and was divided into eight granitoid bodies (Erler and Göncüoğlu 1996). One of these, the Kerkenez granitoid contains discrete ductile shear zones recording lower amphibolite facies metamorphic conditions (Isik et al. 2008). Mineral stretching lineations indicate a top-to-the-northwest shear sense, and  $^{40}\text{Ar}/^{39}\text{Ar}$  dating on hornblendes from the mylonitic zone has yielded plateau ages of  $71.6 \pm 0.3$  Ma and  $71.7 \pm 0.2$  Ma (Isik et al. 2008). Within the Akdağ Massif itself, intrusives are scarce. The only coherent pluton is the Ortaköy granite (east of Akdağmadeni, Figure 4.2) where a contact metamorphic aureole of hornfels and skarns indicates that the intrusion postdates the regional peak metamorphism (Erkan 1980). An intense network of brittle faults affects both the Yozgat Batholith and the Akdağ Massif (Dirik and Göncüoğlu 1996). The region is dominated by a conjugate fault system (40-70° striking left lateral faults and 140-150° striking right lateral, oblique normal faults) which cut through the crystalline rocks and developed local depressions at the vicinity of NE-SW trending faults (e.g.

Sarıkaya, Çayıralan and Sızır depressions) (Dirik and Göncüoğlu 1996). This fault pattern has been interpreted as the result of a  $\sim 15^\circ\text{N}$  oriented compression, which may correspond to the final phase of collision of the CACC with the Pontides, followed by reactivation in the late Miocene by a strike-slip tectonic regime in the context of the Arabia-Eurasia collision (Dirik and Göncüoğlu 1996). In the southwest of the Akdağ Massif, the Kursunludağ north-directed thrust zone of Dirik and Göncüoğlu (1996) probably forms the eastern prolongation of the Savcı Thrust zone (Görür et al. 1998, Genç and Yürür 2010) (Figures 4.1 and 4.2).

#### 4.2.3 The Kırşehir Massif

In the northwest of the CACC, the Kırşehir Massif (Figures 4.1 and 4.3) consists of an association of intrusive and metamorphic rocks. The metamorphic rocks are essentially metasediments ( $\sim 2000$ - $2500$  m thick), and are divided into four different units from bottom to top (Seymen 1981) (Figure 4.3). The Kalkanlıdağ Formation dominated by metapelitic to semi-pelitic calcareous compositions, corresponds to quartz-mica-schists interlayered with calcsilicate and calcschist. The Kargasekmezdağ Formation is a thin homogenous quartzite layer. The Tamadağ or Nadölkendağ Formation contains mainly calcsilicate and impure marble with minor schist, amphibolite and quartzite bands. The uppermost unit is the Bozçaldağ Formation, characterized by a thick succession of pure marble. At the scale of the massif, the regional metamorphism ranges from greenschist to upper amphibolite/granulite facies (Erkan 1976, Seymen 1981, Whitney et al. 2001). However, the orientation of the metamorphic field gradient is debated. Erkan (1976) proposed that the metamorphic temperature increases from south to north / north-east, while other authors claimed that the grade of metamorphism west of Kırşehir city increases from east to west (Seymen 1984, Whitney et al. 2001) (Figure 1.3). Metamorphism accompanied the formation of a shallowly dipping foliation and associated isoclinal folding, and pervasive shearing affected the metamorphic rocks (Seymen 1983, Tolluoğlu and Erkan 1989). In the west, close to Kaman, thermobarometric calculations on high-grade sillimanite schists suggested metamorphic equilibration around 700-770°C at 6.5-7.5 kbar followed by decompression at 2.5-4 kbar based on cordierite-spinel assemblage (Whitney et al. 2001). The age of regional metamorphism is constrained by U/Pb SHRIMP analyses on monazites, giving  $84.1 \pm 0.8$  Ma (Whitney and Hamilton 2004). In

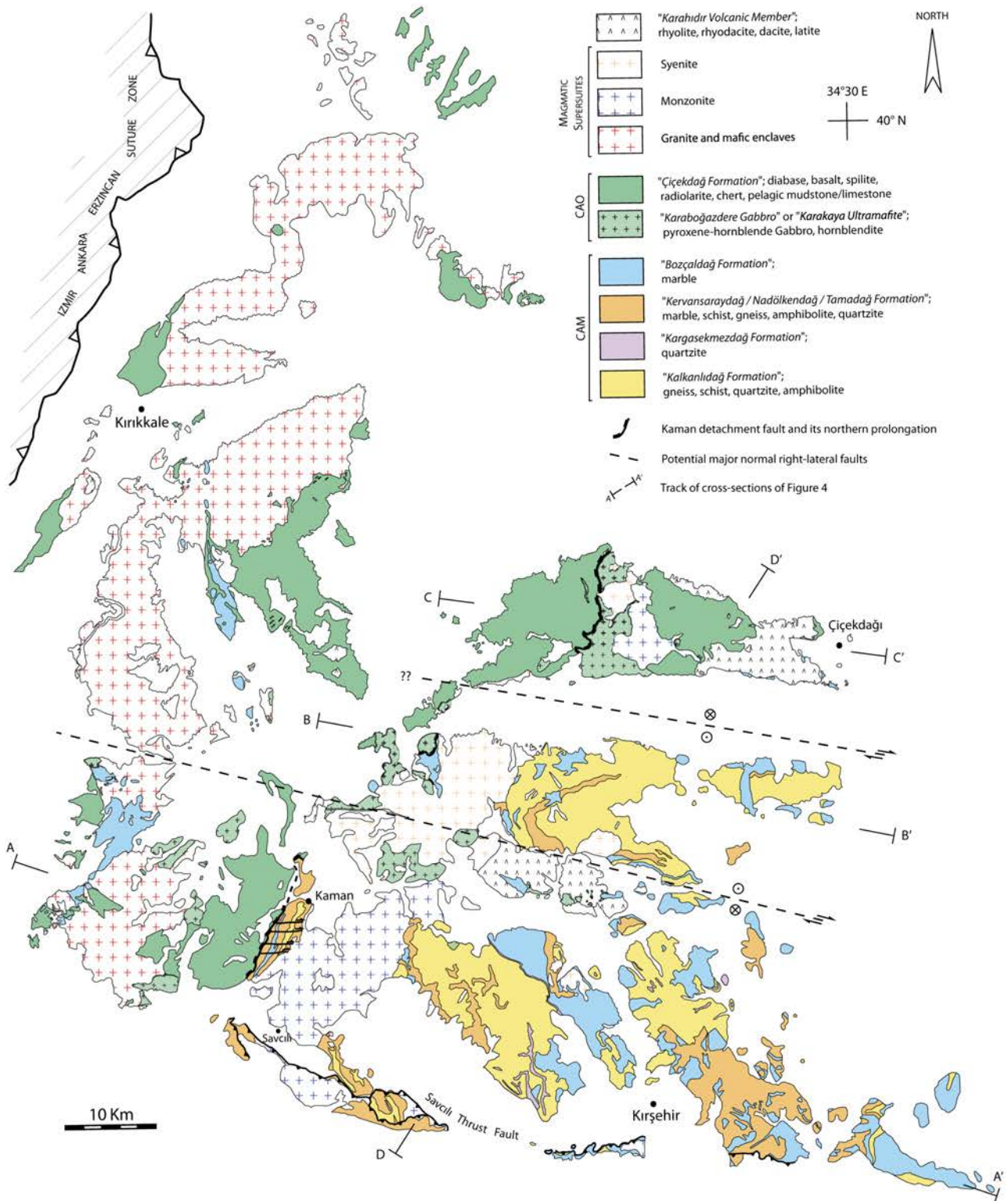


Figure 4.3 Geological map of the Kırşehir Massif.

Kaman, marble mylonites and proto-mylonites with a top to the W-NW normal shear senses were recognized at the interface between the high-grade metasediments of the CAM, and the non-metamorphic ophiolitic sequence of the CAO (Lefebvre et al. 2011). Those mylonitic bands were overprinted by cataclastic corridors parallel to the main foliation. This sequence of deformation has been interpreted as the consequence of the activity

of an upper crustal detachment between 84 and 74Ma (Lefebvre et al. 2011). Field relationships (e.g. xenoliths of marble in the intrusives) show that the intrusions post-date the peak of regional metamorphism as well as the formation of the main foliation (Seymen 1983, Tolluoğlu and Erkan 1989). The intrusives are organized into two elongated NNE-SSW trending belts. Granites and intrusive gabbros are located to the west of

Kaman while monzonite and syenite are located in the east (Akıman et al. 1993, Otlu and Boztuğ 1998). Crystallization ages of the Baranadağ quartz-monzonite (east of Kaman) are ~74Ma (Köksal et al. 2004, Boztuğ et al. 2009b). Timing of cooling of those magmatics is constrained by hornblende  $^{40}\text{Ar}/^{39}\text{Ar}$  plateau ages ranging around 69-72 Ma (Boztuğ et al. 2009b). In the south, the metamorphic and magmatic rocks and their sedimentary cover are affected by the western segment of the Savcılı Thrust Zone, which displays a NNE-vergent thrust motion and postdates the middle Eocene (Figure 4.3) (Seymen 2000).

### 4.3 Structure and metamorphism of the Akdağ Massif

#### 4.3.1 Structure

The Akdağ Massif presents a ~150km wide NE-SW oriented arched structure. Its convex geometry results from change in trend varying from NNE-SSW trend in the western part of the massif where its width is ~50km (near Akdağmadeni), toward a ENE-WSW trend in the east where its width is reduced to ~10km north of Sivas. Even though parts of the metamorphic rocks are affected by NE trending steep brittle faults, or covered by sediments and volcanics, the overall shape of the massif dominated by a NE-SW structure. Along NW-SE transects (Figure 4.4), the presence of the uppermost marble unit at the margins and the lower unit schist in the centre of the massif define

the geometry of a broad antiform (Figure 4.2). Cross-sections through the entire massif (Figure 4.4) reveal the regionally gentle open antiformal architecture of the massif, intruded by occasional plutons. The north-eastern part of the massif, which is in immediate contact with the IAESZ, is more affected by brittle faults than the rest of the massif (Figures 4.2 and 4.4c). The major NE-SW steep faults dissecting the dome form several blocks, laterally displaced from each other.

Apart from brittle structures, a well-developed metamorphic foliation, sub-parallel to the regional compositional layering of the metasediments, defines the geometry of the antiform (Figure 4.5). This foliation is pervasively developed throughout the massif and consistently strikes in the same direction as the margins of the dome (e.g. NNE-SSW trend in the west and ENE-WSW trend in the east). Our foliation measurements are presented in Figure 4.5, together with the ones reported on some of the 1:100000 geological maps from MTA (Directorate of Mineral Research and Exploration of Turkey, 1/100.000 scale sheets of I34, I35, I36, I37, I38 and J34). The foliation commonly shows relatively shallow dips (~30°), however, with locally steeper deviations (~50-60°) in areas highly affected by brittle faulting. In cross-section (Figure 4.4), the foliation defines large, open antiforms and synforms of up to 10-20km of wavelength (see Figure 4.7a). The metamorphic foliation is axial planar to isoclinal folds ranging from millimeter to kilometer scales, with well-developed folds that are easily identifiable in

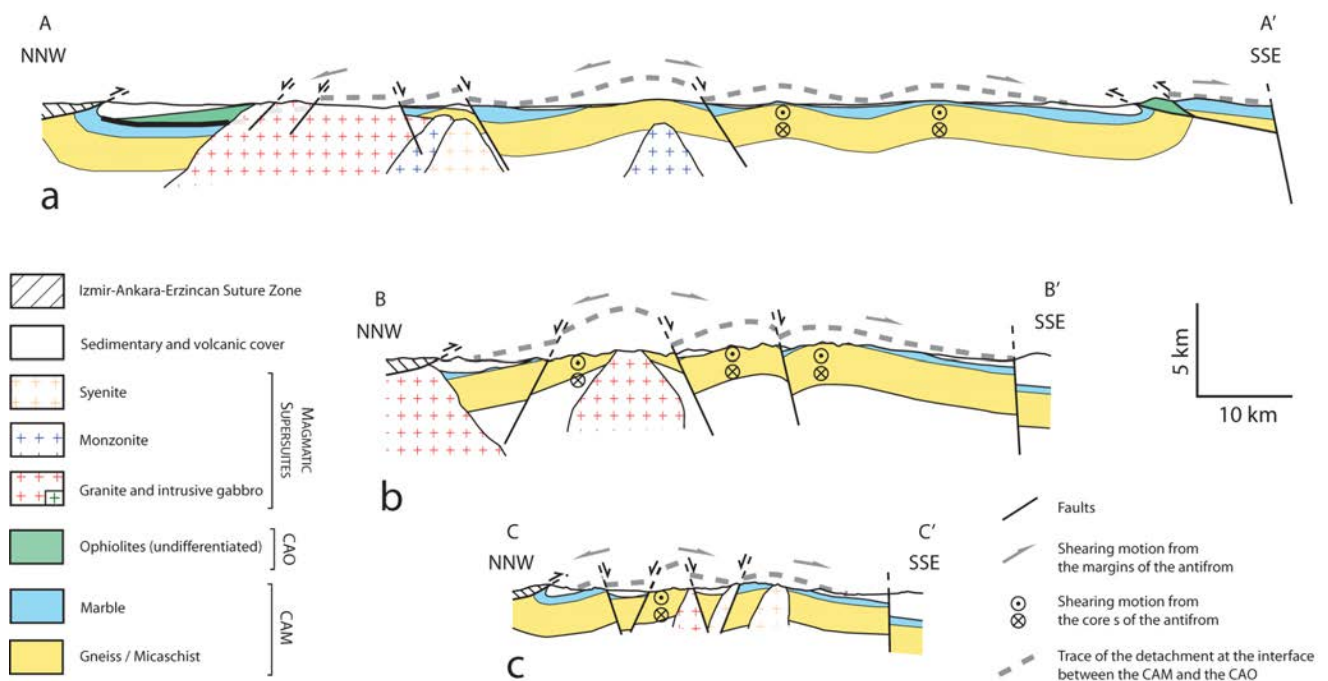


Figure 4.4 North-west south-east oriented upper-crustal cross-sections across the Akdağ Massif: a) western section, b) central section, and c) eastern section. Note vertical exaggeration.

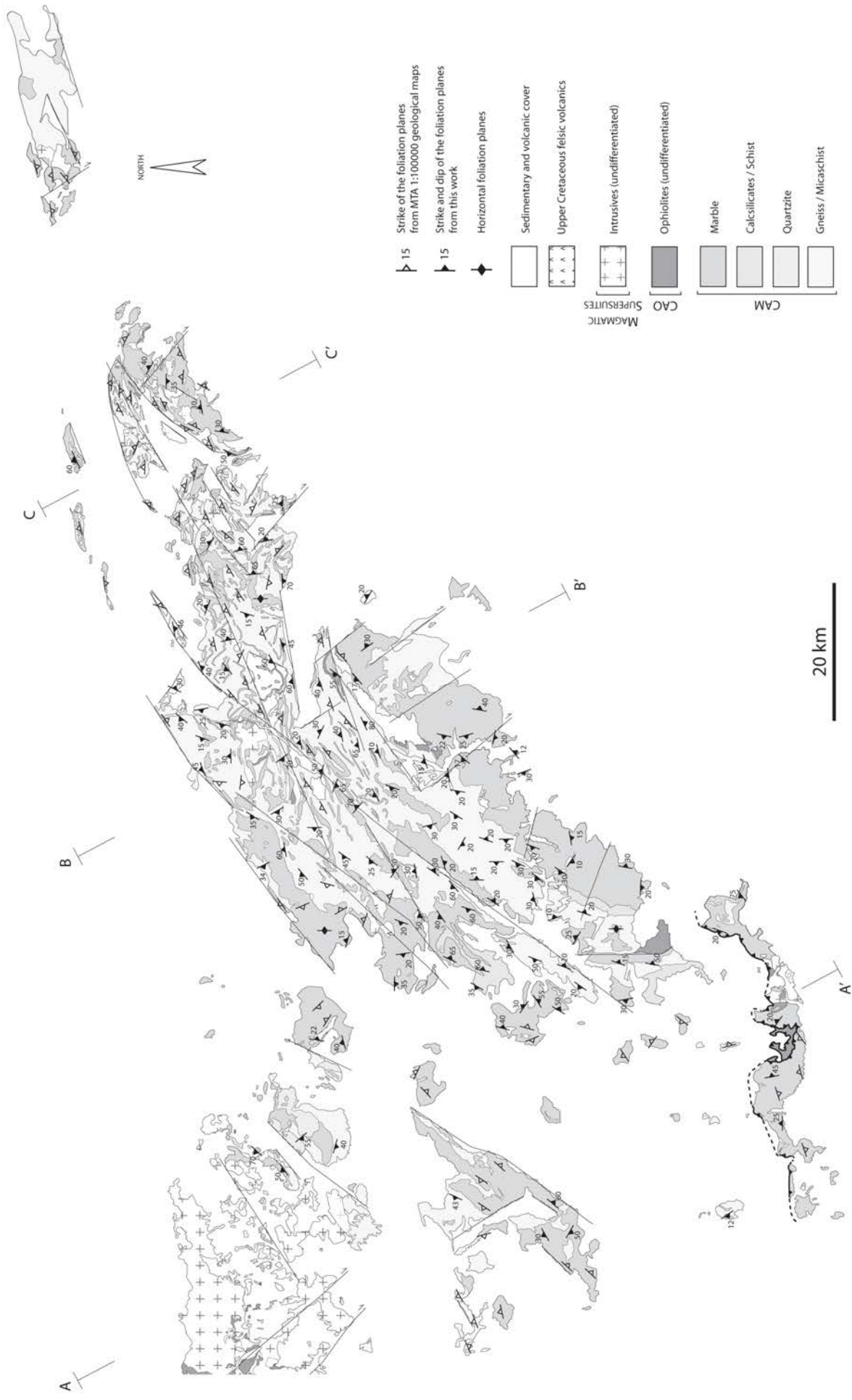


Figure 4.5 Map showing foliation planes in the Akdağ Massif, compiled from data reported on the 1:100000 geological maps from MTA (Directorate of Mineral Research & Exploration of Turkey, sheets I34, I35, I36, I37, I38 and J34), and data collected in this study.

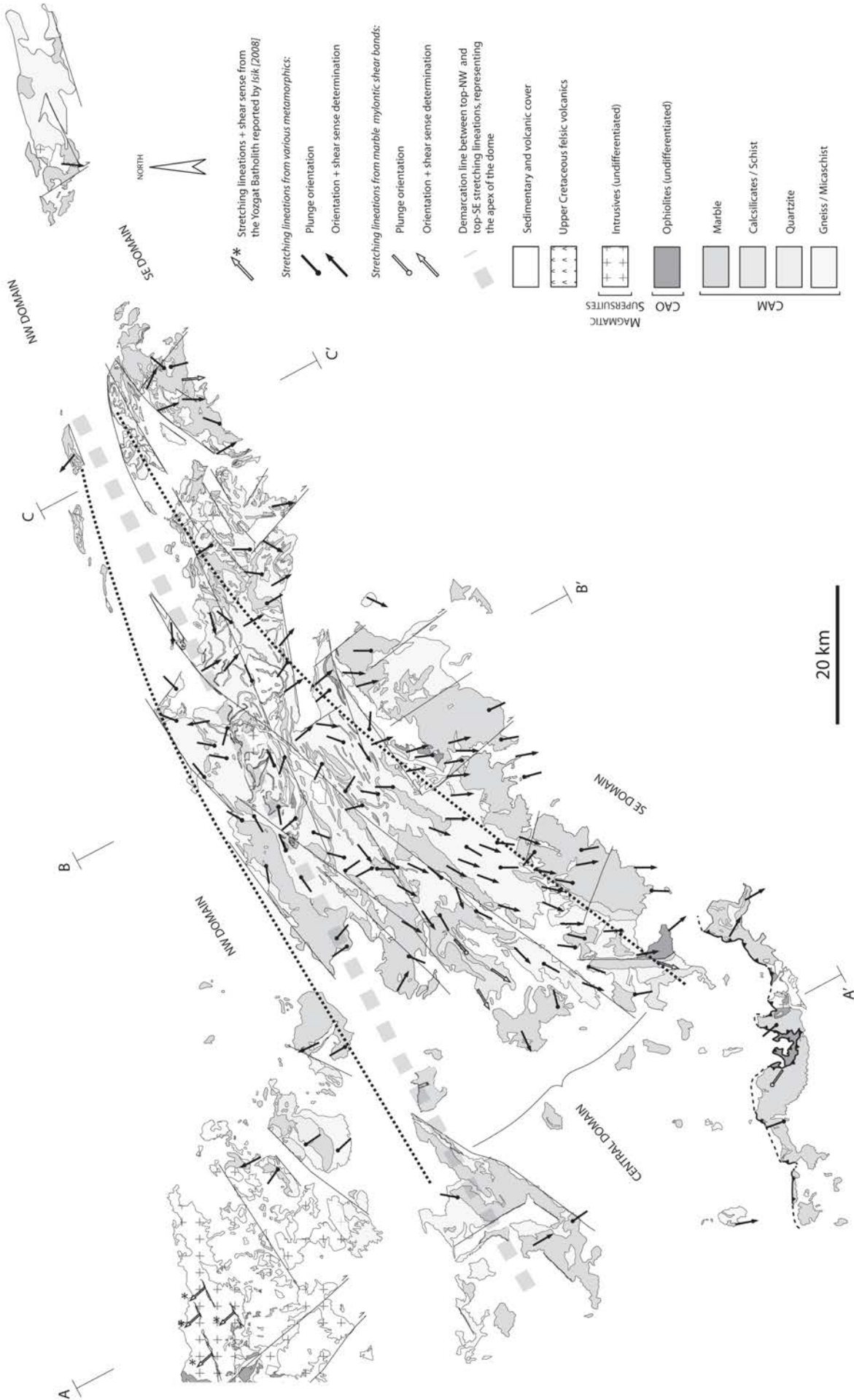
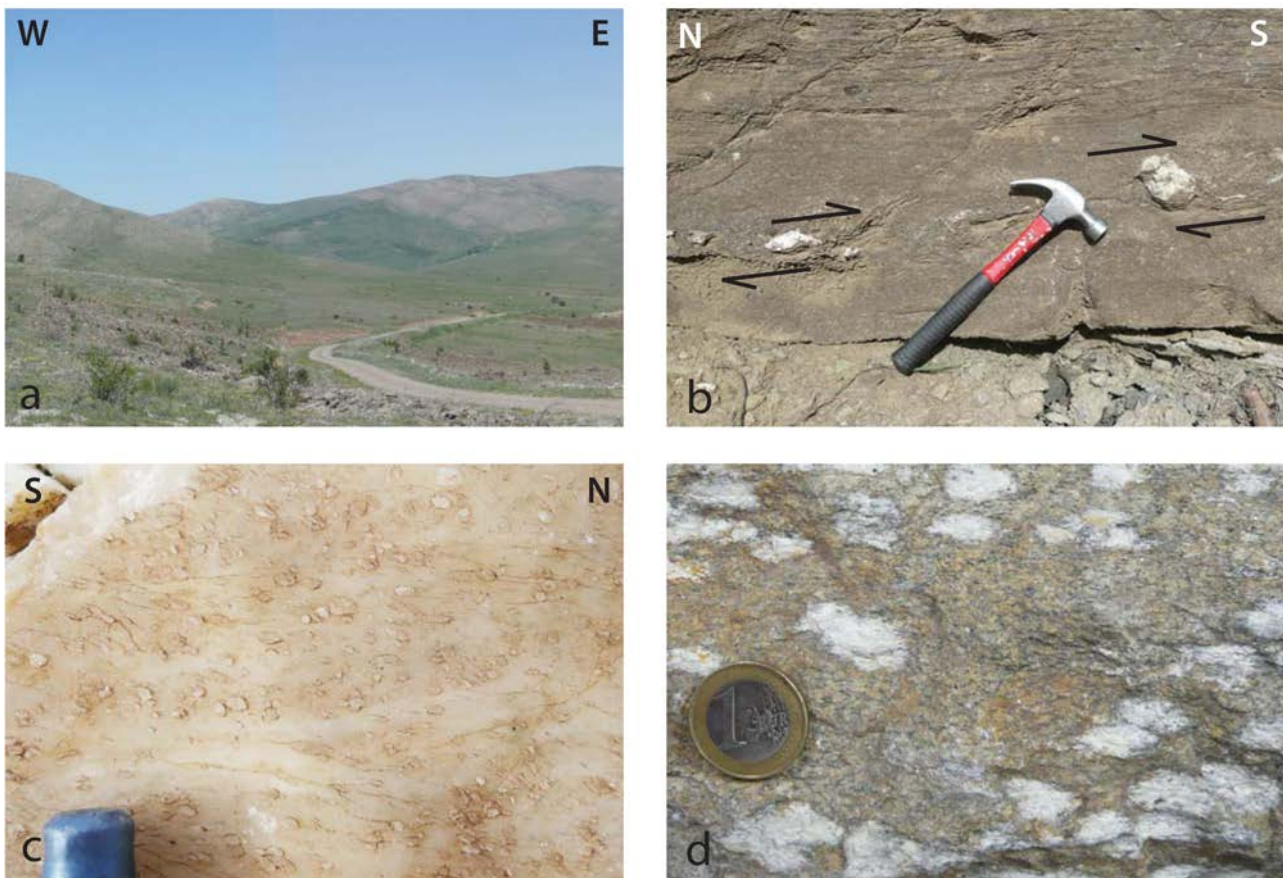


Figure 4.6 Map of stretching lineations in the Akdağ Massif.

the marble-rich layers in particular (see the maps presented in Figure 4.2 and 5). Across the entire massif, the foliation planes contain stretched minerals associated with a shearing deformation. Stretching lineations have been identified in the field via the preferred orientation of needle-shaped minerals such as amphiboles and sillimanite, in mafic, semicalcareous, semipelitic and pelitic compositions. Figure 4.6 depicts the directions and sense of shear, inferred from asymmetric clasts (Figure 4.7b) or extensional crenulation cleavages, and associated mineral stretching lineations. We separated the kinematic data obtained from the regional foliation from those collected from cross-cutting marble mylonites (Figure 4.7c). At the scale of the massif, the lineation map allows to distinguish 3 different domains where the direction and sense of shear associated with ductile stretching show a consistent pattern: (1) the “NW Domain”, which is only exposed in the northwest, north of Sarıkaya, and in the northeast around Yıldızeli, displays NNW-SSE oriented stretching lineations with a sub-horizontal top-to-the-NNW sense of shear. We note that the shearing data reported from the metamorphics of the NW domain are

in excellent agreement with the kinematic data from discrete mylonitic shear zones crossing the Kerkenez granitoid, identified by Isik et al. (2008) (see Figure 4.6). (2) the “Central Domain” is defined by the area where the stretching lineations are trending dominantly parallel to the ~NE-SW main foliation strike (i.e. also parallel to the margin of the massif). In this domain, stretching lineations are consistently associated with a top-to-the-SW sense of shear. However, few NNW-SSE oriented lineations are also present in this domain. Given its central position, the central domain would correspond to the core of the antiform. At the scale of the massif, we observe that the central domain is almost absent in the east and is progressively widening toward the west, reaching a width of nearly 50 km. Finally, (3) the “SE Domain” corresponds to the SE marble-rich margin of the massif, and is associated with a clear pattern of N-S oriented lineations and a top-to-the-South shear motion (Figure 4.6).

At the scale of the entire massif, it is possible to relatively precisely trace a boundary separating areas affected by top-NNW and top-S direction of shear (Figure 4.6). We note that this boundary is



*Figure 4.7* Field pictures and micrographs of metamorphic rocks from the Akdağ Massif. a) Large scale antiformal structure from the south of the massif, b) asymmetrical clasts used for shear sense determination. In the picture from the south of the massif, quartzitic clasts embedded in a calcareous matrix show typical  $\sigma$ -clast (in the left) and  $\delta$ -clast (in the right) consistent with a top-south shear motion, c) protomylonitic marbles composed of elongated asymmetric clasts of calcite surrounded by a matrix of very fine recrystallized grains, d) hand specimen from the high grade central belt consisting of a sillimanite quartz muscovite schist. The white patches consist entirely of an intergrown sillimanite and quartz.

located near the transition between the NW and central domains and does not correspond to the center of central domain. The transition between the NW and central domains, where the lineations appear at high angles to each other, seems much sharper than the transition between the central and SE domain, which shows a progressive rotation of the lineation from a NE-SW to NS direction. We note that stretching lineations in the marble mylonitic shear bands are found in both the central and SE domains and follow the main trend of lineations of their respective domains.

#### 4.3.2 Regional metamorphic pattern

The metamorphics of the Akdağ Massif cover a very large area and, except for the central high grade belt (Şahin and Erkan 1994, 1999, Whitney et al. 2001), are mostly unexplored. Therefore, we aimed at mapping the first-order regional pattern of the metamorphism and associated field gradient. For this purpose, the samples were collected throughout the entire massif such as to ensure sufficient and adequate coverage. We focused mainly on metapelitic compositions as these rocks likely contain the typical aluminosilicates characteristic of distinctive metamorphic grades. We report single minerals or mineral assemblages, which appear as dominant within the paragenesis of the collected samples. Each sample, containing characteristic minerals and paragenesis, has been studied under the microscope to determine and corroborate the assemblage. For mineral abbreviations, we follow the updated list proposed by Whitney and Evans (2010). Identified characteristic single minerals (Sil, Ky, St, Bt, Ms) and mineral assemblages (Sil+Kfs, Sil+Qz, Sil+St, Ky+Sil, Ky+Grt, Ky+St, Bt+Grt, Bt+Ms, Bt+Act, Ms+Chl) from the Akdağ Massif are reported in Figure 4.8 together with the index minerals and assemblages reported in the literature.

The widespread occurrence of sillimanite (see handspecimen in Figure 4.7d) demonstrates that metamorphism is dominated by high temperatures. The occurrence of kyanite seems to be concentrated in the NE-SW trending central high-grade belt in the western part of the Akdağ Massif (Figure 4.8). We note that the area where kyanite is present corresponds to the core of the Akdağ Massif antiform, previously characterized by top-to-the-southwest shearing kinematics (i.e. the Central Domain). Sillimanite is present all the way toward the Yozgat batholith and at the vicinity of the IAESZ in the northeast, and no obvious metamorphic temperature gradient can be established between the central and northerneastern domains (Figure 4.8). However the area from the

core of the dome toward the SE margin presents a clear change in metamorphic assemblage. Typical high temperature assemblages involving the presence of sillimanite, kyanite or staurolite are absent, and replaced by an assemblage of biotite, muscovite and chlorite (and minor actinolite in semipelitic compositions). Along the NE margin, we take the disappearance of sillimanite minerals as a marker of the transition between the high grade metamorphic zone (HG Zone) where sillimanite is present, toward the medium/low grade metamorphic zone (M/LG Zone) where the characteristic paragenesis consists of biotite, muscovite and chlorite. Based on the general FASH petrogenetic grid of Bucher and Frey (2002), this transition would correspond to an isotherm of ~500°C. In the field, the sillimanite isograd may be traced from west to east, and follow the curvature of the margin toward the north-east. We note that the M/LG Zone matches exactly the SE Domain where shearing kinematic data reveals consistent top-to-the-S motion (Figures 4.6 and 4.8). We note that all metamorphic minerals previously described were stable during the formation of the regional ductile foliation and associated shearing as the metamorphic paragenesis supports the foliated ductile fabric.

### 4.4 Structure and Metamorphism of the Kırşehir Massif

#### 4.4.1 Structure

The metamorphic domain of the Kırşehir is smaller (70x50km) than the Akdağ Massif. The entire western part of the massif is covered by ophiolites (CAO), which overlie the metamorphics, and by plutons intruding the CAM as well as the CAO (Figures 4.3 and 4.12a). The NW border of the Kırşehir Massif presents a thrust contact with the IAESZ, and the main trace of the suture follows the NNE-SSW boundary of the massif. This is different from the Akdağ Massif where the general structural trend of the massif is truncated by the overriding IAESZ. In the east, the Kırşehir metamorphics are locally intruded by occasional syenitic plutons (Figure 4.3 and 4.12a). The metamorphic domain of the Kırşehir Massif is characterized by an overall gently dipping antiform-shaped structure, and the uppermost marble unit concentrated at the eastern margin, and the centre of the massif dominated by the schists (Figure 4.3). The western margin also exposes marble, but there are only few outcrops and they appear as roof pendants on top of the granitoids (see map Figure 4.3 and cross-sections in Figure 4.9). As in Akdağ, a strong metamorphic foliation,

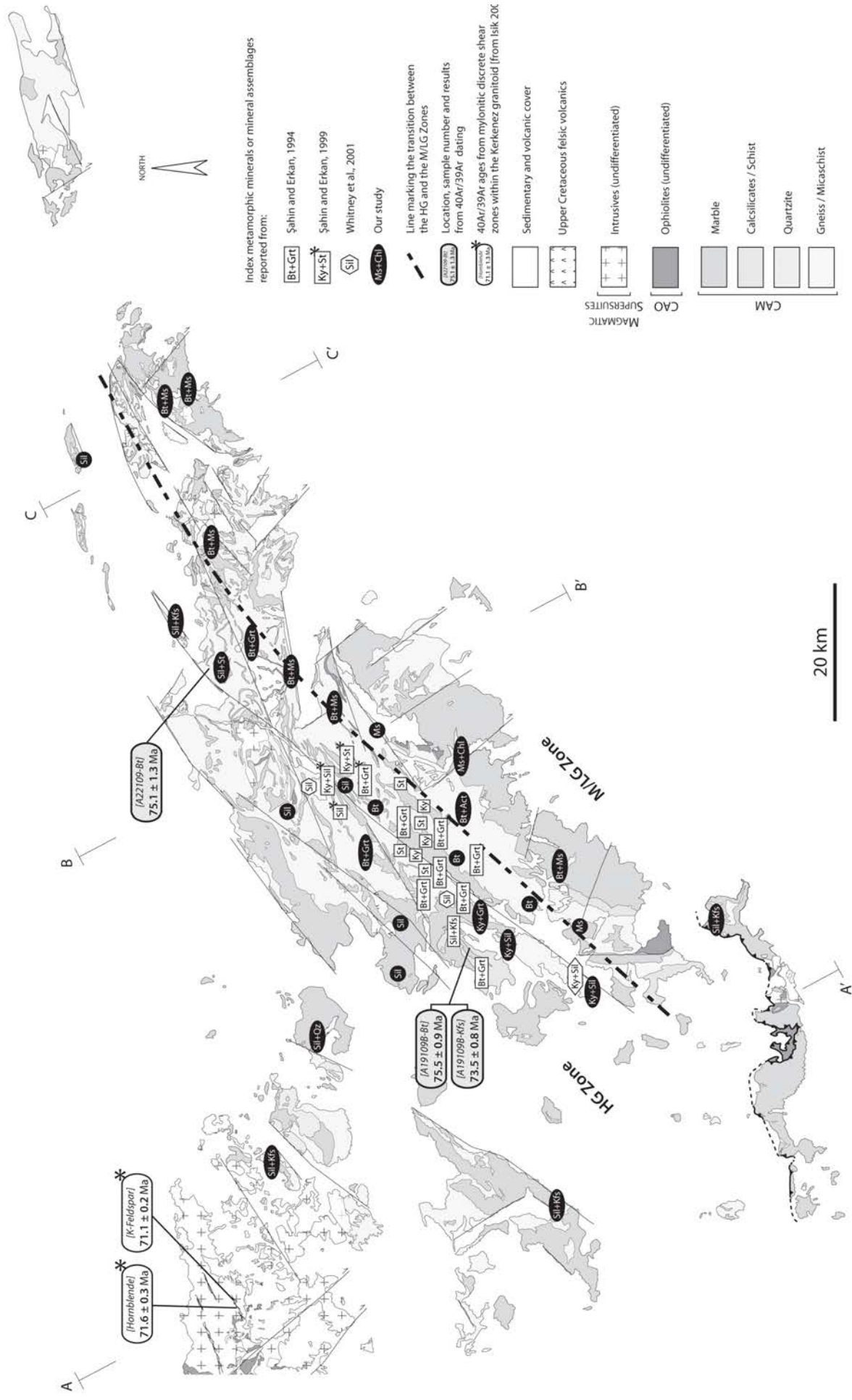


Figure 4.8 Map of index metamorphic minerals and mineral assemblages in the Akdağ Massif. Locations and interpreted ages of samples used for 40Ar/39Ar thermochronology are also shown.

with related isoclinal folding and pervasive ductile shearing is developed throughout the entire massif. Our foliation measurements are presented in Figure 4.10, together with the ones reported on the Kırşehir-G17 and -G18 1:100.000 scale geological maps from MTA. Shallow dipping foliations are subparallel to the main lithostratigraphic units and define NW-SE oriented antiforms. The overall antiform-shaped structure includes smaller scale antiforms and synforms which occur on a ~10 km scale. Those anti/synforms are NW-SE trending and are separated from each-other by depressions filled by sediments. This structure is particularly well defined by the uppermost marble unit, continuously exposed along the NW-SE edge of the block situated to the west of Kırşehir city (Figure 4.3). We note that the NW-SE trending crests of the antiform/synform structures are parallel to the trend of the Savcılı Thrust Zone located in the south of the study area.

Stretched minerals define lineations associated with pervasive shearing and was measured in mafic, semicalcareous, semipelitic and pelitic compositions (Figure 4.12b). Where possible, the

sense of shear associated with those lineations has been determined either directly in the field or under the microscope (Figure 4.12c), and the results are shown on the map of Figure 4.11. At the scale of the massif, two patterns of lineations can be distinguished in two different domains. The (1) “Western Domain” is an area where both metamorphic lineations and marble mylonitic shear bands coincide with the WNW-ESE oriented top-WNW shearing recognized from the Kaman detachment. Unfortunately, this domain is poorly exposed as it corresponds to the area dominated by intrusives and the remnants of the CAO. The (2) “Central Domain” is defined by the area covering most of the metamorphics of the Kırşehir Massif, and presents a remarkable consistency of N-S orientated lineations with a top-S sense of shear. Like in the Western Domain, shearing kinematics from marble mylonitic bands present same direction as the lineation associated with the regional metamorphism (Figure 4.11). The line of demarcation between these two domains has a NNE-SSW orientation, which seems to follow the eastern margin of the monzonite/syenite belt

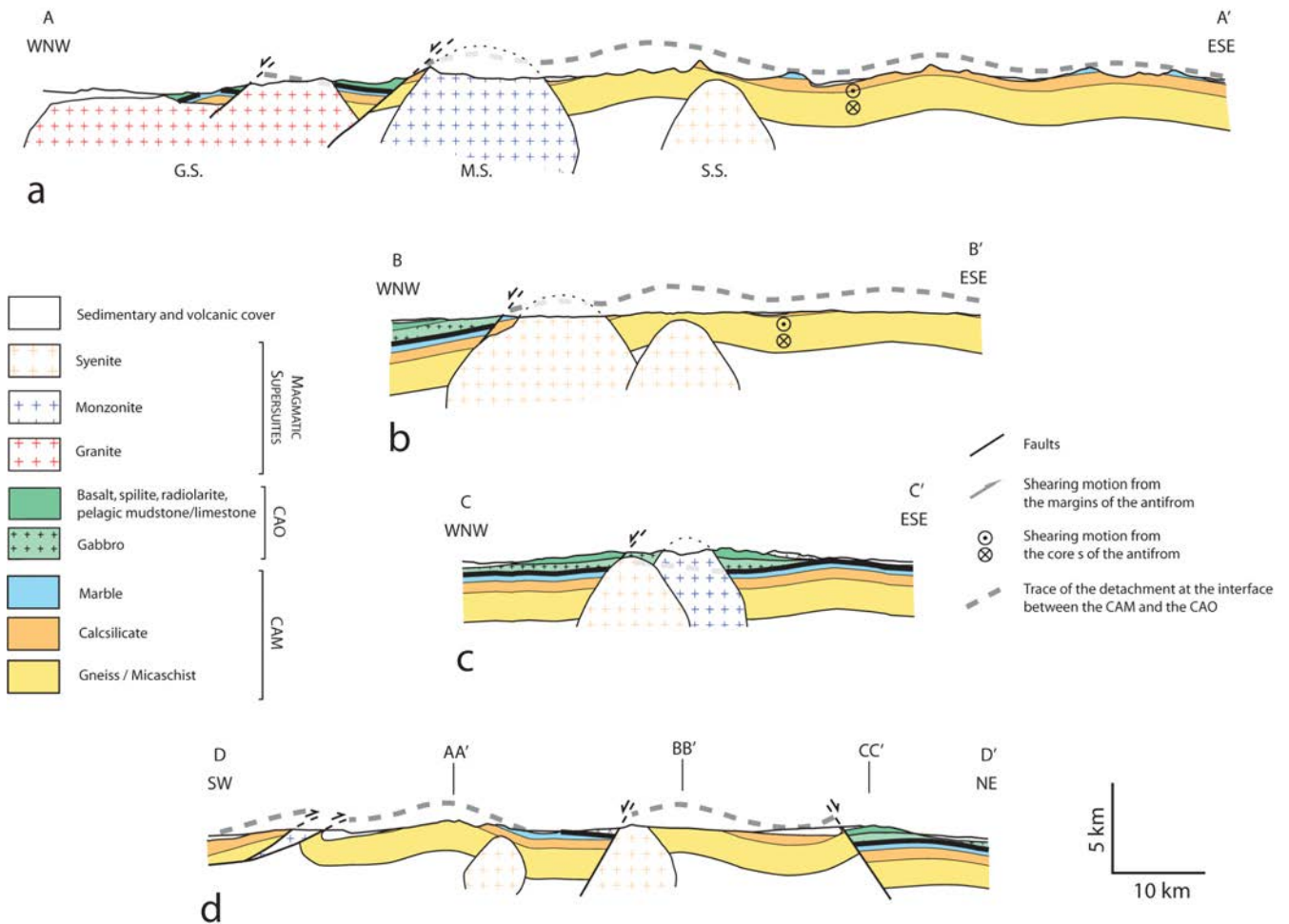


Figure 4.9 Upper crustal cross-sections across the Kırşehir Massif: a) WNW-ESE oriented southern section, b) WNW-ESE oriented central section, c) WNW-ESE oriented northern section, and d) NNE-SSW oriented section. Note vertical exaggeration.

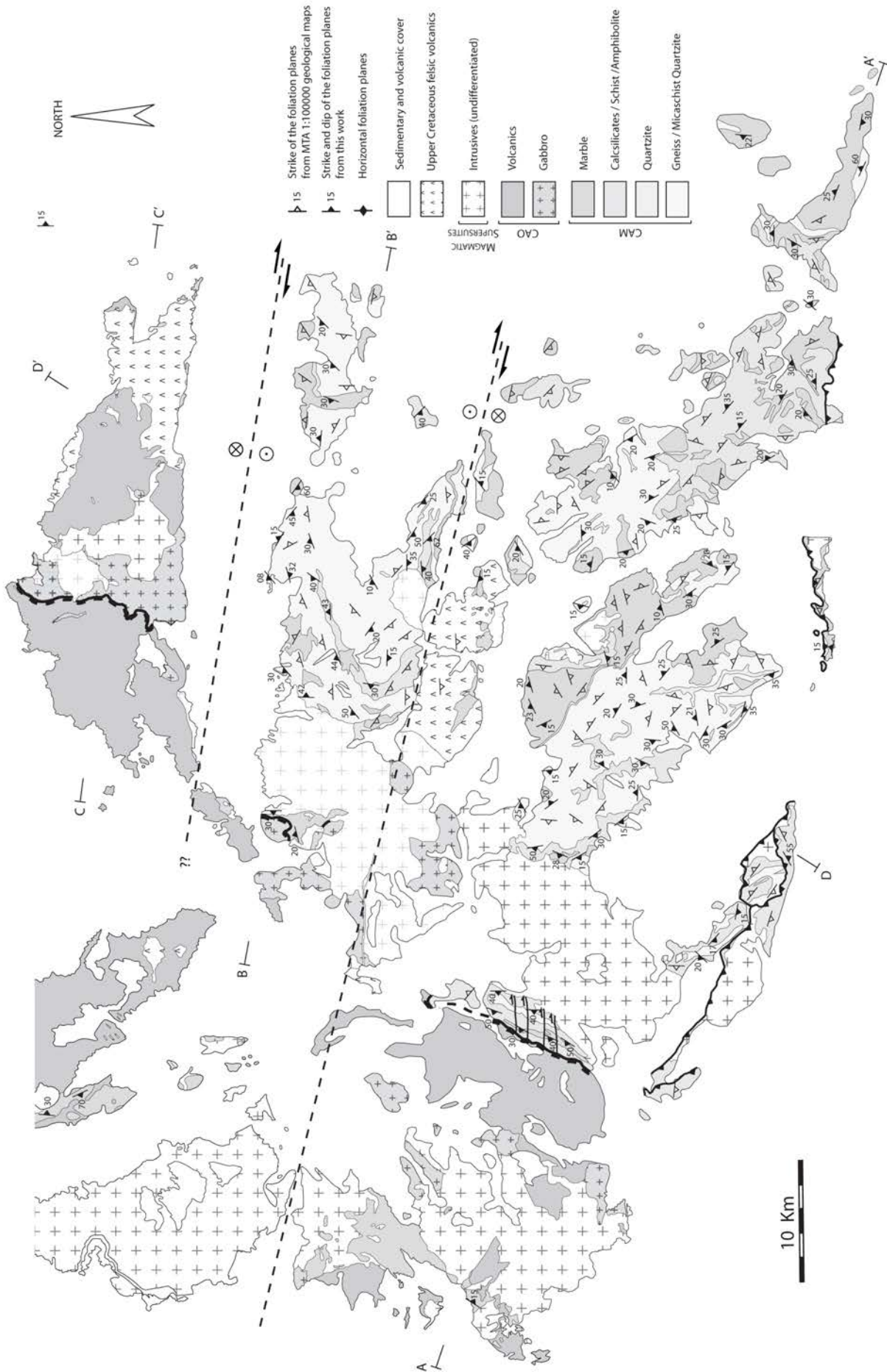


Figure 4.10 Map of foliation planes in the Kırşehir Massif, compiled from data reported on the 1:100000 geological maps from MTA (Directorate of Mineral Research & Exploration of Turkey, sheets Kırşehir-G17 and G18), and data collected in this study.

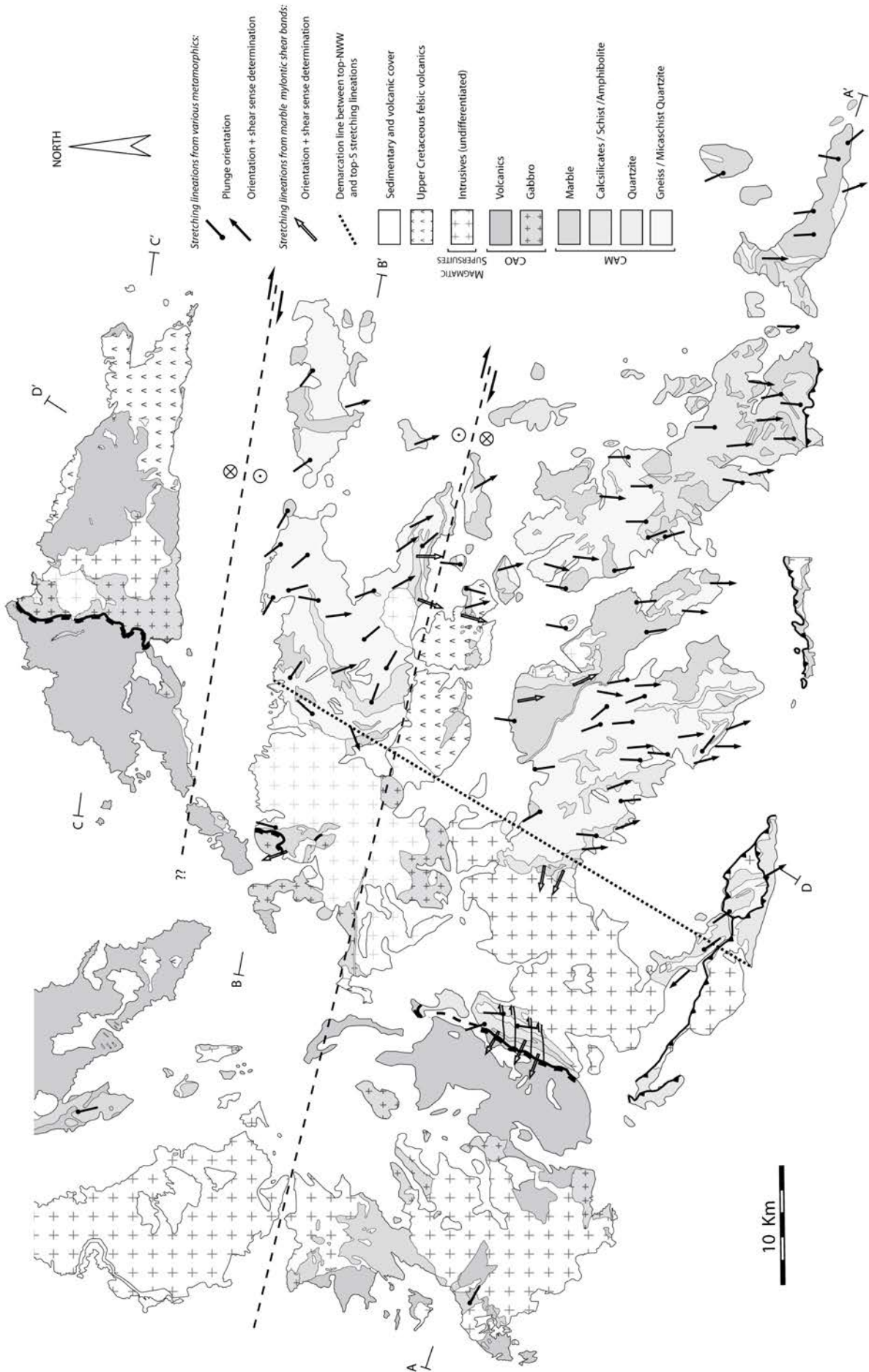


Figure 4.11 Map showing stretching lineations in the Kırşehir Massif.

(Figure 4.11). The transition between the Western and Central domains occurs in a zone of few kilometers wide.

Near Kaman, the NNE-SSW trending Kaman detachment is exposed [Lefebvre et al., 2011]. To the north, more or less along-strike, similar contacts separating high-grade marbles from non-metamorphic ophiolitic gabbros are found (Figure 4.3). We tentatively trace the Kaman detachment northeastward to the Çiçekdağı area, where a ~N-S trending fault has been described to separate the Akçakent gabbro from the Çökelik volcanics (Yılmaz and Boztuğ 1998). Although speculated to represent a thrust by these authors, we believe that this tectonic contact likely represents an extensional structure (Figure 4.3 and cross-sections Figure 4.9) parallel to, and probably continuous with the Kaman detachment. We also emphasize that the strike of the Kaman detachment fault is following exactly the trend of the monzonite/syenite belt located to the east of the detachment. In this configuration, the three segments we infer to relate to the Kaman detachment, are not aligned but are right-laterally offset. Similar offsets may be observed from the trend of the eastern margin of the monzonite/syenite belt. Constructed cross-

sections (Figure 4.9) throughout the massif also shows sudden changes of vertical positions of the main lithologies across valleys, and we infer the possible presence of E-W trending high-angle faults to explain these (Figure 4.9). In the central part of the massif, shallow marbles are covered by upper Cretaceous rhyolites (the ‘Karahıdır’ volcanics, Figures 4.3 and 4.9d). The northern contact of this volcanic rock-unit with the lithostratigraphically deeper levels of the metamorphic series and syenitic bodies is markedly abrupt. The same probably applies for the northern Çiçekdağı basin, where high grade metamorphics in the south are separated from the northern CAO by an upper Eocene sedimentary basin, which may be underlain by a (pre-sedimentary) normal fault hidden below the basin (Gülyüz et al. submitted). We propose that these two E-W oriented structures may represent two steep, post-detachment normal faults with a right-lateral component of motion (Figures 4.3 and 4.9d), separating the Kırşehir Massif in three E-W oriented “blocks”, of which the central one has been uplifted relative to the southern and northern blocks (Figure 4.3 and cross-sections Figure 4.9).

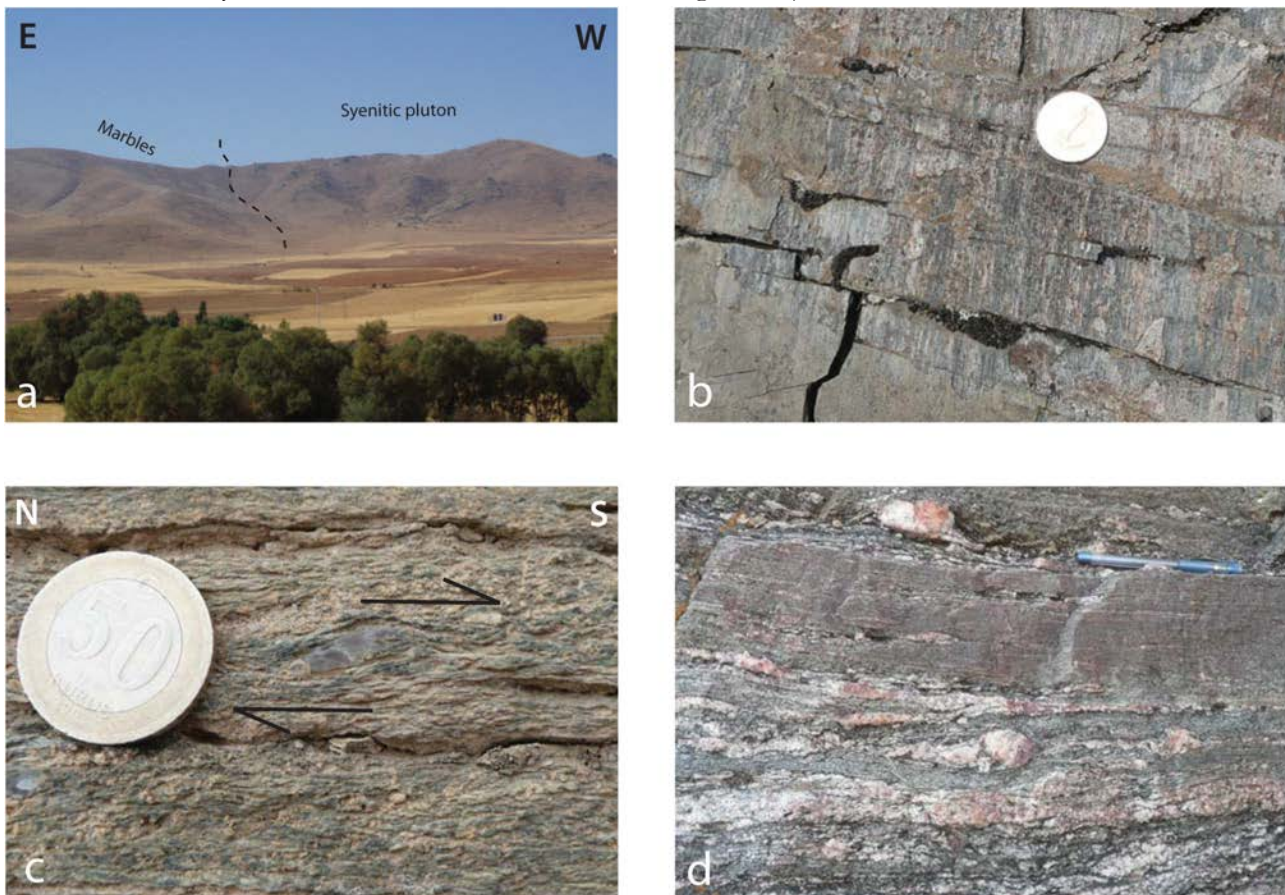


Figure 4.12 Field pictures of metamorphic rocks from the Kırşehir Massif. a) Panorama view from the centre of the massif showing the relation between marbles and syenitic intrusions. Note that the west-dipping foliation in the metasediments is crosscut by the massive intrusion (b) example of a well developed stretching lineation from the area east of Kırşehir, (c) Actinolite-quartz muscovite schist from the low grade zone, east of Kırşehir. The  $\sigma$ -clast of quartz indicates a top-to-the-south sense of shear, (d) migmatites exposed in the vicinity of the Baranadağ pluton, west of Kırşehir.

#### 4.4.2 Regional metamorphic pattern

The spatial distribution of the regional metamorphism and associated field gradient in the Kırşehir Massif is subject of debate. Two contradictory metamorphic patterns have been proposed, in which temperatures of regional metamorphism increase either from south to north (Erkan 1976), or from east to west (Seymen 1981, Whitney et al. 2001) (Figure 1.3). These two different metamorphic field gradients are both based on the mapping of mineral isograds. A compilation of the index metamorphic minerals from metapelitic compositions reported in the literature is presented in Figure 4.13. To resolve this matter, we performed a widespread sampling, focusing preferentially on areas that were not previously covered (Figure 4.13). As in the Akdağ Massif, we mainly focused on metapelitic rocks. Dominant characteristic single metamorphic minerals are sillimanite, biotite and muscovite, and the mineral assemblages are sillimanite-Kfeldspar, cordierite-spinel, biotite-garnet, biotite-muscovite, biotite-actinolite and muscovite-chlorite. In addition, migmatites occur near the contact with the western Baranadağ pluton (Figure 4.12d). The spatial distribution of those index minerals and assemblages are reported in Figure 4.13. In comparison with previous studies (Seymen 1984, Whitney et al. 2001), the domain where sillimanite is present in the southern part of area, has been extended toward the east. In this part of the massif, our extended petrological sampling confirms the tendency of decreasing temperature of metamorphism toward the east, with typical mineral assemblages of the M/LG Zone (muscovite, muscovite+chlorite, biotite+actinolite) in the area east of Kırşehir city (Figure 4.12c). The transition between the HG Zone and the M/LG Zone occurs to the NW of the city of Kırşehir and has a NE-SW orientation (Figure 4.13). In addition, we also confirm the presence of sillimanite+K-feldspar assemblages in the north of the massif, as previously reported by Erkan (1976) and used to postulate a N-S oriented metamorphic field gradient. In this area south of the Çiçekdağı basin, no significant variations of metamorphic conditions are observed, and the rocks belong to the HG Zone. From the eastern part of the Kırşehir Massif, we ascribe the abrupt change of the metamorphic contrast from south to north to the offset of the inferred E-W oriented right-lateral normal faults, leading to exposure of deeper levels of the metamorphic succession in the northern area as a result of differential uplift (Figures 4.9d and 4.13). We note that in the case of the southern Kırşehir Massif, the transition

between the HG Zone toward the M/LG Zone from west to east does not affect the consistently N-S oriented top-south stretching lineations (Figures 4.11 and 4.13). As in the Akdağ Massif, the metamorphic assemblages were formed during formation of the regional pervasive foliation and shearing (Figure 4.12).

#### 4.5 $^{40}\text{Ar}/^{39}\text{Ar}$ geochronology

To obtain chronological control on the timing of cooling of the metamorphic rocks of the Akdağ and Kırşehir Massifs, and the timing of extrusion of the Karahıdır volcanics, we selected several samples for  $^{40}\text{Ar}/^{39}\text{Ar}$  geochronology.

From the low-grade metamorphic rocks in the east of the Kırşehir Massif, we selected two metapelitic schists with a paragenesis of Bt+Ms+Chl+Qz±Act (samples [K16107A] and [K18099B]). From the high grade schists exposed in north of the massif we sampled a Sil+Kfs+Bt+Qz bearing schist [sample K21099A]. From the center of the massif a coarse grained rhyolite belonging the Karahıdır volcanics (Seymen 1982, Tolluoğlu 1993) was dated [sample K06108H]. In the eastern part of the Akdağ Massif we collected sample A22109C, a high-grade metapelitic Sil+Bt+Ms+Qz schist. Sample A19109B from the west of the massif, is a high-grade schist with Sil+Bt+Qz as main mineral assemblage, containing centimeter large patches of intergrown sillimanite and quartz. Locations of the samples are presented in Figures 4.8 and 4.13.

Samples were crushed, sieved and washed in acetone and distilled water. Biotite (K16107A, K18099B, K21099A, A22109C and A19109B) and K-feldspar (K06108H, A19109B) were separated using standard techniques and fresh inclusion-free mineral grains were handpicked under the binocular microscope.

The transformation  $^{39}\text{K}(n, p)^{39}\text{Ar}$  was performed during irradiation at the IFE Kjeller reactor in Norway, using the Taylor Creek Rhyolite as flux monitor (28.619 +/- 0.034 Ma; (Renne et al. 2010)). Samples were step heated in the  $^{40}\text{Ar}/^{39}\text{Ar}$  lab at the Geological Survey of Norway using a Merchantek MIR-10 CO<sub>2</sub> laser. The extracted gases were swiped over getters (SAES AP-10) for 2 minutes, and then for 9 minutes in a separate part of the extraction line. The peaks were determined by peak hopping (at least 8 cycles) on masses  $^{41}\text{Ar}$  to  $^{35}\text{Ar}$  on a Balzers electron multiplier on a MAP 215-50 mass spectrometer. Data from unknowns were corrected for blanks (every 4th analysis is a blank) prior to being reduced with the IAAA software package (Interactive Ar-Ar Analysis, written by M. Ganerød, NGU Trondheim,

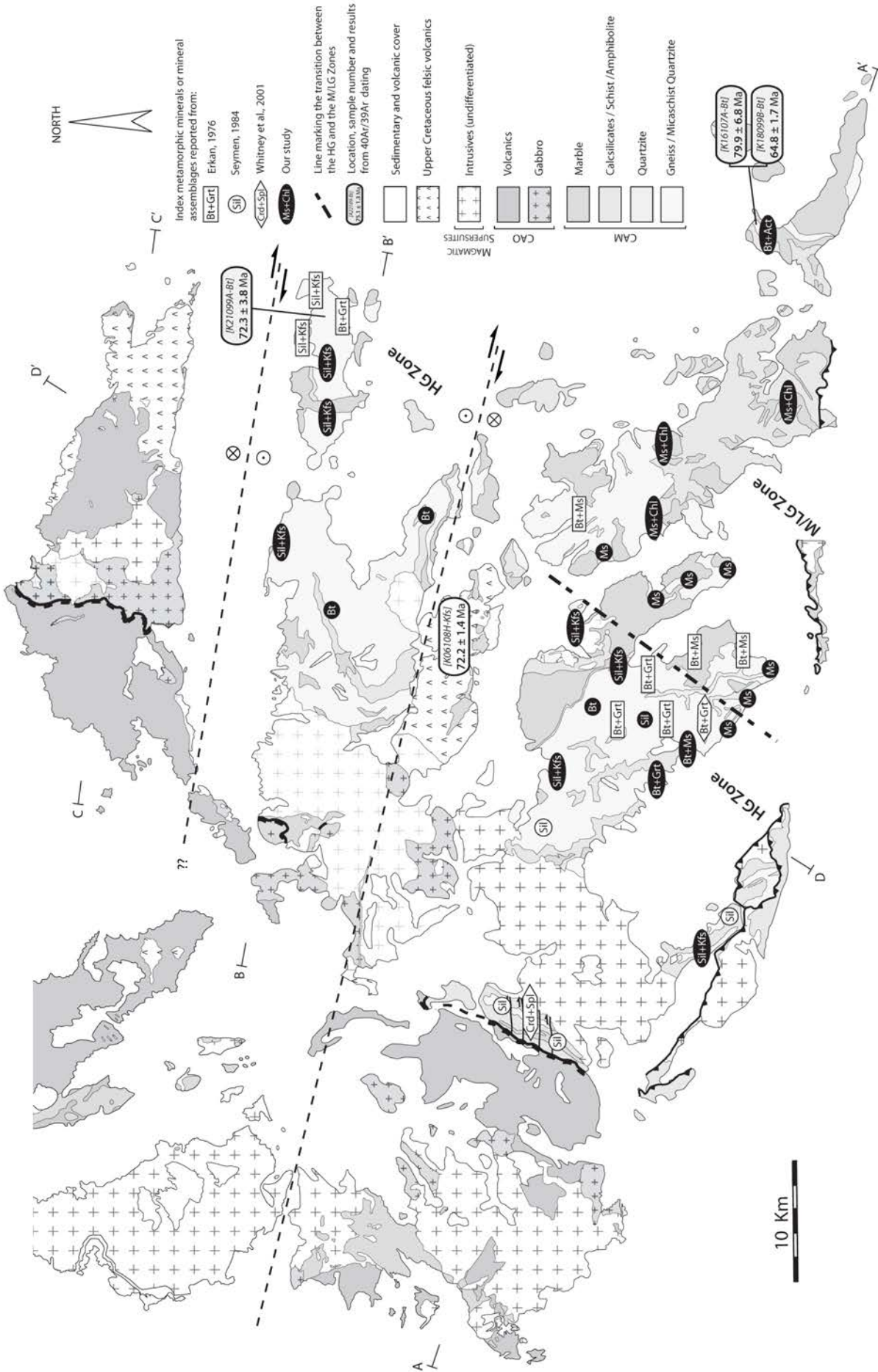


Figure 4.13 Map of index metamorphic minerals and mineral assemblages in the Kırşehir Massif. Locations and interpreted ages of samples used for 40Ar/39Ar thermochronology are shown. The grey and white panels represent ages of the metamorphic rocks and rhyolite, respectively.

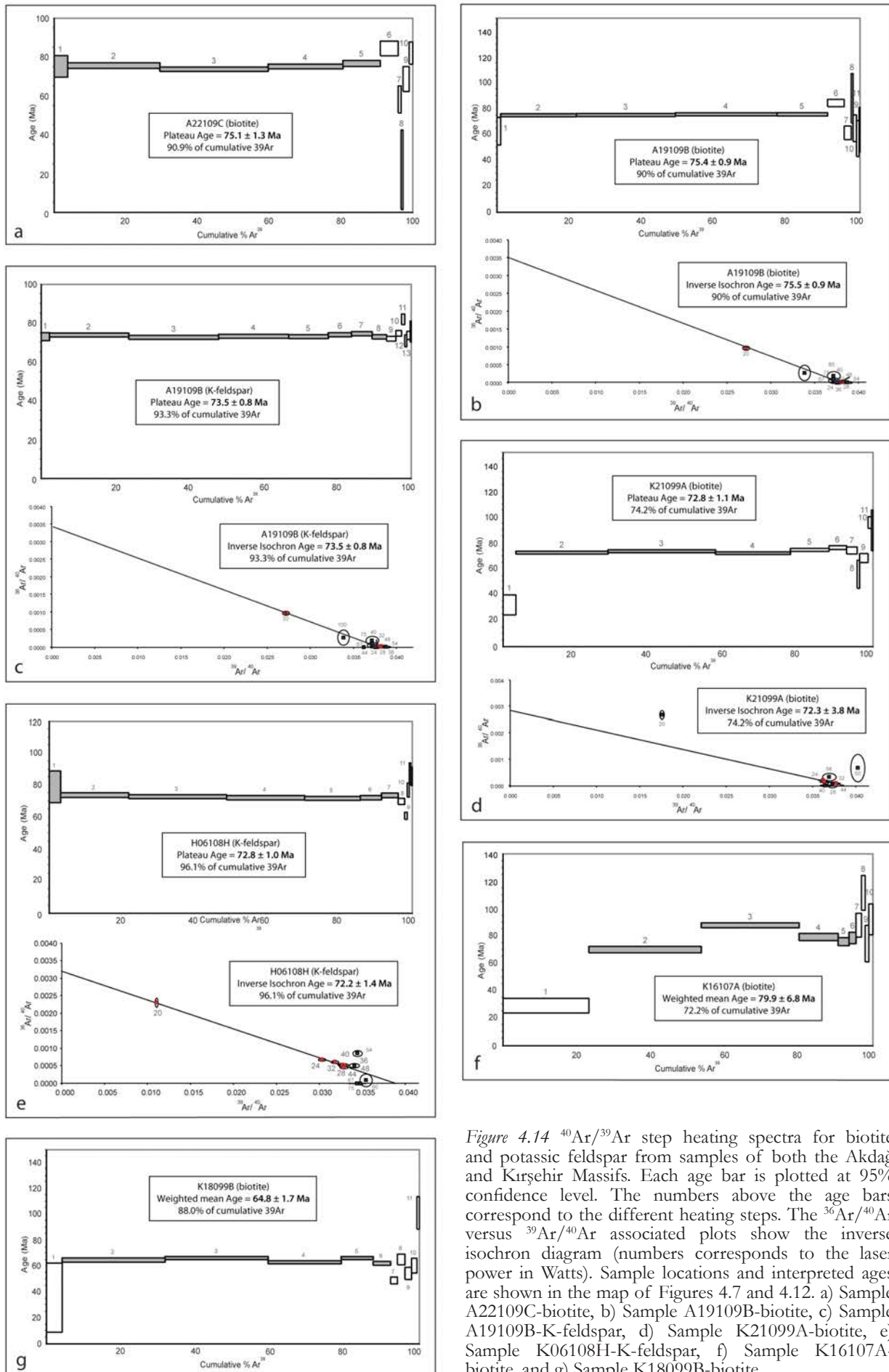


Figure 4.14  $^{40}\text{Ar}/^{39}\text{Ar}$  step heating spectra for biotite and potassic feldspar from samples of both the Akdağ and Kırşehir Massifs. Each age bar is plotted at 95% confidence level. The numbers above the age bars correspond to the different heating steps. The  $^{36}\text{Ar}/^{40}\text{Ar}$  versus  $^{39}\text{Ar}/^{40}\text{Ar}$  associated plots show the inverse isochron diagram (numbers corresponds to the laser power in Watts). Sample locations and interpreted ages are shown in the map of Figures 4.7 and 4.12. a) Sample A22109C-biotite, b) Sample A19109B-biotite, c) Sample A19109B-K-feldspar, d) Sample K21099A-biotite, e) Sample K06108H-K-feldspar, f) Sample K16107A-biotite, and g) Sample K18099B-biotite.

Norway) that implements the equations in McDougall and Harrison (1999) using the decay constants of Renne et al. (2010) and the trapped  $^{40}\text{Ar}/^{36}\text{Ar}$  ratio of  $298.56 \pm 0.31$  of Lee et al. (2006). Data reduction in IAAA incorporates corrections for interfering isotopes (based on  $\text{K}_2\text{SO}_4$  and  $\text{CaF}_2$  salts included in the irradiation package), mass discrimination, error in blanks and decay of  $^{37}\text{Ar}$  and  $^{39}\text{Ar}$ . We define a plateau according to the following requirements: at least three consecutive steps, overlapping at the 95% confidence level, together comprising at least 50% of total  $^{39}\text{Ar}$  and mean square of weighted deviates (MSWD) less than the two tailed student T critical value (Spiegel 1991). We use the weighted York-2 method to calculate the inverse isochron results, with statistically valid isochrons having a MSWD value less than the two tailed F-test critical value.

The high grade schist [A22109C-biotite] in the east of the Akdağ Massif has a plateau age of  $75.1 \pm 1.3$  Ma (Figure 4.14a). In the west of the Akdağ, the high grade schist [A19109B-biotite] yields an inverse isochron age of  $75.5 \pm 0.9$  Ma, and [A19109B-K-feldspar] gives  $73.5 \pm 0.8$  Ma (Figures 4.14b-c).

The high grade schist from the north of the Kırşehir Massif [K21099A-biotite] yields an inverse isochron age of  $72.3 \pm 3.8$  Ma (Figure 4.14d). The sample from the central Karahıdır rhyolite [K06108H-K-feldspar] yields an inverse isochron age of  $72.2 \pm 1.4$  Ma (Figure 4.14e). The two samples from the low grade metamorphics from the eastern part of the Kırşehir Massif failed the statistical requirements for a plateau or isochron age. However, a potential age for those samples can be derived via calculation of weighted mean ages: [K16107A-biotite] weighted mean age gives  $79.9 \pm 6.8$  Ma, and the [K18099B-biotite] weighted mean age is  $64.8 \pm 1.7$  Ma (Figures 4.14f-g). Note that the obtained cooling ages from the eastern low grade schists differ by 15Ma, while the samples were collected from nearby localities close. However, for sample K18099B the spectrum (Figure 4.14g) is still relatively flat but the heating steps do not overlap each other. For sample K16107A the spectrum is clearly more disturbed and the geological relevance of the weighted mean age calculated here is limited.

## 4.6 Discussion: development and evolution of the northern central Anatolian HT domes

### 4.6.1 Structure

The overall shape and shear senses of the Akdağ and Kırşehir Massifs is summarized in the interpretative sketches of Figure 4.15. Even

though few foliation planes may appear relatively steep in places (especially in the Akdağ Massif), the cross-sections across these massifs (Figures 4.4a and 4.9a) show that the large-scale enveloping surfaces to the foliated metamorphic succession have relatively gently dipping antiformal shapes at the scale of the massifs ( $> 100\text{-km}$  wide).

In both massifs, the antiforms are bounded by major faults (except for the eastern side of the Kırşehir Massif which is unconformably covered by sediments). In the case of the Kırşehir Massif, ophiolites and intrusives which cover the western part of the area, are more common than in the Akdağ Massif. The two metamorphic massifs have a strikingly similar internal organization (Figures 4.4, 4.9 and 4.15): (1) in the northern (Akdağ) or western (Kırşehir) margin, the IAESZ over-thrust the crystalline massifs toward the south and east respectively. We note that along the northern margin of the Akdağ Massif, the IAESZ clearly covers a part of the metamorphic dome, while in Kırşehir the IAESZ rocks are mostly exposed outside of the crystallines (Figure 4.15). (2) Within the massifs and near the IAESZ, large plutons of  $\sim 100\text{km}$  long and few tens of kilometers wide are bordering the massifs. As noticed by Kadioğlu (2006), the migration and geochemical evolution of the magmatic supersuites can clearly be observed from an outer towards an inner position within the massifs (Figure 4.15). The intrusive rocks comprise granite, monzonite and syenite supersuites, and their crosscutting relationships demonstrate that the magmatic activity migrated in a southerly (in Akdağ), or easterly (in Kırşehir) direction through time. (3) A large area of  $\sim 70\text{-}80\text{km}$  wide south and east of the intrusive suite is almost essentially composed of metasediments with a few syenitic intrusions (Figures 4.3 and 4.15). Within those metasediments, the regional pattern of stretching lineations reveals distinctive domains within the domes. First, we distinguished a central domain mostly located in the center of each antiform where the sense of ductile shearing is contemporaneous with regional metamorphism and consistently top-to-the-SW in Akdağ and top-to-the-S in Kırşehir. We note the similarity between the direction of shearing in the central domains and the trend of the magmatic belts. Secondly, marginal domains make up the adjacent sides of the massifs, where shearing occurs in a different direction. Also associated with the regional metamorphism, stretching and mineral lineations in the marginal domains occur at high angles (nearly orthogonal) to those in the central domain. In the Akdağ Massif, the widespread exposure of metamorphic rocks allows a good appreciation of the regional pattern of shearing (Figure 4.15). The stretching lineations

from both the NW and SE margins of the Akdağ Massif are more or less parallel, but have opposite senses of shear, with top motion away from the apex of the antiformal central domain. On the other hand, in the Kırşehir Massif, the marginal domains are not so well preserved, probably

because of the ubiquitous plutons in the west and a sedimentary cover in the east. The coexistence of two contemporaneous domains of ductile shearing is a characteristic for all central Anatolian metamorphics as they have been found in each of the large metamorphic massifs. Gautier (2008)

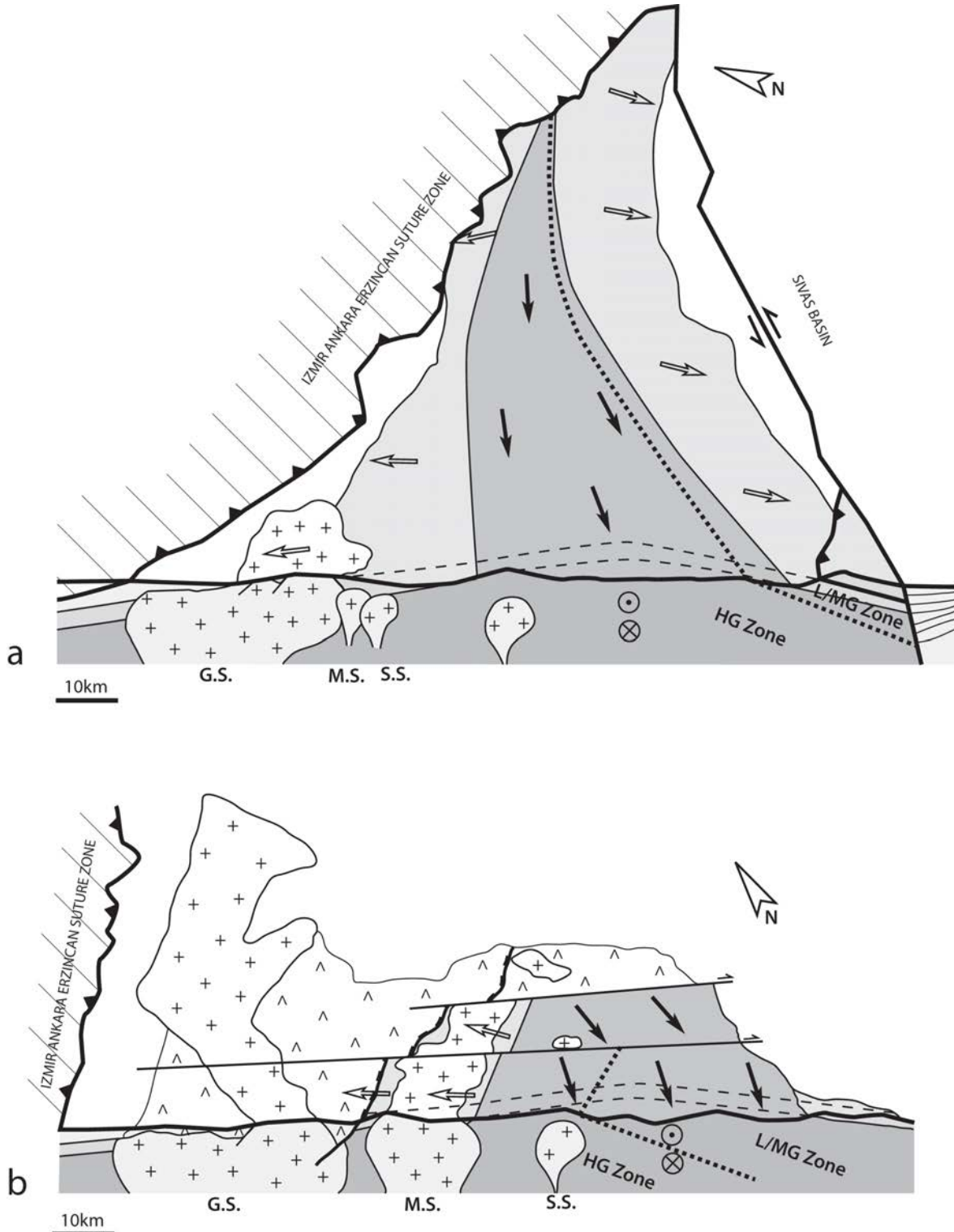


Figure 4.15 Interpretative sketches of the main morphology of the northern central Anatolian domes. a) The Akdağ Massif, and b) the Kırşehir Massif. The dark grey areas represent domains affected by lateral flow in the cores of the antiformal domains. The associated shearing is illustrated by the black arrows. The light grey areas represent domains affected by shearing at the edges of the antiformal domains, which is at high angles with the inner flow. The associated shearing is illustrated by the white arrows. G.S., M.S., and S.S. refer to granite supersuite, monzonite supersuite and syenite supersuites (Kadioğlu et al. 2006). The thick dashed black line represents the sillimanite isograd.

proposed that such coeval shearing structures may result from lateral flow in the core of the dome, orthogonal to shearing at higher levels, reflecting deformation related to the displacement along extensional detachment faults at the sides of the dome. Our structural analysis from the northern massifs seems at first inspection to be in good agreement with this proposal, with the Kaman detachment as upper crustal detachment fault identified in the western marginal domain, and acting sub-perpendicular to the dominant stretching direction of the central domain (Figure 4.11) (Lefebvre et al. 2011; Chapter 1).

However, we notice important differences between the detachment described in the Niğde Massif (Gautier et al. 2002) and the one in Kaman. In the Niğde area, below gabbros of the CAO, the metamorphic rocks are ductily sheared, overprinted by limited brittle deformation along planes parallel to the main foliation. These authors argued that this structure is very similar to Cordilleran-type extensional detachments, which typically root in the middle or lower crust (Lister and Davis 1989). On the other hand, in Kaman, the detachment is only developed in localized calcite shear-bands, and crosscut the regional metamorphic foliation. From this, we infer that the extensional detachment in Kaman probably acted at upper crustal greenschist facies conditions postdating the regional metamorphic shearing deformation. This detachment is very similar to the one described in the Hırkadağ Block (Chapter 2). Therefore, it seems that 2 types of detachments coexist in the CACC: (1) detachments which penetrate into the lower crust, such as the one in the Niğde Massif. At the scale of the northern metamorphic domes, the syn-metamorphic shearing characteristic of the marginal domains is likely associated with this type of detachment responsible for exhuming the metamorphics from lower crustal to mid/upper crustal depths; (2) upper crustal detachments, which exhumed rocks from mid/upper -crustal depths to near the surface (like in Kaman and Hırkadağ).

Finally, from the displacement of the northward prolongation of the Kaman detachment, we inferred the presence of steep normal faults with a right lateral component of motion. They cross-cut and therefore postdate the latest Cretaceous activity of the detachments. We presume that both metamorphic massifs are affected by a network of those steep dextral normal faults, which are ~E-W oriented in the Kırşehir Massif, and NW-SE oriented in the Akdağ Massif. The Eocene Çiçekdağı basin, with a ~38-35 Ma old stratigraphy covers, hence postdates the activity of one of these inferred faults (Gülyüz et al. submitted).

#### 4.6.2 Metamorphism

The sillimanite isograd mapped in the Akdağ and Kırşehir Massifs has been chosen as a marker for the transition between HG and M/LG Zones. In the Akdağ Massif, this transition trends NE-SW and runs close to the boundary between the central and southern domains of shearing. In the Kırşehir Massif, the transition is NNE-SSW orientated and situated in the center of the metamorphic massif (Figure 4.15). Taking the geometry of the antiforms and the distribution of index minerals into account, we interpreted the sillimanite isograd as dipping to the SE in Akdağ, and to the SSE in Kırşehir. The difference in the position of the sillimanite isograds within the Akdağ and Kırşehir domes relative to the shearing domains may be explained by the fact that both massifs present different structural levels of the domes, with the Akdağ Massif showing a deeper section than the Kırşehir Massif. This is consistent with the occurrence of kyanite in the central Akdağ Massif, which has not been found in the Kırşehir Massif.

In the interpretation of Gautier et al. (2008) of the kinematics of shearing in the Niğde Massif, the southward oriented ductile flow would be effective at the deepest crustal levels of the dome, corresponding to a low-viscosity lower crust. However, our data show that even if the lateral flow is mostly situated in the core of antiforms, the example of the Kırşehir Massif shows that it also affects shallower crustal levels, as the eastern M/LG Zone also recorded the lateral inner flow.

It is important to realize that at the scale of the Akdağ and Kırşehir dome-shaped antiforms, the thermal distribution is asymmetric because low grade metamorphism only occurs in the SE and E margins respectively, while the rest of the massifs record high grade regional metamorphism. The concentration of intrusions at the NW and W margins of the massifs (corresponding to the HG Zone) also lends support to an asymmetric transient thermal structure within the domes. In addition, we note that the sillimanite isograds are distributed along, and parallel to the elongated intrusives bodies, with a decrease of the metamorphic grade away from these bodies. However, even though the magmatic intrusions cannot have produced the observed regional HT metamorphism (as they are mostly postdating peak metamorphism (e.g. Akıman et al. 1993) and cut across the syn-metamorphic foliation planes), we notice a strong correlation between the regional trends of metamorphism and following magmatism.

Consistent with previously published dating results, our  $^{40}\text{Ar}/^{39}\text{Ar}$  ages show that the cooling

of the two northern massifs of the CACC is remarkably synchronous, with cooling below the  $\sim 350^{\circ}\text{C}$  isotherm (corresponding to the blocking temperature of Ar in biotite (Grove and Harrison 1996)) around  $\sim 75$  Ma, and cooling below the  $\sim 250^{\circ}\text{C}$  isotherm (blocking temperature of Ar in K-feldspar (Harrison and McDougall 1982, McDougall and Harrison 1999)) around  $\sim 73.5$ -72 Ma. These ages are on the young end of the published spectrum of exhumation ages of 88-67 Ma (Whitney et al. 2003, Whitney et al. 2007, Gautier et al. 2008, Isik et al. 2008, Boztuğ et al. 2009b, Chapter 2). This suggests that cooling and exhumation of the CAM occurred more or less simultaneously, during the same tectonic period.

The identical ages obtained in the Kırşehir Massif, from both metamorphics cooling down at crustal depths and from the volcanics extruded at the surface, suggest the presence of a major tectonic contact in between them. We suggest that the system of steep E-W-trending dextral normal faults may be a good candidate (Figures 4.3 and 4.13).

#### 4.6.3 *The Akdağ and Kırşehir Massifs: a single or two different dome(s)?*

Although the Akdağ and Kırşehir Massifs present an internal consistency in the geometry of their ductile structures and distribution of regional metamorphic grade, there seems to be a discontinuity of the main trends between the two massifs in the present-day configuration of the CACC (Figure 4.16a). Our recent paleomagnetic survey carried on central Anatolian granitoids (Chapter 3), however, shows that the metamorphic antiforms, in their present configuration, are not representative for their original orientation and relative position during the late Cretaceous. Large rotations and potentially associated deformation have been recorded in the neighboring granites. The granitoids north of the Akdağ Massif (the YYB) underwent  $\sim 30^{\circ}$  (or  $15^{\circ}$ ) of clockwise rotation since their magnetization during cooling. The granitoids situated in the west of the Kırşehir Massif (the KKB) did not record any significant rotation (or rotated  $\sim 10^{\circ}$  ccw). In order to accommodate these relative rotations and explain offset granitoid belts, the Delice-Kozaklı Fault Zone (DKFZ) was postulated between the YYB (Akdağ) and KKB (Kırşehir), and has been defined as a potential major dextral-transpressive fault with an offset of  $\sim 100$  km. In Figure 4.16b, we present the relative positions of the Kırşehir and Akdağ Massifs for the case that the entire Akdağ Massif is rotated back over  $\sim 30^{\circ}$  (or  $15^{\circ}$ ), and restored  $\sim 90$  km along the DKFZ toward the NW.

The restored configuration (Figure 4.16b) clearly shows a continuity between stretching lineations of the central and the marginal domains for both Akdağ and Kırşehir Massifs. The central domain exhibit consistent top-south direction of shear, while the marginal domains show a general WNW-ESE oriented shearing with opposite sense of shear on each side of the central domain. The sillimanite isograds delimitating the HG Zone from the M/LG Zone have similar strike. The previously described network of steep dextral normal faults, with  $\sim$ E-W orientation in the Kırşehir Massif, and NW-SE direction in Akdağ Massif also appear parallel to each other in this configuration. In addition, the reconstructions of Chapter 3 lead to the alignment of the each of the three magmatic supersuites (i.e. granite, monzonite and syenite supersuites) (see Chapter 3). All these independent datasets seem to be consistent with the late Cretaceous configuration inferred from paleomagnetic data. We therefore propose that during the late Cretaceous, the two northern metamorphic massifs formed one single NNE-SSW oriented crustal-scale dome-shaped antiform (Figure 4.16b).

## 4.7 Conclusion

The structural and metamorphic evolution of the northern central Anatolian massifs have been investigated via large scale mapping of structures (such as foliations and stretching lineations) and index metamorphic minerals and mineral assemblages. The two metamorphic Akdağ and Kırşehir Massifs have striking similarities: (1) a general structure of a gently dipping widely opened antiform of 150 km wide, defined by the regional foliation, (2) the presence of two differently oriented, coeval syn-metamorphic shearing domains, one in the relatively deep core and one in the relatively shallow margins of the antiforms, (3) a regional HT metamorphic gradient decreasing from high to low temperature towards the southeast (Akdağ) and east (Kırşehir), away from the location of magmatic belts. As already proposed for the southern Niğde Massif (Gautier et al. 2008), it is likely that the two shearing directions reflect lateral flow in the core of the antiform-like structures. This lateral flow occurred at high angles to the shearing at shallower levels which records deformation in response to displacement along detachment faults. In their current configuration, it is difficult to link the structures mapped in Akdağ and Kırşehir Massifs. However, a restoration involving  $30^{\circ}$  (or  $25^{\circ}$ ) of relative clockwise rotation between the massifs and displacement along the Delice-Kozaklı Fault Zone (DKFZ) (inferred on

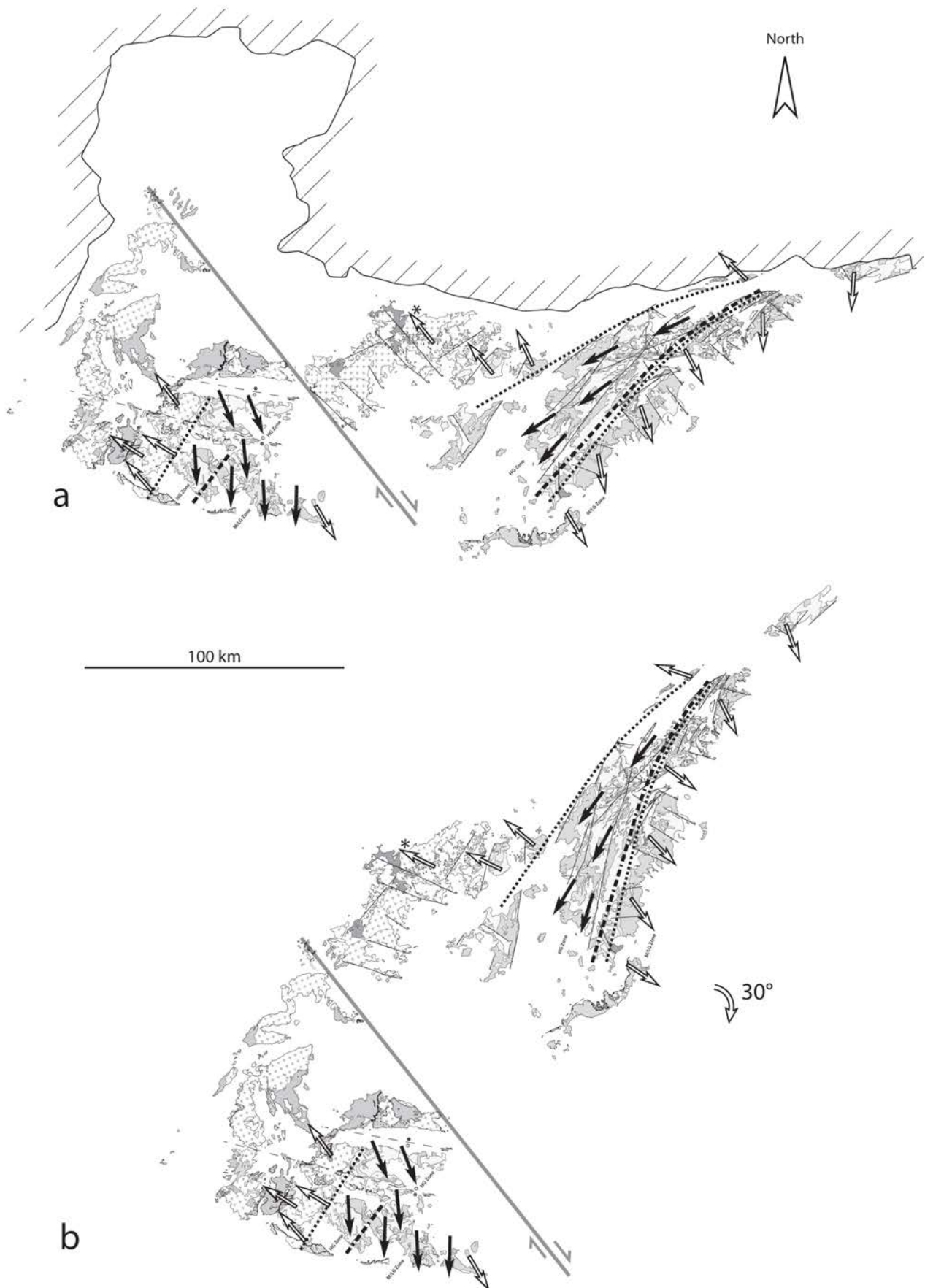


*Figure 4.16* Reconstruction and assemblage of the two massifs via the DKFZ. a) Present configuration, b) possible reconstruction for the northern central Anatolian massifs in the late Cretaceous, taking into account the rotations of the YYB relative to the KKB ( $\sim 30^\circ$  CW) and the presence of the DKFZ (see chapter 3). The thick dashed-dot line represents the sillimanite isograd. Black dotted lines delineate the boundaries between domains affected by lateral flow in the core and oblique shearing at the edge of the domes. Black and white arrows show direction and sense of ductile shearing in the cores and the margins of the antiformal domains, respectively (as in Figure 4.15).

the basis of the paleomagnetic results presented in chapter 3) leads to a restored configuration in which all structural and metamorphic data of the two massifs become aligned and consistent. In this restored configuration, the ductile shearing in the core of the antiformal domains show a consistent top-to-the-south direction of shear, while a general WNW-ESE oriented shearing occurring at the margins of those domains, indicates a regional ~E-W extension. In addition, the metamorphic pattern becomes aligned, as does the main trend of the magmatic belts. We therefore propose that in the late Cretaceous, the northern metamorphic massifs likely formed part of a single NNE-SSW oriented antiformal HT domain.

### **Acknowledgements**

Pierre Gautier (Université Rennes 1) is highly thanked for the discussions about the tectonic and metamorphic evolution of the CACC. The age dating have been processed by Bart Hendriks and Morgan Ganerød (Geological Survey of Norway, Trondheim). The comments of my supervisors onto the manuscript were highly appreciated.

# CHAPTER 5



## The CACC during the Late Cretaceous: tectonic evolution and geodynamic setting

### Abstract

The Central Anatolian Crystalline Complex (CACC) mainly consists of metamorphic rocks, ophiolites and magmatic intrusions, which record a complicated tectonic history occurring during a relatively short time span in the late Cretaceous. In order to arrive at a plausible tectonic model for the evolution of the CACC, we reconcile published and newly collected structural, metamorphic and paleomagnetic data from the entire complex. The results of the paleomagnetic study (Chapter 3) permit a restoration of the CACC during the late Cretaceous, when its overall structure likely formed a NNE-SSW elongated and narrow dome-shaped antiform of ~500x150km. In this configuration, we can establish that the regional Barrovian metamorphism was accompanied with a top-to-the-SSW ductile crustal flow active in the deeper part of the antiform, while shallower parts of the antiform were synchronously affected by a WNW-ESE direction of extension during the exhumation of the CACC. Two generations of detachments accommodating the exhumation of the crystalline complex have been recognized. Mainly in the west of the CACC, three magmatic belts presenting, from west to east, a consistent younging and chemical evolution (from calc-alkaline to alkaline), have been recognized to have developed in a supra-subduction environment. It is likely that the island-arc tholeiitic lavas from the Central Anatolian Ophiolites represent an early-stage volcanic arc, while the central Anatolian magmatic suites reflect a more mature stage of the arc. At the scale of Anatolia, the vicinity between the newly recognized CACC magmatic arc and the western contemporaneous HP-LT Tavşanlı belt may be interpreted as a paired metamorphic belt, very similar to what have been described in Japan by Miyashiro (1961, 1973). Finally, northward subduction below the Pontides along an EW-trending suture in the late Cretaceous was coeval with eastward subduction on a NNE-SSW trending subduction system below the CACC. This suggests the presence of a Trench-Trench-Trench type (TTT) triple junction at the intersection of these two subduction zones.

## 5.1 Introduction

The Central Anatolian Crystalline Complex (CACC) is a wide domain of crystalline rocks including metamorphic and ophiolitic rocks and igneous intrusions, covered by mostly Cenozoic deposits. The burial, subsequent metamorphism and exhumation of the CACC is dominantly of late Cretaceous in age as inferred from geochronological studies of the different rock-units shaping the CACC. During the late Cretaceous, an oceanic crust of supra-subduction-zone affinity obducted onto Paleozoic-Mesozoic platform sediments (e.g. Yaliniz and Göncüoğlu 1998). Following ophiolite emplacement, the underthrust sediments became metamorphosed under regional Barrovian conditions (Erkan 1976, Seymen 1981, Whitney and Dilek 2001). This was soon followed by widespread intrusion of plutons into the foliated metasediments (Göncüoğlu et al. 1991, Akiman et al. 1993) (Figure 5.1). Therefore, the main crystalline components forming the CACC have been involved in a complicated tectonic history occurring during a short time span in the late Cretaceous. Understanding the genesis of, and relationships between these different crystalline units is a key to unravel this history, and to infer a plausible setting in which the CACC evolved during this period. Previous studies, mainly based on metamorphic and magmatic petrology as well as on structural analysis of the crystalline rocks, have proposed a variety of tectonic scenarios for the evolution of the CACC in the late Cretaceous. However, no consensus has been reached so far on the tectonic setting of the CACC.

In this chapter, we attempt to reconcile the published and newly collected data from the Central Anatolian metamorphic rocks, ophiolites and intrusions, based on structural, metamorphic and paleomagnetic techniques, into the simplest plausible (plate) tectonic scenario. We will first synthesize a regional compilation of structural and metamorphic data at the scale of the entire CACC. On the basis of the results obtained in our paleomagnetic study (chapter 3), we then propose a restoration of the CACC during late Cretaceous time. Based on this restoration, we will discuss the structural and magmatic evolution of the CACC at the scale of the massif, and view it in a wider Anatolian plate tectonic context.

## 5.2 Geology of the Central Anatolian Crystalline Complex

### 5.2.1 The Izmir-Ankara Suture zone between the CACC and the Pontides

In northern Turkey, the fold-thrust belt of the Pontides is separated from the CACC to the south by the Izmir-Ankara-Erzincan Suture Zone (IAESZ) (e.g. Okay and Tüysüz 1999) (Figure 5.1a). The IAESZ contains a sedimentary-tectonic mélange of pillow basalts and oceanic pelagic sediments (radiolarites) that were scraped off a subducting oceanic plate, as well as continental clastic foreland basin sediments shed from the Pontides. The pillow basalts in the Izmir-Ankara suture zone have MORB geochemical signatures, and the radiolarites have upper Triassic and Jurassic ages (Tekin et al. 2002).

The Pontides contain a volcanic arc with ages of at least ~95 Ma and younger (e.g. Okay et al. 2001). In addition, there are HP-metamorphic rocks exposed in a window below the Pontides north of the CACC that have ages of ~105 Ma (Okay et al. 2006). This shows that in late Cretaceous time, there was a north-ward dipping subduction zone below the Pontides.

### 5.2.2 The Central Anatolian Metamorphics (CAM): metamorphosed Paleozoic-Mesozoic sediments

The Central Anatolian Metamorphics (CAM) represent the oldest rock-unit exposed in central Anatolia (Göncüoğlu 1977, Göncüoğlu et al. 1991). The metasediments exposed near Ağaören contain *Heliolites paekelmannophora* sp. and fragments of *Retiolites* sp., suggesting a Silurian or early Devonian age of deposition (Kocak and Leake 1994). The stratigraphic succession present within the CAM is relatively similar throughout the CACC and mostly consists of a coherent sequence (from bottom to top) of gneiss, micaschist, quartzite, amphibolite, calcsilicate and marble (Figure 5.1c). The type of metamorphism which regionally affects those metasediments is Barrovian, and ranges from upper-amphibolite / granulite to greenschist facies (Erkan 1976, Seymen 1981, Whitney and Dilek 2001). Temperature and pressure estimates at peak metamorphic conditions are around 700-800°C for 6-8 kbar, with a local HT overprint at lower pressure (2-4 kbar) (Kocak and Leake 1994, Whitney and Dilek 1998, Whitney and Dilek 2001, Chapter 2) (Figure 5.1d). The age of the regional Barrovian metamorphism was assessed in high-grade metapelites of the Kırşehir and Niğde massifs, and constrained at around 91-84 Ma (using monazite and zircon U-Pb SHRIMP analysis) (Whitney et al. 2003, Whitney and Hamilton 2004) (Figures 5.1b and 5.1d). The regional metamorphism of the CAM was accompanied by ductile deformation, expressed by a pervasive, gently dipping foliation and associated isoclinal folding, and pervasive shearing

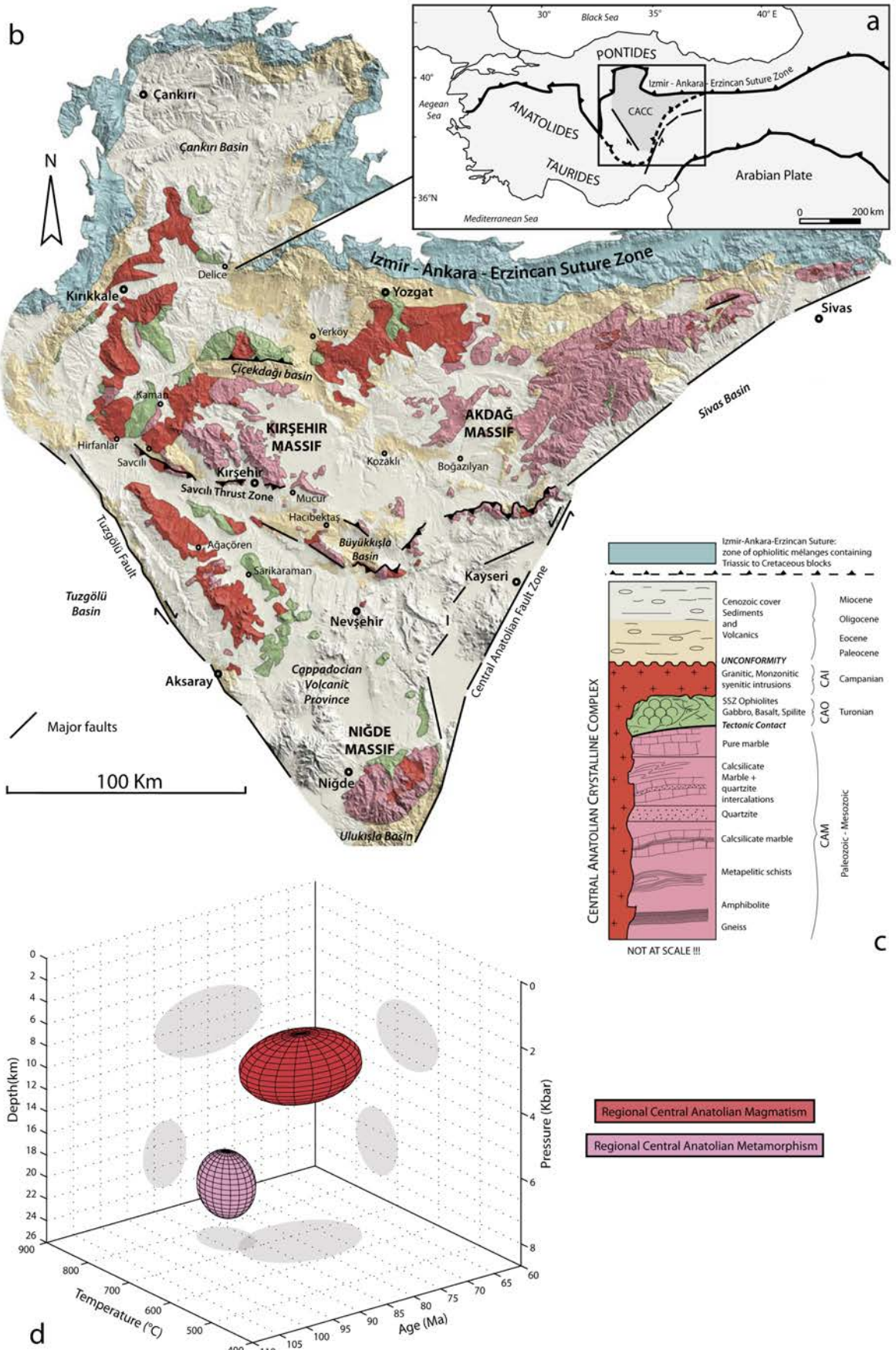


Figure 5.1 a) Location of the Central Anatolian Crystalline Complex (CACC) in the Turkish orogenic system. b) Simplified geological map of the CACC projected on a Digital Elevation Model. c) Simplified tectono-stratigraphic column showing the relationships between the main units of the CACC (not to scale). d) Pressure-Temperature-Time diagram representing constraints on Alpine regional metamorphic and magmatic events in Central Anatolia. For pertinent references see text.

(Göncüoğlu 1977, Seymen 1983, Tolluoğlu and Erkan 1989, Chapters 2 and 4).

### 5.2.3 *The Central Anatolian Ophiolites (CAO): Supra-subduction zone ophiolites*

The Central Anatolian Ophiolites (CAO) contain rock-units typical for a remnant oceanic crust, including metamorphic tectonites, gabbroic cumulates, isotropic gabbros, plagiogranites, dolerite sheeted dykes, basaltic lavas and a sedimentary cover (e.g. Yaliniz and Göncüoğlu 1998, Yaliniz 2008). They are found as isolated bodies in the CACC, and its best preserved example is the Sarikaraman Ophiolite (Figure 5.1b) (Yaliniz et al. 1996). At the interface between the high-grade metasediments and essentially non metamorphic remnants of the CAO, extensional detachments have been identified both in the Niğde massif (Gautier et al. 2002) and in the Kırşehir Massif near Kaman (Lefebvre et al. 2011).

Geochemically, the CAO magmatics have been characterized as a dominantly co-magmatic differentiated series of island-arc tholeiites, with typical geochemical features suggesting that they formed above an intra-oceanic subduction zone, i.e., in a supra-subduction zone (SSZ) setting (Yaliniz et al. 1996, 2000a). The timing of emplacement of the CAO on top of the CAM is rather well-constrained, as it should largely postdate the pelagic sedimentation of the epi-ophiolitic cover containing fossils from Turonian - Santonian age (e.g. from the Çiçekdağı ophiolite (Erdoğan et al. 1996); and the Sarikaraman Ophiolite (Yaliniz et al. 2000b)), and predate the widespread central Anatolian magmatics which intrude both the CAM and CAO (Erlor and Göncüoğlu 1996) (Figure 5.1c). It is important to note that a geochemical distinction exists between the oceanic material directly present on top of the CAM (i.e. the SSZ-CAO), and the offscraped oceanic sediments and the pillow basalts in the IAESZ which separate the CACC from the Pontides.

### 5.2.4 *Central Anatolian magmatic intrusive suites*

The third main crystalline rock-unit of the CACC consists of widespread magmatic intrusions. They are usually called the Central Anatolian Granitoids (CAG) (Göncüoğlu et al. 1991, Göncüoğlu et al. 1992). However, the term “Granitoids” is not representative of all central Anatolian magmatic rocks, as also quartz-monzonites, monzonites and syenites are found in the CACC. Therefore, we will refer to them as Central Anatolian Intrusions (CAI) or magmatic suites. Those magmatic bodies form large, elongated plutons (~100 km long) preferably

localized at, and following the trend of the western and northern borders of the CACC (Akiman et al. 1993) (Figure 5.1b). They are generally of granitic, granodioritic, monzonitic and syenitic composition, of calc-alkaline to alkaline affinity, and display characteristics of I, S and A-type granites. Their trace element geochemistry plots in the island arc, within-plate, and syn- to post-collision granitoids fields of the discrimination diagrams (e.g. Akiman et al. 1993, Aydın et al. 1998, Ilbeyli et al. 2004, Kadioğlu et al. 2006). The CAI show evidence for a spatial and temporal evolution of the magmatism: (1) the oldest magmatic rocks are granitic (the granite supersuite), and associated with intrusive gabbros. They occur directly along the western and northern edges of the CACC, forming an outer magmatic belt; (2) toward the center of the CACC, the monzonite supersuite is found with intrusive contacts across the granite supersuite, and (3) the youngest intrusions are syenites (the syenite supersuite) and occur as small plutonic bodies in the inner part of the complex (Kadioğlu et al. 2006) (Figure 5.2a). Constraints on the age of emplacement of the plutons compiled from the literature indicates that the magmatic pulse lasted from ~95 to 75 Ma (based on Rb/Sr whole rock, U/Pb on titanite and zircon and Pb/Pb evaporation on zircon methods) (Göncüoğlu 1986, Whitney et al. 2003, Köksal et al. 2004, Boztuğ et al. 2007, Chapter 2). However, we noticed in chapter 3 that the oldest crystallization ages are problematic as they contradict cross-cutting relationships with the CAM. With the exception of foliated leucogranites and some discrete extensional ductile shear zones affecting the outer granitoids, the CAI are generally not affected by ductile deformation (Akiman et al. 1993, Boztuğ 1998, Düzgören-Aydın et al. 2001). Geothermobarometric calculations (Al and Ti on amphibole) indicate that crystallization of some of the plutons took place at ca. 600-750°C, at pressures of ca. 2.5-4.5 kbar (Ilbeyli 2005, Boztuğ et al. 2009a) (Figures 5.1b and 5.1d). The timing of unroofing of the CAI is constrained by apatite fission-track ages around 57-60 Ma (Boztuğ and Jonckheere 2007).

## 5.3 Restoration and internal architecture of the CACC in the late Cretaceous

### 5.3.1 *The distinction of three domains within the CACC*

Since the early geological investigations in Central Anatolia, distinctive areas within the crystalline complex have been recognized. First, large domains exposing metamorphic and magmatic

rocks were geographically distinguished because they are separated by depressions filled with a Cenozoic sedimentary and volcanic cover:

- The metasediments making up the Central Anatolian Metamorphics have been distinguished in three major massifs: the Akdağmadeni or Akdağ Massif in the north-east (Vache 1963), the Niğde Massif in the south (Göncüoğlu 1977), and the Kırşehir Massif in the north-west (Seymen 1981) (Figure 5.1).

- The widespread magmatic rocks have also been defined as linear suites or belts: the Yozgat Batholith in the north, the NW intrusive belt near Kırıkkale, and the Ağaçören Intrusive suite in the south-west (Akıman et al. 1993, Kadioğlu and Güleç 1996) (Figure 5.1).

- Paleomagnetic results from the outer granites suggest the existence of three “blocks” which underwent different vertical axis rotations: the Yerköy-Yozgat block (YYB) in the north-east, the Kırıkkale-Kaman block (KKB) in the north-west, and Ağaçören-Aksaray block (AAB) in the south-west (Figure 3.6).

- The patterns of ductile shearing and distribution of regional metamorphism at the scale of the entire Kırşehir and Akdağ Massifs clearly indicated internal consistency, but also marked obliquities between these massifs (Chapter 4).

Figure 5.2a shows a simplified geological map of the CACC, with the different magmatic suites as proposed by Kadioğlu (2006). We also report the main directions of ductile shearing and metamorphic zoning in the CAM at the scale of the CACC. The data from northern Akdağ and Kırşehir massifs (Chapter 4) are presented together with those from the Hırkadağ Block (Chapter 2). The stretching lineations from the discrete shear zones crossing the Yozgat Batholith and the Ağaçören Intrusive Suite (Isik et al. 2008, Isik 2009), and the ones from the CAM of the southern Niğde massif (Gautier et al. 2002, Whitney et al. 2007, Gautier et al. 2008) are also indicated (Figure 5.2a). As briefly discussed in chapter 2, the direction of shear in the mylonitic marbles from the northern margin of the Hırkadağ Block seems to coincide with the orientations of stretched minerals in discrete shear zones through the Ağaçören granitoid in the west (Isik 2009), and also with the stretching direction associated with the ductile-to-brittle detachment in the southern Niğde Massif (Gautier et al. 2002). Those structures carry a top-to-the-NE or E-NE sense of shear in both Hırkadağ and Niğde areas, while a top-to-the-SW motion is mostly present within the Ağaçören granitoid. It is interesting to note that all of these three cases with mutually consistent shearing kinematics, have been related to processes associated with the exhumation

of the central Anatolian crystalline rocks in the latest Cretaceous. Moreover, the ductile shearing associated with the regional metamorphism in the southern margin of the Hırkadağ Block (Chapter 2) and in the core of the Niğde metamorphic dome (Gautier et al. 2008), shows a top-to-the-SE and top-to-the-S motion, respectively. The few exposures of CAM in the southern CACC do mostly record high-grade metamorphic conditions (Kocak and Leake 1994, Whitney and Dilek 1998, Chapter 2). At the scale of the Niğde Massif, which contains migmatites and sillimanite gneisses in the core and along the eastern margin, no clear metamorphic field gradient is observable (D. Whitney, pers. comm. 2009).

In our view, the similarities of the ductile shearing directions and metamorphic patterns in the crystalline rocks from north (Hırkadağ Block and Ağaçören Intrusive Suite (AIS)) and south (Niğde massif) of the Neogene Cappadocian volcanic province (Figure 5.1) suggest that they represent one and the same tectono-metamorphic domain. The internal consistency shown in Figure 5.2 suggests that the Niğde Massif may in fact represent the southern prolongation of the Ağaçören Intrusive Suite, with their missing connecting segment actually hidden below the young volcanics of Cappadocia. The southern CACC (comprising the crystalline rocks of the Hırkadağ/IdişDağı Blocks, the AIS and the Niğde Massif) thus probably forms a coherent NNW-SSE elongated structure, characterized by an approximate top-to-the-SSE regional metamorphic shearing, and a WSW-ENE direction of extension recorded during its exhumation.

To simplify the present analysis, we redefine the three crystalline, internally coherent domains as follows:

- (1) The Akdağ-Yozgat Domain, bounded by the IAESZ in the north, the DKFZ in the west and the Central Anatolian Fault Zone in the southeast. It comprises the Akdağ metamorphics, and the Yozgat Batholith including the YYB (Figures 5.1 and 5.2a and Chapter 3).

- (2) The Kırşehir-Kırıkkale Domain, bounded by the IAESZ in the north-west, the DKFZ in the east and the HHFZ in the south. It comprises the Kırşehir metamorphics, and the NW intrusive belt including the KKB (Figures 5.1 and 5.2a and Chapter 3).

- (3) The Niğde-Ağaçören Domain, bounded by the HHFZ in the north, the Tuzgölü Fault in the west and the Central Anatolian Fault Zone in the east. It comprises the Niğde metamorphics, and the Ağaçören Intrusive Belt including the AAB (Figures 5.1 and 5.2a and Chapter 3).

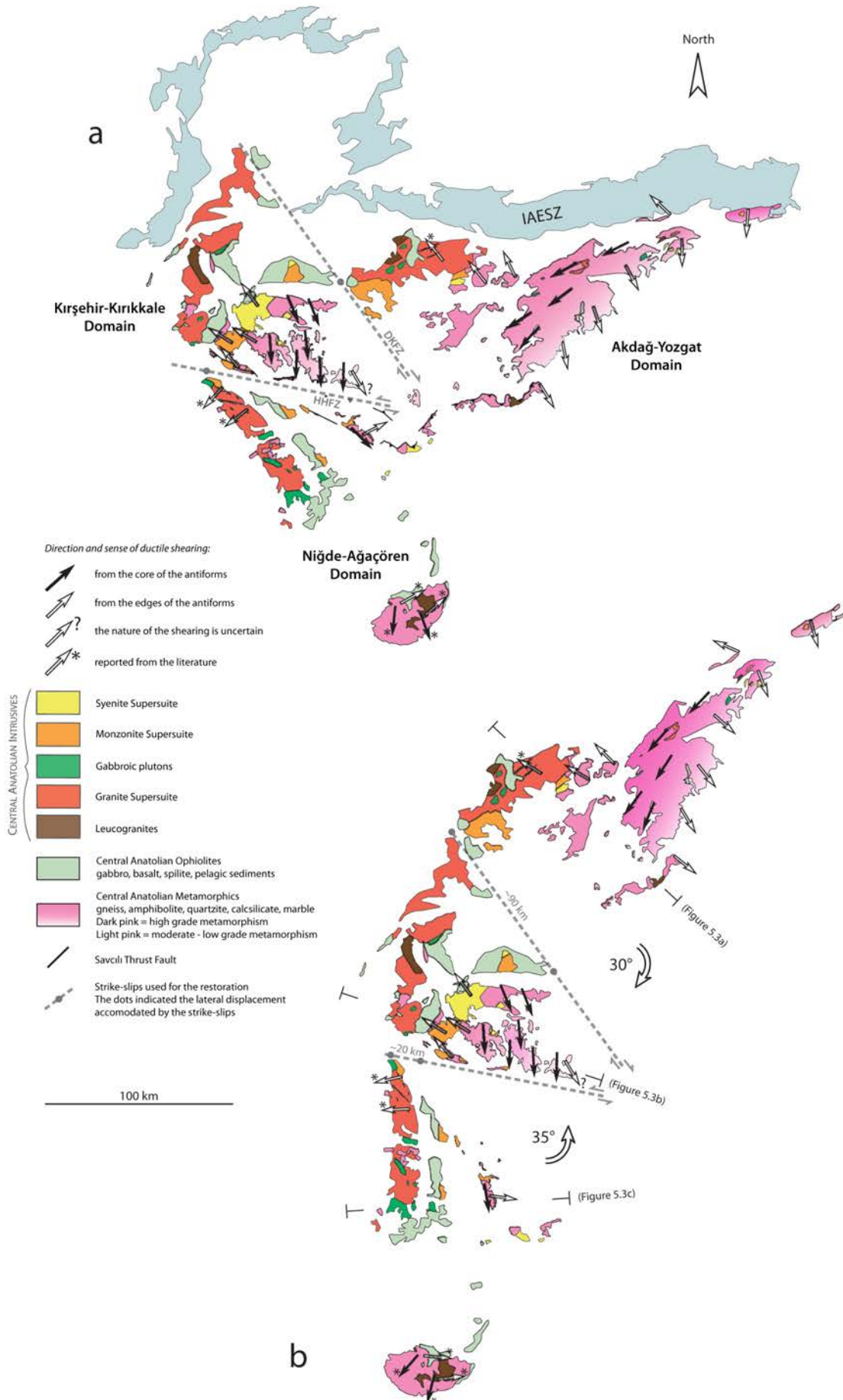


Figure 5.2 a) Simplified geological map of the CACC showing general shearing and metamorphic data. b) Restoration of the entire CACC configuration in the late Cretaceous.

5.3.2 Restoration of the CACC to its late Cretaceous configuration

In chapter 3, the pattern of paleomagnetic declination from the outer late Cretaceous granitoids indicates that significant vertical axis rotations have affected the previously described domains. Accommodating part of these rotations, we proposed that two major transpressive faults existed in between the central Anatolian domains. They are the NNW-SSE oriented dextral DKFZ situated between the Akdağ-Yozgat and the Kırşehir-Kırıkkale Domains, and the WNW-ESE oriented sinistral HHFZ between the Kırşehir-Kırıkkale and the Niğde-Ağaçören Domains. Figure 5.2b shows a restoration of the CACC, in which the relative positions of the Akdağ-Yozgat and the Kırşehir-Kırıkkale Domains are corrected for a clockwise rotation of  $\sim 30^\circ$  of the Akdağ-Yozgat domain and a transpressive deformation along the DKFZ involving 90 km dextral displacement and  $\sim 50$  km NE-SW shortening. The position of the Niğde-Ağaçören Domain is restored relative to the Kırşehir-Kırıkkale Domain correcting for a counterclockwise rotation of  $\sim 35^\circ$ , accompanied with a left lateral displacement of  $\sim 20$  km, and an eastward increasing N-S shortening of up to  $\sim 60$  km on the HHFZ (as presented in chapter 3). In the restored configuration (Figure 5.2b), the entire CACC forms a 500x150km, NNE-

SSW trending elongate structure. We observe a remarkably consistent overall pattern of the intrusive belts, patterns of ductile shearing, and distribution of the regional metamorphism. The aligned magmatic belts are all concentrated along the western side of the system, and show the same orientation as the overall CACC. The granite (with gabbroic plutons), monzonite and syenite supersuites show a clear spatial organization and are strictly distributed in three belts from west to east, respectively (Figure 5.2b). The first-order structural and metamorphic characteristics of the Akdağ and Kırşehir Massifs combined with the data from Niğde-Ağaçören Domain thus leads to a late Cretaceous configuration dominated by a major 500 x 150 km antiformal structure (Figure 5.2b).

The regionally high-grade Barrovian metamorphism in central Anatolia shows a net decrease from WNW toward the ESE (Figure 5.2b). The ductile syn-metamorphic flow in the deeper parts of the antiformal structure (see chapter 4) consistently indicates an along-strike  $\sim$ top-to-the-SSW shearing motion in the entire restored CACC, suggesting NNE-ward crustal flow. Orthogonal to the main trend of the antiform and to this inner ductile flow, the western and eastern margins of the CACC display clear NNE-SSW antipodal directions of shear related to the exhumation of the CACC during the late Cretaceous (Figure 5.2b).

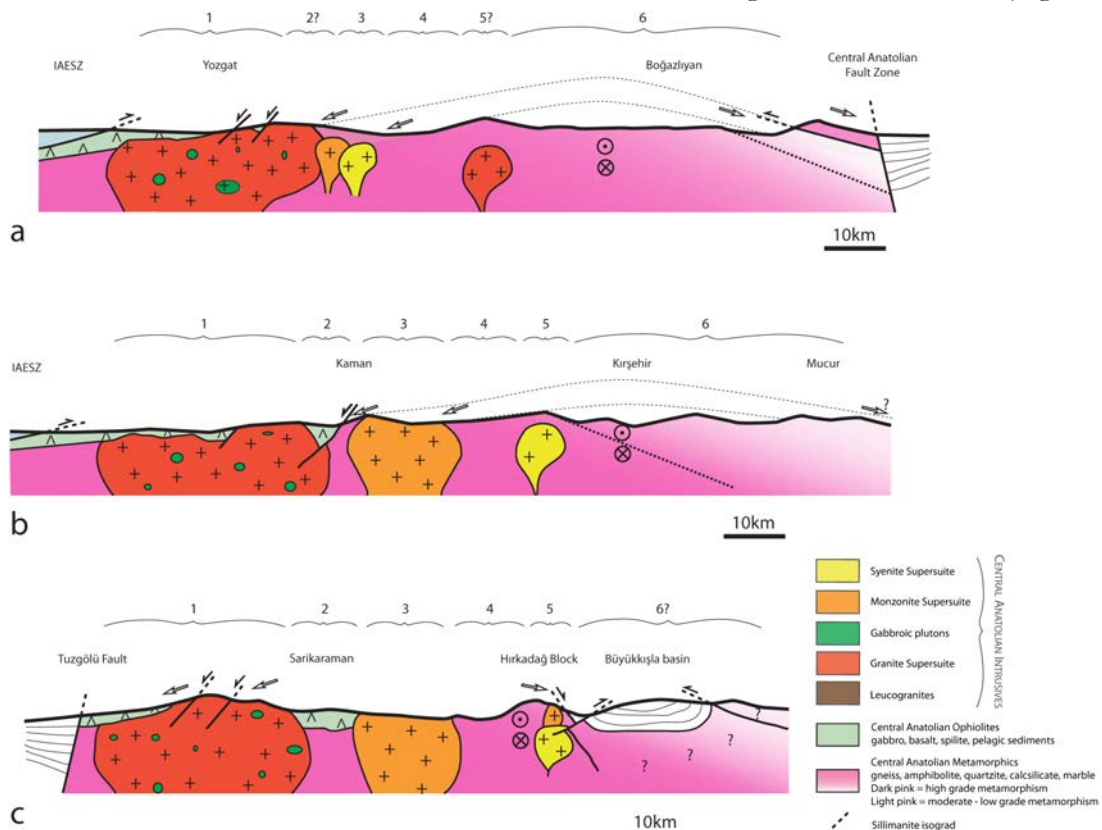


Figure 5.3 Upper crustal cross-sections showing the internal architecture of the CACC in the: a) Akdağ-Yozgat Domain, b) Kırşehir-Kırıkkale Domain, c) Niğde-Ağaçören Domain.

### 5.3.3 The internal architecture of the CACC

Reconstructed to its late Cretaceous configuration, the CACC shows a very different “anatomy” as compared to that exposed today. Crustal-scale cross sections orthogonal to the long axis of the restored CACC reveal that from north to south the internal architecture of the CACC is remarkably consistent (Figures 5.2 and 5.3). In Figure 5.3 we show schematic sections through the Akdağ-Yozgat (Figure 5.3a), Kırşehir-Kırıkkale (Figure 5.3b), and Niğde-Ağaçören Domains (Figure 5.3c), and identify six main components (Table 5.1) that define the general architecture of the restored CACC, namely, from the WNW toward the ESE:

- (1) A ~30km wide magmatic belt essentially composed of bimodal granitic and gabbroic plutons (Kadıoğlu et al. 2003), often covered by remains of the oceanic crust of the CAO. Discrete top-to-the-WNW ductile shear zones (in restored position) have been described from this westernmost belt of intrusives (Isik et al. 2008, Isik 2009).
- (2) A ~10km wide depression where successions of the CAO are preserved between two magmatic belts. The best documented example is the Sarikaraman Ophiolite east of Ağaçören (Yaliniz et al. 1996).
- (3) A ~15km wide magmatic belt essentially corresponding to the monzonite supersuite. Examples of this component of the CACC are the Baranadağ pluton near Kaman and the Terlemez quartz-monzonites intruding the eastern part of the Sarikaraman Ophiolite (Aydın and Önen 1999, Yaliniz et al. 1999).
- (4) A ~10-15km wide zone consisting of high-grade metasediments. Marble mylonitic shear bands cutting through the HT metamorphic

foliation have typically been found in this zone (e.g., in the Kaman and Hırkadağ areas). These structures developed in a relatively internal position of the large-scale antiforms have been described as upper crustal detachments that postdate regional metamorphism and formation of the pervasive foliation (Lefebvre et al. 2011, Chapters 1 and 2).

- (5) A ~5-10km wide zone corresponding to the third and less-well developed magmatic belt, and characterized by few syenitic plutons. Occasional remains of upper Cretaceous volcanism on top of the CACC are believed to be cogenetic with some of the syenitic bodies (Köksal et al. 2001).
- (6) A ~50km wide zone essentially composed of partly high-grade metasediments. This zone corresponds to the eastern side of the restored CACC not affected by magmatism. The eastern part of this zone also shows the lowest grade of regional metamorphism, which decreases from high grade in the west toward moderate/low grade in the east. The Akdağ-Yozgat and Kırşehir-Kırıkkale Domains include extensive exposure of this zone (see chapter 4).

A synthesis and additional information about the characteristics of these six main components structuring the initially NNE-SSW oriented CACC is presented in the Table 5.1. We note that the above zones are not completely represented in all three tectonic domains of the CACC. In the Akdağ-Yozgat Domain, the monzonitic and syenitic magmatic belt are much less developed than in the other domains (Figures 5.2 and 5.3a). In the Niğde-Ağaçören Domain, the metamorphics are mostly not exposed as they are covered by young volcanics (Figures 5.2 and 5.3b). The Kırşehir-Kırıkkale Domain on the other hand contains a most complete representation of all components of the CACC (Figures 5.2 and 5.3c).

Position from WNW to ESE	Rock type	Characteristic	Type locality	Type of Deformation	Averaged Width
(1)	Magmatic intrusives	Granite/Gabbro supersuite	Ağaçören	locally ductile and brittle	~30 km
(2)	Ophiolites (SSZ-type)	Gabbro, basalt, sediments...	Sarikaraman	brittle	~10 km
(3)	Magmatic intrusives	Monzonite supersuite	Baranadağ	brittle	~15 km
(4)	Metamorphic metasediments	high grade metamorphism	Kaman, Hırkadağ	mostly ductile and brittle	~10-15 km
(5)	Magmatic intrusives	Syenite supersuite	near Kırşehir, İdişDağı	brittle	~5-10 km
(6)	Metamorphic metasediments	high → low grade metamorphism	Kırşehir and Akdağ Massif	mostly ductile and brittle	~50 km

Table 5.1 Characteristics of the six main components structuring the NNE-SSW oriented CACC in the late Cretaceous. The location of the type-localities are shown in Figure 5.1.

## 5.4 Structural and magmatic evolution of the CACC

Using the available time constraints and the structural and magmatic criteria mentioned above, the evolution of the CACC can now be placed in a time frame.

Based on the literature and the findings of this study, we propose an evolution of the CACC involving a sequence of six main stages, and illustrate these in a series of interpretative block diagrams shown in Figure 5.4. Note that the ages assigned to each of these stages are rough estimates, and that the proposed stages may have started earlier or ended later than the proposed timing, and that stages could even overlap. The six stages recognized in the late Cretaceous evolution of the CACC can be summarized as follows:

(1) The first stage corresponds to the underthrusting of a Paleozoic-Mesozoic continental carbonate platform underneath a young oceanic crust of supra-subduction zone affinity (ophiolite emplacement) (Figure 5.4a). In figure 5.4a, we represent an oceanic crust which overrides ~5km of Paleozoic sediments. To complete the crustal scale diagram, we add an unknown, hence speculative basement below these sediments. The emplacement of the CAO on top of the CAM should largely postdate the pelagic sedimentation of the epi-ophiolitic cover (containing Turonian – Early Santonian fauna, ~93-85Ma) (Erdoğan et al. 1996, Yaliniz et al. 2000b), and predate the regional peak metamorphism which affected the entire CAM below the CAO around 91-84 Ma (Whitney et al. 2003, Whitney and Hamilton 2004). We emphasize that the timespan between effective obduction and the peak of regional Barrovian metamorphism is extremely short. In order to estimate a plausible time span when the obduction may have occurred, we consider that despite the contemporaneous age of the CAO sedimentary cover it must have happened prior to the HT metamorphism of the CAM. In addition, the formation of metamorphic soles below the SSZ-ophiolites belonging to the Tauride ophiolites also range around 91-93Ma ( $^{40}\text{Ar}/^{39}\text{Ar}$  analysis on hornblendes) (Dilek et al. 1999, Çelik et al. 2006). Consequently, we propose that obduction occurred around ~95-90Ma.

(2) The second stage corresponds to the peak of the regional Barrovian metamorphism affecting the CAM (Figure 5.4b). U/Pb SHRIMP analysis on metamorphic monazite and zircon from the high-grade metapelites of the Niğde and Kaman regions yield age estimates of this stage of ~91-84 Ma (Whitney et al. 2003, Whitney and Hamilton

2004). Estimates of pressure and temperature conditions in the high grade metasediments indicate temperatures of 700-800°C at 6-8 kbar (e.g. Whitney and Dilek 2001, Chapter 2), which would correspond to depths of ~20km. Contemporaneous with regional metamorphism, pervasive ductile deformation affected the entire CAM leading to the development of a synmetamorphic foliation, associated folds and stretched minerals as a response to shearing motion (Figure 5.4b) (Erkan 1976, Seymen 1981, Tolluoğlu and Erkan 1989, Whitney and Dilek 1998, Gautier et al. 2002, Lefebvre et al. 2011). Similar to the structure of the Niğde metamorphic dome described by Gautier et al. (2008), a set of two coeval lineations is present at the scale of the CACC (Chapter 4). In the deeper core of the antiform, ductile flow is consistently associated with a ~top-to-the-SSW shearing motion, and an orthogonally-oriented NNE-SSW symmetric direction of shear at the western and eastern margins of the CACC. The latter shearing has been related to the exhumation of the crystalline rocks toward shallower crustal levels, via detachment faults at the interface between the CAM and CAO (as described in the Niğde Massif (Gautier et al. 2002)). Therefore, the overall shearing kinematics recorded at the margins of the CACC suggests that the extension direction was ~E-W. The cause and forces driving the along-strike inner flow perpendicular to the dominant extension direction remains enigmatic. The Akdağ Massif is the area where the evidence for coeval, orthogonal ductile shearing is best preserved (chapter 4). Associated with this tectonic stage, the deeper part of the crust underwent extreme HT conditions favorable for the formation of migmatites and subsequent syntectonic crustal-derived leucogranites, as described from the Niğde Massif (Göncüoğlu 1977, Whitney and Dilek 1997).

(3) The third stage corresponds to the first phase of magmatic intrusion (Figure 5.4c), consisting of bimodal magmatism creating both granitic and gabbroic plutons (Kadioğlu et al. 2003) and localized along the westernmost border of the CACC. This magmatic event is late to post-tectonic relative to the regional syn-metamorphic shearing, as it mostly intrudes across foliated metasediments, and only few discrete ductile shear zones have been described (Isik et al. 2008, Isik 2009). Most of the available age constraints for this outer granitic/gabbroic suite suggests emplacement of this magmatic belt around ~85-80Ma, in agreement with  $^{40}\text{Ar}/^{39}\text{Ar}$  cooling ages of some of the outer plutons (İlbeyli et al. 2004, Isik et al. 2008, Boztuğ et al. 2009a)(see Table 3.1).

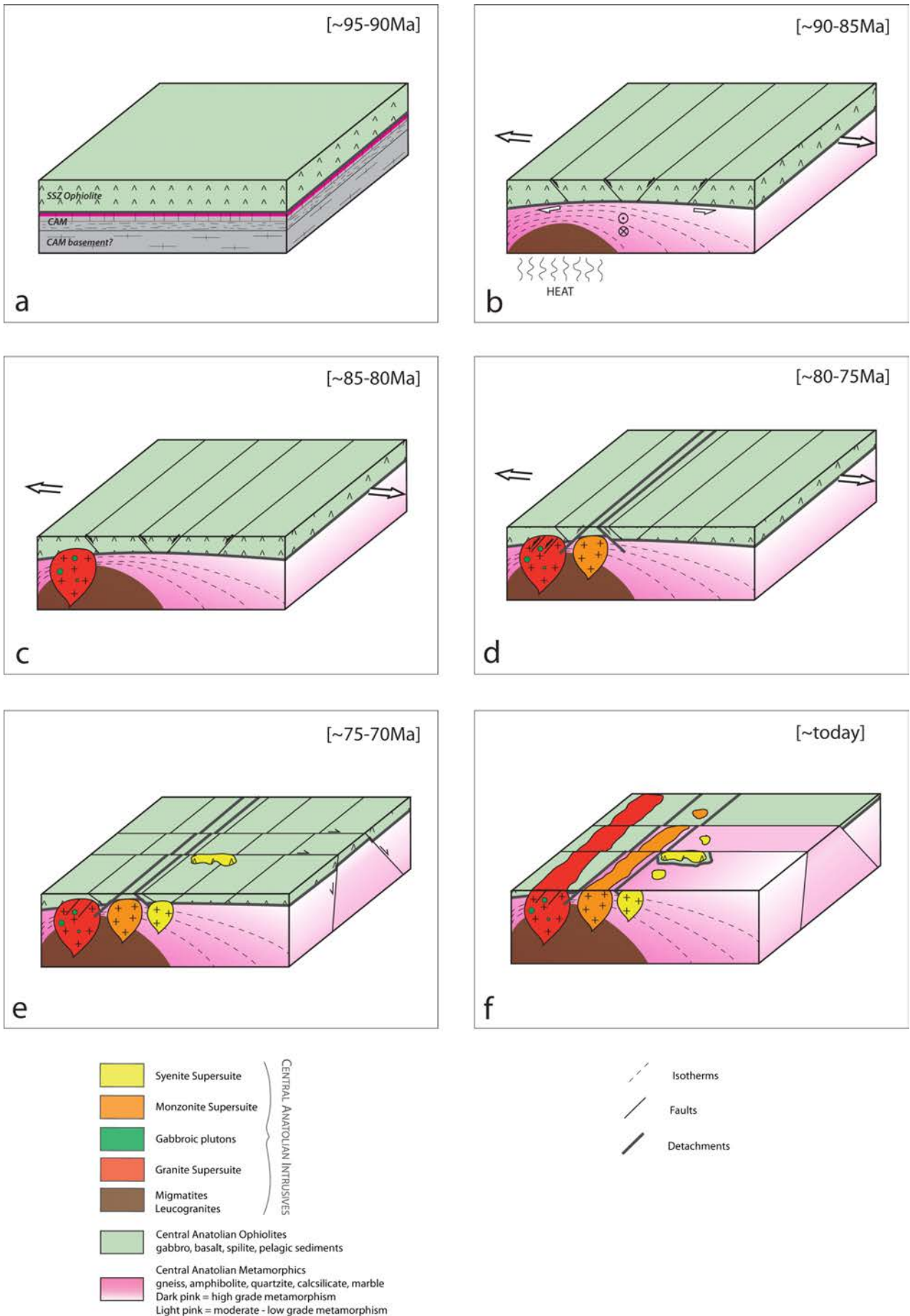


Figure 5.4 Structural and magmatic evolution of the CACC in six stages: a) ~95-90Ma, b) ~90-85Ma, c) ~85-80Ma, d) ~80-75Ma, e) ~75-70Ma, f) ~present-day geometry.

It is important to note that the outer granitic and gabbroic belt most likely intruded at relatively shallow, upper crustal levels (Boztuğ et al. 2009a), through both the CAM and CAO, and consequently cuts across the large scale detachments and associated marginal shearing structures that existed at this time. It is, therefore, likely that those detachment were not active anymore after this tectonic stage.

(4) The fourth stage (Figure 5.4d) corresponds to the activation of secondary upper crustal detachments in an internal position within the CACC. Two good examples of such localized structures have been recognized as a sequence of mylonitic marbles and associated breccias near Kaman (chapter 1) (Lefebvre et al. 2011), and in the Hırkadağ Block (chapter 2). It is interesting to note that, in the restored configuration of the CACC (Figure 5.2b), those two structures are located exactly on either side of, and striking parallel to the plutons of the Monzonite supersuite. The Kaman detachment is situated on the western side of the monzonite and displays a top-to-the-WNW sense of shear. The Hırkadağ detachment is located on the eastern side of the monzonite supersuite and shows a top-to-the-E sense of shear. In the Ömerhacılı area (chapter 1), detailed microstructural analysis from mylonitic marbles have shown static HT recrystallization at the vicinity of the Baranadağ quartz monzonite, which demonstrates that the ductile deformation (at  $\sim 300\text{--}400^\circ\text{C}$ , see Chapter 1) associated with this upper Cretaceous detachment predates the intrusion of the monzonite at  $\sim 75\text{Ma}$  (Boztuğ et al. 2009a). Therefore, taking the similar orientation and relative chronology between the upper crustal detachments and the monzonite supersuite into account, it is possible that the detachments and the intrusions were in some way related. Other intrusion ages from the monzonite magmatic belt are similar:  $81.5 \pm 1.9\text{ Ma}$  for the Terlemez quartz monzonite (Yaliniz et al. 1999), and  $\sim 77.2 \pm 0.4\text{ Ma}$  for the Hırkadağ pluton (Chapter 2). Therefore, we propose that the tectonic stage comprising the development of shallow secondary detachments and the emplacement of the monzonite supersuite roughly took place around  $\sim 80\text{--}75\text{Ma}$ .

(5) The fifth stage (Figure 5.4e) corresponds to the emplacement of the third and youngest magmatic belt in the center of the CACC antiform, and characterized by  $\text{SiO}_2$ -undersaturated magmas. The nepheline syenite from the Kortundağ pluton in the Kırşehir-Kırıkkale Domain (Figure 1.3) yields a  $^{40}\text{Ar}/^{39}\text{Ar}$  cooling age on amphibole of  $69.8 \pm 0.3\text{ Ma}$  (Kadioğlu et al. 2006). In the Gülşehir area,

it has been proposed that the Karahıdır volcanics are cogenetic with the nearby İdiş Dağı syenite (Köksal et al. 2001). New  $^{40}\text{Ar}/^{39}\text{Ar}$  age from a syn-sedimentary Karahıdır andesite exposed at the base of the Ayhan basin yields at  $72.06 \pm 1.8\text{ Ma}$  (Advokaat et al. submitted). Further to the NW, the rhyolite from the centre of the Kırşehir-Kırıkkale Domain shows a similar age of  $72.2 \pm 1.4\text{ Ma}$  (Figures 4.13 and 4.14). Therefore, it is likely that most of the remaining upper Cretaceous volcanics in the CACC are contemporaneous with the youngest syenitic magmatic activity in the late Cretaceous, occurring around  $\sim 75\text{--}70\text{Ma}$ . At this time,  $^{40}\text{Ar}/^{39}\text{Ar}$  ages from high-grade schists also suggest that the CAM were already exhumed to shallower depths corresponding to temperatures ranging between  $300\text{--}500^\circ\text{C}$  (Chapters 2 and 4). We hypothesize that the network of steep EW-oriented normal and dextral faults displacing the Kaman detachment and localizing the Upper Cretaceous volcanics (e.g. in centre of the Kırşehir-Kırıkkale Domain) was active at this stage.

(6) Following the period when the CACC formed one single, NNE-SSW oriented  $\sim 150\text{km}$  wide antiformal structure, progressive northward collision with the central Pontides likely resulted into the break-up, during the Paleogene, of the elongated CACC into three distinctive domains (see chapter 3). At this stage, it is interesting to point out the different tectonic relationships between the crystalline rocks of the northern central Anatolian domains and the IAESZ. In the Akdağ-Yozgat Domain, the IAESZ clearly covers the magmatic and metamorphic rocks along its northern margin, while in Kırşehir-Kırıkkale the suture is mostly restricted to the west of the domain (Figure 4.15). In the restored configuration, the Akdağ-Yozgat Domain represents the northernmost part of the CACC. Considering a main N-S direction of convergence between the African and Eurasian plates since the latest Cretaceous (Torsvik et al. 2008), the northern Akdağ-Yozgat Domain would be the first part of the CACC to collide with the accretionary prism of the IAESZ and the Pontides, consistent with the most intense brittle faulting in this part of the CACC. We suggest that, following frontal collision, the northern margin of the Akdağ-Yozgat Domain underthrust below the IAESZ, and resisted ongoing convergence. As a consequence, the Akdağ-Yozgat Domain likely rotated counterclockwise, while the Kırşehir-Kırıkkale Domain extruded toward the north-west, “pushing away” the IAEZ and creating the Omega shape of the Çankırı basin (see Figure 3.11).

As discussed in Chapter 3, it is likely that the rotations and associated transpressional

displacements documented in this study largely occurred before or during the Eocene. This notion on the timing of the onset of collision in Central Anatolia is also in good agreement with the recently established latest Cretaceous to earliest Paleocene oroclinal bending scenario of the central Pontides (Meijers et al. 2010). Therefore, after collision started, consequent compressional tectonic regime took place in the CACC during the Paleogene, as recorded within the central Anatolian basins (e.g. Poisson and Guezou 1996, Görür et al. 1998, Kaymakci et al. 2009, Advokaat et al. submitted, Gülyüz et al. submitted). Figure 5.4f shows today's exhumation and erosion state of the CACC.

## 5.5 Plate tectonic setting and evolution of the CACC since the late Cretaceous

### 5.5.1 Previously proposed models

Numerous models have been proposed to explain the clearly complicated evolution of the CACC during the late Cretaceous. Proposed scenarios for the origin of the CACC may be grouped by geological disciplines as follows.

Mainly based on metamorphic studies in the three main Central Anatolian Massif, Whitney et al. (e.g. 1998, 2001) suggested that the CAM underwent its regional mid-crustal Barrovian metamorphism in response to crustal thickening following Alpine contraction. However, they also suggested that strong differences exist between the tectonic histories of the southerly Niğde Massif and the Akdağ and Kırşehir Massifs in the north.

Based on the decrease of metamorphic grade from north (at the contact with the IAESZ) to south (toward the Taurides), Boztuğ (2000) interpreted the synchronous late Cretaceous metamorphism and magmatism in Central Anatolia as being related to an inverted metamorphism induced by the collision of the Anatolides with the Pontides.

Many plate tectonic models for the tectonic evolution of the CACC are based on geochemical interpretations of the CAI. Most authors agree upon a trend of the magmatism evolving from calc-alkaline, sub-alkaline to alkaline. It is also generally accepted that magmas were derived from a melt source containing both crustal and mantle components, and that their relative proportion varied in space and time. However, the meaning of such chemical evolution, and the role of the mantle-derived magmas is debated. On the one hand, some authors invoke a collision-related progression from syncollisional to postcollisional magmatism across the CACC, involving lithospheric delamination or removal of the thermal boundary

layer of the continental lithosphere (e.g. Erler and Göncüoğlu 1996, Boztuğ 1998, Düzgören-Aydın et al. 2001). On the other hand, several authors suggest that the mantle-sourced magmas contain a clear subduction signature, and prefer to relate the evolution of magmatism in Central Anatolia to subduction processes, with or without a possible break-off of the slab or delamination of mantle lithosphere (Kocak and Leake 1994, Kadioğlu et al. 2003, Ilbeyli et al. 2004, Ilbeyli 2005, Kadioğlu et al. 2006, Boztuğ et al. 2007). In addition, the inferred tectonic setting in which the CAO oceanic crust formed just before its obduction onto the CAM may also help to infer the initial tectonic environment of the CACC. Detailed chemical analyses of the magmatic units of the CAO reveal typical supra-subduction zone (SSZ) characteristics suggesting that during the late Cretaceous the CAO developed by ocean-floor spreading above an intra-oceanic subduction zone (Yaliniz 2008).

Finally, there are also models largely based on the sedimentary records from the major basins surrounding the CACC. Görür (1998) proposed that during the late Cretaceous the large basins west of the CACC (e.g. Haymana, Tuzgölü, Ulukışla) formed arc-related (forearc and intra-arc) basins, whereas others suggest that these central Anatolian basins evolved within an extensional context from Late Maastrichtian until Paleocene time, allowing the accumulation of several kilometers of clastic materials as in the Tuzgölü and Sivas basins (Çemen et al. 1999, Dirik et al. 1999).

### 5.5.2 Summary of the main new findings constraining the late Cretaceous plate tectonic setting of the CACC

In this study, we integrate multiple sets of data from our structural, metamorphic and paleomagnetic studies of the central Anatolian crystalline rocks. Evidence from the ductile shearing and the regional metamorphic pattern in the CAM, the distribution of the magmatic suites of the CAI, and paleomagnetic data from the outer granitoids all converge toward the restoration of a more or less linear, NNE-SSW orientated geometry of the CACC during the late Cretaceous. As a consequence, the commonly accepted notion that the CACC underwent its widespread HT metamorphism and associated deformation in its present triangular configuration, is in our view misleading. Recognizing this, the CACC provides newly recognized, important characteristics, especially in terms of spatial and temporal organization, pertinent to the plate tectonic and geodynamic setting in which the CACC evolved.

The main characteristics of the CACC in the late Cretaceous as inferred in this study can be

summarized as follows:

- The CACC formed an elongated and narrow antiformal structure of  $\sim 500 \times 150$  km in dimension.
- The regional pattern of HT regional metamorphic field gradient is asymmetric, with a progressive decrease from high to moderate/low metamorphic grade along a WNW-ESE transect across the CACC, i.e., orthogonal to the NNE-SSW orientated structural trend of the belt.
- Along-strike ductile flow occurred in the deeper part of the antiform, and the structures consistently indicate a top-to-the-SSW direction of shear at the scale of the entire CACC.
- Shallower shearing affecting the margins of the antiformal structure reflects a regional WNW-ESE direction of extension during the exhumation of the CAM.
- Two generations of detachments active at different stages of the evolution of the CACC, have been recognized.
- Three narrow and long magmatic belts developed along the western margin of the CACC. From an external (western) to a more internal (eastern) position within the broad antiformal structure they show a consistent younging and chemical change from calc-alkaline to alkaline. Only the westernmost outer granitic-gabbroic belt is locally affected by ductile deformation, the other two inner belts postdate the regional ductile deformation and metamorphism.

Within the light of these new findings, we now discuss possible crustal- and lithosphere-scale processes that may have affected the CACC during the Late Cretaceous.

### 5.5.3 Potential plate tectonic and geodynamic setting of the CACC

- What was the heat source causing the late Cretaceous regional HT metamorphism?

The structure and metamorphism of the CACC (chapter 4) clearly shows that the grade of regional metamorphism increases toward the structurally deeper parts of the massifs. The metamorphism, therefore, cannot be explained as an inverted metamorphism as suggested by Boztuğ (2000). In addition, few outcrops of ocean-derived material in direct contact with the low grade CAM in the southeast of the Akdağ Massif show that the high temperatures are not related to heating from above.

The pressure-temperature conditions recorded during regional Barrovian metamorphism is in good agreement with processes involving thickening of the crust as a result of the obduction of the CAO around 95-90 Ma. However, there is insufficient

time (less than 10 My) between obduction and peak metamorphism in the CAM to explain the heating implied by the observed metamorphic temperatures as a result of radiogenic heat production within a thickened crust (e.g. Brouwer et al. 2004).

In addition, petrological and chemical data from the central Anatolian magmatic suites clearly indicate a contribution of mantle sources in the central Anatolian magmatism immediately following the metamorphism (e.g. Kadioğlu et al. 2003). In addition, the spatial distribution of the metamorphism largely parallel to the elongate plutons, and the predominance of the three magmatic belts within in the high-grade zone strongly suggest that metamorphism and magmatism in the CACC are strongly linked and related to one common process. We therefore hypothesize that, soon after obduction of the CAO, a perturbation in the mantle caused the uprise of magmas and an abnormal heat pulse below the developing CACC crust. This interpretation is in line with most of the geochemical data from the CAI suggesting a process at the scale of the lithosphere and underlying asthenospheric mantle (e.g. Boztuğ 1998, Düzgören-Aydın et al. 2001, Ilbeyli et al. 2004, Kadioğlu et al. 2006). In this context, we emphasize again the geometry of the restored CACC, showing N-NE oriented metamorphic isograds, inner ductile flow and three successive magmatic belts. The combination of this elongate structured geometry and the contribution of a metasomatized mantle in the production of magmas (Ilbeyli et al. 2004, Ilbeyli 2005, Kadioğlu et al. 2006) in a major zone of convergence may very well reflect the presence of a N-NE trending lithospheric slab descending below the CACC. This interpretation seems in line with the first-order upper mantle structure underneath modern magmatic arc systems such as that of Japan. As corollary of such an interpretation we note that transient processes such as delamination or detachment of lithospheric mantle, though possible and consistent with our data, may not be a priori necessary to explain the metamorphic peak conditions seen in the CACC.

- Late Cretaceous polarity of the descending slab below the CACC

In order to assess a plausible polarity of the N-NE trending descending lithospheric slab below the CACC, different evidences at different scales may be used:

The overall arcuate shape of the CACC may be used as an indirect indication of the direction of subduction. In map view, the overall structure

of the CACC suggests a lense-shaped extensional domain, which is convex to the west. This curvature is also observed at the smaller scale of the Akdağ massif alone (chapter 4). Because extension occurred in a setting of plate convergence, the convex shape of the overriding extending CACC may thus reflect an eastward dip of the subduction zone.

The Anatolide high-pressure belt, composed of the late Cretaceous Tavşanlı and Eocene Afyon zones, partly surround the CACC (Sherlock et al. 1999, Candan et al. 2005). In their present-day configuration they are located in the southwest, south and southeast of the CACC (Figure 5.5b). Based on a review of sparse paleomagnetic data, Pourceau et al. (2010) suggested that the Anatolides HP belt located in the SE of the CACC, underwent major compression and a  $\sim 40^\circ$  counterclockwise rotation, and therefore its eastern localization results from the collision with the CACC. This conclusion is also supported by the fact that the Sivas basin, to the east of the CACC, underwent major folding and thrusting till as recent as middle Miocene time (Poisson and Guezou 1996, Dirik et al. 1999). The presence of a continuous HP belt to the west of CACC, therefore, also suggests eastward subduction below the CACC during the late Cretaceous.

- Maturation of the late Cretaceous subduction zone below the CACC

The characteristics of the central Anatolian magmatic events and their evolution with time may reflect the evolution of the subduction zone below the CACC. A clear spatial, temporal and chemical trend emerges from the three magmatic belts of Central Anatolia. While showing an evolution from calc-alkaline to alkaline, those three belts reflect a migration of the magmatic system from west to east. Similar magmatic trends are well documented in the literature and generally refer to supra-subduction zone from magmatic arc environments, where typically three volcanic series are recognized (Gill 1981, Baker 1982): (1) the tholeiitic series dominated by basaltic lavas, (2) the calc-alkaline series dominated by andesites, and (3) the alkaline series. In general, the tholeiitic magma series is well represented above young subduction zones, while the calc-alkaline and alkaline series are encountered in more mature subduction systems. In addition, some island arcs exhibit typical spatial distributions of the volcanic series, as in Japan for example, where the tholeiitic/calc-alkaline/alkaline trend is apparent with increasing distance from the trench (Gill 1981). Moreover, large and linear belts of plutonic rocks typically occur

in arc magmatic environments. The magmatic characteristics of the CACC thus closely resemble those expected for an evolving supra-subduction zone magmatic arc. We may even consider the island-arc tholeiitic lavas from the CAO, which have been generated above an intra-oceanic subduction zone soon after the inception of subduction (Yaliniz et al. 1996, 2000a), to represent the early stages of the arc, while the central Anatolian magmatic suites represent the following, more mature series of the arc. In addition, the regional HT-MP metamorphism with a local HT-LP peak associated with intrusions in the CACC, are typical features of metamorphism taking place at the vicinity of magmatic arcs (Lucassen and Franz 1996). We therefore believe that the environment in which the Barrovian regional metamorphism followed by widespread magmatism occurred in Central Anatolia is directly related to burial of the CACC below an oceanic plate, immediately followed by ongoing maturation of a magmatic arc above a subduction zone (Figure 5.5a). Upon maturation of this subduction system, the Anatolides HP-LT belt of the Tavşanlı zone formed. In Figure 5.5a, a schematic WNW-ESE section at the scale of the lithosphere represents the possible setting in which the CACC evolved during the late Cretaceous. A similar geodynamic scenario for the CACC was proposed by Görür in (1984) while focusing on the evolution of the Central Anatolian basins, and by (Kadioğlu et al. 2003) based on the genesis and evolution of the large plutons of the area.

## 5.6 Implications at a plate tectonic scale

The tectonic and magmatic history of the CACC and the Anatolide HP belt are best explained by an eastward dipping subduction zone which evolved during the late Cretaceous. Above we briefly noted the presence of the Tavşanlı high pressure located at  $\sim 100$  km to the west of the CACC. The Tavşanlı Zone is composed of carbonate-rich metasediments metamorphosed under high-pressure blueschist to eclogite facies conditions (e.g. Okay 1982, Whitney and Davis 2008, Pourceau et al. 2010). It is interesting to note that the HP metamorphic ages of the Tavşanlı Zone (88–80 Ma) (Harris et al. 1994, Okay et al. 1998, Sherlock et al. 1999, Seaton et al. 2009) are within the range of the HT-MP metamorphic ages of the CACC (91–84 Ma (Whitney et al. 2003, Whitney and Hamilton 2004)). Taking into account their contrasting pressure-temperature histories, it is likely that the CACC constitutes the overriding magmatic-arc of a NNE-oriented subduction zone, while the HP Tavşanlı zone represents remnants of

the underlying subducted plate (Figures 5.5a and 5.5b). The HP-LT Tavşanlı belt and the HT-M/LP CACC thus formed a late Cretaceous paired metamorphic belt similar to the one described in the Japanese island arc, where Miyashiro (1961, 1973) recognized juxtaposed metamorphic terranes forming a paired metamorphic belt composed of M/LP type on the concave side of the arc and a HP type on the convex side of the arc. Finally, we note that the mineral stretching lineations from the blueschist to eclogite-facies Tavşanlı zone (Figure 5.5b), which must have formed during exhumation (Okay et al. 1998), also indicate E-W directions of shear, i.e. very similar to those in the CACC. This lends further support to the idea that the evolutions of the Tavşanlı zone and the CACC are linked.

At this stage, it is important to emphasize that there has been a continuous E-W trending, and northward dipping subduction zone below the Pontides throughout the late Cretaceous since ~105 Ma (e.g. Okay and Tüysüz 1999, Okay et al. 2001). The restored orientation of NNE-SSW magmatic arc of the CACC, would suggest synchronous E-directed subduction. It follows that two subduction plate boundaries, at high angles to each other, must have coexisted at this time. As such plate boundaries should meet at a triple junction (Cox and Hart 1986) we suggest that during the late Cretaceous the subduction zone west of the CACC must have joined the EW trending subduction below the Pontides such as to form a Trench-Trench-Trench type (TTT) triple junction. This late Cretaceous TTT geometry in

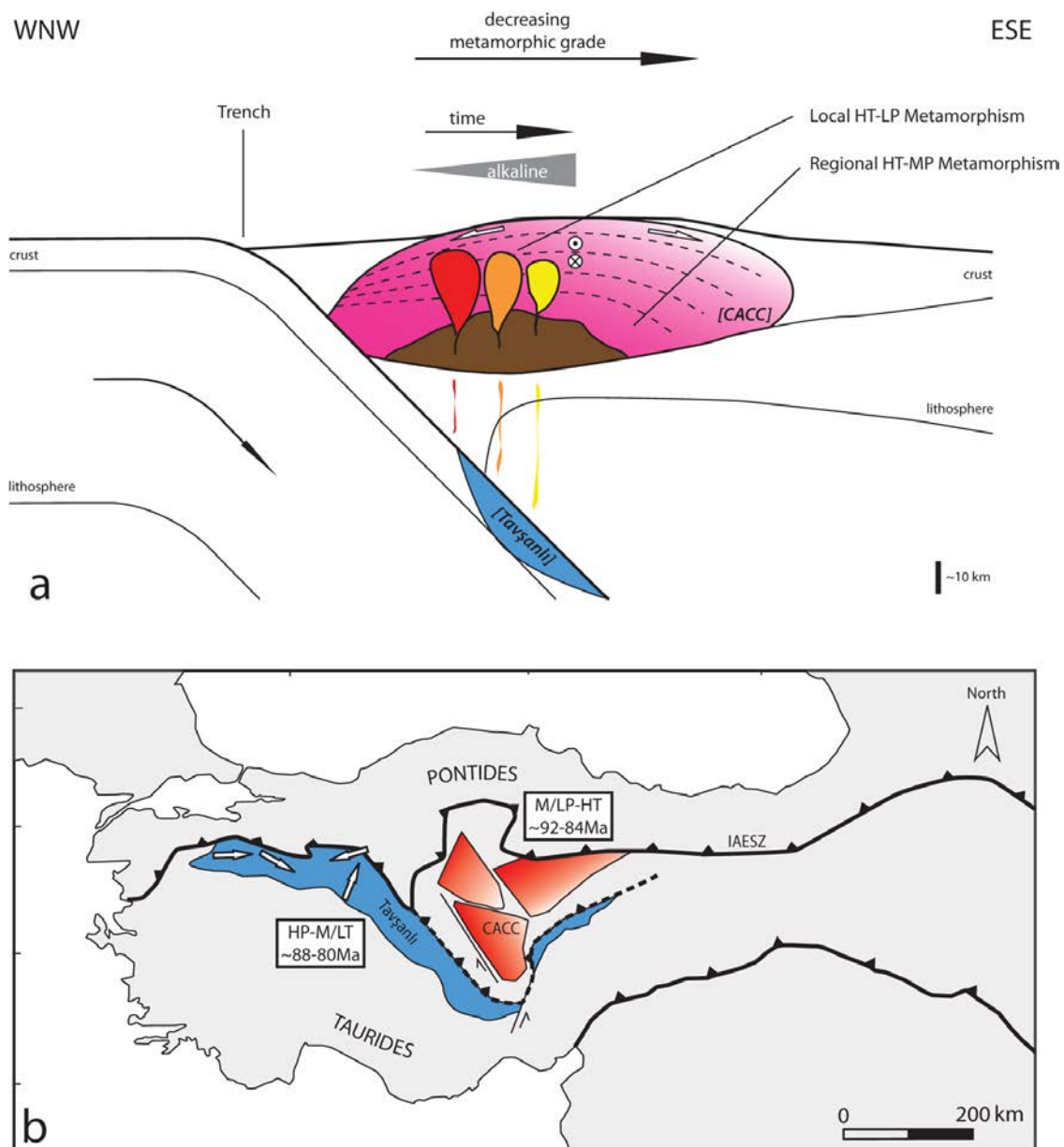


Figure 5.5 a) Schematic E-W lithospheric section through the CACC during the late Cretaceous. b) Simplified tectonic map of Turkey showing contrasted metamorphic terranes of the HP-LT Tavşanlı zone and the M/LP-HT CACC. Mineral lineation data in the Tavşanlı zone adopted from Lisenbee (1971), Okay (1981), Gautier (1984) and Seaton (2009).

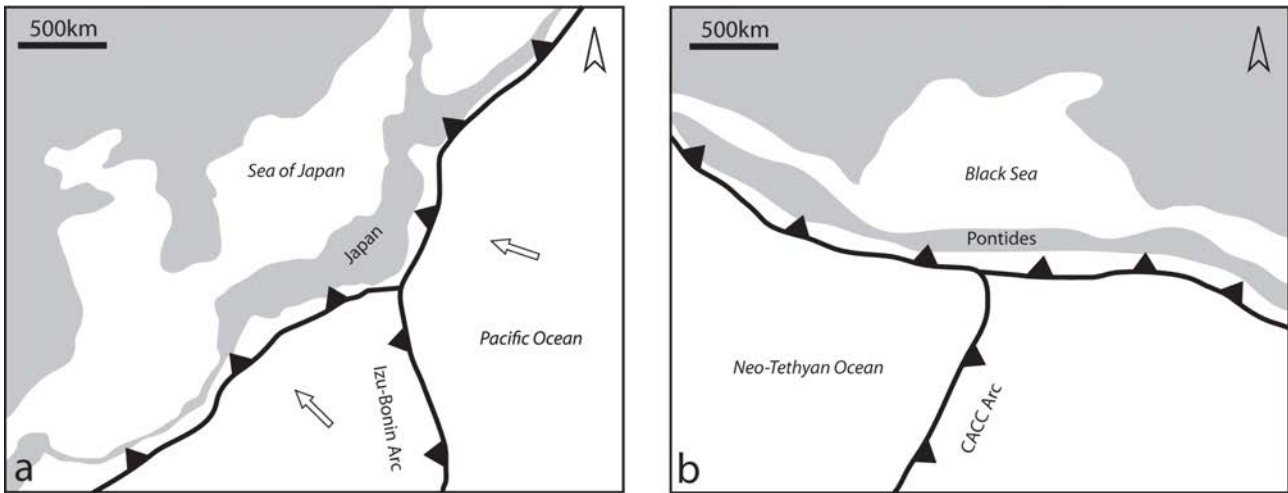


Figure 5.6 a) Simplified map view of the modern subduction system around Japan. The arrows represent the direction of plate motions relative to Eurasian Plate from Niitsuma (1996). b) A possible geometry of the the late Cretaceous subduction system in Central Anatolia.

Central Anatolia, may be compared with the modern example of Japan, where the southern Izu-Bonin arc forms a TTT triple junction with the SW and NE Japan Arc (e.g. Niitsuma 1996, Taira 2001). Our schematic map-view representation of the subduction configuration around the CACC in the late Cretaceous (Figure 5.6b) reveals remarkable similarities with the modern subduction system active under Japan (Figure 5.6a). Those similarities mainly concern the geometry of the subduction zones, the sizes of the tectonic terranes, and the locations of respectively the Japan Sea and the Black Sea, in the overriding plate close to the TTT triple junction.

## 5.7 Conclusions

By integrating structural, metamorphic and paleomagnetic data from the central Anatolian crystalline rocks, we arrive at a restoration of the late Cretaceous structure and geometry of the CACC. This restoration leads us to seriously reconsider the geometry and structure of the CACC during the late Cretaceous when it formed a NNE-SSW elongated and narrow antiformal structure of  $\sim 500 \times 150$  km. Regional Barrovian metamorphism was accompanied with a top-to-the-SSW ductile crustal flow active in the deeper parts of the antiform, while the shallower parts of the antiform were synchronously affected by a WNW-ESE direction of extension during the exhumation of the CACC. This exhumation was accommodated by two generations of detachments effective at different stage of the evolution of the CACC. In the western part of the dome-shaped antiform, three long and narrow magmatic belts show a consistent younging from west to east, i.e., from an external to a more internal position in the

orogen, allied with a chemical evolution from calc-alkaline to alkaline. This magmatic trend has been recognized as a typical evolution associated with a supra-subduction environment, where the island-arc tholeiites lavas from the CAO may represent the early stages of the development of a volcanic arc, while the central Anatolian magmatic suites indicate a more mature stage of the arc. At a larger scale, the association of the CACC magmatic arc with the contemporaneous HP-LT Tavşanlı belt may be interpreted as a paired metamorphic belt, very similar to what has been described in Japan by Miyashiro (1961, 1973). Finally, the synchronous activity, during the late Cretaceous, along the EW trending north-directed subduction system below the Pontides and the NNE-SSW trending, east-directed subduction system below the CACC leads us to infer that these plate boundaries must have met at a Trench-Trench-Trench type (TTT) triple junction comparable to the present-day subduction configuration acting below Japan.

## Acknowledgements

The comments of my supervisors onto the manuscript were highly appreciated. Prof. dr. M.J.R. Wortel is highly thanked for his suggestions to improve the figures of this chapter.





## CONCLUSION

This thesis provides and integrates multiple sets of geological data from the Central Anatolian Crystalline Complex (CACC) with the aim to unravel its tectonic and geodynamic evolution during the late Cretaceous. The tectono-metamorphic history of the metamorphic rocks of the CACC has been investigated at various scales; this includes detailed microstructural, metamorphic and geochronological analysis, together with local and regional mapping of ductile structures and metamorphic field gradients. In addition, an extensive set of paleomagnetic data from the central Anatolian granitoids provides constraints a restoration of the large-scale geometry of the CACC during the late Cretaceous. Based on the results from this multi-scale and multi-disciplinary study, the main findings of this thesis can be summarized as follows:

- During the late Cretaceous, the CACC consisted of a NNE-SSW elongated and narrow dome-shaped antiformal structure overridden by ophiolites (~500x150km).
- The CACC underwent a regional Barrovian metamorphism, which in its restored latest Cretaceous position shows a progressive decrease, from WNW to ESE, from high to moderate/low metamorphic grade.
- Regional metamorphism was accompanied with a top-to-the-SSW ductile crustal flow in the deeper parts of the antiform, while the shallower levels were synchronously affected by WNW and ESE directed shear, in the western and eastern sides of the antiformal dome respectively, related to the exhumation of the CACC.
- This extensional exhumation was accommodated by two generations of detachments operating during different stage of the evolution of the CACC.
- Shortly after peak metamorphism, the western side of the dome-shaped antiform was intruded by successive NNE-SSW-oriented magmatic plutons showing a chemical evolution from calc-alkaline in the west to alkaline in the east (i.e. from an external to a more internal position in the antiform). This magmatic trend, together with published geochemical data from the central Anatolian plutonic rocks, has been recognized as a typical evolution associated with the maturation of a magmatic arc above a juvenile subduction zone.
- The contemporaneous late Cretaceous L/MP-HT metamorphism of the CACC and the contemporaneous HP-LT Tavşanlı zone in the west most likely formed a paired metamorphic belt.
- The contemporaneous northward subduction below the Pontides along an EW-trending subduction system and eastward subduction of a NNE-SSW trending subduction system below the CACC suggests the presence, during the late Cretaceous, of a Japan-type Trench-Trench-Trench triple junction at the intersection of these two subduction zones.
- The NNE-SSW-oriented antiformal structure of the CACC converged and collided into the Pontides and consequently broke into three separate blocks. Differential rotation and translation of these three blocks led to the present triangular geometry of the CACC. These large-scale deformations were associated with significant N-S shortening in central Anatolia during the Paleogene.



## References

- Advokaat, E.L., van Hinsbergen, D.J.J., Lefebvre, C., Kaymakci, N., Vissers, R.L.M., Hendriks, B.H.W., (submitted). Reconstruction of the upper Eocene Savçılı-Mucur fold-thrust zone near the Hırkadağ Block (central Turkey) reveals the relict upper Cretaceous-Paleogene Ayhan supradetachment basin. *Tectonics*.
- Akiman, O., Erler, A., Göncüoğlu, M.C., Güleç, N., Geven, A., Türel, T.K., Kadioğlu, Y.K., 1993. Geochemical characteristics of granitoids along the western margin of the CACC and their tectonic implications. *Geological Journal* 28, 371-382.
- Akkök, R., 1983. Structural and Metamorphic Evolution of the Northern Part of the Menderes Massif - New Data from the Derbent Area and Their Implication for the Tectonics of the Massif. *Journal of Geology* 91(3), 342-350.
- Atabey, E., Tarhan, N., Akarsu, B., Taskiran, A., 1987. Serefelikochisar, Panli (Ankara) - Acipinar (Niğde) yöresinin jeolojisi. *M.T.A. Report No.* 8155, Ankara.
- Aydın, N., 1985. Geological evolution of Gümüşkent town and its surrounding in the Middle Anatolian Massif. *Communications de La Faculté des Sciences de l'Université d'Ankara, série C1 Géologie* 31, 43-56.
- Aydın, S.N., Önen, A.P., 1999. Field, petrographic and geochemical features of the Baranadağ quartz monzonite of the Central Anatolian granitoids, Turkey. *Turkish Journal of Earth Sciences* 8, 113-123.
- Aydın, S.N., Göncüoğlu, M.C., Erler, A., 1998. Latest Cretaceous magmatism in the CACC: Review of field, petrographic and geochemical features. *Turkish Journal of Earth Sciences* 7, 259-268.
- Bailey, E., McCallien, W.J., 1950. The Ankara Melange and the Anatolian Thrust. *Bulletin of the Mineral Research and Exploration Institute of Turkey* 40, 12-22.
- Baker, P.E., 1982. Evolution and classification of orogenic volcanic rocks. In *Thorpe, R.S. (ed.) Andesites, Wiley, Chichester*, 11-23.
- Barnhoorn, A., Bystricky, M., Burlini, L., Kunze, K., 2005. Post-deformational annealing of calcite rocks. *Tectonophysics* 403(1-4), 167-191.
- Bestmann, M., Kunze, K., Matthews, A., 2000. Evolution of a calcite marble shear zone complex on Thassos Island, Greece: microstructural and textural fabrics and their kinematic significance. *Journal of Structural Geology* 22(11-12), 1789-1807.
- Bestmann, M., Prior, D.J., 2003. Intragranular dynamic recrystallization in naturally deformed calcite marble: diffusion accommodated grain boundary sliding as a result of subgrain rotation recrystallization. *Journal of Structural Geology* 25(10), 1597-1613.
- Bhattacharya, A., Mohanty, L., Maji, A., Sen, S.K., Raith, M., 1992. Nonideal Mixing in the Phlogopite-Annite Binary - Constraints from Experimental-Data on Mg-Fe Partitioning and a Reformulation of the Biotite Garnet Geothermometer. *Contributions to Mineralogy and Petrology* 111(1), 87-93.
- Bozkurt, E., Oberhänsli, R., 2001. Menderes Massif (Western Turkey): structural, metamorphic and magmatic evolution - a synthesis. *International Journal of Earth Sciences* 89(4), 679-708.
- Boztuğ, D., 1998. Post-collisional central Anatolian alkaline plutonism, Turkey. *Turkish Journal of Earth Sciences* 7, 145-165.
- Boztuğ, D., 2000. S-I-A-type intrusive associations: geodynamic significance of synchronism between metamorphism and magmatism in Central Anatolia, Turkey. *Geological Society of London, Special Publications* 173, 441-458.
- Boztuğ, D., Jonckheere, R.C., 2007. Apatite fission track data from central Anatolian granitoids (Turkey): Constraints on Neotethyan closure. *Tectonics* 26(3), TC3011, doi: 10.1029/2006TC001988.
- Boztuğ, D., Tichomirowa, M., Bombach, K., 2007. 207Pb-206Pb single-zircon evaporation ages of some granitoid rocks reveal continent-oceanic island arc collision during the Cretaceous geodynamic evolution of the Central Anatolia, Turkey. *Journal of Asian Earth Sciences* 31, 71-86.
- Boztuğ, D., Güney, O., Heizler, M., Jonckheere, R.C., Tichomirowa, M., Oflu, N., 2009a. 207Pb-206Pb, 40Ar-39Ar and Fission-Track Geothermochronology Quantifying Cooling and Exhumation History of the Kaman-Kırşehir Region Intrusions, Central Anatolia, Turkey. *Turkish Journal of Earth Sciences* 18, 85-108.
- Boztuğ, D., Jonckheere, R.C., Heizler, M.,

- Ratschbacher, L., Harlavan, Y., Tichomirova, M., 2009b. Timing of post-obduction granitoids from intrusion through cooling to exhumation in central Anatolia, Turkey. *Tectonophysics* 473(1-2), 223-233.
- Brinkmann, R., 1972. Mesozoic Troughs and Crustal Structure in Anatolia. *Geological Society of America Bulletin* 83(3), 819-8.
- Brouwer, F.M., Van de Zedde, D.M.A., Wortel, M.J.R., Vissers, R.L.M., 2004. Late-orogenic heating during exhumation: Alpine PTt trajectories and thermomechanical models. *Earth and Planetary Science Letters* 220(1-2), 185-199.
- Bucher, K., Frey, M., 2002. Petrogenesis of metamorphic rocks. *Springer-Verlag, Berlin, Heidelberg 7th Edition*, 341.
- Burkhard, M., 1993. Calcite twins, their geometry, appearance and significance as stress-strain markers and indicators of tectonic regime: a review. *Journal of Structural Geology* 15(3-5), 351-368.
- Butler, R.F. 1992. Paleomagnetism: Magnetic domains to geologic terranes. *Blackwell Scientific Publications, Boston*.
- Candan, O., Cetinkaplan, M., Oberhansli, R., Rimmele, G., Akal, C., 2005. Alpine high-Pressure low-Temperature metamorphism of the Afyon Zone and implications for the metamorphic evolution of Western Anatolia, Turkey. *Lithos* 84(1-2), 102-124.
- Çelik, O.F., Delaloye, M., Feraud, G., 2006. Precise (40)Ar-(39)Ar ages from the metamorphic sole rocks of the Tauride Belt Ophiolites, southern Turkey: implications for the rapid cooling history. *Geological Magazine* 143(2), 213-227.
- Çemen, I., Göncüoğlu, M.C., Dirik, K., 1999. Structural evolution of the Tuzgölü basin in Central Anatolia, Turkey. *The Journal of Geology* 107, 693-706.
- Clark, M., Robertson, A., 2002. The role of the Early Tertiary Ulukışla Basin, southern Turkey, in suturing of the Mesozoic Tethys ocean. *Journal of the Geological Society* 159(6), 673-690.
- Clarke, G.L., Powell, R., 1991. Decompressional Coronas and Symplectites in Granulites of the Musgrave Complex, Central Australia. *Journal of Metamorphic Geology* 9(4), 441-450.
- Corfu, F., 2004. U-Pb age, setting and tectonic significance of the anorthosite-mangerite-charnockite-granite suite, Lofoten-Vesteralen, Norway. *Journal of Petrology* 45(9), 1799-1819.
- Cox, A., Hart, R.R., 1986. Plate tectonics: how it works. *Blackwell Science*.
- Creer, K.M., Irving, E., Nairn, A.E.M., 1959. Paleomagnetism of the Great Whin Sill. *Geophysical Journal of the Royal Astronomical Society* 2, 306-323.
- Creer, K.M., 1962. The Dispersion of the Geomagnetic Field Due to Secular Variation and its Determination for Remote Times from Paleomagnetic Data. *Journal of Geophysical Research* 67(9), 3461-3476.
- Davis, G.A., Fowler, T.K., Bishop, K.M., Brudos, T.C., Friedmann, S.J., Burbank, D.W., Parke, M.A., Burchfiel, B.C., 1993. Pluton Pinning of an Active Miocene Detachment Fault System, Eastern Mojave Desert, California. *Geology* 21(7), 627-630.
- de Bresser, J.H.P., Evans, B., Renner, J., 2002. On estimating the strength of calcite rocks under natural conditions. *Geological Society of London, Special Publications* 200, 309-329.
- de Capitani, C., 1994. Gleichgewichts-Phasendiagramme: Theorie und Software. *European Journal of Mineralogy* 6(48).
- de Capitani, C., Petrakakis, K., 2010. The computation of equilibrium assemblage diagrams with Theriak/Domino software. *American Mineralogist* 95(7), 1006-1016.
- Deenen, M.H.L., Langereis, C.G., van Hinsbergen, D.J.J., Biggin, A.J., 2011. Geomagnetic secular variation and the statistics of palaeomagnetic directions. *Geophysical Journal International* 186, 509-520.
- Denèle, Y., Lecomte, E., Jolivet, L., Lacombe, O., Labrousse, L., Huet, B., Le Pourhiet, L., 2011. Granite intrusion in a metamorphic core complex: The example of the Mykonos laccolith (Cyclades, Greece). *Tectonophysics* 501(1-4), 52-70.
- Dilek, Y., Thy, P., Hacker, B., Grundvig, S., 1999. Structure and petrology of Tauride ophiolites and mafic dike intrusions (Turkey): Implications for the Neotethyan ocean. *Geological Society of America Bulletin* 111(8), 1192-1216.
- Dirik, K., Göncüoğlu, M.C., 1996. Neotectonic characteristics of Central Anatolia. *International Geology review* 38, 807-817.
- Dirik, K., Göncüoğlu, M.C., H., K., 1999. Stratigraphy and pre-Miocene tectonic evolution of the southwestern part of the Sivas Basin, Central Anatolia, Turkey. *Geological Journal* 34, 303-319.
- Dökmeci, I., 1980. Akdağmadeni yöresinin jeolojisi. *MTA Report* No: 6953.
- Düzgören-Aydın, N.S., Maplas, J., Göncüoğlu, M.C., Erler, A., 2001. A review of the nature of magmatism in Central Anatolia during the Mesozoic post-collisional period. *International Geology Review* 43, 695-710.

- Erdoğan, B., Akay, E., Uğur, M.S., 1996. Geology of the Yozgat Region and evolution of the collisional Çankırı Basin. *International Geology Review* 38, 788-806.
- Erkan, E., 1976. Isogrades determined in the regional metamorphic area surrounding Kırşehir and their petrological interpretation (in Turkish with English summary). *Yerbilimleri* 2(1), 23-54.
- Erkan, Y., 1980. A study on regional metamorphism of northeastern part of Central Anatolian massif (Akdağmadeni, Yozgat) (in Turkish with English abstract). *Bulletin of the Geological Society of Turkey* 23, 213-218.
- Erlor, A., Göncüoğlu, M.C., 1996. Geologic and tectonic setting of the Yozgat Batholith, Northern Central Anatolian Crystalline Complex, Turkey. *International Geology Review* 38, 714-726.
- Fayon, A.K., Whitney, D.L., Teyssier, C., Garver, J.I., Dilek, Y., 2001. Effects of plate convergence obliquity on timing and mechanisms of exhumation of a mid-crustal terrain, the Central Anatolian Crystalline Complex. *Earth and Planetary Science Letters* 192(2), 191-205.
- Fisher, D.A., 1953. Dispersion on a sphere. *Proceedings of the Royal Society of London A* 217, 295-305.
- Floyd, P.A., Göncüoğlu, M.C., Winchester, J.A., Yaliniz, M.K. 2000. Geochemical character and tectonic environment of Neotethyan ophiolitic fragments and metabasites in the Central Anatolian Crystalline Complex, Turkey. *In: Geological Society Special Publication* 173, 183-202.
- Gautier, P., Bozkurt, E., Hallot, E., Dirik, K., 2002. Dating the exhumation of a metamorphic dome: geological evidence for pre-Eocene unroofing of the Niğde Massif (Central Anatolia, Turkey). *Geological Magazine* 139(5), 559-576.
- Gautier, P., Bozkurt, E., Bosse, V., Hallot, E., Dirik, K., 2008. Coeval extensional shearing and lateral underflow during Late Cretaceous core complex development in the Niğde Massif, Central Anatolia, Turkey. *Tectonics* 27, TC1003, doi:10.1029/2006TC002089.
- Gautier, Y., 1984. Déformations et métamorphismes associés à la fermeture téthysienne en Anatolie Centrale (Région de Sivrihisar, Turquie). Ph.D. thesis, University Paris-Sud, 236 pp. (unpublished)
- Genç, Y., 2004. Savcılı migmatite-dome hosted gold-quartz veins in Kırşehir Metamorphic Core Complex (KMCC), Central Anatolia, Turkey. *Proceedings of the 5th International Symposium on Eastern Mediterranean Geology, Thessaloniki, Greece*. April 2004 3(1394-1397), 14-20.
- Genç, Y., Yürür, M.T., 2010. Coeval extension and compression in Late Mesozoic-Recent thin-skinned extensional tectonics in central Anatolia, Turkey. *Journal of Structural Geology* 32(5), 623-640.
- Gençalioğlu-Kuşcu, G., Floyd, P.A., 2002. Geochemical correlations between effusive and explosive silicic volcanics in the Saraykent region (Yozgat), central Anatolia, Turkey. *Geological Journal* 37(2), 143-165.
- Ghent, E.D., Stout, M.Z., 1981. Geobarometry and geothermometry of plagioclase-biotite-garnet-muscovite assemblages. *Contributions to Mineralogy and Petrology* 76, 92-97.
- Gill, J.B., 1981. Orogenic Andesites and Plate Tectonics. *Springer-Verlag, Berlin*.
- Gökten, E., Floyd, P.A., 1987. Geochemistry and Tectonic Environment of the Şarkışla Area Volcanic-Rocks in Central Anatolia, Turkey. *Mineralogical Magazine* 51(362), 553-559.
- Göncüoğlu, M.C., 1977. Geologie des westlichen Niğde Massivs. Phd Thesis Bonn University.
- Göncüoğlu, M.C., 1986. Geochronological data from the southern part (Niğde area) of the Central Anatolian Massif. *Bulletin of the Mineral Research and Exploration Institute of Turkey* 105-106, 83-96.
- Göncüoğlu, M.C., Toprak, V., Kuşcu, I., Erlor, A., Olgun, E., 1991. Orta Anadolu Masifinin orta bölümünün jeolojisi - bölüm 1: Güney kesim. *Turkish Petroleum Corporation (TPAO) Report* no. 2909, 140 pp (unpublished).
- Göncüoğlu, M.C., 1992. Structural and stratigraphic framework of the Central Anatolian Tertiary basins. Introduction to the Early Paleogene of the Haymana-Polatlı basin, *Field-trip book IGCP Project* no. 286 Early Paleogene Benthos Third Meeting, Ankara (Turkey)(October 08-13).
- Göncüoğlu, M.C., Erlor, A., Toprak, V., Yaliniz, K.M., Olgun, E., Rojay, B., 1992. Orta Anadolu Masifinin orta bölümünün jeolojisi - bölüm 2: Orta kesim. *Turkish Petroleum Corporation (TPAO) Report* no. 3155 (unpublished), 76 pp (in Turkish).
- Göncüoğlu, M.C., Erlor, A., Toprak, V., Olgun, E., Yaliniz, K.M., Kuşcu, I., Köksal, S., Dirik, K., 1993. Orta Anadolu Masifinin orta bölümünün jeolojisi - bölüm 3: Orta Kızılırmak Tersiyer Baseninin jeolojik evrimi. *Turkish Petroleum Corporation (TPAO) Report* no. 3313, 104 pp (unpublished).
- Göncüoğlu, M.C., Türel, T.K., 1993. Petrology and Geodynamic interpretation of plagiogranites from Central Anatolian Ophiolites (Aksaray-Turkey). *Turkish Journal of Earth Sciences* 2, 195-

- 203.
- Göncüoğlu, M.C., Türeli, T.K., 1994. Alpine collisional-type granitoids from western Central Anatolian Crystalline Complex, Turkey. *Journal of Kocaeli University*, Earth science section 1, 39-46.
- Görür, N., Oktay, F.Y., Seymen, I., Şengör, A.M.C., 1984. Palaeotectonic evolution of the Tuzgölü basin complex, Central Turkey: sedimentary record of a Neo-Tethyan closure. *Geological Society, London, Special Publications* 17(1), 467-482.
- Görür, N., Tüysüz, O., Şengör, A.M.C., 1998. Tectonic evolution of the central Anatolian basins. *International Geology Review* 40(9), 831-850.
- Gradstein, F.M., Ogg, J.G., Smith, A.G., Agterberg, F.P., Bleeker, W., Cooper, R.A., Davydov, V., Gibbard, P., Hinnov, L.A., House, M.R., Lourens, L., Luterbacher, H.P., McArthur, J., Melchin, M.J., Robb, L.J., Shergold, J., Villeneuve, M., Wardlaw, B.R., Ali, J., Brinkhuis, H., Hilgen, F.J., Hooker, J., Howarth, R.J., Knoll, A.H., Laskar, J., Monechi, S., Plumb, K.A., Powell, J., Raffi, I., Röhl, U., Sadler, P., Sanfilippo, A., Schmitz, B., Shackleton, N.J., Shields, G.A., Strauss, H., Van Dam, J., van Kolfshoten, T., Veizer, J., Wilson, D. 2004. A New Geologic Time Scale, with special reference to Precambrian and Neogene. *Cambridge University Press*.
- Grove, M., Harrison, T.M., 1996. Ar-40(\*) diffusion in Fe-rich biotite. *American Mineralogist* 81(7-8), 940-951.
- Gülyüz, E., Kaymakci, N., Meijers, M.J.M., van Hinsbergen, D.J.J., Lefebvre, C., Vissers, R.L.M., Hendriks, B.W.H., Peynircioğlu, A., (submitted). Late Eocene synsedimentary folding of the Çiçekdağı basin, Central Turkey, during the final stages of the Kırşehir Block-Pontides collision. *Journal of Geological Society*.
- Harris, N.B.W., Kelley, S., Okay, A.I., 1994. Postcollision Magmatism and Tectonics in Northwest Anatolia. *Contributions to Mineralogy and Petrology* 117(3), 241-252.
- Harrison, T.M., McDougall, I., 1982. The Thermal Significance of Potassium-Feldspar K-Ar Ages Inferred from Ar-40/Ar-39 Age Spectrum Results. *Geochimica Et Cosmochimica Acta* 46(10), 1811-1820.
- Henry, D.J., Guidotti, C.V., Thomson, J.A., 2005. The Ti-saturation surface for low-to-medium pressure metapelitic biotites: Implications for geothermometry and Ti-substitution mechanisms. *American Mineralogist* 90(2-3), 316-328.
- Hetzl, R., Ring, U., Akal, C., Troesch, M., 1995. Miocene Nne-Directed Extensional Unroofing in the Menderes-Massif, Southwestern Turkey. *Journal of the Geological Society* 152, 639-654.
- Holland, T.J.B., Powell, R., 1998. An internally consistent thermodynamic data set for phases of petrological interest. *Journal of Metamorphic Geology* 16(3), 309-343.
- İlbeyli, N., Pearce, J.A., Thirlwall, M.F., Mitchell, J.G., 2004. Petrogenesis of collision-related plutonics in Central Anatolia, Turkey. *Lithos* 72, 163-182.
- İlbeyli, N., 2005. Mineralogical-geochemical constraints on intrusives in Central Anatolia, Tectono-magmatic evolution and characteristics of mantle source. *Geological Magazine* 142(2), 187-207.
- Isik, V., Lo, C.-H., Göncüoğlu, M.C., Demirel, S., 2008. 39Ar/40Ar Ages from the Yozgat Batholith: Preliminary Data on the Timing of Late Cretaceous Extension in the Central Anatolian Crystalline Complex, Turkey. *The Journal of Geology* 116(5), 510-526.
- Isik, V., 2009. The ductile shear zone in granitoid of the Central Anatolian Crystalline Complex, Turkey: Implications for the origins of the Tuzgölü basin during the Late Cretaceous extensional deformation. *Journal of Asian Earth Sciences* 34(4), 507-521.
- Isik, V., Seyitoglu, G., Caglayan, A., Uysal, T., Zhao, J., Sozeri, K., Esat, K., 2010. Cataclastic Zones within the Savcılı Fault Zone, Central Turkey. *American Geophysical Union Fall Meeting 2010* (abstract #T51A-2011).
- Jaffey, A.H., Flynn, K.F., Glendeni, L.E., Bentley, W.C., Essling, A.M., 1971. Precision Measurement of Half-Lives and Specific Activities of U-235 and U-238. *Physical Review C* 4(5), 1889-&.
- Jelinek, V., 1981. Characterization of the magnetic fabric of rocks. *Tectonophysics* 79(3-4), T63-T67.
- Jelinek, V., 1984. On a mixed quadratic invariant of the magnetic-susceptibility tensor. *Journal of Geophysics - Zeitschrift fur Geophysik* 56(1), 58-60.
- Jolivet, L., Faccenna, C., Goffe, B., Burov, E., Agard, P., 2003. Subduction tectonics and exhumation of high-pressure metamorphic rocks in the Mediterranean orogens. *American Journal of Science* 303(5), 353-409.
- Jolivet, L., Lecomte, E., Huet, B., Denele, Y., Lacombe, O., Labrousse, L., Le Pourhiet, L., Mehl, C., 2010. The North Cycladic Detachment System. *Earth and Planetary Science Letters* 289(1-2), 87-104.
- Kadioğlu, Y.K., Güleç, N., 1996. Mafic microgranular enclaves and interaction between felsic and mafic magmas in the Ağaören

- Intrusive Suite: evidence from petrographic features and mineral chemistry. *International Geology Review* 38, 854-867.
- Kadioğlu, Y.K., Dilek, Y., Güleç, N., Foland, K.A., 2003. Tectonomagmatic evolution of bimodal plutons in the central Anatolian crystalline complex, Turkey. *Journal of Geology* 111(6), 671-690.
- Kadioğlu, Y.K., Dilek, Y., Foland, K.A., 2006. Slab break-off and syncollisional origin of the Late Cretaceous magmatism in the Central Anatolian crystalline complex, Turkey. *Geological Society of America Special Papers* 409, 381-415.
- Kaymakci, N., White, S.H., Van Dijk, P.M., 2000. Paleostress inversion in a multiphase deformed area: kinematic and structural evolution of the Çankırı Basin (central Turkey), Part 1 - northern area. In: Bozkurt, E., Winchester, J.A. and Piper, J.A.D. (eds.) *Tectonics and Magmatism in Turkey and the Surrounding area Geological Society London Special Publication* 173, 445-473.
- Kaymakci, N., Duermeijer, C.E., Langereis, C., White, S.H., Van Dijk, P.M., 2003a. Palaeomagnetic evolution of the Çankırı Basin (central Anatolia, Turkey): implications for oroclinal bending due to indentation. *Geological Magazine* 140(3), 343-355.
- Kaymakci, N., White, S.H., Vandijk, P.M., 2003b. Kinematic and structural development of the Çankırı Basin (central Anatolia, Turkey): a paleostress inversion study. *Tectonophysics* 364(1-2), 85-113.
- Kaymakci, N., Özçelik, Y., White, S.H., Van Dijk, P.M., 2009. Tectono-stratigraphy of the Çankırı Basin: Late Cretaceous to early Miocene evolution of the Neotethyan Suture Zone in Turkey. *Geological Society, London, Special Publications* 311(1), 67-106.
- Kaymakci, N., Inceöz, M., Ertepinar, P., Koç, A., 2010. Late Cretaceous to Recent kinematics of SE Anatolia (Turkey). In: M.Sosson, N. Kaymakci, R. Stephanson, F. Bergarat, and v. Storatchenko (eds.) *Sedimentary basin tectonics from the Black Sea and Caucasus to the Arabian Platform, Geological Society of London, Special Publication* 340(409-435).
- Ketin, I., 1966. Tectonic units of Anatolia (Asia Minor). *Mineral Research Exploration Bulletin* 66, 23-34.
- Kirschvink, J.L., 1980. The least-square line and plane and the analysis of paleomagnetic data. *Geophysical journal of the Royal Astronomical Society* 62, 699-718.
- Kissel, C., Laj, C., Poisson, A., Görür, N., 2003. Paleomagnetic reconstruction of the Cenozoic evolution of the Eastern Mediterranean. *Tectonophysics* 362, 199--217.
- Kocak, K., Leake, B.E., 1994. The Petrology of the Ortaköy District and Its Ophiolite at the Western Edge of the Middle Anatolian Massif, Turkey. *Journal of African Earth Sciences* 18(2), 163-174.
- Koçyiğit, A., Beyhan, A., 1998. A new intracontinental transcurrent structure: the Central Anatolian Fault Zone, Turkey. *Tectonophysics* 284(3-4), 317-336.
- Köksal, S., Göncüoğlu, M.C., 1997. Geology of the İdiş Dağı - Avanos area (Nevşehir - Central Anatolia). *Mineral Research Exploration Bulletin* 119, 41-58.
- Köksal, S., Göncüoğlu, M.C., Floyd, P.A., 2001. Extrusive members of post-collisional A-type magmatism in Central Anatolia: Karahıdır volcanics, İdiş Dağı - Avanos, Turkey. *International Geology review* 43, 683-694.
- Köksal, S., Romer, R.L., Göncüoğlu, M.C., Toksoy-Köksal, F., 2004. Timing of post-collisional H-type to A-type granitic magmatism: U-Pb titanite ages from the Alpine central Anatolian granitoids (Turkey). *International Journal of Earth Sciences* 93, 974-989.
- Krogh, T.E., 1982. Improved Accuracy of U-Pb Zircon Ages by the Creation of More Concordant Systems Using an Air Abrasion Technique. *Geochimica Et Cosmochimica Acta* 46(4), 637-649.
- Kröner, A., Şengör, A.M.C., 1990. Archean and Proterozoic ancestry in late Precambrian to early Paleozoic crustal elements of southern Turkey as revealed by single-zircon dating. *Geology* 18, 1186-1190.
- Kuşcu, G., Floyd, P.A., 1995. Petrography and geochemistry of dacites and rhyodacites from Saraykent Region, Yozgat, central Anatolia, Turkey. *International Earth Science Colloquium on the Aegean Region (IESCA 1995) Abstracts*, p.37.
- Lee, J.Y., Marti, K., Severinghaus, J.P., Kawamura, K., Yoo, H.S., Lee, J.B., Kim, J.S., 2006. A redetermination of the isotopic abundances of atmospheric Ar. *Geochimica Et Cosmochimica Acta* 70(17), 4507-4512.
- Lefebvre, C., Barnhoorn, A., van Hinsbergen, D.J.J., Kaymakci, N., Vissers, R.L.M., 2011. Late Cretaceous extensional denudation along a marble detachment fault zone in the Kırşehir massif near Kaman, Central Turkey. *Journal of Structural Geology* 33(8), 1220-1236.
- Lisenbee, A., 1971. The Orhaneli ultramafic-gabbro thrust sheet and its surroundings. In: Campbell, A.S. (Ed.), *Geology and History of Turkey, Petroleum Exploration Society of Lybia, Tripoli*, 349-360.

- Lister, G.S., 1984. Metamorphic Core Complexes of Cordilleran Type in the Cyclades, Aegean Sea, Greece. *Geology* 12(4), 221-225.
- Lister, G.S., Davis, G.A., 1989. The Origin of Metamorphic Core Complexes and Detachment Faults Formed during Tertiary Continental Extension in the Northern Colorado River Region, USA. *Journal of Structural Geology* 11(1-2), 65-94.
- Lucassen, F., Franz, G., 1996. Magmatic arc metamorphism: Petrology and temperature history of metabasic rocks in the Coastal Cordillera of northern Chile. *Journal of Metamorphic Geology* 14(2), 249-265.
- Ludwig, K.R., 2003. Isoplot 3.0. A geochronological toolkit for Microsoft Excel. *Berkeley Geochronology Center Special Publication* 4, 70.
- Lulu, T.T., 1993. Geology and petrography of Gülşehir area, Nevşehir, Turkey. MSc Thesis, Middle East Technical University, Ankara, Turkey [unpublished].
- MacKenzie, W.S., Adams, A.E., 2003. A colour atlas of rocks and minerals in thin section. *Manson Publishing Ltd, London*.
- McDougall, I., Harrison, T.M., 1999. Geochronology and Thermochronology by the  $^{40}\text{Ar}/^{39}\text{Ar}$  Method (2nd edition). *Oxford Univ. Press, New York*, 269.
- McFadden, P.L., McElhinny, L.W., 1988. The combined analysis of remagnetization circles and direct observations in palaeomagnetism. *Earth and Planetary Science Letters* 87, 161-172.
- Mckenna, L.W., Hodges, K.V., 1988. Accuracy Versus Precision in Locating Reaction Boundaries - Implications for the Garnet Plagioclase Aluminum Silicate Quartz Geobarometer. *American Mineralogist* 73(9-10), 1205-1208.
- Meijers, M.J.M., Kaymakci, N., van Hinsbergen, D.J.J., Langereis, C.G., Stephenson, R.A., Hippolyte, J.C., 2010. Late Cretaceous to Paleocene oroclinal bending in the central Pontides (Turkey). *Tectonics* 29, TC4016, doi:10.1029/2009TC002620.
- Miyashiro, A., 1961. Evolution of metamorphic belts. *Journal of Petrology* 2(3), 277-311.
- Miyashiro, A., 1973. Metamorphism and metamorphic belts. *G. Allen & Unwin, London*, 492 pp.
- Moix, P., Beccaletto, L., Kozur, H.W., Hochard, C., Rosselet, F., Stampfli, G.M., 2008. A new classification of the Turkish terranes and sutures and its implications for the Paleotectonic history of the region. *Tectonophysics* 451(1-4), 7-39.
- Niitsuma, N., 1996. The trench-trench-trench type triple junction and tectonic evolution of Japan. *Geoscience Reports of Shizuoka University* 23, 1-8.
- Okay, A.I., 1981. The geology and blueschist metamorphism of the ophiolites in northwest Turkey (Tavşanlı-Kütahya) (in Turkish). *Türkiye Jeoloji Kurumu Bülteni* 24, 85-95.
- Okay, A.I., 1982. Incipient Blueschist Metamorphism and Metasomatism in the Tavşanlı Region, Northwest Turkey. *Contributions to Mineralogy and Petrology* 79(4), 361-367.
- Okay, A.I., 1989. Tectonic units and sutures in the Pontides, northern Turkey. In: A.M.C. Şengör (Editor), Tectonic evolution of the Tethyan region. *Kluwer Academic Publications, Dordrecht* 109-115.
- Okay, A.I., Harris, N.B.W., Kelley, S.P., 1998. Exhumation of blueschists along a Tethyan suture in northwest Turkey. *Tectonophysics* 285(3-4), 275-299.
- Okay, A.I., Tüysüz, O., 1999. Tethyan sutures of northern Turkey. In: The Mediterranean Basins: Tertiary Extension within the Alpine Orogen (Eds. Durand, B., Jolivet, L., Horváth, F., Séranne, M.). *Geological Society, London, Special Publication* 156, 475-515.
- Okay, A.I., Tansel, I., Tüysüz, O., 2001. Obduction, subduction and collision as reflected in the Upper Cretaceous-Lower Eocene sedimentary record of western Turkey. *Geological Magazine* 138(2), 117-142.
- Okay, A.I., Tuysuz, O., Satir, M., Ozkan-Altiner, S., Altiner, D., Sherlock, S., Eren, R.H., 2006. Cretaceous and Triassic subduction-accretion, high-pressure-low-temperature metamorphism, and continental growth in the Central Pontides, Turkey. *Geological Society of America Bulletin* 118(9-10), 1247-1269.
- Oktay, F.Y., 1982. Ulukışla ve çevresinin stratigrafisi ve jeolojik evrimi. *Türkiye Jeoloji Kurumu Bülteni* 25, 15-25.
- Otlu, N., Boztağ, A., 1998. The coexistence of the silica oversaturated (ALKOS) and undersaturated alkaline (ALKUS) rocks in the Kortundağ and Baranadağ plutons from the Central Anatolian Alkaline Plutonism, East Kaman / NW Kırşehir, Turkey. *Turkish Journal of Earth Sciences* 7, 241-257.
- Özcan, A., Erkan, A., Keskin, A., Oral, A., Sümengen, M., Tekeli, O., 1980. Kuzey Anadolu Fayı-Kırşehir Masifi arasının temel jeolojisi. *MTA Report* 6722 (unpublished), Ankara, Turkey.
- Piper, J.D.A., Gursoy, H., Tatar, O., 2002. Palaeomagnetism and magnetic properties of the Cappadocian ignimbrite succession, central Turkey and Neogene tectonics of the Anatolian

- collage. *Journal of Volcanology and Geothermal Research* 117(3-4), 237-262.
- Platzman, E.S., Tapirdamaz, C., Sanver, M., 1998. Neogene anticlockwise rotation of central Anatolia (Turkey): preliminary palaeomagnetic and geochronological results. *Tectonophysics* 299, 175-189.
- Poisson, A., Guezou, J.C., 1996. Tectonic setting and evolution of the sivas basin, Central anatolia, Turkey. *International Geology Review* 38, 838-853.
- Pourteau, A., Candan, O., Oberhänsli, R., 2010. High-pressure metasediments in central Turkey: Constraints on the Neotethyan closure history. *Tectonics* 29, TC5004, doi:10.1029/2009TC002650.
- Renne, P.R., Mundil, R., Balco, G., Min, K.W., Ludwig, K.R., 2010. Joint determination of K-40 decay constants and Ar-40\*/K-40 for the Fish Canyon sanidine standard, and improved accuracy for Ar-40/Ar-39 geochronology. *Geochimica Et Cosmochimica Acta* 74(18), 5349-5367.
- Ring, U., Johnson, C., Hetzel, R., Gessner, K., 2003. Tectonic denudation of a Late Cretaceous-Tertiary collisional belt: regionally symmetric cooling patterns and their relation to extensional faults in the Anatolide belt of western Turkey. *Geological Magazine* 140(4), 421-441.
- Ring, U., Will, T., Glodny, J., Kumerics, C., Gessner, K., Thomson, S., Gungor, T., Monie, P., Okrusch, M., Druppel, K., 2007. Early exhumation of high-pressure rocks in extrusion wedges: Cycladic blueschist unit in the eastern Aegean, Greece, and Turkey. *Tectonics* 26, TC2001, doi:10.1029/2005TC001872.
- Ring, U., Glodny, J., Will, T., Thomson, S., 2010. The Hellenic Subduction System: High-Pressure Metamorphism, Exhumation, Normal Faulting, and Large-Scale Extension. *Annual Review of Earth and Planetary Sciences* 38, 45-76.
- Şahin, M.B., Erkan, Y., 1994. Petrological features of the metamorphics of the Yukarıçulhalı-Başçatak segment of the Akdağmadeni Massif. *Mineral Research Exploration Bulletin* 116, 39-46.
- Şahin, M.B., Erkan, Y., 1999. The index minerals and mineral assemblages determined in metamorphites of Evciler-Çatköy (Çayıralan-Yozgat) segment of the Akdağmadeni Massif. *Mineral Research Exploration Bulletin* 121(83-100).
- Sanver, M., Ponar, E., 1981. Kırşehir ve dolaylarına ilişkin paleomanyetik bulgular, Kırşehir Masifinin rotasyonu. *Istanbul Yerbilimleri* 2, 231-238.
- Satir, M., Friedrichsen, H., 1986. The Origin and Evolution of the Menderes Massif, Western Turkey - a Rubidium Strontium and Oxygen Isotope Study. *Geologische Rundschau* 75(3), 703-714.
- Seaton, N.C.A., Whitney, D.L., Teyssier, C., Toraman, E., Heizler, M.T., 2009. Recrystallization of high-pressure marble (Sivrihisar, Turkey). *Tectonophysics* 479(3-4), 241-253.
- Şengör, A.M.C., Yılmaz, Y., 1981. Tethyan Evolution of Turkey - a Plate Tectonic Approach. *Tectonophysics* 75(3-4), 181-241.
- Şengör, A.M.C., Satir, M., Akkök, R., 1984. Timing of Tectonic Events in the Menderes Massif, Western Turkey - Implications for Tectonic Evolution and Evidence for Pan-African Basement in Turkey. *Tectonics* 3(7), 693-707.
- Seymen, I., 1981. Stratigraphy and metamorphism of the Kırşehir Massif around Kaman (Kırşehir - Turkey). *Bulletin of Geological Society of Turkey* 24, 7-14.
- Seymen, I., 1982. Kaman Dolayında Kırşehir masifi'nin Jeolojisi. . ITÜ Maden Fakültesi, Doçentlik Tezi, İstanbul, 164 p.
- Seymen, I., 1983. Tectonic features of Kaman Group in comparison with those of its neighbouring formations around Tamadağ (Kaman-Kırşehir). *Bulletin of Geological Society of Turkey* 26, 89-98.
- Seymen, I., 1984. Geological evolution of the metamorphic rocks in the Kırşehir Massif. *Keleşim Sempozyumu*, 133-148.
- Seymen, I., 2000. Geology of the Kırşehir Massif between the Savcılıbeyit (Kaman) and Yeşilli (Kırşehir) villages. *Congress of Geosciences and Mining for the 75th anniversary of the Turkish Republic*. Proceedings Book 1, MTA Ankara, 67-91 (in Turkish with english abstract).
- Sherlock, S., Kelley, S., Inger, S., Harris, N., Okay, A., 1999. Ar-40-Ar-39 and Rb-Sr geochronology of high-pressure metamorphism and exhumation history of the Tavsanlı Zone, NW Turkey. *Contributions to Mineralogy and Petrology* 137(1-2), 46-58.
- Spear, F., Cheney, J., 1989. A petrogenetic grid for pelitic schists in the system SiO<sub>2</sub>-Al<sub>2</sub>O<sub>3</sub>-FeO-MgO-K<sub>2</sub>O-H<sub>2</sub>O. *Contributions to Mineralogy and Petrology* 101(2), 149-164.
- Spiegel, M.R., 1991. Theory and problems of statistics. 2nd edition (Shaum's Outline Series).
- Taira, A., 2001. Tectonic evolution of the Japanese island arc system. *Annual Review of Earth and Planetary Sciences* 29, 109-134.
- Tatar, O., Piper, J.D.A., Gürsoy, H., Temiz, H., 1996. Regional Significance of Neotectonic

- Counterclockwise Rotation in Central Turkey. *International Geology Review* 38, 692-700.
- Tauxe, L., Kent, D.V. 2004. A simplified statistical model for the geomagnetic field and the detection of shallow bias in paleomagnetic inclinations: Was the ancient magnetic field dipolar? In: Timescales of the Paleomagnetic Field (edited by Channell, J. E. T., Kent, D. V., Lowrie, W. & Meert, J. G.) 145. *AGU Geophysical Monograph, Washington*, 101-115.
- Tekin, U.K., Göncüoğlu, M.C., Turhan, N., 2002. First evidence of Late Carnian radiolarians from the Izmir-Ankara suture complex, central Sakarya, Turkey: implications for the opening age of the Izmir-Ankara branch of Neo-Tethys. *Geobios* 35(1), 127-135.
- Teklehamanot, L.T., 1993. Geology and Petrography of Gülşehir area, Nevşehir, Turkey. MSc thesis, Middle East Technical University, Ankara, Turkey [unpublished].
- Titton, G.R., Grunefelder, M.H., 1968. Sphe-ne: uranium-lead ages. *Science* 159, 1458-1461.
- Tolluoğlu, A.Ü., Erkan, Y., 1989. Regional progressive metamorphism in the Central Anatolian Crystalline Basement, NW Kırşehir Massif, Turkey. *METU Journal of Pure and Applied Sciences* 22(3), 19-41.
- Tolluoğlu, A.Ü., 1993. Kırşehir Masifini kesen felsik intruziflerin (Kötüdağ ve Buzlukdağ) petrografik ve Jeokimyasal karakterleri. *Hacettepe Üniversitesi Yerbilimleri Dergisi* 16, 19-41 (in Turkish with English abstract).
- Toprak, V., 1994. Central Kızılırmak Fault Zone: Northern margin of Central Anatolian Volcanics. *Turkish Journal of Earth Sciences* 3, 29-38.
- Torsvik, T.H., Muller, R.D., Van der Voo, R., Steinberger, B., Gaina, C., 2008. Global plate motion frames: Toward a unified model. *Reviews of Geophysics* 46(3).
- Türel, T.K., 1991. Geology, petrography and geochemistry of Ekecikdağ plutonic rocks (Aksaray region - Central Anatolia). Ph.D. Thesis, Middle Eastern Technical University (METU), Ankara, 194 pp.
- Tüysüz, O., Dellaloglu, A.A., Terzioglu, N., 1995. A magmatic belt within the Neo-Tethyan suture zone and its role in the tectonic evolution of northern Turkey. *Tectonophysics* 243(1-2), 173-191.
- Umhoefer, P.J., Whitney, D.L., Teyssier, C., Fayon, A.K., Casale, G., Heizler, M.T., 2007. Yo-yo tectonics in a wrench zone, Central Anatolian fault zone, Turkey. *Geological Society of America Special Papers* 434, 35-57.
- Vache, R., 1963. Akdağmadeni kontak yatakları ve bunların Orta Anadolu Kristalinine karşı olan jeolojik çerçevesi (in Turkish with English Abstract). *Bulletin of the Mineral Research and Exploration Institute of Turkey* 60, 20-34.
- Van der Voo, R., 1990. The reliability of paleomagnetic data. *Tectonophysics* 184, 1-9.
- van Hinsbergen, D.J.J., 2010. A key extensional metamorphic complex reviewed and restored: The Menderes Massif of western Turkey. *Earth Science Reviews* 102(1-2), 60-76.
- van Hinsbergen, D.J.J., Kaymakci, N., Spakman, W., Torsvik, T.H., 2010. Reconciling the geological history of western Turkey with plate circuits and mantle tomography. *Earth and Planetary Science Letters* 297(3-4), 674-686.
- Whitney, D.L., Dilek, Y., 1997. Core complex development in central Anatolia, Turkey. *Geology* 25(11), 1023-1026.
- Whitney, D.L., Dilek, Y., 1998. Metamorphism during Alpine crustal thickening and extension in central Anatolia, Turkey: the Niğde metamorphic core complex. *Journal of Petrology* 39(7), 1385-1403.
- Whitney, D.L., Dilek, Y., 2001. Metamorphic and tectonic evolution of the Hırkadağ Block, Central Anatolian Crystalline Complex. *Turkish Journal of Earth Sciences* 10, 1-15.
- Whitney, D.L., Teyssier, C., Dilek, Y., Fayon, A.K., 2001. Metamorphism of the Central Anatolian Crystalline Complex, Turkey: influence of orogen-normal collision vs, wrench-dominated tectonics on P-T-t paths. *Journal of Metamorphic Geology* 19(4), 411-432.
- Whitney, D.L., Teyssier, C., Fayon, A.K., Hamilton, M.A., Heizler, M., 2003. Tectonic controls on metamorphism, partial melting, and intrusion: timing and duration of regional metamorphism and magmatism in the Niğde Massif, Turkey. *Tectonophysics* 376(1-2), 37-60.
- Whitney, D.L., Hamilton, M.A., 2004. Timing of high-grade metamorphism in central Turkey and the assembly of Anatolia. *Journal of the Geological Society, London* 161, 823-828.
- Whitney, D.L., Teyssier, C., Heizler, M.T., 2007. Gneiss domes, metamorphic core complexes, and wrench zones: Thermal and structural evolution of the Niğde Massif, central Anatolia. *Tectonics* 26, TC5002, doi:10.1029/2006TC002040.
- Whitney, D.L., Davis, P.B., 2008. Petrogenesis and structural petrology of high-pressure metabasalt pods, Sivrihisar, Turkey. *Contributions to Mineralogy and Petrology* 156(2), 217-241.
- Whitney, D.L., Evans, B.W., 2010. Abbreviations for names of rock-forming minerals. *American Mineralogist* 95(1), 185-187.
- Yaliniz, K.M., Göncüoğlu, M.C., 1998. General geological characteristics and distribution of

- the Central anatolian Ophiolites. *Yerbilimleri* 20, 19-30.
- Yaliniz, M.K., Floyd, A.P., Göncüoğlu, M.C., 1996. Supra-subduction zone ophiolites of Central Anatolia: geochemical evidence from the Sarikaraman Ophiolite, Askaray, Turkey. *Mineralogical Magazine* 60(402), 697-710.
- Yaliniz, M.K., Aydın, N.S., Göncüoğlu, M.C., Parlak, O., 1999. Terlemez quartz monzonite of CA (Askaray-Sarikaraman): age, petrogenesis and geotectonic implications for ophiolite emplacement. *Geological Journal* 34, 233-242.
- Yaliniz, M.K., Floyd, A.P., Göncüoğlu, M.C., 2000a. Geochemistry of volcanic rocks from the Çiçekdağ Ophiolite, Central Anatolia, Turkey, and their inferred tectonic setting within the northern branch of the Neotethyan Ocean. *Geological Society of London, Special Publications* 173, 203-218.
- Yaliniz, M.K., Göncüoğlu, M.C., Ozkan-Altiner, S., 2000b. Formation and emplacement ages of the SSZ-type Neotethyan ophiolites in Central Anatolia, Turkey: palaeotectonic implications. *Geological Journal* 35(2), 53-68.
- Yaliniz, M.K., 2008. A Geochemical Attempt to Distinguish Forearc and Back Arc Ophiolites from the "Supra-Subduction" Central Anatolian Ophiolites (Turkey) by Comparison with Modern Oceanic Analogues. *Ofioliti* 33(2), 119-134.
- Yilmaz, S., Boztuğ, D., 1998. Petrogenesis of the Çiçekdağ Igneous Complex, N of Kırşehir, Central Anatolia, Turkey. *Turkish Journal of Earth Sciences* 7, 185-199.
- Zijderveld, J.D.A. 1967. A. C. demagnetization of rocks: analysis of results. In: *Methods in Palaeomagnetism* (edited by Collinson, D. W., Creer, K. M. & Runcorn, S. K.). Elsevier, Amsterdam, New York, 254-286.

Faculty of Geosciences  
Department Earth Sciences



**Universiteit Utrecht**

ISBN 978-90-6266-283-8